Nuclear Science

OECD
OCDE

Shielding Aspects of Accelerators, Targets and Irradiation Facilities – SATIF-4

Workshop Proceedings
Knoxville, Tennessee, USA
17-18 September 1998

NUCLEAR • ENERGY • AGENCY

Proceedings of the Fourth Specialists Meeting on

Shielding Aspects of Accelerators, Targets and Irradiation Facilities

Knoxville, Tennessee, USA
17-18 September 1998

jointly organised by
OECD/Nuclear Energy Agency
Oak Ridge National Laboratory
Radiation Safety Information Computational Centre
Shielding Working Group of the Reactor Physics Committee of Japan

NUCLEAR ENERGY AGENCY
ORGANISATION FOR ECONOMIC CO-OPERATION AND DEVELOPMENT

ORGANISATION FOR ECONOMIC CO-OPERATION AND DEVELOPMENT

Pursuant to Article 1 of the Convention signed in Paris on 14th December 1960, and which came into force on 30th September 1961, the Organisation for Economic Co-operation and Development (OECD) shall promote policies designed:

- to achieve the highest sustainable economic growth and employment and a rising standard of living in Member countries, while maintaining financial stability, and thus to contribute to the development of the world economy;
- to contribute to sound economic expansion in Member as well as non-member countries in the process of economic development; and
- to contribute to the expansion of world trade on a multilateral, non-discriminatory basis in accordance with international obligations.

The original Member countries of the OECD are Austria, Belgium, Canada, Denmark, France, Germany, Greece, Iceland, Ireland, Italy, Luxembourg, the Netherlands, Norway, Portugal, Spain, Sweden, Switzerland, Turkey, the United Kingdom and the United States. The following countries became Members subsequently through accession at the dates indicated hereafter; Japan (28th April 1964), Finland (28th January 1969), Australia (7th June 1971), New Zealand (29th May 1973), Mexico (18th May 1994), the Czech Republic (21st December 1995), Hungary (7th May 1996), Poland (22nd November 1996) and the Republic of Korea (12th December 1996). The Commission of the European Communities takes part in the work of the OECD (Article 13 of the OECD Convention).

NUCLEAR ENERGY AGENCY

The OECD Nuclear Energy Agency (NEA) was established on 1st February 1958 under the name of OEEC European Nuclear Energy Agency. It received its present designation on 20th April 1972, when Japan became its first non-European full Member. NEA membership today consists of all OECD Member countries, except New Zealand and Poland. The Commission of the European Communities takes part in the work of the Agency.

The primary objective of the NEA is to promote co-operation among the governments of its participating countries in furthering the development of nuclear power as a safe, environmentally acceptable and economic energy source.

This is achieved by:

- *encouraging harmonization of national regulatory policies and practices, with particular reference to the safety of nuclear installations, protection of man against ionising radiation and preservation of the environment, radioactive waste management, and nuclear third party liability and insurance;*
- *assessing the contribution of nuclear power to the overall energy supply by keeping under review the technical and economic aspects of nuclear power growth and forecasting demand and supply for the different phases of the nuclear fuel cycle;*
- *developing exchanges of scientific and technical information particularly through participation in common services;*
- *setting up international research and development programmes and joint undertakings.*

In these and related tasks, the NEA works in close collaboration with the International Atomic Energy Agency in Vienna, with which it has concluded a Co-operation Agreement, as well as with other international organisations in the nuclear field.

FOREWORD

Accelerators play an increasingly important role in technological, energy and medical applications. As accelerators become more widely used and as their power increases, challenging new problems arise that require attention from the point of view of the characterisation of radiation environments and radiological safety.

The Nuclear Science Committee of the OECD Nuclear Energy Agency has sponsored a series of meetings on *Shielding Aspects of Accelerators and Irradiation Facilities (SATIF)* which have been held every 18 months since 1994. SATIF-1 was held on 28-29 April 1994 in Arlington, Texas; SATIF-2 on 12-13 October 1995 at CERN in Geneva, Switzerland; SATIF-3 on 12-13 May 1997 at Tohoku University in Sendai, Japan; and SATIF-4 was held from 17-18 September 1998 in Knoxville, Tennessee.

A specific task force was set up to co-ordinate the group's activities. Objectives include:

- identifying needs and carrying out experiments to improve the knowledge of thin and thick target neutron yields, neutron penetration, streaming, skyshine, etc.;
- making proposals, having discussions and executing shielding experiments in order to improve shield modelling;
- exchanging information on the status of computer codes and nuclear data files currently in use;
- selecting shielding benchmark experiments in order to establish international collaboration in the area of method validation;
- investigating high-energy dosimetry aspects including anthropomorphic computing models.

The task force meetings were held in conjunction with the seminar on Simulating Accelerator Radiation Environments (SARE), which concentrates on presenting new developments and experience in simulating radiation environments and on exchanging information. Holding the meetings simultaneously has improved synergy between the different aspects and research committees. This year, a topical meeting on Accelerator Applications (AccApp'98) served to further complement the activities and discussion of SATIF-4 and SARE.

The current proceedings provide a summary of the discussions, decisions and conclusions together with the text of the presentations made at the fourth SATIF meeting.

Acknowledgements

The high quality of the SATIF-4 meeting and its excellent organisation would not have been possible without the hard work of the Local Organising Committee at ORNL and its Chairman, Dr. Tony Gabriel.

Acknowledgements are also due to the members of the SATIF-4 Technical Programme Committee, F. Clapier, A. Fassò, D. Filges, T. Gabriel, N. Ipe, B. Kirk, T. Nakamura, M. Pelliccioni, R. Roussin (Chairman), Y. Sakamoto, E. Sartori, M. Silari, P. Vaz and N. Yoshizawa, for their contribution in shaping the technical programme. Special thanks go to Amanda McWhorter for her dedication in editing these proceedings and her efforts to improve the layout of the text.

TABLE OF CONTENTS

EXECUTIVE SUMMARY

The main objectives of the SATIF meetings are:

- to promote the exchange of information among scientists in this particular field;
- to identify areas in which international co-operation could be fruitful;
- to carry on a programme of work in order to achieve progress in specific priority areas.

The first SATIF meeting (SATIF-1) took place in Arlington, Texas (USA) from 29-30 April 1994, the second meeting (SATIF-2) was held from 12-13 October 1995 at CERN (European Laboratory for Particles Physics) in Geneva, Switzerland and the third meeting took place from 12-13 May 1997 at Tohoku University (Sendai, Japan).

As a consequence of the success of these conferences, the seventh meeting of the NEA Nuclear Science Committee, held on 29-30 May 1996, approved the establishment of a specific Task Force on Shielding Aspects of Accelerators, Targets and Irradiation Facilities. Consequently, the SATIF specialists meetings became regular meetings of this Task Force.

It is generally recognised that the three SATIF meetings preceding SATIF-4 have fostered considerable and significant co-operative actions and efforts at the international level, in areas such as:

- *Basic data:* New measurements, compilation of existing neutron, proton, light ion and pion cross-section data in the intermediate energy range above a few dozens of MeV, forward bremsstrahlung yields from thick targets at energies above 100 MeV, photoproduction data (namely photonuclear cross-sections and photonuclear yields and angular distributions for all common elements at all energies), photo-pion yields and angular distributions at energies above 200 MeV, isotope production data, etc.

- *Nuclear models and computer codes in the intermediate energy range*: Code validation, intercomparison of codes, comparison between experimental data and predictions from existing computer codes implementing nuclear models.

- *Shielding experiments*: Measurements of forward and lateral attenuation of iron and concrete for proton and ion accelerators up to a few tens of GeV and as deep as possible, i.e. at least 5-6 meters, measurement of forward and lateral attenuation at electron accelerators.

- *Benchmark data*: Development of new benchmark exercises, compilation of existing benchmark data sets, etc.

- *Anthropomorphic computational models*: Compilation of existing models, phantom geometry and material compositions, dosimetry studies, etc.

- *New or better measurements of many activation detector excitation functions*: In particular ^{11}C production by neutrons and pions in the energy range above 100 MeV and Bi production.

The SATIF meetings are held in conjunction with SARE (Simulating Accelerator Radiation Environment) meetings. Both are attended by (and share) a community of users coming from different fields of science and technology, and the two meetings tend to be complementary in their subject matter. Indeed, SATIF was originally designed as a forum of discussion and exchange of information in order to identify areas in which international co-operation is needed or needs to be strengthened. In the past, special attention has been paid to:

- the availability and compilation of experimental data for different applications;

- the organisation of international benchmark exercises;

- the availability of computer codes and data libraries for the use of the scientific community involved in various aspects related to accelerator shielding and applications;

- identifying areas in which international co-operation can contribute to solve existing problems.

The presentations made at the successive SATIF meetings can generally be categorised according to the following topics:

- data;

- benchmarks;

- computer codes and models;

- facilities;

- shielding techniques;

- conversion coefficients;

- code intercomparisons;

- status of codes.

The fourth meeting – SATIF-4

The fourth meeting of the SATIF Task Force (SATIF-4) took place from 17-18 September 1998 at the Hyatt Regency Hotel in Knoxville, Tennessee, USA. It was jointly organised by:

- the OECD Nuclear Energy Agency;

- the Oak Ridge National Laboratory (ORNL);

- the Radiation Safety Information Computational Centre (RSICC);
- the Shielding Working Group of the Reactor Physics Committee of Japan.

About fifty specialists attended the meeting, among them physicists, engineers and technicians from laboratories, institutes, universities and industries in France (IN2P3), Germany (DESY, KFA Jülich, University of Munich), Italy (INFN, ENEA), Spain (University of Barcelona), Japan (CYRIC, JAERI, KEK, RIKEN, Universities of Kyoto, Tokyo and Tohoku, Mitsubishi and Hitachi Corporation), USA (ANL, CEBAF, Fermilab, LANL, LLNL, ORNL, RSICC, SLAC, Georgia Institute of Technology, Universities of Michigan and Northern Illinois), the Russian Federation (IHEP, INR, MRI) and P.R. of China, as well as representatives from international organisations (CERN and OECD/NEA).

The meeting was organised in seven sessions, each addressing different issues:

- *Session 1*: Source Term and Related Data – Electron Accelerators
- *Session 2*: Source Term and Related Data – Proton and Ion Accelerators
- *Session 3*: Shielding Design Problems on High Intensity Medium Energy Accelerators and Target Facilities
- *Session 4*: Shielding Benchmark Calculations and Results
- *Session 5*: Miscellaneous Topics
- *Session 6*: Present Status of Computer Codes and Cross-Section and Shielding Data Libraries
- *Session 7*: Discussions and Future Actions

Twenty-four papers were presented at the meeting. An extensive discussion took place during Session 7, with the following pre-established objectives:

- to review the progress achieved since the SATIF-3 meeting;
- to monitor the status of the agreed actions (on experiments, benchmark organisation, compilation of basic data, codes and methods) undertaken since then;
- to identify and initiate new co-operative actions;
- to improve common understanding of problems that have technical and safety significance;
- to review the current organisation of the SATIF meetings and to discuss the organisation of future meetings.

At SATIF-4, the following categories of facilities involving the operation of particle accelerators have been identified as potentially benefiting from the activities of the SATIF Task Force:

- medium energy proton accelerators;
- spallation sources;

- heavy ion facilities, for:
  - nuclear physics (including radioactive ion beams);
  - radiation therapy;
- synchrotron radiation facilities;
- very high energy radiation facilities;
- accelerator production of tritium;
- free electron lasers.

Furthermore, for each of the following types of facility, priority items have been listed as indicated below and actions should be undertaken in the corresponding domains:

- *Heavy ion accelerators*:
  - attenuation length calculations;
  - models;
  - source terms;
  - codes and parametrisations.
- *Spallation sources and medium energy proton accelerators*:
  - attenuation length calculations for iron and concrete;
  - availability of elastic and inelastic cross-sections for different energies;
  - thin and thick targets yields;
  - source terms;
  - material damage data.
- *Electron accelerators*:
  - photonuclear cross-sections and yields;
  - angular bremsstrahlung yields.
- *All accelerators*:
  - soil and groundwater activation data;
  - techniques and data to predict activation in structural components;
  - activation cross-sections.

Concerning the organisation of benchmark and intercomparison exercises:

- Results were presented on the intercomparison of neutron transmission benchmark analysis for iron and concrete in TIARA and on the intercomparison of the medium-energy neutron attenuation in these materials. It was decided to extend the intercomparisons and to include other codes which have not yet been used.

- A proposal for the organisation of an international Benchmark Exercise on Electron and Photon physics (BEEP) was discussed and accepted. A special group was created, under the chairmanship of A. Bielajew, to define the benchmark specifications and to conduct the benchmark exercise which should in principle gather experts and code developers for the major codes such as CALOR95, EGS, FLUKA, ITS, MCNP and PENELOPE (for further details please refer to A. Bielajew's contribution in this proceedings).

With regard to the state-of-the-art computer codes and data libraries available for the use of scientists in the field of radiation shielding, an exhaustive and updated list of computer codes, data libraries and databases has been produced which is included in this proceedings. This compilation issued by RSICC in collaboration with the NEA Data Bank is a valuable reference for the community of users.

Among other actions decided upon at the discussion session were:

- to pursue the collection of experimental data sets available;

- to continue the activities on data compilations, giving particular emphasis to data availability for the user community;

- to further develop the activities on intercomparison exercises, between modelling methods (e.g. computer codes) available and experimental data;

- to discuss and confront the different approaches to "deep penetration problems" (e.g. hybrid (ORNL and Jülich), pure Monte Carlo (CERN and Fermilab) or both (Japan));

- to develop and strengthen the activities on conversion coefficients and anthropomorphic computational models.

In order to make sure that significant progress is achieved and that an effective follow up is performed, it was decided to assign the coordination of the actions undertaken in specific domains to the following persons or institutions:

- electron transport benchmark – A. Bielajew;

- conversion coefficients, antropomorphic computational models – N. Yoshizawa;

- attenuation lengths (extension to other codes and to higher energies) – H. Hirayama;

- photonuclear cross-sections – A. Fassò;

- deep penetration problems (different approaches) – G. Stevenson and J. Bull;

- ground activation – CERN.

Concerning the organisation of future SATIF meetings, it was felt by the majority of the SATIF participants that:

- Although both the SARE and SATIF meetings play a complementary role, there is an overlap between the two sets of presentations and subjects discussed.

- In order to avoid duplication, there is a need for defining a new organic structure for the organisation of the next meetings, eventually leading to the nomination of a unified Technical Programme Committee for both SARE and SATIF meetings.

- Future meetings will be held every 24 months, instead of every 18 months, as has been the case up to now.

Therefore, the next meeting (SATIF-5) should be held during the year 2000 in Europe.

In this respect, the co-ordination role of the NEA in co-operation with the RSICC in promoting and sponsoring SATIF activities has been stated. The NEA will submit for discussion a proposal for the definition of a new group structure and the templates for the organisational details.

ORGANISATION FOR ECONOMIC CO-OPERATION AND DEVELOPMENT

Pursuant to Article 1 of the Convention signed in Paris on 14th December 1960, and which came into force on 30th September 1961, the Organisation for Economic Co-operation and Development (OECD) shall promote policies designed:

- to achieve the highest sustainable economic growth and employment and a rising standard of living in Member countries, while maintaining financial stability, and thus to contribute to the development of the world economy;
- to contribute to sound economic expansion in Member as well as non-member countries in the process of economic development; and
- to contribute to the expansion of world trade on a multilateral, non-discriminatory basis in accordance with international obligations.

The original Member countries of the OECD are Austria, Belgium, Canada, Denmark, France, Germany, Greece, Iceland, Ireland, Italy, Luxembourg, the Netherlands, Norway, Portugal, Spain, Sweden, Switzerland, Turkey, the United Kingdom and the United States. The following countries became Members subsequently through accession at the dates indicated hereafter: Japan (28th April 1964), Finland (28th January 1969), Australia (7th June 1971), New Zealand (29th May 1973), Mexico (18th May 1994), the Czech Republic (21st December 1995), Hungary (7th May 1996), Poland (22nd November 1996) and Korea (12th December 1996). The Commission of the European Communities takes part in the work of the OECD (Article 13 of the OECD Convention).

NUCLEAR ENERGY AGENCY

The OECD Nuclear Energy Agency (NEA) was established on 1st February 1958 under the name of the OEEC European Nuclear Energy Agency. It received its present designation on 20th April 1972, when Japan became its first non-European full Member. NEA membership today consists of all OECD Member countries, except New Zealand and Poland. The Commission of the European Communities takes part in the work of the Agency.

The primary objective of the NEA is to promote co-operation among the governments of its participating countries in furthering the development of nuclear power as a safe, environmentally acceptable and economic energy source.

This is achieved by:

- *encouraging harmonization of national regulatory policies and practices, with particular reference to the safety of nuclear installations, protection of man against ionising radiation and preservation of the environment, radioactive waste management, and nuclear third party liability and insurance;*
- *assessing the contribution of nuclear power to the overall energy supply by keeping under review the technical and economic aspects of nuclear power growth and forecasting demand and supply for the different phases of the nuclear fuel cycle;*
- *developing exchanges of scientific and technical information particularly through participation in common services;*
- *setting up international research and development programmes and joint undertakings.*

In these and related tasks, the NEA works in close collaboration with the International Atomic Energy Agency in Vienna, with which it has concluded a Co-operation Agreement, as well as with other international organisations in the nuclear field.

SESSION I

Source Term and Related Data – Electron Accelerator

Chairs: H. Hirayama and A. Bielajew

DOSE MEASUREMENTS OF BREMSSTRAHLUNG-PRODUCED NEUTRONS FROM THICK TARGETS AT THE ADVANCED PHOTON SOURCE

P.K. Job, M. Pisharody, E. Semones
Experimental Facilities Division
Argonne National Laboratories, 9700 S. Cass Ave., Argonne IL 60439, USA

Abstract

Bremsstrahlung is produced in the Advanced Photon Source storage ring when the positron beam interacts with the storage ring components or with the residual gas molecules in the storage ring vacuum. This bremsstrahlung has an energy range of zero to 7.0 GeV, which is the maximum energy of the positron beam. Bremsstrahlung photons of sufficiently high energy can interact with beam line components such as beam stops and collimators, generating neutrons of varying energies. This paper presents the results of simultaneous measurements, conducted at the Advanced Photon Source, of bremsstrahlung and the corresponding photoneutron production from thick targets of iron, copper, tungsten and lead, which allow one to correlate photoneutron dose rates from these metals as a function of bremsstrahlung power. The average photoneutron dose equivalent rates, normalised to the bremsstrahlung power, are measured as 2.7 ± 0.5 rem/h/W for iron, 3.2 ± 0.5 rem/h/W for copper, 3.9 ± 0.5 rem/h/W for tungsten and 4.6 ± 0.8 rem/h/W for lead targets. These are measured at 80 cm lateral from the centre of the targets, perpendicular to the photon beam direction.

Introduction

Bremsstrahlung is generated at the Advanced Photon Source (APS) storage ring by the radiative interaction of the circulating positron beam with both the residual gas molecules and the storage ring components. Bremsstrahlung, produced along a typical 15.38 m straight path of the insertion device beam line of the APS, has been measured and analysed in previous studies [1,2]. The bremsstrahlung photons having sufficiently high energies ($E_\gamma > 5.0$ MeV), interacting with the beam line components like beam stops and collimators, can produce neutrons of varying energies by means of photonuclear interactions [3-6]. There are three processes by which photoneutrons may be produced by the high-energy bremsstrahlung photons: giant nuclear dipole resonance and decay ($E_\gamma < 40$ MeV), quasi-deuteron production and decay ($50 < E_\gamma < 300$ MeV), and intranuclear cascade and evaporation ($E_\gamma > 140$ MeV). The giant resonance neutrons (GRN) are emitted almost isotropically and have an average energy of about 2 MeV. High-energy neutrons ($E_n > 10$ MeV) emitted from quasi-deuteron decay and intranuclear cascade are peaked in the forward direction. At the APS, where bremsstrahlung energy can be as high as 7 GeV, production of photoneutrons is possible from all the above processes although the fraction from giant resonance interaction dominates.

A simultaneous measurement of bremsstrahlung and the corresponding photoneutron production provides photoneutron dose rates as a function of bremsstrahlung power. Along with our bremsstrahlung spectrum measurements [1,2], we conducted simultaneous dose measurements at the APS from thick targets of iron (Fe), copper (Cu), tungsten (W) and lead (Pb) that are placed in the bremsstrahlung beam inside the first optics enclosure (FOE) of the insertion device beam lines. An Andersson-Braun remmeter, that houses a very sensitive pressurised ^{3}He detector, is used primarily for the giant resonance neutron dose equivalent rate measurements. The dose equivalent rates, normalised to bremsstrahlung power, beam current and storage ring vacuum are measured for various targets.

Experimental set-up and procedure

Four targets, Fe, Cu, W and Pb, each approximately 20 radiation lengths (X_0) long and six Moliere radii in the lateral dimension, are used for these measurements. The dimensions of the target have been chosen such that approximately 99% of the electromagnetic shower in both the longitudinal and the lateral directions are contained within the targets. The selection of the typical lateral dimension of the targets is also to minimise self-absorption of the generated giant resonance photoneutrons within the target. Only an approximately 6% reduction in dose equivalent rate is estimated in these target dimensions [7]. A complete description of the four targets used is summarised in Table 1.

A schematic of the combined bremsstrahlung-photoneutron experimental set-up is shown in Figure 1. The target is placed inside the FOE of the beam line at about 170 cm from the beam exit window, aligned lengthways along the photon beam. The lead-glass electromagnetic calorimeter, the central tube of which is also aligned along the photon beam, is placed approximately 40 cm behind the target. During bremsstrahlung measurements, the target is removed from the photon beam. The neutron dose equivalent rate measurements are made perpendicular to the incident photon beam direction. The Andersson-Braun (AB) remmeter is placed at a distance of about 80 cm at right angles to the aligned target, with the centre of the remmeter aligned with the centre of the target. The insertion device gap is kept in full open position to minimise the low-energy synchrotron radiation. A copper shield, which is about $0.5X_0$ thick, is placed in front of the lead-glass calorimeter to screen against the low-energy residual synchrotron radiation arriving at the FOE.

Experimental runs are conducted in such a way that each of the photoneutron measurement is preceded and followed by one bremsstrahlung measurement. Once the bremsstrahlung data set is collected, the target is placed in its marked position and the corresponding photoneutron data set is acquired. Then another bremsstrahlung data set is taken by removing the target. The average power from the two bremsstrahlung data sets is then used to normalise the photoneutron data. The changes in the beam current during this time is minimal due to the long particle beam life time in the storage ring and thus the measurements are approximately simultaneous.

Results and discussion

The bremsstrahlung power and the corresponding photoneutron dose equivalent rates as a function of the beam current, measured 80 cm lateral from the targets, are given in Tables 2 and 3. The dose equivalent rates (DE) have been obtained from the net AB count rate using the calibration factors determined earlier. The errors shown on DE are statistical. The variation of neutron dose equivalent rate from each target as a function of the bremsstrahlung power is plotted in Figure 2 for the data given in Tables 2 and 3. The bremsstrahlung power plotted on the x-axis is an accurately measured quantity that relates to the actual storage ring vacuum and beam current variation. Thus, if the bremsstrahlung power is known, photoneutron dose equivalent rates from these four target materials can be normalised without having to rely on the storage ring parameters, like vacuum and beam current. The data from Figure 2, averaged over each target, is plotted in Figure 3 as a function of the atomic number Z of the target material. The error on these average dose rates due to elemental impurities in the targets is less than 1%. It can be seen that the average bremsstrahlung normalised photoneutron dose equivalent rates, measured 80 cm perpendicular to the target centre is 2.7 ± 0.5 rem/h/W for iron, 3.2 ± 0.5 rem/h/W for copper, 3.9 ± 0.5 rem/h/W for tungsten and 4.6 ± 0.8 rem/h/W for lead targets.

The systematic corrections to the measured photoneutron dose equivalent (DE) rates should include thick target correction, correction due to wall-reflected neutrons, and a correction for the non-giant resonance neutron dose contribution. The thick target correction addresses the reduction in the giant resonance neutron fluence due to self absorption in the targets. With our target dimensions, calculations indicate a 6% reduction in the DE rates due to self absorption [7]. The neutrons produced could also reflect from the concrete ratchet wall close to the target (Figure 2) resulting in a net artificial increase in fluence. The AB response to this artificial increase in fluence depends upon its proximity to the reflecting wall and the nature of the neutron spectrum. Calculations estimate a 10% increase in DE rates detected by the AB remmeter due to neutron reflection. An estimation of the dose correction due to high-energy neutrons (non-GRN) requires the high-energy photoneutron neutron yield, corresponding dose conversion factors, and the AB remmeter detection efficiency to these neutrons. Calculations using PICA [8] gives a 12% reduction in the measured DE rates due to non-GRN neutrons. The final result of the above discussed corrections is an 8% net increase in the measured dose equivalent rates.

Comparison with previous results

Not many measurements of photoneutron dose equivalent rates have been conducted previously at energies as high as 7 GeV. Therefore, a true comparison of the present results with the existing ones is difficult. The existing results from earlier measurements are mostly either from low-energy incident electrons and photons [9,10] or from analytical relations and Monte Carlo simulations [11,12]. However, comparisons have been made with photoneutron dose equivalent rates from low-energy

incident electrons deduced from the previous calculations [11]. These calculations do not take into account self-shielding effects. These results are also plotted in Figure 3 along with our measurements. The agreement is fairly good for tungsten and lead targets. For iron and copper targets the calculated values are smaller than the measurements.

The neutron dose equivalent rates from copper and tungsten, struck by bremsstrahlung produced from a 3 GeV electron storage ring are also discussed elsewhere [10]. These results are given normalised to storage ring vacuum and beam current. However an effort has been made to compare these results with our measurements from the beam line with the largest bremsstrahlung power. The comparison showed an order of magnitude difference in the photoneutron yield with our measurements. This is because the photoneutron dose rates normalised to beam current and vacuum may vary from beam line to beam line.

Conclusion

Photoneutron dose equivalent rates are measured as a function of bremsstrahlung power, from iron, copper, tungsten and lead thick targets placed in the bremsstrahlung beam at the insertion device beam lines of the Advanced Photon Source. The average photoneutron dose equivalent rates, normalised to the bremsstrahlung power, are measured as 2.7 ± 0.5 rem/h/W for iron, 3.2 ± 0.5 rem/h/W for copper, 3.9 ± 0.5 rem/h/W for tungsten, and 4.6 ± 0.8 rem/h/W for lead targets. These are measured at 80 cm lateral from the centre of the targets, perpendicular to the photon beam direction. The measured photoneutron dose equivalent rates normalised to beam current and the storage ring vacuum vary from beam line to beam line because of the difference in the corresponding bremsstrahlung power.

Acknowledgements

Work supported in part by the US Department of Energy, Contract No. W-31-109-ENG-38, BES-Material Sciences, Argonne National Laboratory.

REFERENCES

[1] M. Pisharody *et al*., Measurement of Gas Bremsstrahlung from the Insertion Device Beam Lines of the APS, Argonne National Laboratory Report, ANL-APS-LS-260 (1997).

[2] M. Pisharody *et al*., Measurement of Bremsstrahlung from the Electron Storage Rings, *Nucl. Instr. Meth*., A401, 442 (1997).

[3] J.S. Levinger, Theories of Photonuclear Reactions, *Ann. Rev. Nucl. Sci*., 4, 13 (1954).

[4] K. Strauch, Recent Studies of Photonuclear Reactions, *Ann. Rev. Nucl. Sci*., 2, 105 (1952).

[5] J.S. Levinger and H.A. Bethe, Neutron Yield from Nuclear Photoeffect, *Phy. Rev.*, 85, 577 (1952).

[6] J.S. Levinger, The High Energy Nuclear Photoeffect, *Phy. Rev*., 84, 43 (1951).

[7] G.T. Chapman, and C.L. Storrs, Effective Neutron Removal Cross-Sections for Shielding, AECD-3978 (1955).

[8] T.A. Gabriel *et al*., PICA – An Intranuclear Cascade Calculation for High Energy Photon Induced Nuclear Reactions, Oak Ridge National Laboratory Report, ORNL-4687 (1971).

[9] W.C. Barber and W.D. George, Neutron Yields from Targets Bombarded by Electrons, *Phy. Rev*. 116, 1551 (1959).

[10] J.C. Liu, *et al*., Gas Bremsstrahlung and Associated Photoneutron Shielding Calculations for the Electron Storage Rings, *Health Phy*. 68, 205 (1995).

[11] W.P. Swanson, Improved Calculation of the Photoneutron Yields Released by Incident Electrons, *Health. Phy*. 37, 347 (1979).

[12] X.S. Mao *et al*., Giant Dipole Resonance Neutron Yields Produced by Electrons as a Function of Target Material and Thickness, *Health Phy*. 70, 207 (1996).

Table 1. Target dimensions and elemental purities

Target material	Length	Width	Elemental purity
Fe	21.9 X_0 (38.4 cm)	5.9 X_m (9.6 cm)	93% Fe
Cu	19.5 X_0 (28.0 cm)	6.2 X_m (8.8 cm)	93% Cu
W	21.3 X_0 (8.0 cm)	6.1 X_m (6.0 cm)	95% W
Pb	20.5 X_0 (11.6 cm)	5.6 X_m (9.0 cm)	99% Pb

Table 2. Photoneutron dose equivalent rates at 80 cm lateral from target centres in beam line 11 ID

Target material	Beam current I_b (mA)	Measured vacuum P (nT)	Bremsstrahlung power (kW)	Net AB count rate N_n (cps)	Neutron dose equivalent rate DE (μrem/h)	Normalised neutron dose equivalent rate DE (μrem/h/kW)
Fe	96.6	9.26	1.66×10^{-8}	0.081	37.5±3.2	$(2.26\pm0.19)\times10^{9}$
Fe	93.3	8.95	1.72×10^{-8}	0.091	41.8±6.8	$(2.43\pm0.39)\times10^{9}$
Fe	90.2	8.70	1.63×10^{-8}	0.070	32.1±6.0	$(1.97\pm0.37)\times10^{9}$
Fe	81.2	8.04	1.24×10^{-8}	0.070	32.1±6.0	$(2.59\pm0.48)\times10^{9}$
Fe	80.3	7.96	1.20×10^{-8}	0.057	26.5±5.4	$(2.21\pm0.45)\times10^{9}$
Fe	72.5	7.23	8.96×10^{-8}	0.045	20.6±4.8	$(2.30\pm0.54)\times10^{9}$
Cu	96.0	9.20	1.81×10^{-8}	0.116	53.6±7.6	$(2.96\pm0.42)\times10^{9}$
Cu	93.2	8.92	1.68×10^{-8}	0.091	41.8±6.8	$(2.49\pm0.40)\times10^{9}$
Cu	87.3	9.51	1.48×10^{-8}	0.094	43.1±6.8	$(2.91\pm0.46)\times10^{9}$
Cu	83.2	8.12	1.28×10^{-8}	0.091	41.8±6.8	$(3.27\pm0.53)\times10^{9}$
Cu	77.5	7.71	1.14×10^{-8}	0.060	27.5±5.6	$(2.41\pm0.49)\times10^{9}$
W	88.3	8.64	1.53×10^{-8}	0.122	56.4±7.8	$(3.68\pm0.51)\times10^{9}$
W	87.9	8.56	1.58×10^{-8}	0.119	54.8±5.4	$(3.46\pm0.34)\times10^{9}$
W	79.5	7.82	1.18×10^{-8}	0.082	38.0±6.4	$(3.22\pm0.54)\times10^{9}$
W	79.2	7.90	1.10×10^{-8}	0.081	37.4±3.2	$(3.40\pm0.29)\times10^{9}$
W	76.5	7.61	1.07×10^{-8}	0.092	42.4±6.8	$(3.95\pm0.63)\times10^{9}$
Pb	90.9	8.87	1.62×10^{-8}	0.129	59.5±8.0	$(3.67\pm0.49)\times10^{9}$
Pb	79.4	7.79	1.20×10^{-8}	0.099	45.7±7.0	$(3.79\pm0.58)\times10^{9}$
Pb	78.5	7.76	1.12×10^{-8}	0.099	45.7±7.0	$(4.08\pm0.62)\times10^{9}$
Pb	70.8	7.08	8.96×10^{-8}	0.079	36.2±6.2	$(4.04\pm0.69)\times10^{9}$

Table 3. Photoneutron dose equivalent rates at 80 cm lateral from target centres in beam line 6 ID

Target material	Beam current I_b (mA)	Measured vacuum P (nT)	Bremsstrahlung power (kW)	Net AB count rate N_n (cps)	Neutron dose equivalent rate DE (μrem/h)	Normalised neutron dose equivalent rate DE (μrem/h/kW)
Fe,BF_3	93.4	9.77	5.31×10^{-9}	0.033	15.4±3.0	$(2.90\pm0.56)\times10^{9}$
Fe, BF_3	92.7	9.62	5.06×10^{-9}	0.031	14.5±2.8	$(2.87\pm0.55)\times10^{9}$
Fe,^{3}He	89.1	9.27	4.93×10^{-9}	0.102	12.9±1.4	$(2.61\pm0.28)\times10^{9}$
Fe,BF_3	78.2	8.41	3.71×10^{-9}	0.026	11.8±2.6	$(3.18\pm0.70)\times10^{9}$
Cu,^{3}He	90.3	9.44	4.10×10^{-9}	0.081	10.3±1.2	$(2.06\pm0.24)\times10^{9}$
Cu, BF_3	89.9	9.37	4.88×10^{-9}	0.034	15.7±3.0	$(3.20\pm0.61)\times10^{9}$
Cu, BF_3	81.1	8.59	4.09×10^{-9}	0.028	13.1±1.8	$(3.21\pm0.44)\times10^{9}$
Cu, BF_3	62.9	7.02	2.43×10^{-9}	0.018	8.5±2.2	$(3.50\pm0.91)\times10^{9}$
W,^{3}He	90.0	9.38	5.06×10^{-9}	0.139	17.7±1.6	$(3.49\pm0.32)\times10^{9}$
W,BF_3	87.0	9.19	4.64×10^{-9}	0.042	19.4±3.2	$(4.17\pm0.69)\times10^{9}$
W,^{3}He	85.7	9.10	4.63×10^{-9}	0.107	13.5±1.4	$(2.92\pm0.30)\times10^{9}$
W,BF_3	82.3	8.76	4.19×10^{-9}	0.034	15.5±3.0	$(3.71\pm0.72)\times10^{9}$
W,^{3}He	77.7	8.30	3.61×10^{-9}	0.111	14.0±1.0	$(3.89\pm0.28)\times10^{9}$
Pb,BF_3	76.1	8.22	3.55×10^{-9}	0.038	17.7±3.2	$(4.98\pm0.90)\times10^{9}$
Pb,BF_3	63.9	7.12	2.54×10^{-9}	0.027	12.3±2.6	$(4.84\pm1.02)\times10^{9}$

Figure 1. Schematic of the top view of the Andersson-Braun remmeter and the calorimeter along with the associated data acquisition systems that measure the photoneutron dose equivalent rates and the bremsstrahlung power

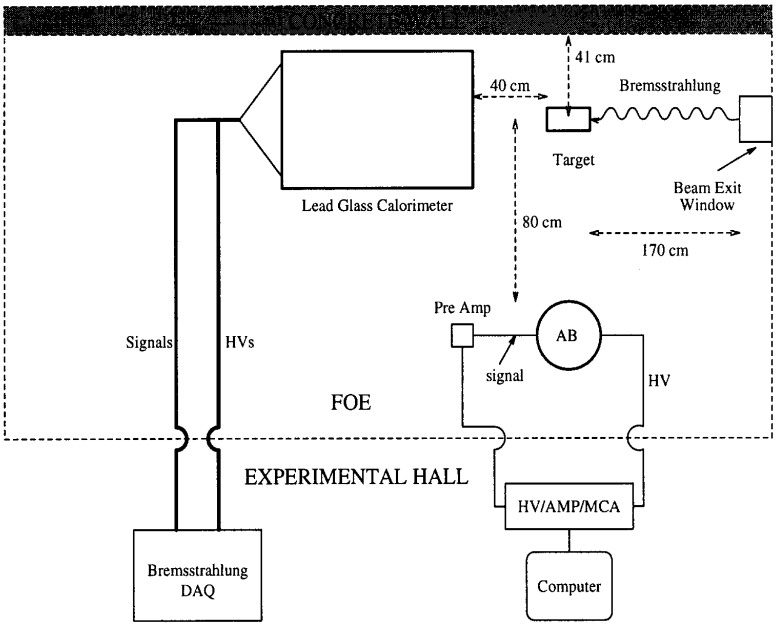

Figure 2. The photoneutron dose equivalent rate, measured 80 cm lateral from each target centre, as a function of the incident bremsstrahlung power

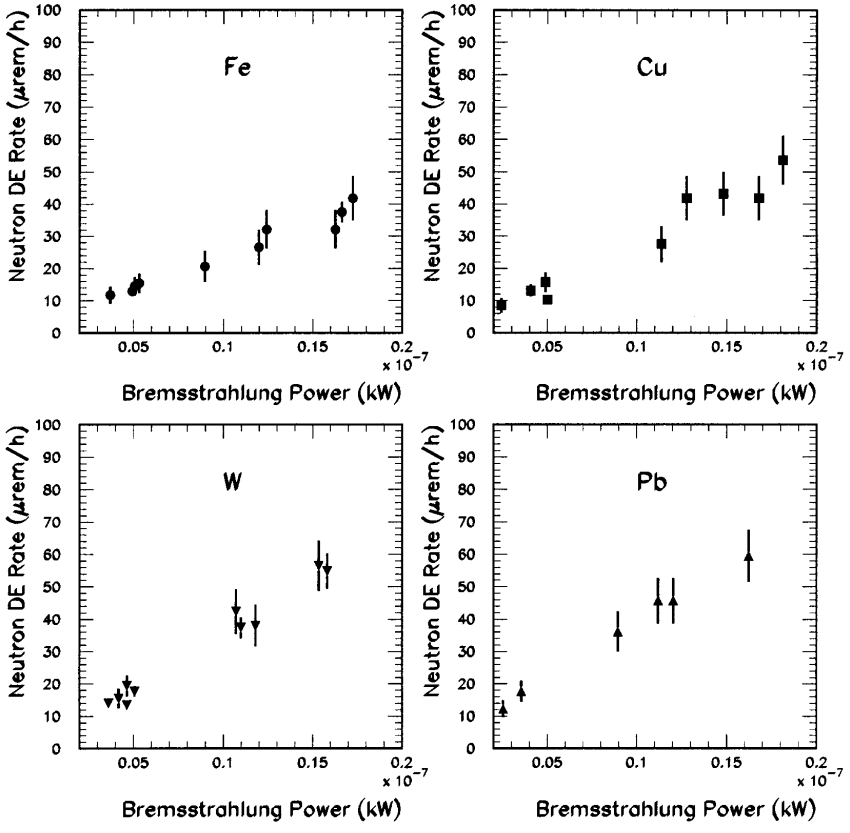

Figure 3. The photoneutron dose equivalent rate at 80 cm perpendicular to each of the target centres, normalised to the incident power, shown plotted as a function of the atomic number

The present measurements are the average of all the data from both beam lines 11 ID and 6 ID. The results deduced from previous calculations of photoneutron yields released by incident electrons [11] are also shown for comparison.

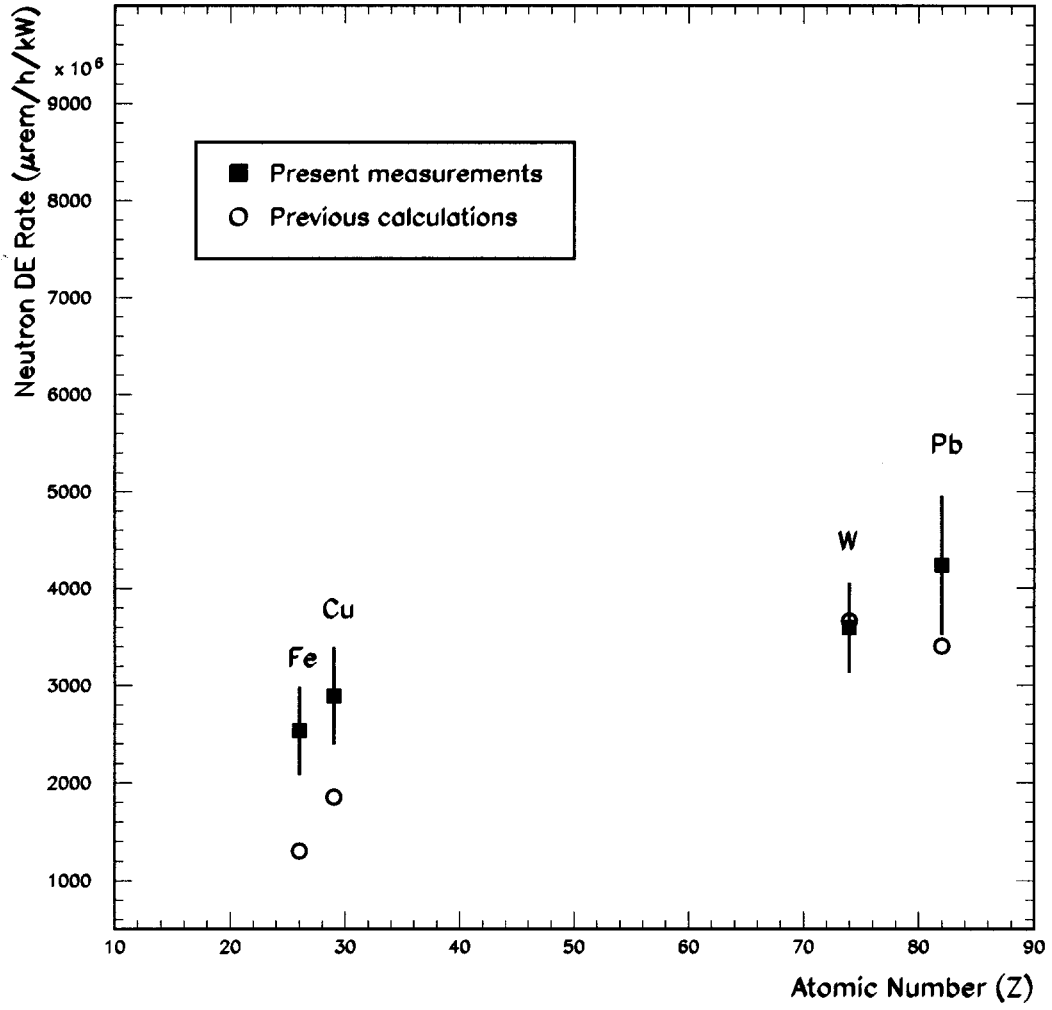

FURTHER MEASUREMENTS OF BREMSSTRAHLUNG FROM THE INSERTION DEVICE BEAM LINES OF THE ADVANCED PHOTON SOURCE

P.K. Job, M. Pisharody, E. Semones
Experimental Facilities Division
Argonne National Laboratories, 9700 S. Cass Ave., Argonne IL 60439, USA

Abstract

Bremsstrahlung is produced in the Advanced Photon Source (APS) storage ring when the positron beam interacts with the storage ring components or with the residual gas molecules in the storage ring vacuum. The interaction of the positrons with the gas molecules occurs continually during storage ring operation. Bremsstrahlung is important at the insertion device straight sections because the contribution from each interaction adds up to produce a narrow mono-directional beam that travel down the beam lines. At the APS, with long storage ring beam straight paths (15.38 meters), gas bremsstrahlung in the insertion device beam lines can be significant. The preliminary results of the bremsstrahlung measurements in the insertion device beam lines of the APS was presented at SATIF-3. This paper presents the results of further measurements at the two insertion device (ID) beam lines with higher statistics in the data collection. The beam current and the vacuum normalised bremsstrahlung power is fairly constant in a beam line for a given storage ring fill pattern, but may vary from beam line to beam line. The average bremsstrahlung power is measured as 118 ± 9 GeV/s/nT/mA at beam line 11 ID and as 36 ± 2 GeV/s/nT/mA at beam line 6 ID. These results, along with the results from the four previous independent bremsstrahlung measurements, enabled us to conclude upon the various reasons causing this variation.

Introduction

High-energy electron storage rings generate energetic bremsstrahlung photons through radiative interaction of the electrons (positrons) with the storage-ring components or with the residual gas molecules inside the vacuum chamber. The resulting radiation exits at an average emittance angle of mc^2/E radian with respect to the electron beam path, where mc^2 is the rest mass of the electron and E its kinetic energy. Thus, at straight sections of storage rings, moving electrons will produce a narrow and intense mono-directional photon beam. At the synchrotron radiation facilities, where beam lines are channelled out of the storage ring a continuous bremsstrahlung spectrum, with the maximum energy of the particle beam, will be present. This may pose a radiation hazard to the personnel in the experimental floor [1].

Experimental set-up and procedure

Bremsstrahlung energy spectra from insertion device (ID) beam lines at the APS have been measured by a fast and sensitive electromagnetic calorimeter made of 25 lead glass detectors, each 6.3 cm×6.3 cm×35 cm, stacked into a 5×5 array [1,2]. The energy resolution of this detector is $(7 \pm 2)/\sqrt{E}$ % and the time response is typically 20 ns. The bremsstrahlung beam is aligned along the central lead glass detector. The central 3×3 detector matrix of the calorimeter has been found to contain 100% of the electromagnetic shower in the lateral direction and approximately 96% in the longitudinal direction. Energies of the incident bremsstrahlung photons are measured on an event-per-event basis. Individual lead glass detector signals are read through the phototmultiplier tubes; the signals are then fed into fast encoding and readout ADCs (FERA). The signal from the central lead-glass detector is split into a trigger circuit that is used to generate a trigger to ADCs upon real energy deposition. Digitised data from ADCs are stored into a 16 K memory unit for subsequent slow readout by a computer. A schematic of the calorimeter and associated data acquisition system is shown in Figure 1. A more detailed description of the experimental set-up is given elsewhere [2,3].

The intensity of gas bremsstrahlung is a function of the stored beam current, atomic number of residual gas, and the storage ring vacuum. Thus, during the experimental runs, data have been collected in order to determine the correct value of the storage ring vacuum and the molecular composition of the residual gas inside the storage ring. The variation of average vacuum in the straight section, as determined by six ion gauges, is shown in Figures 2a and 2b for beam lines 11 ID and 6 ID respectively. The vacuum can be seen to vary linearly within the beam current range (50 mA to 100 mA) that was available during the measurement. Table 1 shows typical residual gas component information measured at 11 ID and 6 ID at a given beam current.

Results and discussion

The data in this report come from two separate experimental runs: one conducted in October-November 1997 and the other in March 1998. The first run was conducted at beam line 11 ID and the latter at beam line 6 ID. The calibration procedure for the lead-glass calorimeter, the nature of the raw ADC bremsstrahlung distributions, and various systematic corrections involved are discussed elsewhere [2,3]. Figures 3a and 3b show measured bremsstrahlung energy spectra, normalised to storage ring vacuum, for a few typical beam currents of the two experimental runs. Systematic corrections associated with the measurements such as dead-time losses, longitudinal shower leakage, and low energy cut-off, have been applied to the energy spectra in Figure 3 to obtain the corrected results shown in Tables 2 and 3. Results from Table 2 and Table 3 are also shown

plotted in Figures 4a and 4b. Figure 4a shows the variation in bremsstrahlung energy, normalised to the beam current, as a function of the storage ring vacuum. Figure 4b gives the variation of the bremsstrahlung energy, normalised to both the vacuum and beam current, as a function of beam current. The bremsstrahlung contribution from each individual sector is fairly constant (as seen in Figure 4b) – an average of 118 ± 9 GeV/s/nT/mA from 11 ID and $36 \pm$ GeV/s/nT/mA from 6 ID. The bremsstrahlung power in kilowatts, normalised to the storage ring vacuum, is given in Figure 5 for the two beam lines as a function of the beam current. It is clear that the power varies linearly with the beam current. The average normalised bremsstrahlung powers of $(2.0 \pm 0.2) \times 10^{-8}$ W/nT/mA and $(0.6 \pm 0.03) \times 10^{-8}$ W/nT/mA have been measured for beam line 11 ID and 6 ID respectively.

Conclusions

Independent measurements of normalised bremsstrahlung power from six beam lines at the Advanced Photon Source (the present two and four earlier measurements [2,3]) have shown a variation of as much as a factor of ten. Clearly, bremsstrahlung power varies with beam current and storage ring vacuum. Bremsstrahlung power, normalised to the storage ring vacuum and the beam current, is fairly constant within a beam line for a given storage ring fill pattern but may vary from beam line to beam line. The reasons for such a beam line-to-beam line variation of the normalised bremsstrahlung power are attributed to the variation of the vacuum profile along the vacuum chamber, variation of the residual gas composition in the straight section, the variation of temperature profile along the vacuum chamber due to RF heating and the presence of a non-gas bremsstrahlung component. The production of the non-gas bremsstrahlung component depends upon the vacuum chamber dimensions, relative position of the beam with respect to the vacuum chamber and the maximum bunch current in the storage ring as determined by the storage-ring fill pattern. The normalised bremsstrahlung power may vary due to any or a combination of the reasons discussed above. This makes comparing the results of various bremsstrahlung measurements difficult.

Acknowledgements

Work supported in part by US Department of Energy, Contract No. W-31-109-ENG-38, BES-Material Science, Argonne National Laboratory.

REFERENCES

[1] H.J. Moe, Advanced Photon Source – Radiological Design Considerations, ANL-APS-LS-141, Argonne National Laboratory, July 1991.

[2] M. Pisharody *et al*., Measurement of Gas Bremsstrahlung from the Insertion Device Beam Lines of the Advanced Photon Source, ANL-APS-LS 260, Argonne National Laboratory, March 1997.

[3] M. Pisharody *et al*., Measurement of Gas Bremsstrahlung from Electron Storage Rings, *Nucl. Instr. Meth*. A 401, 442, 1997.

Table 1. Typical residual gas measurement results for beam lines 11 ID and for 6 ID at a given beam current

Beam line	Mass number	Residual gas component	Mole fraction (%)	Weight per cent (%)
11 ID	2	H_2	80.0	25.9
	16	CH_4	4.5	11.7
	19	F	5.7	17.7
	28	N_2/CO	9.8	44.7
6 ID	2	H_2	57.4	8.3
	18	H_2O	13.1	17.0
	28	N_2/CO	16.4	33.1
	44	CO_2	13.1	41.6

Table 2. Bremsstrahlung power for various beam currents from the 15.38 m of positron beam straight path at beam line 11 ID. A 12% correction due to the threshold cut-off was determined in the photon count rate and has been incorporated in the bremsstrahlung photon rate.

Beam current I_b (mA)	Estimated vacuum P (nT)	Bremsstrahlung photon rate N_γ (/s/nT/mA)	Bremsstrahlung energy rate E_γ (GeV/s/nT/mA)
63.0	6.33	50±4	99±9
70.1	7.18	55±4	108±9
71.6	7.19	55±4	108±9
72.0	7.35	55±4	108±9
73.4	7.32	61±4	117±9
74.2	7.51	58±4	114±9
76.0	7.53	56±4	109±9
76.1	7.59	60±4	118±9
77.3	7.70	57±4	112±9
78.4	7.77	60±4	116±9
79.4	7.80	61±4	117±9
80.3	7.88	60±4	119±9
80.5	8.09	60±4	116±9
81.1	8.08	61±4	117±9
82.1	8.08	61±4	120±9
82.2	8.13	55±4	111±9
84.0	8.30	64±4	122±9
86.3	8.42	65±4	123±9
88.4	8.67	65±4	125±9
88.9	8.63	68±4	128±9
89.6	8.69	65±4	126±9
91.4	8.91	68±4	129±9
92.2	8.90	65±4	126±9
92.8	8.89	64±4	121±9
94.6	9.10	68±4	129±9
96.0	9.18	70±4	129±9
97.4	9.37	67±4	126±9

Table 3. Bremsstrahlung power for various beam currents from the 15.38 m of positron beam straight path at beam line 6 ID. A 12% correction due to the threshold cut-off was determined in the photon count rate and has been incorporated in the bremsstrahlung photon rate.

Beam current I_b (mA)	Estimated vacuum P (nT)	Bremsstrahlung photon rate N_γ (/s/nT/mA)	Bremsstrahlung energy rate E_γ (GeV/s/nT/mA)
52.1	5.89	21±1	35±2
54.1	6.18	19±1	33±2
61.2	6.80	21±1	35±2
61.4	6.86	19±1	34±2
64.9	7.18	19±1	34±2
66.8	7.41	21±1	35±2
73.4	7.91	20±1	35±2
73.9	7.89	19±1	34±2
76.3	8.13	21±1	35±2
76.3	8.20	21±1	35±2
79.8	8.50	20±1	35±2
80.2	8.52	21±1	36±2
82.1	8.76	19±1	35±2
83.5	8.90	20±1	36±2
84.8	8.97	22±1	36±2
84.8	8.91	22±1	37±2
86.3	9.04	22±1	37±2
86.8	9.06	22±1	37±2
87.2	9.07	20±1	36±2
88.2	9.28	22±1	36±2
89.5	9.42	22±1	36±2
90.0	9.39	22±1	37±2
90.2	9.34	22±1	37±2
92.0	9.60	23±1	38±2
93.4	9.68	22±1	37±2
93.4	9.62	22±1	37±2
93.6	9.59	20±1	36±2
94.0	9.70	22±1	37±2
96.0	10.01	22±1	37±2
96.2	9.99	21±1	37±2
96.2	9.98	20±1	36±2
99.7	10.21	22±1	37±2
100.6	10.21	19±1	33±2
101.6	10.51	20±1	35±2

Figure 1. The lead glass electromagnetic calorimeter and associated data acquisition system that are used to measure the bremsstrahlung spectrum and power

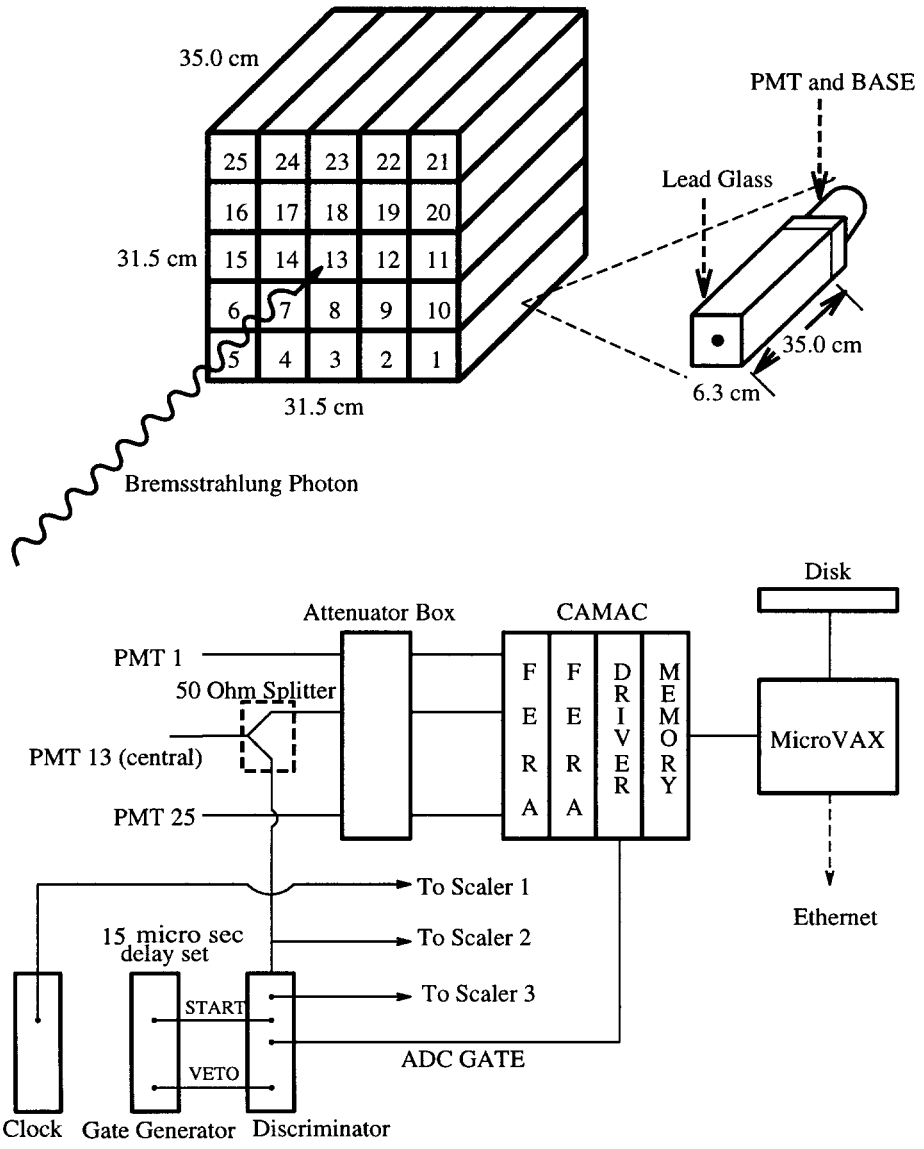

Figure 2. Variation of storage ring vacuum as a function of beam current at beam lines 11 ID and 6 ID

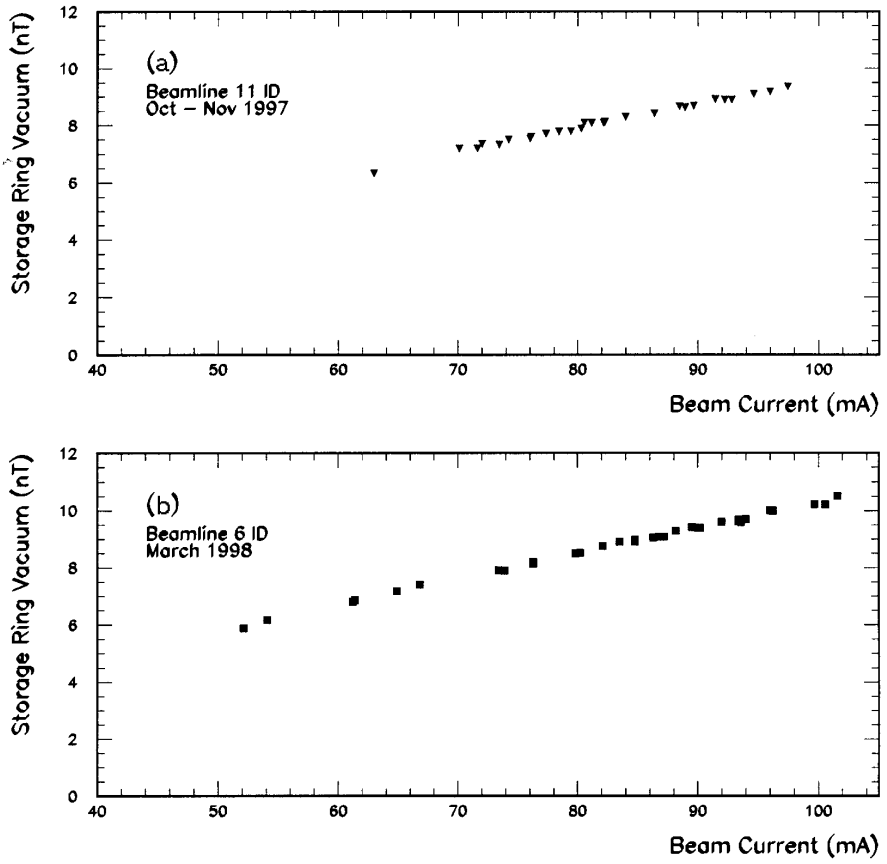

Figure 3. Bremsstrahlung energy spectra, corrected for dead-time losses, for typical beam currents during the two experimental runs at beam lines 11 ID (A) and 6 ID (b)

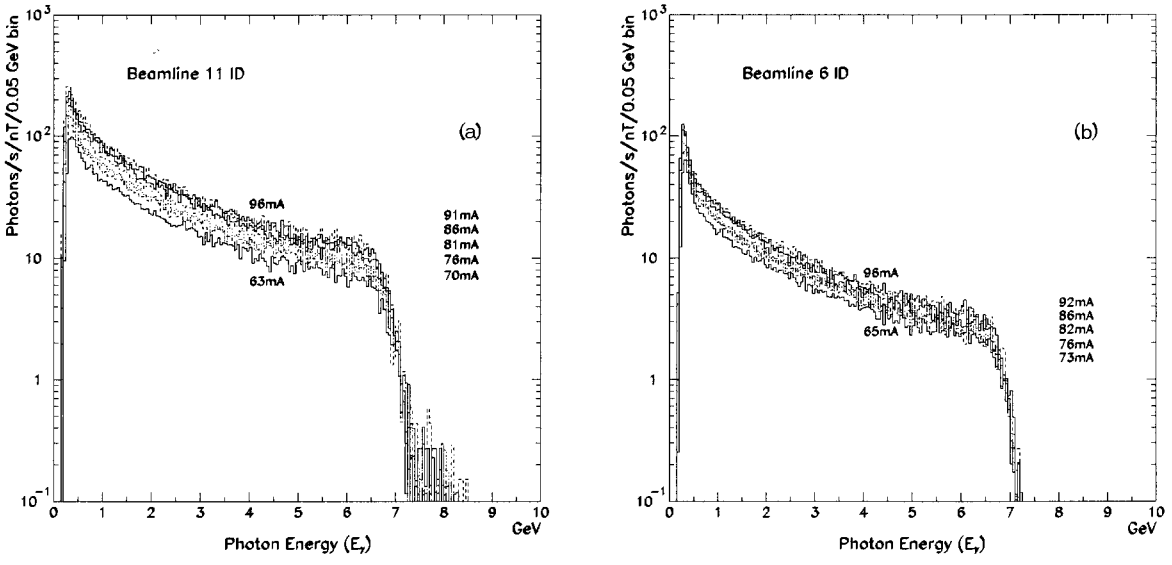

Figure 4. (a) Bremsstrahlung power, normalised to beam current, as a function of the storage ring vacuum for the two experimental runs at beam lines 11 ID and 6 ID. (b) The slopes of the lines in (a), which give the normalised bremsstrahlung contribution from both beam lines, as a function of the beam current.

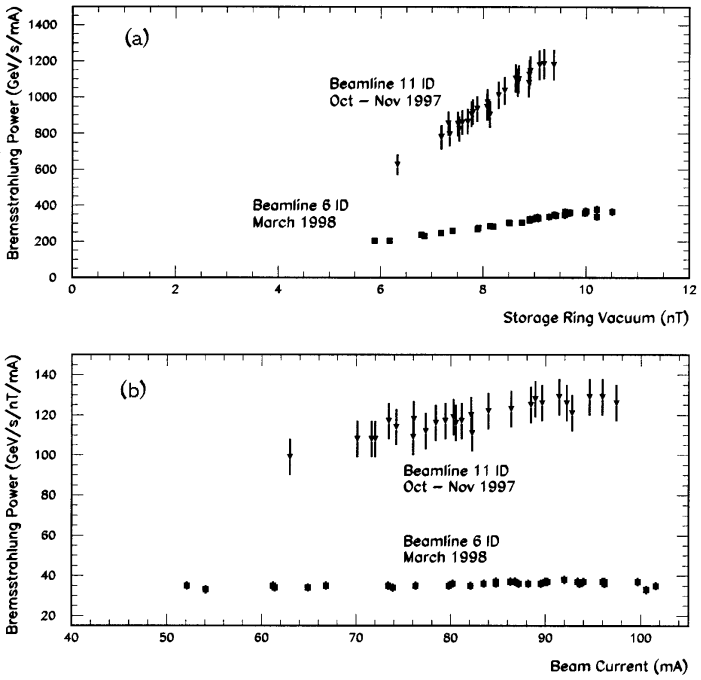

Figure 5. Bremsstrahlung power in kilowatts, normalised to the storage ring vacuum, as a function of the beam current for the two experimental runs at beam lines 11 ID and 6 ID

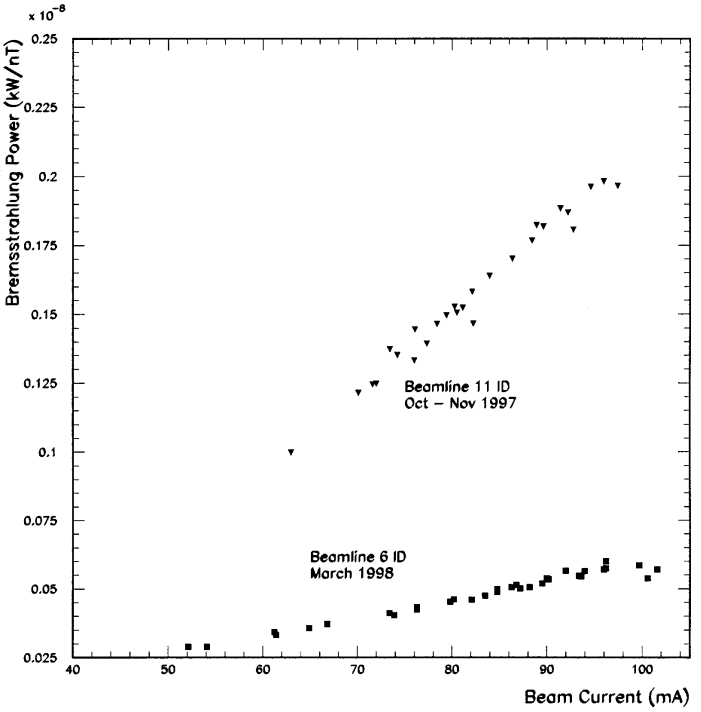

SESSION II

Source Term and Related Data – Proton and Ion Accelerator

Chairs: D. Filges and G. Stevenson

A SYSTEMATIC EXPERIMENTAL STUDY OF THICK-TARGET NEUTRON YIELD FOR HIGH-ENERGY HEAVY IONS

T. Nakamura, T. Kurosawa
Cyclotron and Radioisotope Centre, Tohoku University
Aoba, Aramaki, Aoba-ku, Sendai, 980-8578, Japan

N. Nakao
High Energy Accelerator Research Organisation, Tanashi Branch
Midori-cho 3-2-1, Tanashi, Tokyo, 188-8501, Japan

T. Shibata
High Energy Accelerator Research Organisation
Oho-cho 1, Tsukuba, Ibaraki, 305-0801, Japan

Y. Uwamino
Institute of Physical and Chemical Research
Hirosawa 2-1, Wako, Saitama 351-0198, Japan

A. Fukumura
National Institute of Radiological Sciences
Anagawa 4-9-1, Inageku, Chiba-shi, 263-8555, Japan

Abstract

We measured angular and energy distributions of neutrons produced by 100 and 180 MeV/nucleon He, 100, 180 and 400 MeV/nucleon C, 100, 180 and 400 MeV/nucleon Ne ions stopping in thick carbon, aluminium, copper and lead targets using the heavy ion medical accelerator of the National Institute of Radiological Sciences. The neutron spectra in the forward direction have broad peaks located at about 60-70% of the incident particle energy per nucleon due to break-up process and spreading up to almost twice as much as the projectile energy per nucleon. The neutron spectra at all angles consists of two components of cascade neutrons and evaporation neutrons. The experimental results are also compared with the calculations using the HIC and LCS codes, and the calculated results generally agree with the measured ones within a factor of 2 margin of accuracy, except around the high energy end in the forward direction. This systematic study on neutron production from thick targets by high-energy heavy ions is a first experimental work and will be useful in the shielding design of high-energy heavy ion accelerator facilities.

Introduction

Recently, high-energy heavy ions have been used in various fields of nuclear physics, material physics and medicine, especially cancer therapy. At the National Institute of Radiological Sciences (NIRS) in Chiba, Japan, the HIMAC (Heavy Ion Medical Accelerator in Chiba) has been used for heavy ion cancer therapy for the last three years, and the GSI (Gesellschaft für Schwer Ionen) in Germany has just started heavy ion cancer therapy. Several institutes in the world have started or plan to build radioactive beam facilities, where high-energy radioactive heavy ions are used for investigating exotic nuclei, nuclear synthesis and so on.

To design these facilities, radiation shielding is essential for protecting workers and nearby inhabitants from penetrating neutrons produced by high-energy heavy ions. Data on the energy angle distribution of secondary neutrons from a thick target which fully stops heavy ions, called the thick target neutron yield (TTY), are indispensable for estimating source terms of the accelerator shielding design [1]. For projectiles of energy higher than 100 MeV/nucleon, several experimental results on TTY have been published on neutron production from proton incidence [2-6]; however, for heavier ions, only one experimental data set exists on TTY for 177.5 MeV/nucleon helium ions [7]. Very recently, one experimental study on TTY was performed for 155 MeV/nucleon helium and carbon ions [8].

Under these circumferences, we have performed measurements of differential thick target neutron yields by 100 and 180 MeV/nucleon helium, and 100, 180 and 400 MeV/nucleon carbon and neon ions at the HIMAC facility. The measured results were reported [9-11] by comparing with those calculated with the HIC [12] code based on an intranuclear-cascade and evaporation model. During these experiments, we simultaneously measured the charged particles of proton, deuteron and triton having the atomic number of $Z = 1$ for 100 MeV/nucleon projectiles. The measured spectra are compared with those calculated with the LAHET Code System, LCS [13] as a benchmark test [11]. We are now continuing the TTY experiments using 400 MeV/nucleon argon and 800 MeV/nucleon silicon ions.

Experimental procedure

The measurements were carried out using the HIMAC heavy ion synchrotron of the National Institute of Radiological Sciences. The energy of neutrons produced in the target was measured by the time-of-flight (TOF) method. Figure 1 shows the experimental geometry of a typical arrangement of three neutron counters. A thin NE102A plastic scintillator (30 mm diam. by 0.5 mm thick) coupled with the H3178 photomultiplier and base (Hamamatsu Photonics Co. Ltd.) was placed just behind the end window (made of 0.1 mm-thick aluminium) of the beam line as a beam pick-up scintillator. The output pulses of this scintillator were used as start signals for the TOF measurement. These output pulses were also used to count the absolute number of projectiles incident to the target. A target was set on the beam line 10 cm behind the beam pick-up scintillator. The beam spot size incident to the target was about 1.5 cm in diameter and the beam height was 1.25 m above the concrete floor of the experimental area. The NE213 liquid scintillator (12.7 cm diam. by 12.7 cm thick) coupled with the R4144 photomultiplier connected to E1458 base (Hamamatsu Photonics Co. Ltd.), were used for the neutron detector (E counter). The NE102A plastic scintillator (15 cm by 15 cm square and 0.5 cm thick), coupled with the H1949 photomultiplier and base (Hamamatsu Photonics Co. Ltd.), were used for a Δ-E counter and were placed in front of the E counter to discriminate charged particles from non-charged particles, neutrons and photons. Three sets of E and ΔE counters were used for simultaneous angular distribution measurements at three different

angles. The detection angle is given in Table 1. The detectors were located 2 m (at large angles) to 5 m (at small angles) away from the target to provide better energy resolutions in the forward directions where there are larger yields of high-energy neutrons. To minimise neutron scattering, no local shielding was used near the detectors. By interposing an iron shadow bar (15 cm by 15 cm square and 60 cm thick) between the target and detector, the background neutron components from room scattering were measured.

The incident energies of heavy ions and the target materials with their thicknesses are given in Table 1. Target materials are C (1.77 g/cm^3), Al (2.7 g/cm^3), Cu (8.93 g/cm^3) and Pb (11.34 g/cm^3); each target has a shape of 10 cm by 10 cm square, and its thickness was determined to stop the incident particles completely. When the measurements were carried out at large angles, the target was set at 45° to the beam line to minimise the attenuation effect of neutrons through the target.

Data analysis

Neutrons

As the DE counter does not scintillate by neutrons and gamma rays, the neutron and gamma ray events could be selected from the charged particle events, by using two-dimensional ΔE-E graphical plots shown in Figure 2. After this discrimination, the neutron and the gamma ray events were clearly separated by using two-dimensional graphical plots of total-slow pulse height components of the E counter. After each experimental run, each E counter was calibrated with a ^{60}Co gamma ray source, and the Compton edge in the gamma ray spectrum was used as the bias point. After obtaining the TOF spectrum of neutrons, it was converted into the energy spectrum of neutrons. For this conversion, the detection efficiency of the NE213 E counter is essential. The experimental data of the detection efficiency for this scintillator has been published by Nakao *et al*. [14], but there is no data for neutrons of energy higher than 135 MeV. Therefore, the neutron detection efficiency was calculated with the Monte Carlo code by Cecil *et al*. [15] for all ranges of energy.

Charged particles

To separate proton, deuteron and triton events, three kinds of two-dimensional graphical plots were used. Two-dimensional ΔE-E graphical plots in Figure 2 were first used to identify different Z number particles, but these plots could not identify different mass number particles. From Figure 2 only Z = 1 particles were selected, and only a small fraction of Z = 2 particles can be seen in Figure 2 because the incident alpha particles fully stopped in a thick target. The two-dimensional plots of TOF-E pulse height distributions for Z = 1 particles are shown in Figure 3. In Figure 3, different mass particles of protons (m = 1) deuterons (m = 2) and tritons (m = 3) are clearly separated, although the pulse heights of high energy particles escaped from the E counter intersect between those of different mass particles. This intersection was resolved with the two-dimensional total-slow pulse height plots. The lower graph of Figure 3 gives the resolved results for protons. The TOF spectra were then converted to the energy spectra by approximating 100% detection efficiency of the NE213 detector.

Monte Carlo simulations

These experimental results were compared with calculations. The neutron spectra were calculated by using the Heavy Ion Code, HIC [12]. The HIC code is a Monte Carlo code that

calculates continuum state transitions between projectile and target in heavy ion reactions at energies above 50 MeV/nucleon. As the HIC code only gives the double differential neutron production cross-section, called the thin target yield, the calculations were performed for a series of thin target yield calculations, which were then summed to obtain the neutron yields from heavy ions stopping in a thick target, considering the projectile continuous energy loss and the projectile number attenuation in the target, as follows:

$$\frac{d^2\phi}{dE\ d\Omega} = \sum_{i=1}^{m} \sigma_m N P_m dE_m \Big/ \left(\frac{dE_m}{dx_m} \right)$$

$$P_m = P_{m-1}\ \exp\left(-\sigma_m^{Tot}\ N\, dx_m\right)$$

where σ_m is the double differential neutron production cross-section calculated by HIC, N is the atomic density of target, P_m is the number of beam particles in the target ($P_0 = 1.0$), dE_m/dx_m is the stopping power calculated by the SPAR code [16], σ^{Tot} is the total reaction cross-section given as an experimental formula by Shen *et al*. [17], and dx_m is the thickness of thin target divided. In this analysis, the neutron production from the extranuclear cascade is still neglected, and this approximation can hold in relatively lower-energy regions.

These experimental results were also compared with the calculations by using the LAHET Code System, LCS [13]. The LCS can be used to let stochastically primary particles and secondary products up to alpha particles transport through media of arbitrary configuration and composition. The coupling of LAHET with HMCNP in the LCS allows to include neutrons down to thermal energies. The LCS calculations were performed for 100 MeV/nucleon He incidence on stopping-length C, Al, Cu and Pb targets. The majority of the LAHET parameters was set to their default settings.

Results and discussions

Neutron spectra

As examples, measured neutron spectra for Cu targets bombarded by 100 MeV/nucleon He, C and Ne, and 400 MeV/nucleon C and Ne projectiles are shown in Figures 4-8, respectively. They indicate the following general tendencies:

1) These spectra in the forward direction have a broad peak at high energy end especially a large bump at 0° for 400 MeV/nucleon C and Ne incidences and this peak becomes more prominent for lighter target and for higher projectile energy. The peak energy of this bump is about 60-70% of the projectile energy per nucleon, 70 MeV for 100 MeV/nucleon He and C, 140 MeV for 180 MeV/nucleon He and C, and 230 MeV for 400 MeV/nucleon C projectiles. This means that these high-energy neutron components produced in the forward direction by a break-up process and the momentum transfer from projectile to target nuclei are both higher for lighter nucleus and higher projectile energy than for heavier nucleus and lower projectile energy.

2) The neutron spectra have two components: One below about 10 MeV corresponds to neutrons produced isotropically in the centre of mass system mainly by the equilibrium process; the other above 10 MeV corresponds to those produced by the pre-equilibrium

process. Since the neutron emission by the pre-equilibrium process has a sharp forward peaking of the angular distribution, the neutron spectra become softer at larger emission angles, where the equilibrium process is prominent.

3) The high energy neutrons in the forward direction spread up to about the energy which is about the twice of the incident particle energy per nucleon, 200 MeV for 100 MeV/nucleon He, C and Ne ions, 370 MeV for 180 MeV/nucleon He, C and Ne ions and 800 MeV for 400 MeV/nucleon C and Ne ions. This can be explained by the following. When the Fermi energy is approximated to be 40 MeV, v/c, which is the relative velocity of a nucleon in a nucleus, becomes 0.28. The relative velocities, v/c, of 100, 180 and 400 MeV/nucleon projectiles are 0.43, 0.54 and 0.71 respectively. Thus, the composite relative velocity of a nucleon in a projectile is 0.63, 0.71 and 0.83, and the resultant nucleon energy can be estimated as 270, 400 and 730 for 100, 180 and 400 MeV/nucleon projectiles, respectively.

4) The neutron energy spectra become harder for lighter target nuclei. This can be explained by noting that the energy E_t transferred from a projectile to a target by one collision is proportional to $4M_pM_tE_0/(M_p+M_t)^2$, where M_p and M_t are the atomic masses of the projectile and target nuclei, respectively, and E_0 is the projectile kinetic energy. As a result, the sum of the transferred energies is greater for lighter target nuclei, and it is more likely that a nucleon receives a greater part of this transferred energy and that the fraction of the evaporation process is smaller, since the lighter target nucleus has a smaller number of nucleons.

Comparison of measured neutron spectra with those calculated by HIC and LCS

The spectra calculated by the HIC code are also shown in Figures 4-8, together with the experimental results. The HIC calculation has some statistical errors, especially in the high-energy region coming from the limited history numbers. These figures clarified that a broad high-nergy peak in the forward direction appears around incident particle energy per nucleon, E_0, in the calculation, while on the other hand this peak appears about 60-70% of E_0 as described before. This large discrepancy may come from the fact that the HIC calculation fails to express the break-up process and the superposition of thin target yield dose not well express the thick target yield. From these figures, the following tendencies can be deduced:

1) For 100 MeV/nucleon He ions, the calculated spectra agree rather well with the measured spectra in shapes and absolute values.

2) For 100 MeV/nucleon C ions, the shapes of the calculated spectra rather agree well with the measured ones, but the absolute values are about twice of the measured results. More precisely, the calculated spectra are harder in the forward direction, but softer at large angles than the measured spectra.

3) For 100 MeV/nucleon Ne ions, the shapes of the calculated spectra agree rather well with the measured ones except around the broad high energy peak in the forward direction, but the absolute values are about a few times as large as the measured results.

4) For 400 MeV/nucleon C ions, the deviation of the broad peak positions at 0° and 7.5° can be seen between experiment and calculation. Excluding the twice overestimation of the calculated result at 60°, the calculated results at 15°, 30° and 90° give good agreement with the measured results in absolute values.

5) For 400 MeV/nucleon Ne ions, the deviation of the broad peak positions at 0° and 7.5° can be seen between experiment and calculation. The calculated results at large angle give good agreement with the measured results in absolute values.

As concluding remarks, the HIC calculation has an accuracy within a factor of two, despite various approximations.

The LCS calculation could be done only for He projectile. The neutron spectra calculated by LCS shown in Figure 4 generally give good agreement with the experimental results in absolute values. In the calculation, a broad high energy peak in the forward direction appears more distinctly around incident particle energy per nucleon, compared with more flattened high energy peak in the experiment. This discrepancy also reveals that the LCS calculation gives the underestimation of the neutron spectra in the intermediate energy region of 5 to 50 MeV. The calculated spectra at angles larger than 30° are harder than the measured spectra, which means that the LCS calculation gives the underestimation of evaporation neutrons and the overestimation of pre-equilibrium neutrons extended to higher energy region.

Proton spectra

The experimental proton spectra from copper for 100 MeV/nucleon helium ions are shown in Figure 9 compared with the LCS calculation. The lower energy limit in the measured spectra was estimated to be 27 MeV considering the proton energy absorption through the air between the target and the detector (500 cm), the ΔE counter (0.5 cm thick plastic of CH1.104 and the density of 1.032 g/cm^3) and the aluminium cover (0.5 mm thick) of the E counter. Although proton spectra are similar to neutron spectra in shapes and absolute values at forward angles, proton yields rapidly decrease with increasing angles. At large angles, low energy proton components are dominant which can easily be absorbed by the thick target itself. Compared with measured and calculated proton spectra, calculated proton yields agree rather well with the measured results at forward angle, but the calculated yields give overestimation at large angle.

Deuteron spectra

The experimental deuteron spectra from copper for 100 MeV/nucleon helium ions are shown in Figure 10 compared with the LCS calculation. Minimum detectable deuteron energy is 36.6 MeV. At 90°, the deuterons emitted from the target could not be detected because of its strong forwardness. Measured spectra in the forward direction have a broad peak around 140 MeV and yields decrease drastically with increasing angles. Compared with calculated and measured results, the agreement between calculated and measured deuteron spectra is surprisingly good.

Triton spectra

The experimental triton spectra from copper for 100 MeV/nucleon helium ions are shown in Figure 11 compared with the LCS calculation. Minimum detectable triton energy is 43.7 MeV. Triton could not be detected at 60° and 90° because of much stronger forwardness than deuteron. Measured spectra in the forward direction have a broad peak around 200 MeV and yields decrease drastically with increasing angles. Compared with calculated and measured results, the LCS calculation gives good agreement with the experiment in the forward direction, although the calculation gives underestimation at 30°.

Angular distribution of neutron yields and total neutron yields

Figure 12 shows the neutron yields integrated above 5 MeV at each emission angle. All of the results suggest that the neutron yield is larger for lighter target nucleus in the forward direction and at large angles the yields become larger for heavier target nucleus. This reveals again that the neutron production at forward angle mainly occurs by the direct reaction process which reduces in magnitude with increase of emission angle, and at large angle the low energy neutrons via equilibrium process dominate the yields. The former production process gives that the momentum transfer from a heavier projectile to a lighter target is greater and the velocity of the centre of mass is greater in the laboratory system; then based on the kinematics, a nucleon is emitted in the more forward direction from the heavier projectile and the lighter target. The latter process is proportional to the nucleon numbers that the heavier target have higher values than the lighter target.

The total neutron yields above 5 MeV integrated for a hemisphere from 0° to 90° are shown in Figure 13. The total neutron yields become slightly larger with increase of the target mass, but their dependence on the target mass is very small compared with the difference of neutron numbers of the target. Precisely speaking, for 100 and 180 MeV/nucleon C and Ne ion incidences, the total neutron yields from the lead target are smaller than those from the carbon target. This may partly be explained from the fact that the total neutron yield integrated above 5 MeV does not include the low energy components of evaporation neutrons which are much more dominant for a heavier target like lead.

The difference of neutron yields between He, C and Ne incidences is also very small except for 180 MeV/nucleon He ions where the yield is reduced within a factor of two. This much smaller difference of neutron yields than that of the nucleon numbers of He, C, Ne ions might be caused by the fact that the larger thin target yield for Ne ions than for He and C ions is compensated with additional neutron production due to multiple collisions from the thicker target for He and C ions than for Ne ion. From these data, we obtained that the total neutron yields for C and Ne ions are approximately proportional to the square of incident particle energy per nucleon. This tendency is very similar to the summarised results of the neutron production by incident protons of energies up to 500 MeV [3,17].

Conclusion

We measured angular and energy distributions of neutrons produced by 100 and 180 MeV/nucleon He, 100, 180 and 400 MeV/nucleon C and Ne ions stopping in carbon, aluminium, copper and lead targets, so-called double differential thick target yield. The neutron spectra in the forward direction have broad peaks about 60-70% of the incident particle energy per nucleon due to the break-up process and spread up to almost the twice of the projectile energy per nucleon. The experimental results are compared with the calculations using the HIC code, and the calculated results agree with the measured results within a factor of two margin of accuracy. The measured spectra were also compared with the calculation using the LCS code and the calculated spectra are generally in good agreement with the measured spectra for all cases. This systematic study on neutron production from thick targets by heavy ions is the first experimental work and will be useful for shielding design of high energy heavy ion accelerator facility.

REFERENCES

[1] T. Kato, T. Nakamura, "Estimation of Neutron Yields from Thick Targets by High-Energy ^{4}He Ions for the Design of Shielding for a Heavy Ion Medical Accelerator", *Nucl. Instr. Meth*., A311 548 (1992).

[2] J.W. Wachter, W.A. Gibson, W.R. Burrus, "Neutron and Proton Spectra From Targets Bombarded by 450 MeV Protons", *Phys. Rev*., C6, 1496 (1972).

[3] M.A. Lone, R.T. Jones, B.M. Townes, L. Nikkinen and R.B. Moore, "Total Neutron Yields from 100 MeV Protons on Cu, Fe and Th", *Nucl. Instr. Meth*., A256, 135 (1987).

[4] M.M. Meier, D.A. Clark, C.A. Goulding, J.B. McClelland, G.L. Morgan and C.E. Moss, "Differential Neutron Production Cross-Sections and Neutron Yields from Stopping-Length Targets for 113 MeV Protons", *Nucl. Sci. Eng*., 102, 310 (1989).

[5] M.M. Meier, C.A. Goulding, G.L. Morgan and J.L. Ullmann, "Neutron Yields from Stopping- and Near-Stopping-Length Targets for 256 MeV Protons", *Nucl. Sci. Eng*., 104, 339 (1990).

[6] J.V. Siebers, P.M. DeLuca, Jr., D.W. Pearson and G. Coutrakon, "Shielding Measurements for 230 MeV Protons", *Nucl. Sci. Eng*., 115, 13 (1993).

[7] R.A. Cecil, B.D. Anderson, A.R. Baldwin, R. Madey, A. Galonsky, P. Miller, L. Young and F.M. Waterman, "Neutron Angular and Energy Distributions from 710 MeV Alphas Stopping in Water, Carbon, Steel and Lead, and 640 MeV Alphas Stopping in Lead", *Phys. Rev*., C21, 2471 (1980).

[8] L. Heilbronn, R.S. Cary, M. Cronqvist, F. Deak, K. Frankel, A. Galonsky, K. Holabird, A. Horvath, A. Kiss, A. Kruse, R.M. Ronningen, H. Schelin, Z. Seres, C.E. Stronach, J. Wang, P. Zecher and C. Zeitlin [private communication (submitted to *Nucl. Sci. Eng*.)].

[9] T. Kurosawa *et al*., "Measurements of Secondary Neutrons Produced from Thick Targets Bombarded by High-Energy Helium and Carbon Ions", *Nucl. Sci. Eng*., to be published.

[10] T. Kurosawa *et al*., "Measurements of Secondary Neutrons Produced from Thick Targets Bombarded by High-Energy Neon Ions", *J. Nucl. Sci. Tech*., to be published.

[11] T. Kurosawa *et al*., "Neutron, Proton, Deuteron and Triton Spectra from Thick Target Bombarded by 100 MeV/Nucleon He", *Nucl. Sci. Eng*., to be published.

[12] H.W. Bertini, T.A. Gabriel, R.T. Santoro, O.W. Hermann, N.M. Larson and J.M. Hunt, "HIC-1: A First Approach to the Calculation of Heavy-Ion Reactions at Energies > 50 MeV/Nucleon", ORNL-TM-4134, (1974).

[13] R.E. Prael and H. Lichtenstein, “Users Guide to LCS: The LAHET Code System,” LA-UR-89-3014, Los Alamos National Laboratory (1989).

[14] N. Nakao, T. Nakamura, M. Baba, Y. Uwamino, N. Nakanishi, H. Nakashima and S. Tanaka, “Measurements of Response Function of Organic Liquid Scintillator for Neutron Energy Range up to 135 MeV”, NIM A362 454 (1995).

[15] R.A. Cecil, B.D. Anderson and R. Madey, “Improved Predictions of Neutron Efficiency for Hydrocarbon Scintillators from 1 MeV to about 300 MeV”, *Nucl. Instr. Meth*. 161, 439 (1979).

[16] T.W. Armstrong and K.C. Chandler, “SPAR, a FORTRAN Program for Computing Stopping Powers and Ranges for Muons, Charged Pions, Protons, and Heavy Ions”, ORNL-4869, Oak Ridge National Laboratory (1993).

[17] Shen Wen-qing, Wang Bing, Feng Jun, Zhan Wen-long, Zhu Yong-tai and Feng En-pu, “Total Reaction Cross-Section for Heavy Ion Collisions and its Relation to the Neutron Excess Degree of Freedom”, *Nucl. Phys*. A491 130 (1989).

[18] K. Shin, K. Miyahara, E. Tanabe and Y. Uwamino, “Thick Target Neutron Yield for Charged Particles”, *Nucl. Sci. Eng*. 120, No. 1 40 (1995).

[19] K. Tesch, “A Simple Estimation of the Lateral Shielding for Proton Accelerators in the Energy Range 50 to 1000 MeV”, *Radiat. Protec. Dosim*. 11, 165 (1985).

Table 1. Projectile type with its incident energy per nucleon and target thickness which was estimated to stop the incident particles completely

Incident particle type and energy [MeV/u]	Target thickness [cm]	Detection angle [degree]
He [100]	C [5.0], Al [4.0], Cu [1.5], Pb [1.5]	0, 7.5, 15, 30, 60, 90
He [180]	C [16.0], Al [12.0], Cu [4.5], Pb [5.0]	0, 7.5, 15, 30, 60, 90
C [100]	C [2.0], Al [2.0], Cu [0.5], Pb [0.5]	0, 7.5, 15, 30, 60, 90
C [180]	C [6.0], Al [4.0], Cu [1.5], Pb [1.5]	0, 7.5, 15, 30, 60, 90
C [400]	C [20.0], Al [15.0], Cu [5.0], Pb [5.0]	0, 7.5, 15, 30, 60, 90
Ne [100]	C [1.0], Al [1.0], Cu [0.5], Pb [0.5]	0, 7.5, 15, 30, 60, 90
Ne [180]	C [4.0], Al [3.0], Cu [1.0], Pb [1.0]	0, 7.5, 15, 30, 60, 90
Ne [400]	C [11.0], Al [8.0], Cu [3.0], Pb [3.0]	0, 7.5, 15, 30, 60, 90

Figure 1. Experimental arrangement at HIMAC

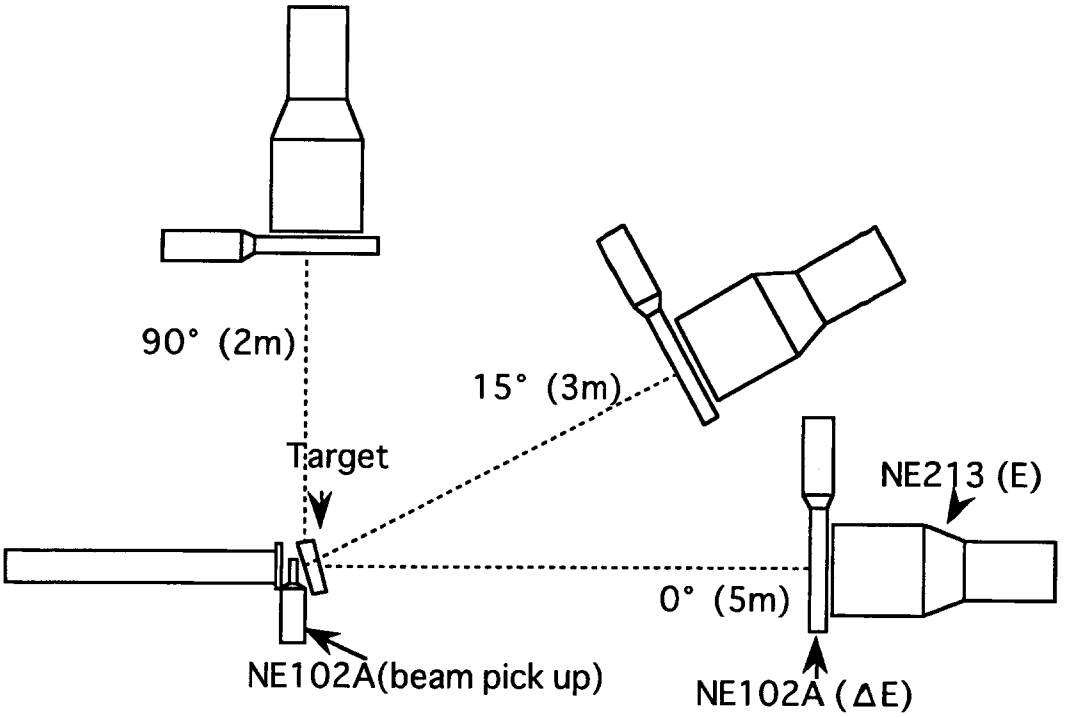

Figure 2. Two-dimensional plot of E and ΔE counter pulse heights

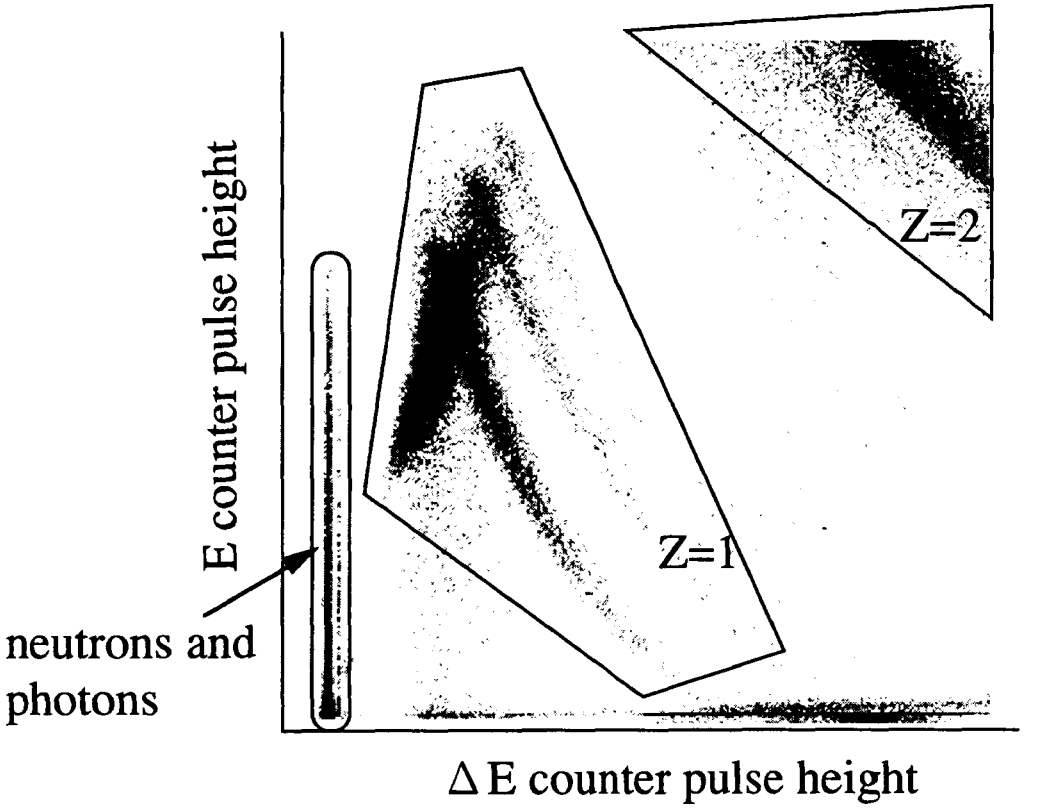

Figure 3. Two-dimensional plot of TOF-E counter pulse height for Z = 1 events selected from two-dimensional plot of E and ΔE counter pulse heights (upper) and that of only proton events (lower)

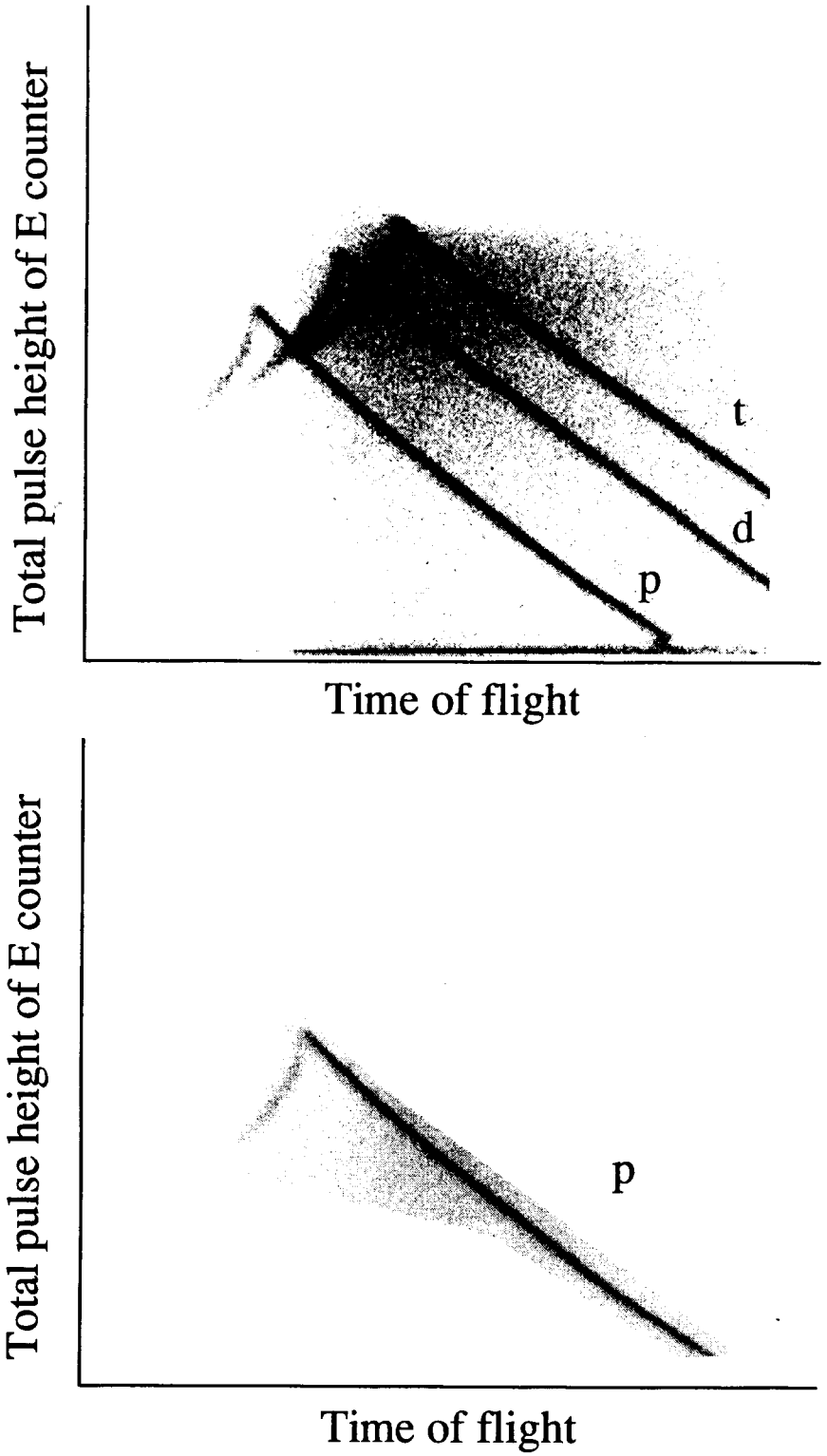

Figure 4. Neutron spectra from 100 MeV/nucleon helium ions in copper target

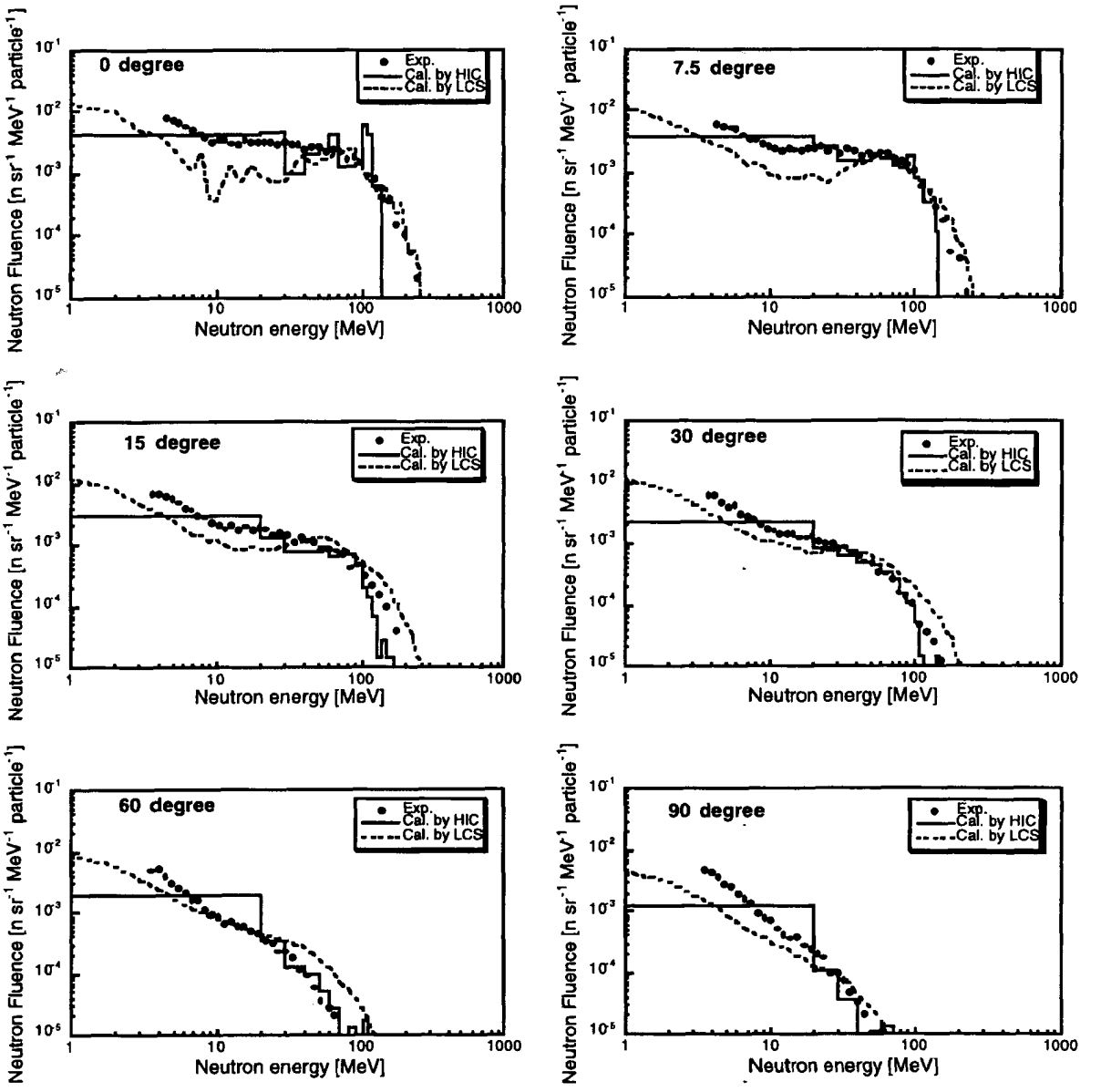

Figure 5. Neutron spectra from 100 MeV/nucleon carbon ions in copper target

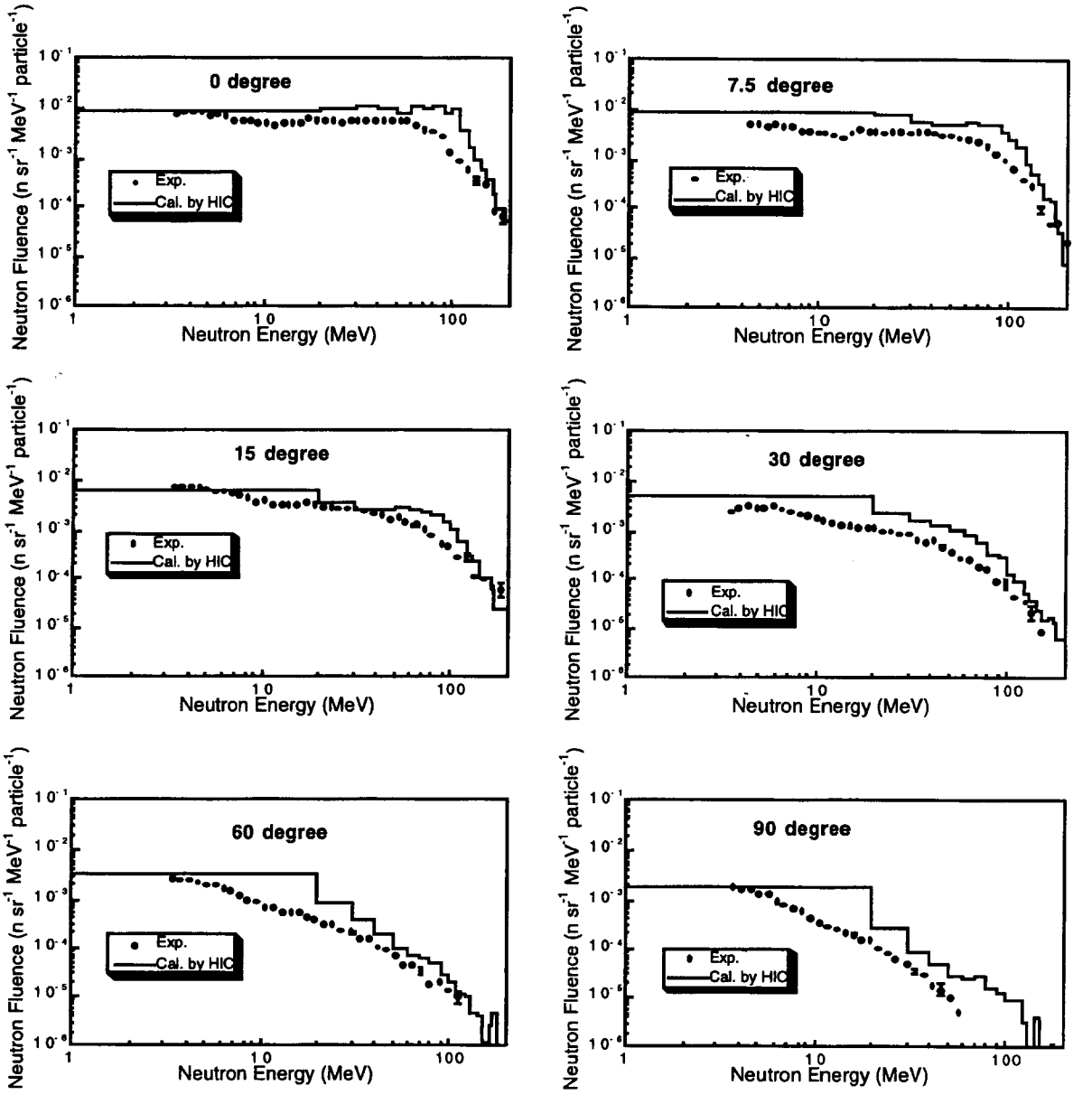

Figure 6. Neutron spectra from 100 MeV/nucleon neon ions in copper target

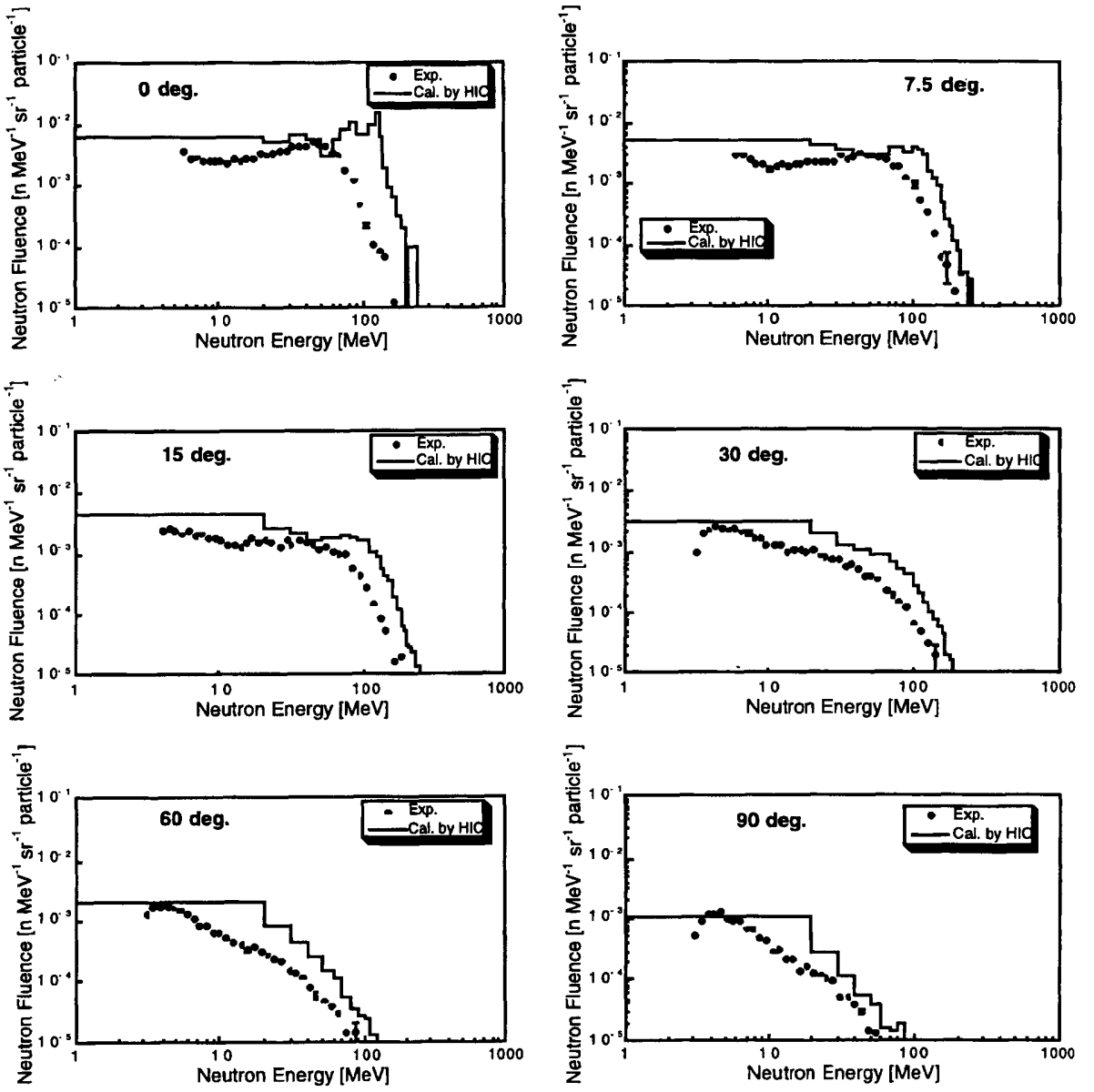

Figure 7. Neutron spectra from 400 MeV/nucleon carbon ions in copper target

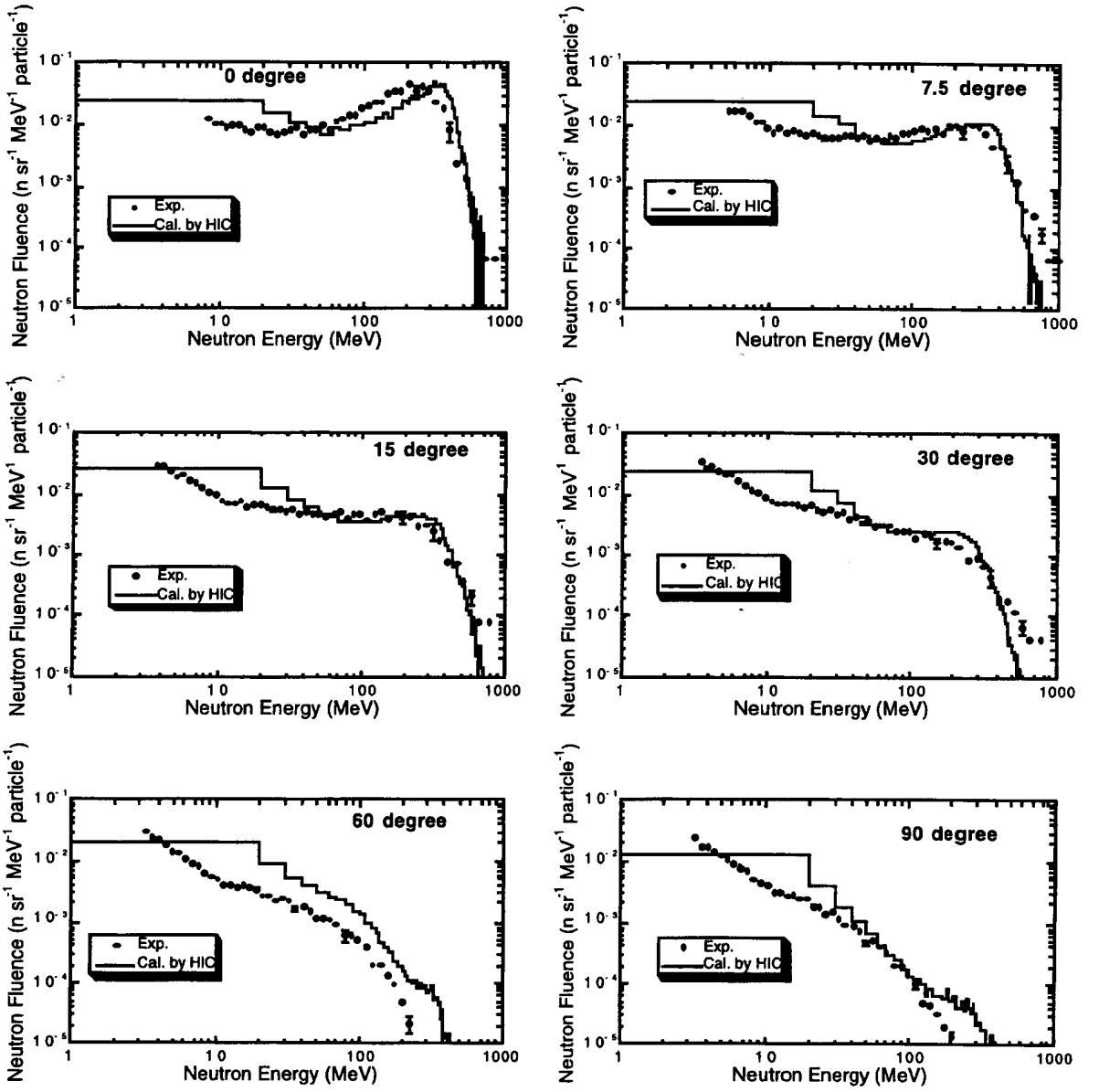

Figure 8. Neutron spectra from 400 MeV/nucleon neon ions in copper target

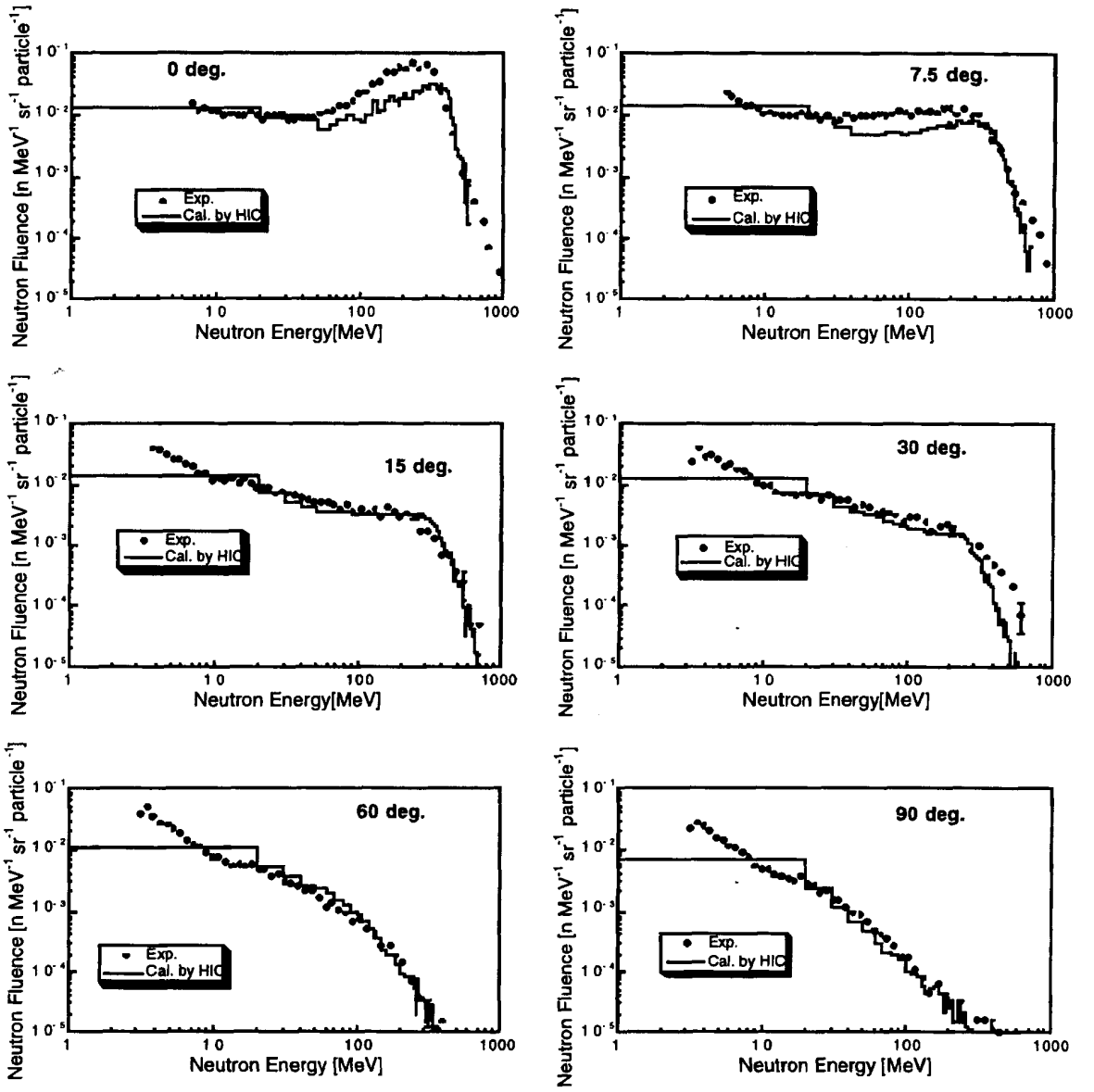

Figure 9. Proton spectra from 100 MeV/nucleon helium ions in copper target

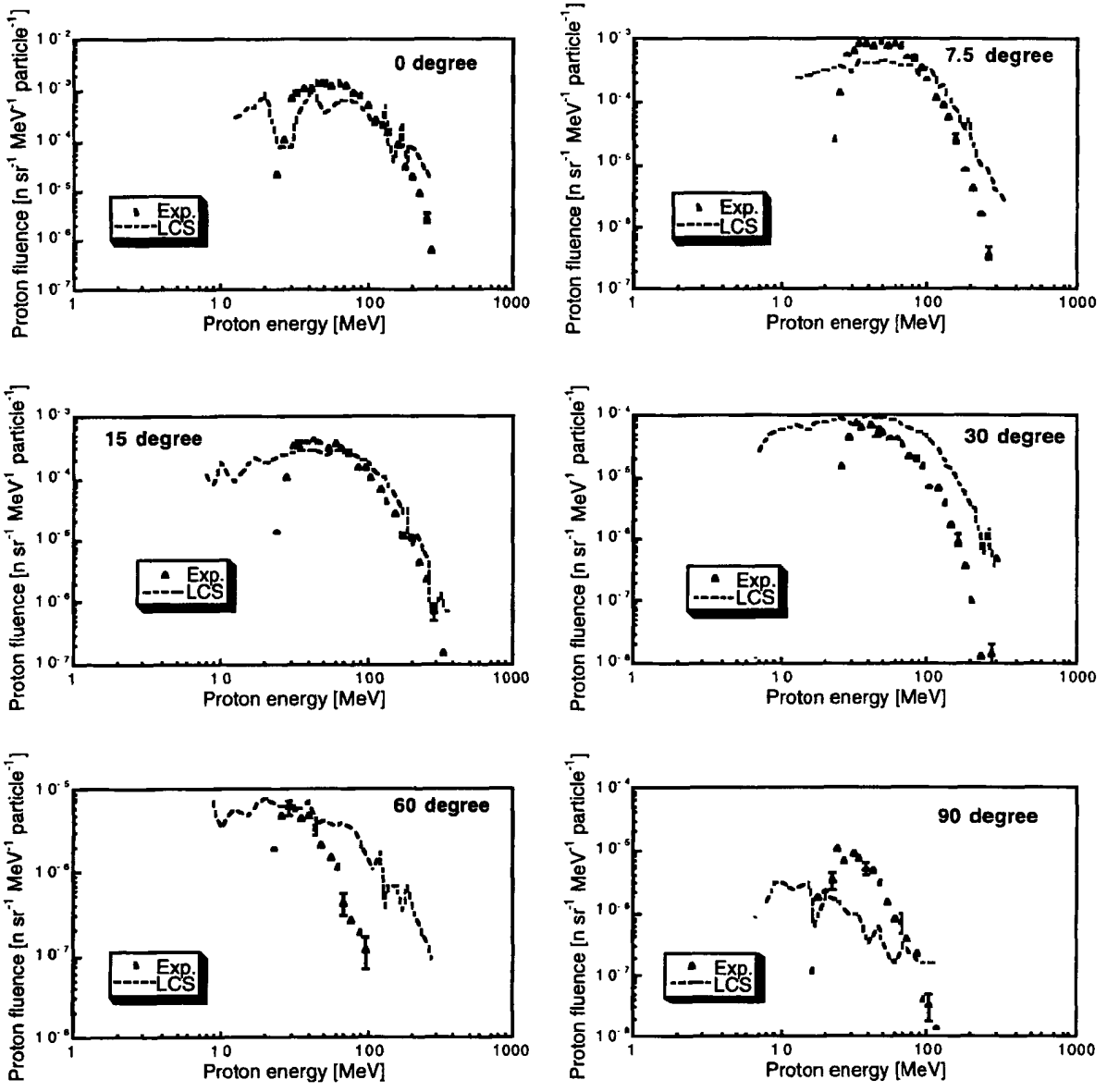

Figure 10. Deuteron spectra from 100 MeV/nucleon helium ions in copper target

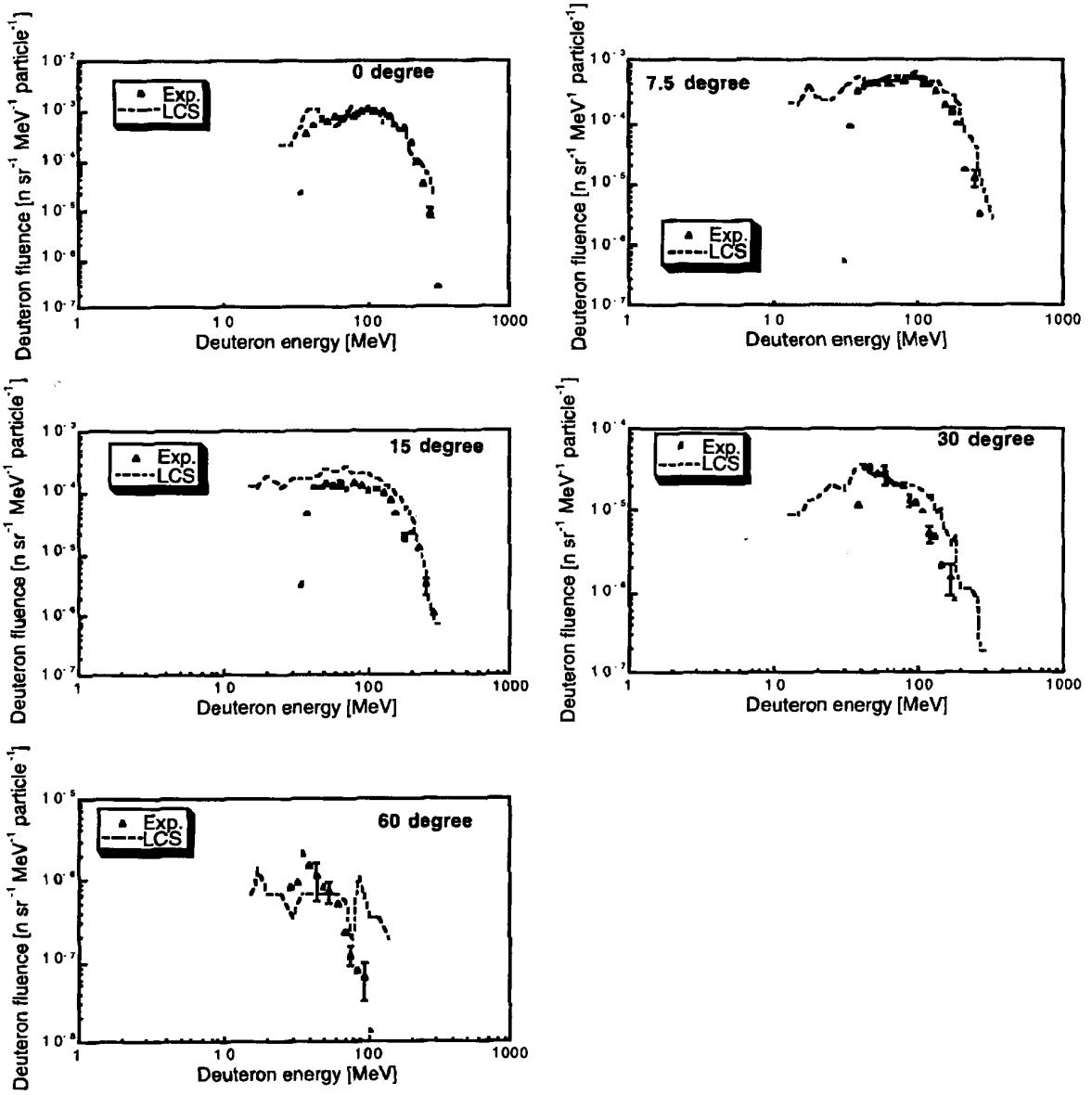

Figure 11. Triton spectra from 100 MeV/nucleon helium ions in copper target

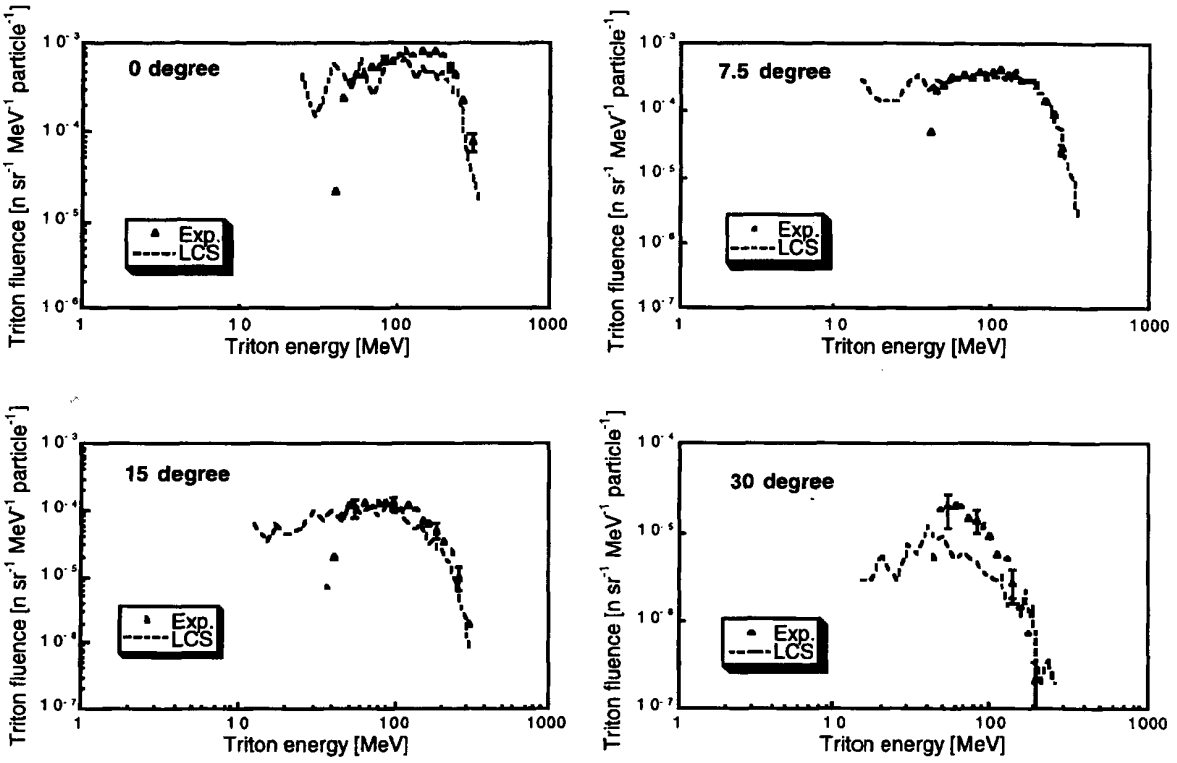

Figure 12. Angular distributions of neutron yields integrated above 5 MeV for 100 MeV/nucleon He, C, Ne, 180 MeV/nucleon He, C, Ne and 400 MeV/nucleon C, Ne ion incidence

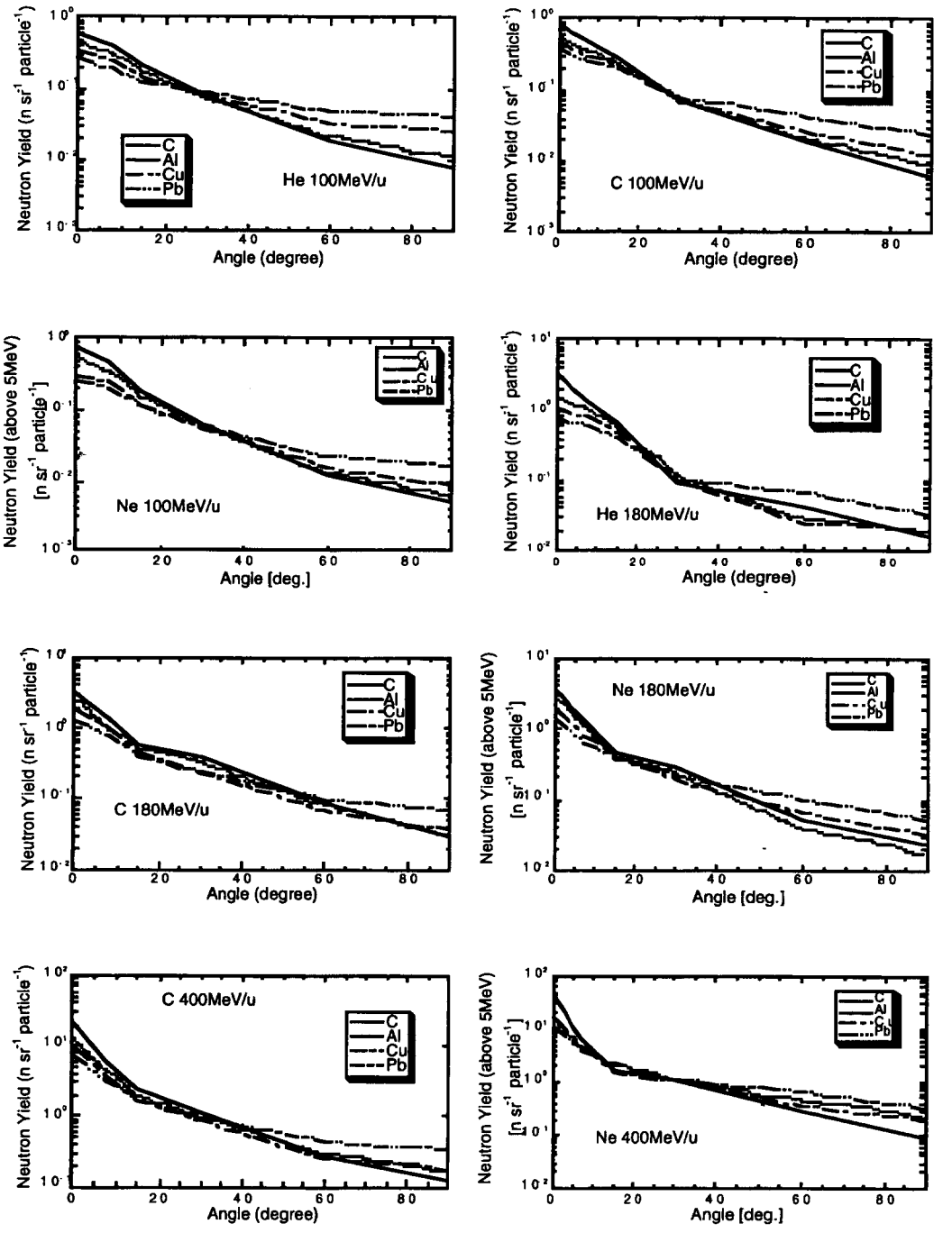

Figure 13. Total neutron yields above 5 MeV integrated for a hemisphere from 0 to 90 degrees for projectile – target combinations used in this work

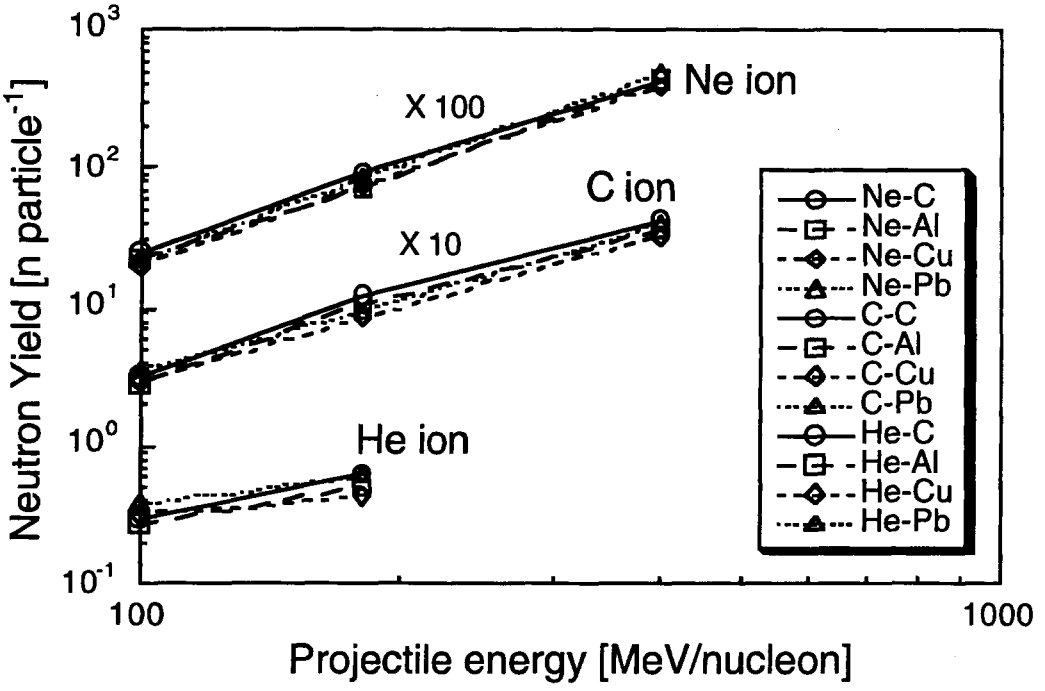

THIN AND THICK TARGET BENCHMARK INVESTIGATIONS TO VALIDATE SPALLATION PHYSICS MODELS

D. Filges, R.-D. Neef
(*For the NESSI Collaboration*)
Forschungszentrum Jülich GmbH, Institut für Kernphysik
D-52425 Jülich, Germany

The NESSI Collaboration
M. Enke [1], D. Filges [2], J. Galin [3], F. Goldenbaum [2], C. Herbach [1], D. Hilscher [1],U. Jahnke [1], A. Letourneau [3], B. Lott [3], R.-D. Neef [2], K. Nünighoff [2], Y. Patois [3], N. Paul [2], A. Peghaire [3], L. Pienkowski [5], H. Schaal [2], W.N. Schröder [4], A. Tietze [2], I. Töke [4]
[1] Hahn-Meitner-Institut GmbH, 14109 Berlin, Germany
[2] Forschungszentrum Jülich GmbH, 52425 Jülich, Germany
[3] Ganil (IN2P3-CNRS), BP 5027, 14021 Caen-Cedex, France
[4] University of Rochester, NY, USA
[5] University of Warsaw, 02-097 Warszawa, Poland

Abstract

In the ESS study report [1] we identified several areas where further spallation physics research and code validation is urgently needed: Neutron and charged particle production and multiplicities above one GeV incident protons, energy deposition and heating, material damage parameters, radioactivity and after heat, and high energy source shielding. All simulation calculations will be done using the Jülich HERMES code system [2].

For this purpose various collaborations were organised. One of the collaborations is NESSI (Neutron Scintillator Silicon Detector), which concerns fundamental data as cross-section measurements on neutron multiplicities and charged particles for different ESS relevant materials.

Introduction

In the ESS study report [1] we identified several areas where further spallation physics research and code validation is urgently needed: Neutron and charged particle production and multiplicities above one GeV incident protons, energy deposition and heating, material damage parameters, radioactivity and after heat, and high energy source shielding. All simulation calculations will be done using the Jülich HERMES code system [2].

For this purpose various collaborations were organised. One of the collaborations is NESSI (Neutron Scintillator Silicon Detector), which concerns fundamental data as cross-section measurements on neutron multiplicities and charged particles for different ESS relevant materials.

Figure 1. HERMES code system flow chart

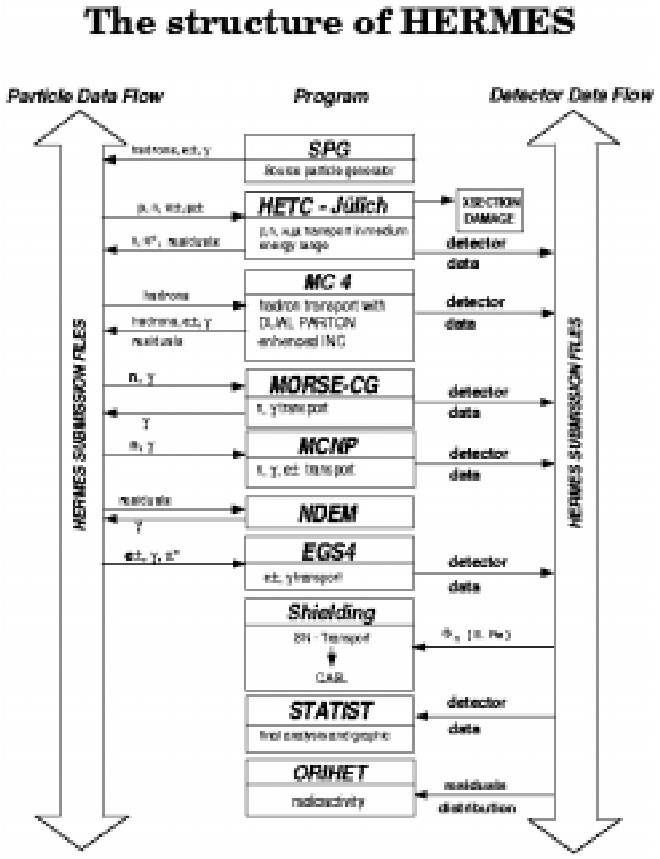

The NESSI Experiment [3]

Within the NESSI collaboration at COSY-Jülich (Cooler Synchrotron) neutron and charged particles multiplicities are measured up to 2.5 GeV incident proton energy for “thin” and “thick” targets for various structure and target materials from Al to Pb (and U). For thin targets (only one nuclear interaction in the target) the number of evaporative neutrons is a good measure of the distribution of the thermal excitation energy induced in the nucleus. In this sense the neutron multiplicity distribution is a sensitive test of the primary spallation process, i.e. the intranuclear cascade part of the theoretical model. At high excitation energies above about 2-3 MeV/nucleon in

heavy nuclei additional information on light charged particles (evaporative protons and He) improves the excitation energy resolution by about a factor of 2-3. For thick targets (multiple reactions) the alteration of the neutron multiplicity distribution reflects the production of additional neutrons produced in secondary reactions and thus it is a sensitive test to both the intra- and internuclear cascade part of theoretical models.

In summary, one can show the advantage of measuring the whole neutron multiplicity distributions instead of single average values. This brings much more constraint to the INCE (IntraNuclear Cascade Evaporation) model. Also the measurements in both thin and thick targets appear quite complementary since, in thick targets, compensation effects between the first reaction and secondary reactions can mask deficiencies in reproducing the primary reaction by the INCE model. The thick target measurement brings an additional, although indirect, test of the thin target measurement insofar as it allows one to follow the fate of the products of the primary interaction in generating extra neutrons.

The experimental equipment consists of two 4π-detectors, namely the large spherical neutron tank (BNB) with 1500 litres of scintillating liquid and 24 photomultipliers on the surface, and, inside the tank and around the target, the silicon detector (BSIB). BNB uses the old principle of slowing down the neutrons and detecting them by their capture in gadolinium. BSIB is a spherical shell of 20 cm diameter, assembled in a self-supporting way from 162 silicon detectors, 12 pentagons and the "magic" number of 150 hexagons. They all have the same size (7.5 cm^2) and thickness (500 μm). BSIB detects and to some degree identifies all charged nuclear particles by energy, or energy loss, and time-of-flight over the 10 cm from the target.

During two experimental phases we measured thin and thick targets.

The first experiment at COSY we measured the neutron multiplicity of a thin Hg target (5 mm thick, diameter 20 mm, stainless steel 0.3 mm container). This is very important because mercury is the favourite target material for ESS (European Spallation Source) and there exist no experimentally estimated cross-sections.

For comparison with the experiment the simulated result of the neutron multiplicity of the thin mercury target set-up is shown in Figure 2.

Figure 2. The NESSI detector

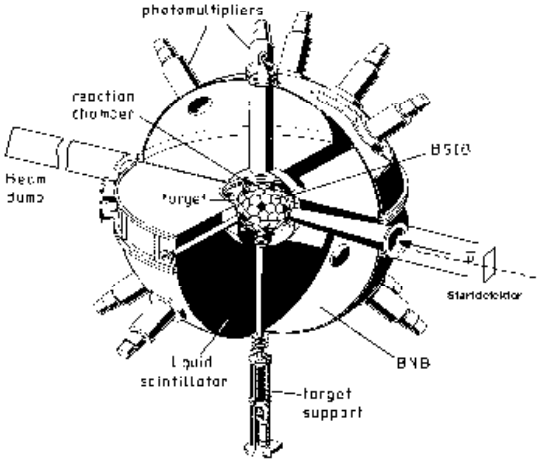

Figure 3. Measured and simulated neutron multiplicity for 1.2 GeV protons on a thin mercury target

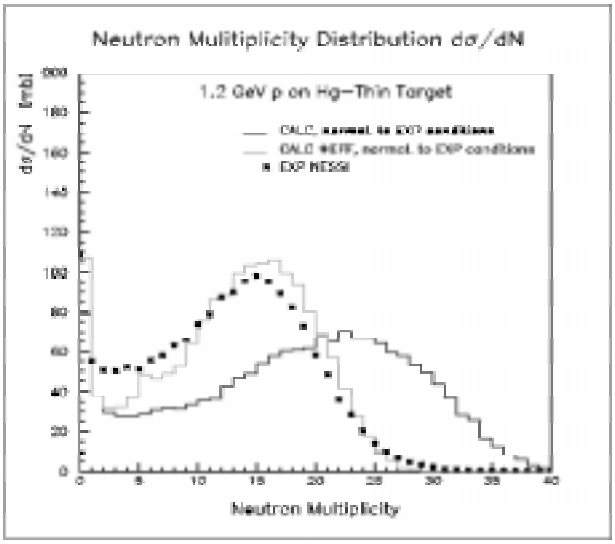

Measured and simulated neutron multiplicities are distributed very differently. Whereas the experimental multiplicity shows its maximum at 15 neutrons the simulation shows the maximum at 23 neutrons. The detector system has an energy dependent detection efficiency which has to be taken into account. If we fold the simulated neutrons with this energy dependent detector efficiency we receive a simulated neutron multiplicity distribution which should be comparable to the measured distribution. In fact we find a simulated distribution which tends to have a higher multiplicity by one neutron at both sides of the maximum. It is not possible to evaluate the real neutron multiplicity by experiment only, even without the knowledge of the energy dependent detector efficiency. Therefore, the simulation is absolutely necessary for the interpretation of the experiment.

For thick targets (multiple reactions) the alteration of the neutron multiplicity distribution reflects the production of additional neutrons produced in secondary reactions and thus it is a sensitive test to both the intra- and internuclear cascade part of theoretical models. We have prepared cylindrical targets (8, 12, and 15 cm in diameter and 35 cm in length) from three materials, tungsten, mercury and lead, which are all suited for spallation neutron sources, with Hg being favoured for the European Spallation Source. These targets are highly segmented in length and diameter, so that the neutron production at some selected proton energies can be simultaneously studied as a function of target geometry, thereby adding constraints also to the transport part of the models. The idea is to provide benchmark data for the high energy transport codes. In Figure 4 the different target materials and geometries are given. In a second and low energy experimental phase at COSY we measured the neutron multiplicity of these thick targets.

In Figures 5-7 a comparison of INCE and low energy neutron transport calculations with first experimental results for thick mercury and lead targets are given for incident proton energies of 1.2 and 2.5 GeV. The open circles represent the calculated values. The stars represent the efficiency folded values, which can be compared with experimental ones.

The comparisons are preliminary. A detailed evaluation of the data together with simulations for all targets and energies are in progress. We hope that the final analysis will be valuable as a benchmark for spallation sources.

Figure 4. Target geometries and target materials

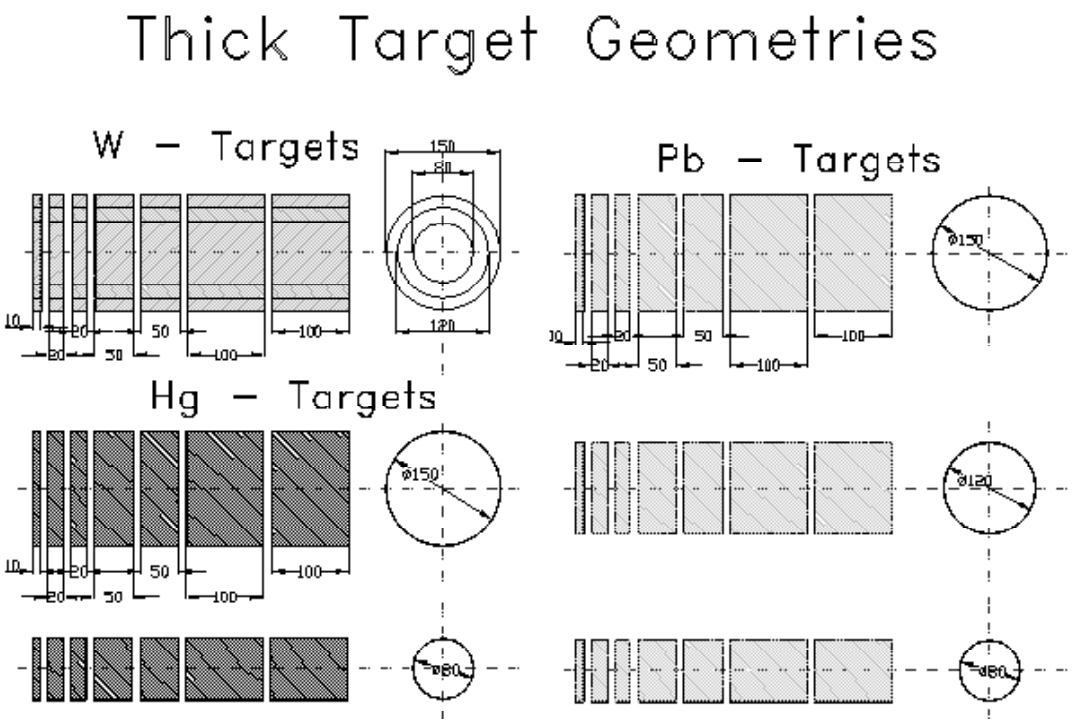

Figure 5. Mean neutron multiplicity for 1.2 GeV incident protons on thick lead targets of 15 cm diameter

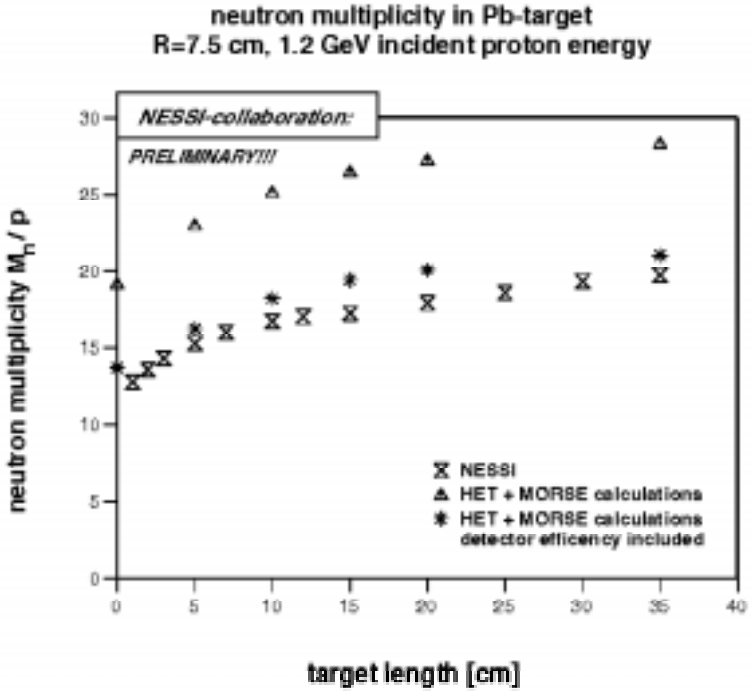

Figure 6. Mean neutron multiplicity for 1.2 GeV incident protons on thick mercury targets of 15 cm diameter

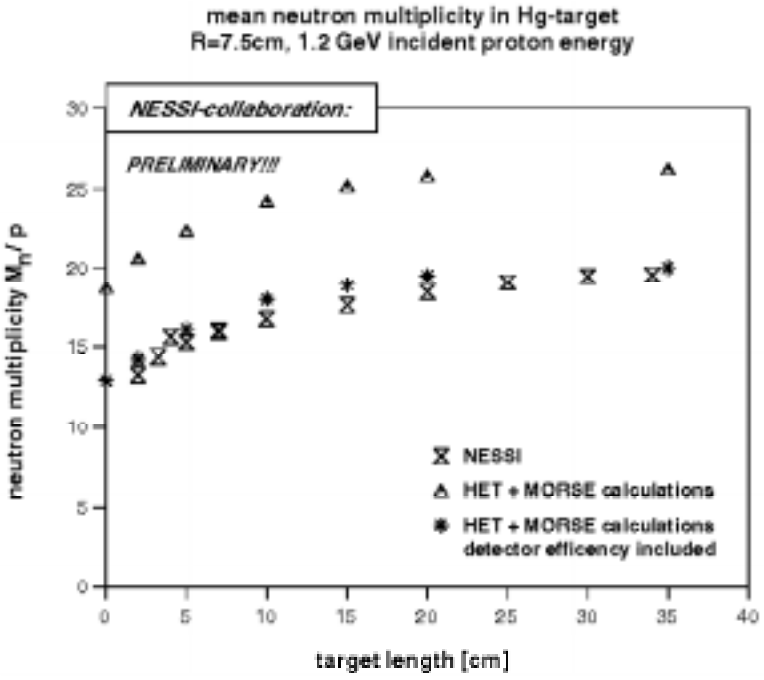

Figure 7. Mean neutron multiplicity for 1.2 GeV incident protons on thick lead targets of 15 cm diameter

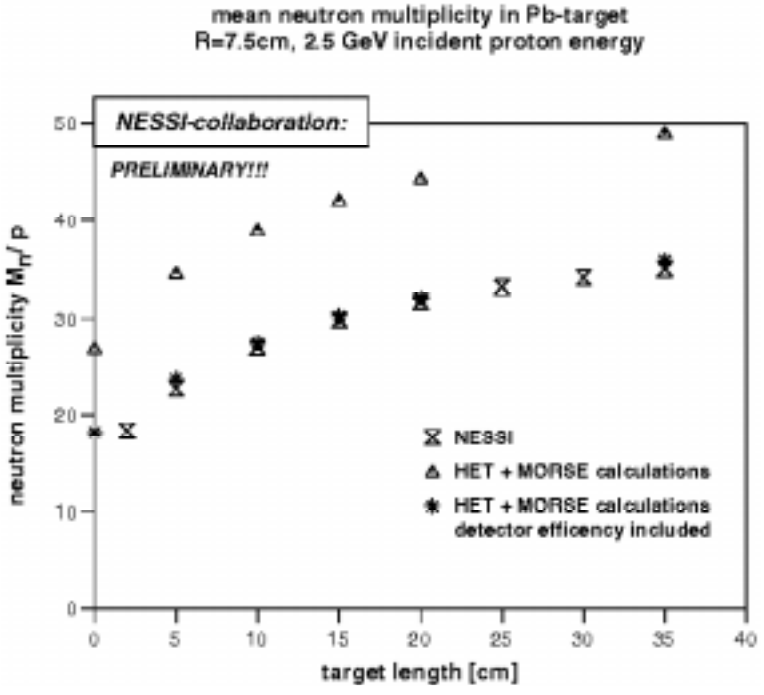

REFERENCES

[1] The European Spallation Source Study, Vol. III, ESS-96-53-M, ISBN-090-237-6-659, Nov. 1996.

[2] P. Cloth, *et al*., HERMES, A Monte Carlo Program System for Beam Materials Interaction Studies, Report JUEL-2203, May 1988.

[3] Goldenbaum, *et al*., *Phys. Rev. Lett*. 77 (1996), 12330 and D. Hilscher, *et al*., Proc. of the Intl. Workshop on Nuclear Methods for Transmutation of Nuclear Waste, Dubna 1997.

RADIATION SHIELDING AT THE HEAVY ION RESEARCH FACILITY IN LANZHOU (HIRFL)

Zheng Huazhi, Su Youwu
Institute of Modern Physics, Chinese Academy of Sciences, Lanzhou, 730000, China

Abstract

The introduction to radiation shielding of HIRFL is presented in this paper, which includes three sections:

1. outline of HIRFL;
2. radiation emission rate;
3. radiation shielding.

Outline of HIRFL

HIRFL was designed for the study of heavy ion nuclear physics and application of heavy ion beam [1]. It is a built-up complex system in series with two cyclotrons. Figure 1 shows the general layout of HIRFL. It consists of five parts:

1) the 1.7 m sector focusing cyclotron (SFC) used as the injector;

2) the large separated sector cyclotron (SSC) used as the main accelerator, of which, the mean extraction radius is 3.21 m;

3) the front transport beam line about 65 m in length between the injector and the main accelerator;

4) from the main accelerator to the experimental terminals, the total length of the post transport beam line is about 110 m;

5) seven experimental terminals and the Radioactive Ion Beam Line in Lanzhou (RIBLL) in the experimental hall.

Figure 1. General layout of HIRFL

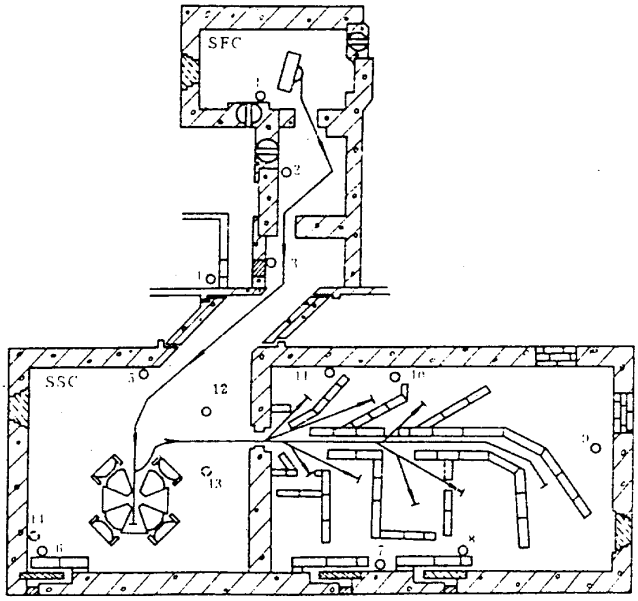

The various heavy ions from CXe can be accelerated at HIRFL. Table 1 gives the designed beam parameters.

Table 1. Beam parameter of HIRFL

Ion	^{12}C		^{14}N	^{40}Ar	^{84}Kr	^{132}Xe
Maximum energy (MeV/u)	50	88	100	46	10	4.8
Beam intensity (10^9 ion/s)	2100	390	250	220	11	5.5

Radiation emission rate

The reaction mechanism for different energy and different kinds of heavy ions on a variety of target materials may be extremely complex.

However it can be sure that neutrons are the dominant component of the secondary radiation field. The second neutron yields, spectra and angular distributions for heavy ion reactions depend on the incident particle, energy and the target materials:

1) The total neutron yields increase distinctly with the increasing of incident ion energy but with less relations to the kinds of ion and target in the range of less than about 15 MeV/u. In higher energy range the total yields increase slightly with the atomic mass of the ion, but still have less effect of target materials when the incident energy per nucleon is the same.

2) The angular distributions of second neutron are strongly peaked in the forward direction.

3) Significant numbers of neutrons are emitted with energy higher than the incident energy per nucleon and a few of them even can reach about twice of the energy, and they determine the shield configuration.

Figure 2 gives the total neutron yields of energy range of HIRFL [2-5]. According to the neutron emission cross-sections calculated by H.W. Bertini *et al.* [6]. and B. Fernandey [7], the neutron spectra and dose equivalent for 58.3 MeV/u and 100 MeV/u ^{12}C on thick Fe target were calculated and are given in Figure 3 and Figure 4.

Figure 2. Neutron yields varies with incident ion energy

(M = measured value, C = calculated value)

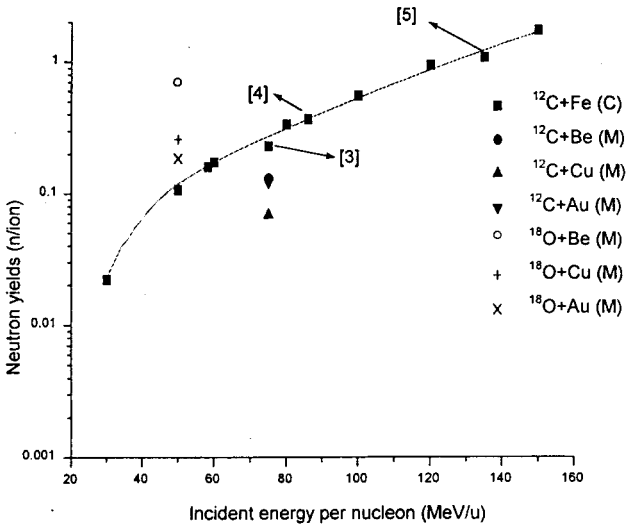

Figure 3. Calculated neutron spectra from 58.3 and 100 MeV/u ^{12}C on thick Fe target

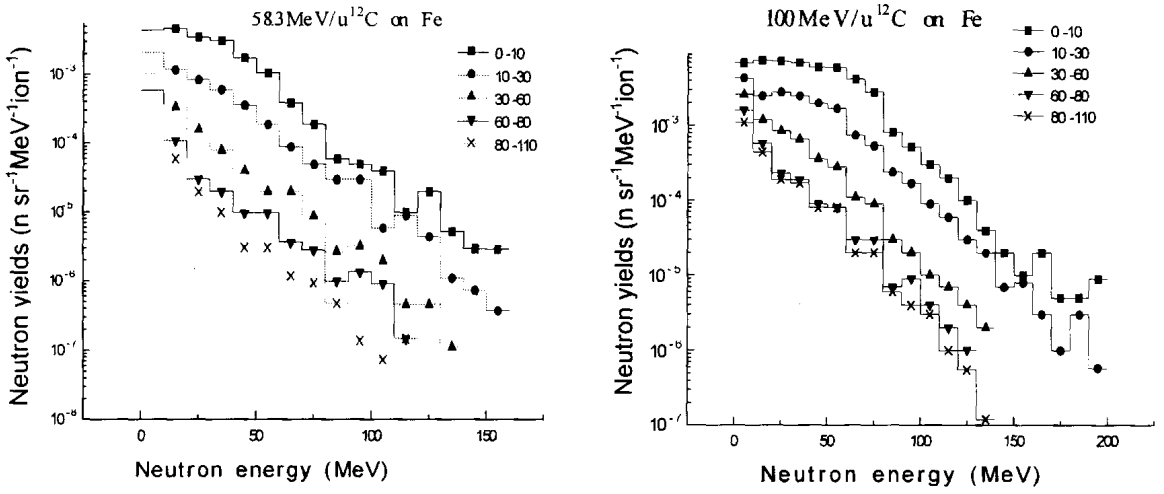

Figure 4. Calculated neutron dose equivalent caused by 58.3 and 100 MeV/u ^{12}C ion at 1 m from thick Fe target

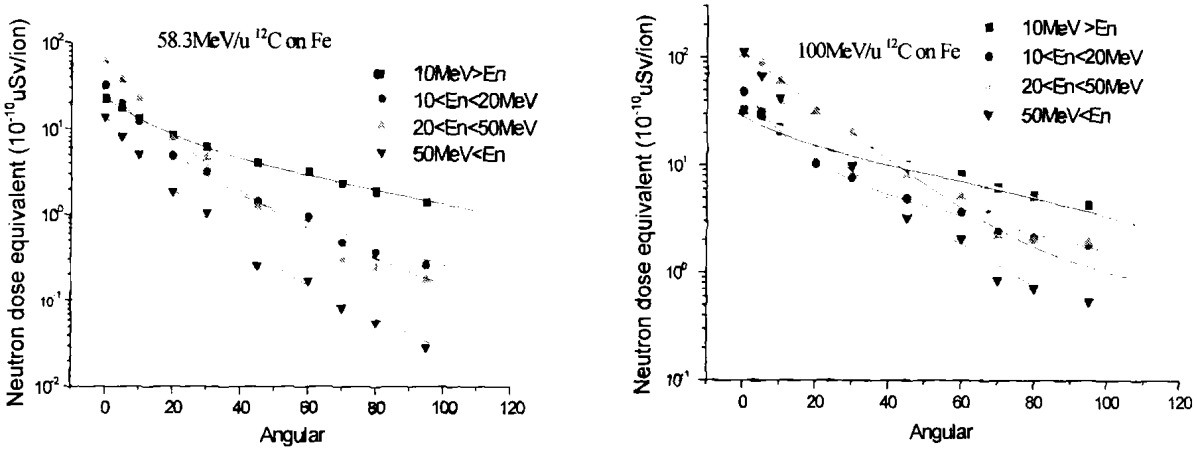

The dose equivalent caused by γ-ray is about ten times less than that by neutron in heavy ion reactions, so the shielding thickness which suit the requirement of neutron protection is enough for γ-ray.

Radiation shielding

According the neutron emission rates, the shielding thickness around HIRFL was calculated with the exponential decay experiential formula [8]. Table 2 gives the shielding thickness of HIRFL, and the movable concrete bricks are widely used in HIRFL to reinforce the shielding effect and to separate the experiment area.

Table 2. The shield wall thickness for HIRFL (ordinary concrete)

Hall	Size (m)	Position of wall	Thickness (cm)
Corridor of front transport line	4.00 × 4.20 (width × height)	side	100
		top	100
SSC hall	26.40 × 29.00 × 12.60 (width × length × height)	east, west, south	260
		north	250
		top	180
Experimental hall	26.40 × 56.45 × 11.80 (width × length × height)	east, west	260
		south	220
		top	180

The entrances of HIRFL were designed with different structure for different purpose, labyrinth for people and shield tank plug with water for big equipment.

The radiation leakage caused by pipe and gap must be carefully considered. Any penetrating pipe should be in an “S” shape and far from the target.

Because the neutron spectra of heavy ion reactions are strongly peak forward, an iron beam dumper is used in HIRFL.

Several measurements have been carried out at HIRFL and have not found any leakage radiation out the shielding.

REFERENCES

[1] B.W. Wei, F. Ye, Proceedings of the 13th International Cyclotrons and Their Applications Conference, Vancouver, 1992.

[2] H.Z. Zheng *et al.*, Neutron Production by Heavy Ion Research Facility in Lanzhou (to be published).

[3] T. Nakamura, Proc. 2nd Symposium on Accelerators Science and Technology, Tokyo (1978).

[4] R.A. Cecil *et. al*., *Phys. Rev*., C21, 2471 (1980).

[5] 理化学研究所リングサイクロトロン放射线安全审查委员会报告书资料,(1982).

[6] H.W. Bertini *et. al*., *Phys. Rev*., C 14, 590 (1976).

[7] B. Fernandez, DPHN-BE/Saclay.

[8] H.Z. Zheng, 辐射防护,Vol. 13, No. 5, 331(1993).

Session III

Shielding Design Problem on High Intensity Medium Energy Accelerators and Target Facilities

Chairs: T. Nakamura and T. Gabriel

METHODS TO CALCULATE SPALLATION SOURCE SHIELDS, COMPARISON WITH EXPERIMENTS AND APPLICATION TO ESS

H. Schaal, D. Filges and G. Sterzenbach
Forschungszentrum Jülich GmbH
Institut für Kernphysik
D-52425 Jülich, Germany

Abstract

The particles which cause the radiation problems of neutron spallation sources are the deep penetrating neutrons with energies above 100 MeV. They determine the dose rate at each point inside the shield because they produce there via cascade a neutron spectrum with energies down to thermal energies. That spectrum is far inside the shield more or less an equilibrium spectrum if the shielding material is not changed.

To calculate neutron spallation source shields different computational methods were developed. One is the so-called coupling procedure. In the vicinity of the neutron spallation target we use the Monte Carlo code HETC of our code system HERMES to calculate the spatial and angular distribution of generated high energy neutrons. This distribution is handed over to the transport code ANISN, which calculates the attenuation of the high-energy neutron flux with distance from the target. The neutron cross-section data necessary for the ANISN calculations are a combination of libraries originally developed at ORNL and LANL for energies up to 800 MeV with data upgraded to 2.8 GeV neutron energy for the materials iron, concrete and soil. The advantage of this calculation method is that it is not very time consuming but that in the target region the geometry can be described exactly and uncharged and charged particles can be treated.

Another method to combine different advantages of codes is to treat the geometry exactly, but to calculate the fast neutron flux and the induced dose rate via semi-empirical equations using attenuation lengths and other parameters derived from transport calculations. The computer code with these features is named CASL. It is a tool to perform design calculations for neutron spallation source shields very easily.

The different calculational methods, which we used for designing the ESS target station shielding, are discussed.

We compared reaction rates and dose rates calculated with our codes with measurements performed at different facilities in the proton energy range from 230 MeV to 2700 MeV. The results of these comparisons are also shown.

Finally we present calculations performed to design shielding for the proposed European Spallation Source (ESS).

Introduction

For high intensity spallation sources like the European Spallation Source (ESS) [1] with proton beam energy of 1334 MeV and beam power of 5 MW, it is important to have properly designed shielding for the accelerator, the proton beam lines, the accumulator rings and the target station. Over-designed shielding would cause immense extra costs, and under-designed shielding would lead to the reduction of maximum intensity and therefore to loss of efficiency of the facility.

The particles which cause the radiation problems are the deep penetrating neutrons with energies above 100 MeV. They determine the dose rate at each point inside the shield because they produce there via cascade a neutron spectrum with energies down to thermal energies, which is for deep penetration more or less an equilibrium spectrum if the material is not changed. Therefore it is clear that the target station shield should consist of materials with short attenuation lengths for high energy neutrons, whereas the shielding of tunnels, etc. might consist of cheaper materials, e.g. concrete or soil.

To calculate shieldings for hadron accelerators, storage rings, and high power spallation target stations it seems to be reasonable to use deterministic methods instead of Monte Carlo codes because deep penetration problems lead to very high computation time to get sufficient statistics. We will discuss here two deterministic methods. We show the main features of these methods, discuss very briefly the generation of the necessary cross-section data sets for these codes in the energy range above 800 MeV, give comparisons of the computational results with experiments in the proton energy range from 230 MeV up to 2700 MeV and show applications of the codes with respect to the shield of the European Spallation Source (ESS).

Codes and data for deep penetration calculations

Codes

For deep penetration, we chose two calculational methods. One is the combination of Monte Carlo codes to calculate the flux in the vicinity of the target with neutron transport codes to calculate the flux inside the bulk shield. We use the Monte Carlo code HETC of the HERMES code system [2] and the one-dimensional deterministic code ANISN [3]. The second method is a semi-empirical one, where the geometry can be described exactly and the neutron flux and dose values are derived from integral parameters using simple penetration equations. The code with these features is called CASL [4,5].

Cross-section data

For both methods neutron transport cross-sections are necessary which were available only up to 800 MeV [6,7]. So the cross-section library LAHI [8] had to be upgraded. This was done for the energy range from 800 MeV to 2800 MeV using HETC code. The calculations ran as follows [9]. For relevant shielding materials calculations with the so-called thin target set-up were performed for each neutron energy group to get the double differential neutron yields. The energy range from 800 MeV to 2200 MeV was divided into seven energy groups with width 200 MeV each, the range up to 2800 MeV into two groups with width 300 MeV each, and the angular space was divided into 60 parts. The deterministic codes need the cross-section data as coefficients of Legendre polynomials. Therefore the angular binned data had to be transformed using orthogonality relations. For details and equations see Ref. [10].

The cross-section generation method was tested by generating data below 800 MeV and comparing it with data of existing libraries. Then it was controlled that the total cross-sections below and above 800 MeV show smooth behaviour. Furthermore a comparison between the neutron flux from a HETC calculation to that from an ANISN calculation for an iron sphere with the neutron source in the centre was performed. Sufficient agreement between both calculations was found for flux distributions as well as for energy spectra. For details see Ref. [10].

Coupling calculation method

The calculational method of coupling HETC with ANISN has several advantages. Geometrical effects and all particle types in the target vicinity can be treated exactly by HETC, so that one gets correct fast neutron flux distributions outside the target region. But bulk shielding calculations with HETC are very time consuming and can lead to erroneous results because of lack of statistics. So it is better to calculate the neutron flux behaviour inside the shield with the one-dimensional deterministic transport code ANISN. This can be done with sufficient accuracy if ANISN gets the correct information of the neutrons generated in the target region.

This information transfer is performed as follows. In the geometry description of a spallation target facility for the HETC calculations we define a sphere with centre in the target and outer radius R in the shield so far from the target, that protons and other charged particles are negligible but neutron statistics are yet reasonable. Then a special part of the spherical surface is defined as coupling area. Neutrons crossing this area are scored in energy group and angle by a special detector of HETC. The energy groups have to be those of the cross-section data sets used in the ANISN calculation. The ANISN calculation is performed in spherical geometry with inner radius R and the surface source generated by HETC at this position. The outer radius of the ANISN sphere is the distance from the target to the outer shield surface of the facility. The used cross-section database is LAHI [9] which was described before. The result of the ANISN calculation is the neutron flux distribution inside that part of the target shield which lies in the direction from the target to the coupling area.

By defining different coupling areas for different solid angles one can calculate the neutron flux behaviour in those parts of the shield which belong to those angles. It should be mentioned that the HETC detector counts different angles in form of amplitudes of Legendre polynomials. So the surface source data handed over to ANISN are a set of Legendre coefficients for each energy group at each coupling radius R. The advantage of this method is that the surface source can be used by ANISN calculations with different angular quadrature sets. Details and equations of the coupling procedure can be found in Ref. [10].

Semi-empirical method

CASL determines the dose and fast flux at each point via semi-empirical equations. Therefore the code does not need much computer time. Another advantage, especially in the design of facilities, is that CASL can treat the geometry exactly using the same geometry description as HETC. The basic idea of CASL is that high-energy neutrons ($E_n > 100$ MeV) have low cross-sections so that these particles are the only wide ranging particles in the shield. These high-energy neutrons produce via cascade a neutron spectrum with energies down to thermal energy. This neutron spectrum is for deep penetration more or less an equilibrium spectrum if the shielding material is not changed, and it determines the dose rate. So it is only necessary to calculate the fast neutron flux to get the desired dose values. Therefore the basic equation of CASL reads:

$$F = S * B * exp(-x/\lambda) / r^2$$

with: *F* the high energy neutron flux at point P
S the angular dependent high energy neutron source strength of the target
B the so called build up factor
x the depth of point P inside the shield
λ the attenuation length of the high energy neutrons
r the distance from target to point P

The desired neutron dose rate *D* at point P is then:

$$D = k * F$$

with *k* the depth dependent fast flux to dose conversion factor.

The tabulated values of *S* are obtained from HETC calculations with thin target option for different proton beam energies and different target materials. The values of *B*, *k*, and the most important parameter λ are taken from ANISN calculations for different neutron energies and different shielding materials.

Comparison of calculated results with experiments

To check the computational methods described above with measurements we chose deep penetration experiments performed at different facilities and with different proton beam energies in the range from 230 MeV up to 2700 MeV.

WNR facility

We start with the experiment performed by W. Amian *et. al*. [11] at the WNR facility of Los Alamos National Laboratory. The proton beam with 800 MeV hit a tungsten target of 4.45 cm diameter and 24 cm length surrounded by a beryllium reflector and water moderator assembly. The flight path 5 of the surrounding WNR shield was filled with iron rings. In the centre of these rings an iron stringer was introduced containing lots of metal foils as threshold detectors to be irradiated. The direction of flight path 5 is perpendicular to the proton beam direction.

For the calculations (see Figure 1) we surrounded the tungsten target by 13 cm of beryllium and modelled the flight path region by a big iron cylinder beginning with radius 100 cm, i.e. at the same distance from the target centre as the inner surface of flight path 5. At those radii where foils were positioned inside the iron container we put volume detectors (denoted as A, B and C) for the HETC calculations. Inside the shield region a sphere (denoted as CS) was used as surface to generate the source for the ANISN coupling calculations. With code HETC we calculated the neutron flux above 15 MeV for the volume detectors A and B and the high energy surface source for ANISN. Detector C is more than 2 m inside the shield and did not get enough events to have sufficient statistics. With ANISN we calculated the deep penetrating neutron flux as well. For the calculated reaction rates we used threshold cross-sections of G. Rudstam [12]. The results from ANISN coupling calculations are denoted as ANISN-CP in the tables.

We compared the reaction rates of the threshold detector material natural copper (see Table 1) at the position B for those reactions which have relevant cross-sections only above 15 MeV. It can be seen that reasonable agreement between measurement and calculations can be found.

ISIS

Y. Uwamino *et al*. [16] performed a shielding experiment at the target station of the ISIS facility (E_p = 800 MeV) at Rutherford Appleton Laboratory (UK) and compared the experimental data with calculations [16]. We calculated the dose rate at the top of the target shield, i.e. perpendicular to the proton beam direction. For the neutron dose determination we used the flux to dose conversion factors derived from ICRP51 [13]. The top position has a distance of 133 cm from the target and the shield thicknesses are 291 cm of cast iron and 96 cm of concrete. The result of the calculations compared to the measured dose rate is shown in Figure 2. It can be seen that CASL overestimates the dose whereas the coupling calculation underestimates the experimental value by a factor of about 5. It should be mentioned that the coupling calculations of Uwamino *et al*. show similar results.

SATURNE

L. Bourgois *et. al*. [14] describe neutron dose measurements performed at SATURNE in Saclay for proton beam energy of 2700 MeV for different targets and different detector positions. We calculated the experiment for a 30 cm long iron target with 8 cm in diameter and with detectors positioned behind the concrete wall in directions of 50, 90, and 100 degrees with respect to the proton beam direction, as can be seen in Figure 3. For the ANISN coupling calculations the spheres have inner radii of about 1 m larger than the line of sight inside the concrete wall. Figure 4 gives the comparison of experimental to calculated dose for 50 degrees, Figure 5 for the perpendicular direction. The ANISN coupling calculations (denoted as HET-ANISN) seem to be in reasonable agreement with the experiment, but the values from CASL are too large. The differences are increasing with increasing angle to proton beam direction. The reason for this behaviour is that the neutron spectrum is weakening with increasing angle, but this effect cannot be taken into account by CASL. Let us mention that we show for comparison pure Monte Carlo results (denoted as HET-MORSE) as far as reasonable statistics was achieved.

Loma Linda test area

For a lower proton beam energy of 230 MeV, J.V. Siebers [15] described a series of neutron dose measurements for different stop targets and different detector positions inside thick concrete walls for the Loma Linda shielding study area at Fermilab (see Figure 6). We calculated the dose for the iron target case. For the calculations with HETC and MORSE we chose volume detectors. The ANISN coupling calculations were performed for different coupling surfaces. The comparison of experimental and calculated dose values for the detectors in beam direction is given in Figure 7, for detectors in direction of 45 degrees in Figure 8, and for those detectors perpendicular to the beam in Figure 9. In all cases it can be seen clearly that with increasing distance and with increasing angle the neutron dose calculated by CASL is reasonably larger than the experimental value whereas the values calculated by ANISN are near to the experimental ones.

The results show that the ANISN coupling method gives reasonable results and that CASL overestimates the neutron dose. This has to be confirmed by comparison with more experimental values. We hope to get results which give information where and how we have to improve our data and/or our codes.

ESS shield design calculations

Target shielding

We used the coupling method to calculate the shielding thickness of the ESS target station. As target we used a system of tungsten cylinders with total length of 50 cm and radius of 5 cm. The target is surrounded by a lead reflector. The target region is embedded in an iron sphere where we put the coupling surface 20 cm inside the iron. The calculations were performed for the proton energy E_p = 1350 MeV and different angular ranges. As the result of the coupling calculations we got the angular dependent bulk shield thicknesses necessary to have dose rates less than 7.5 μSv/h (see Table 2). We used these results to check the CASL code for ESS design calculations. The comparison of coupling results with CASL results was performed for the three angles 5, 85, and 175 degrees relative to the proton beam direction (see also Table 2). It can be seen that only in backward direction CASL gives significantly larger dose rates than the coupling method.

The CASL calculations indicate that an outer concrete wall of thickness 40 cm seems to be reasonable and that the iron shield should be about 1 m thicker in beam direction than in the backward direction. So we find the ESS target shield dimensions shown in Figure 10.

Proton beam line shielding

We assumed linear proton beam losses with maximum loss of 100 nA/m during normal operation, i.e. for ESS proton beam energy 1334 MeV and beam current of 3.748 mA (i.e. 5 MW beam power). The beam tunnel was assumed to have 3 m radius and to be surrounded by a concrete wall of 1.5 m thickness. Outside the concrete the tunnel system had to be shielded by a wall of dry soil. This seems to be a stable and cheap beam line shielding arrangement. The thickness of the surrounding wall had to be determined.

We performed the CASL calculations in the following manner: In the centre line of the beam tunnel we put a metal target of 1 m length and the proton beam current was assumed to be 100 nA to simulate the desired loss of 100 nA/m. This was done because CASL is not able to use linear sources but point sources only. For the calculations we varied the thickness of the wall of dry soil and counted the dose rate parallel to the tunnel axis directly outside this wall. The dose rate distribution for a wall thickness of 8.8 m is shown in Figure 11.

We integrated the dose rates along the distance and got so the entire dose rate at each point outside the wall. The reason for this behaviour is the fact that the addition of a lot of sources put beside each other with distance of 1 m lead to a superposition of dose rates so that for infinite number of targets the dose rate at each point outside the wall is exactly the sum described above. For 8.8 m wall thickness we calculated an integrated dose rate of 2.5 μSv/h.

REFERENCES

[1] ESS – A Next Generation Neutron Source for Europe, Vol. III, ISBN: 090 237 6659 (1996).

[2] P. Cloth *et al.*, HERMES, A Monte Carlo Program System for Beam-Materials Interaction Studies, KFA-Report Jül-2203 (1988).

[3] W.W. Engle Jr., ANISN, K-1693, ORNL-TN (1967).

[4] T.W. Armstrong, CASL – A Computer Aided Shielding Layout Code, unpublished (1985).

[5] B. Wolfertz, "Entwicklung eines ingenieurmäßigen Simulationssystems zur Berechnung von Strahlenschutzparametern an Protonenbeschleunigern im Energiebereich bis 3 GeV", Dissertation D 468, Universität Wuppertal (1995).

[6] R.G. Alsmiller, Jr. and J. Barish, HILO, 66 Neutron, 21 Gamma Ray Group Cross-Sections for Radiation Transport for Neutron Energies up to 400 MeV, Report ORNL/TM-7818 (1981); see also: ORNL-RSIC-DLC-87 (1982); see also: *Nucl. Sci. and Eng.* 80 (1982).

[7] W.B. Wilson, Nuclear Data Development and Shield Design for Neutrons Below 60 MeV, LA-7159-T, Los Alamos (1978).

[8] H. Schaal and D. Filges, Combination of the High Energy Libraries LANL and HILO as LAHI Library for Deep Penetration Calculations, KFA Interne Aktennotiz, SNQ3J/BH120783 (1983); see also: DLC-128/LAHIMACK in RSIC Data Library Collection, RSIC Newsletter, June 1987.

[9] J. Moll, KFA-Report Jül-2435 (1991).

[10] D. Filges *et al.*, Proceedings of the Specialists Meeting on Shielding Aspects of Accelerators, Targets and Irradiation Facilities, Arlington, Texas, April 1994, pp. 253-270.

[11] W. Amian *et al.*, A Medium Energy Neutron Deep Penetration Experiment, KFA-Report Jül-2101, November 1986.

[12] G. Rudstam, Zeitschrift für Naturforschung 21, 1027 (1966) see also: J.T. Rutti, J.V. Sandberg, *Computer Physics Communications* 23, 411 (1981).

[13] ICRP Publication 51, Radiation Protection, Data for Use in Protection Against External Radiation: A Report of a Task Group of Committee 3 of the International Commission of Radiological Protection, March 1987.

[14] L. Bourgois *et al.*, *Health Physics*, Vol. 70, January 1996, p. 36.

[15] J.V. Siebers, Shielding Measurements for a 230 MeV Proton Beam, The University of Wisconsin, Madison (1990).

[16] Y. Uwamino *et al.*, Proceedings of the Specialists Meeting on Shielding Aspects of Accelerators, Targets and Irradiation Facilities, Arlington, Texas, April 1994, pp. 185-194.

Table I: Comparison of calculated and measured reaction rates of natural copper per foil nucleon and per incident proton at radius r = 223 cm in WNR shield

Reaction product	Reaction rate (10^{-36}/nucleon/proton)		
	Experiment	HETC	ANISN-CP
^{59}Fe	11	29	36
^{58}Co	180	270	360
^{57}Co	95	72	100
^{56}Co	17	13	21
^{52}Mn	2.8	3.2	6.1
^{54}Mn	32	29	48
^{48}V	1	0.9	2.1

Table 2. Shield thicknesses for different directions to proton beam calculated by HETC-ANISN coupling to get outer dose rates below .5 μSv/h and dose rates calculated by CASL for those thicknesses

Beam direction (degree)	Thickness coupling method (cm)		CASL calculated dose rate (μSv/h)
	Iron	Concrete	
0 - 20	520	40	1. - 10
20 - 40	470	40	
40 - 80	470	30	
80 - 100	460	30	1. - 10
100 - 150	420	30	
150 - 180	390	30	10. - 100

Figure 1. Geometry set-up of WNR shield for radiation transport calculations

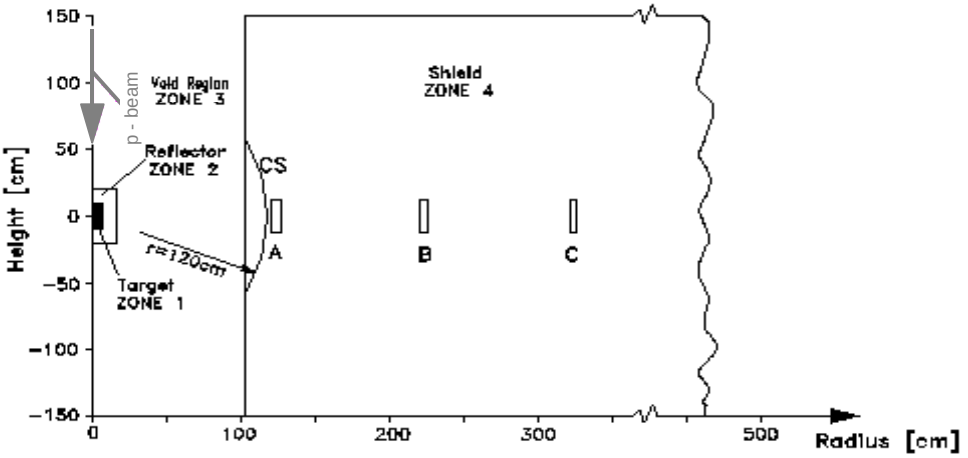

Figure 2. Radial dose rates of ISIS shield perpendicular to proton beam direction

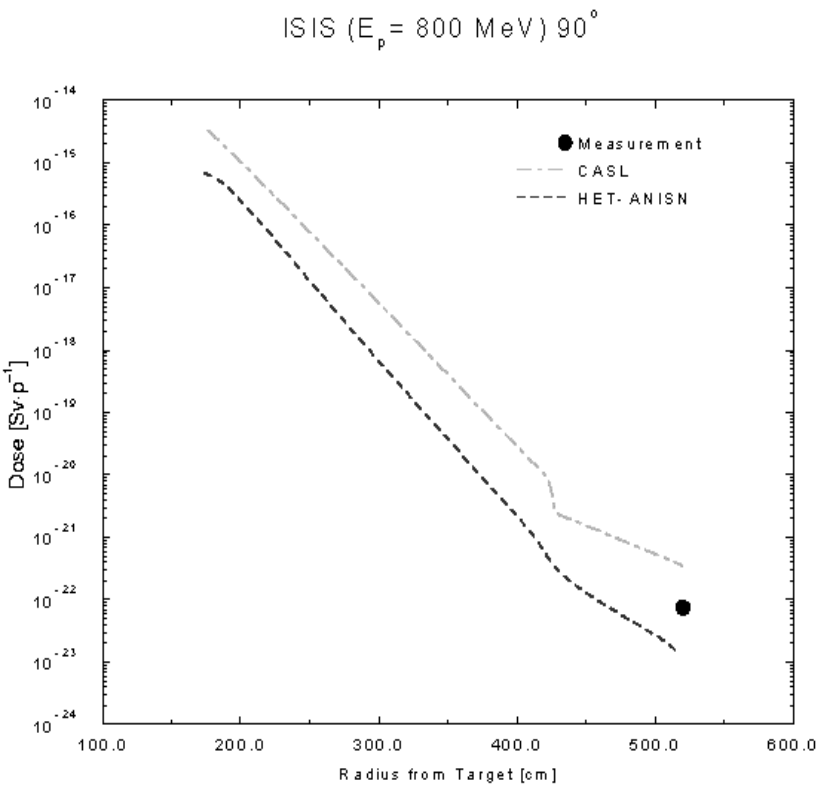

Figure 3. Geometry set-up of SATURNE concrete shield

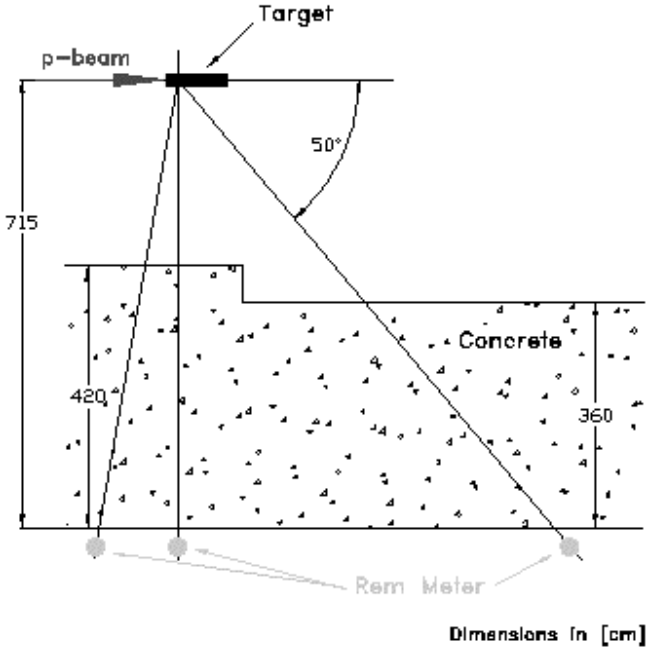

Figure 4. Dose rates of SATURNE shield at 50 degrees to beam direction

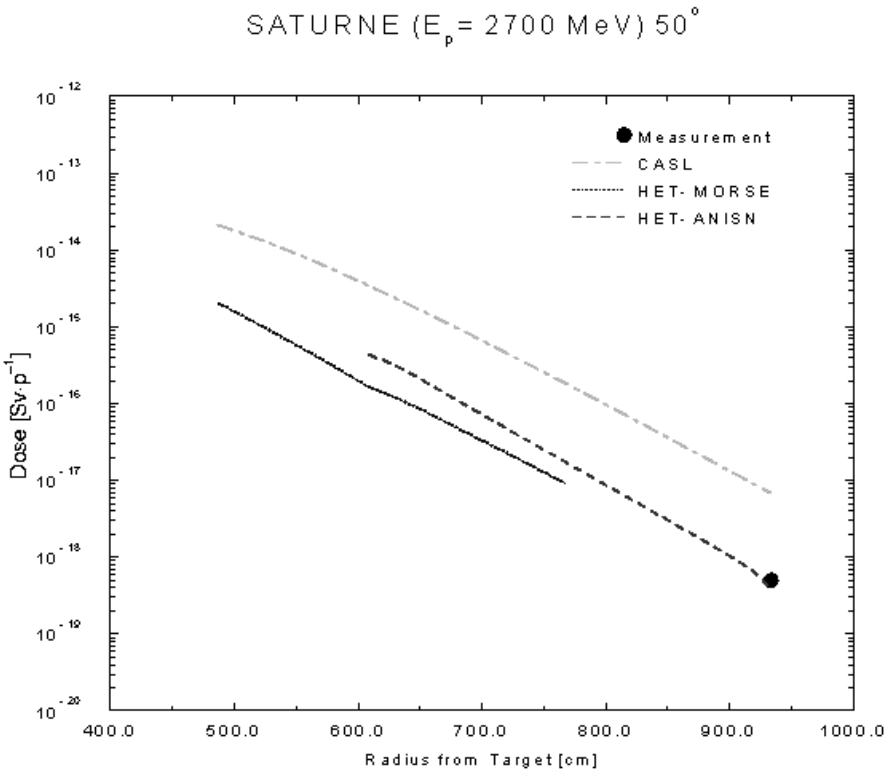

Figure 5. Dose rates of SATURNE shield at 90 degrees to beam direction

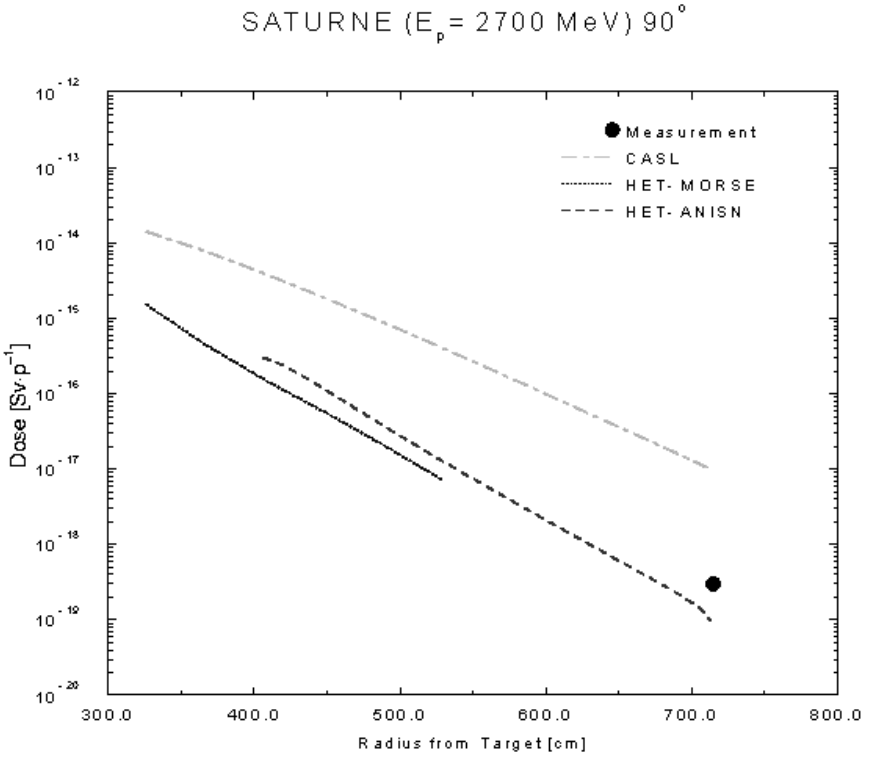

Figure 6. Overhead schematic view of the Loma Linda shielding study area

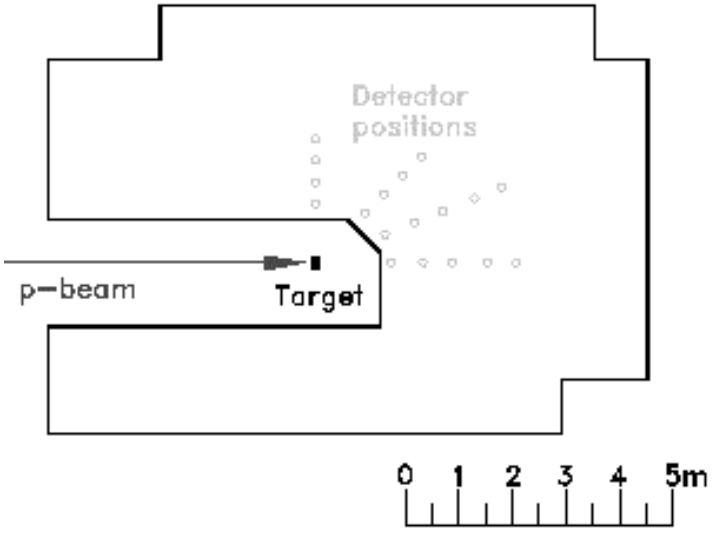

Figure 7. Dose rates of Loma Linda test shield in beam direction

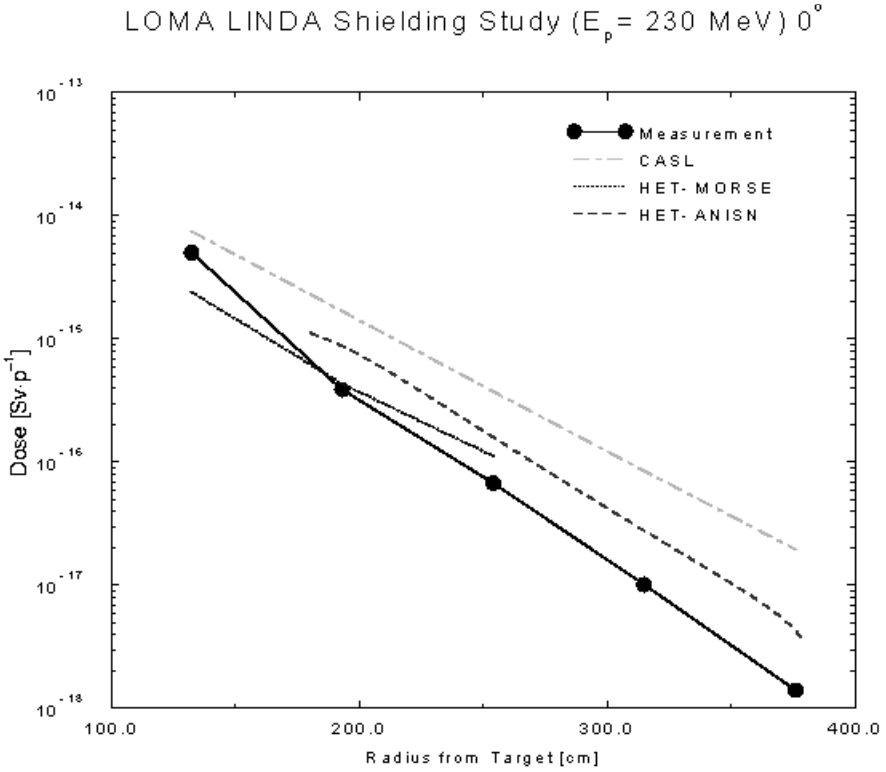

Figure 8. Dose rates of Loma Linda test shield at 45 degrees to beam direction

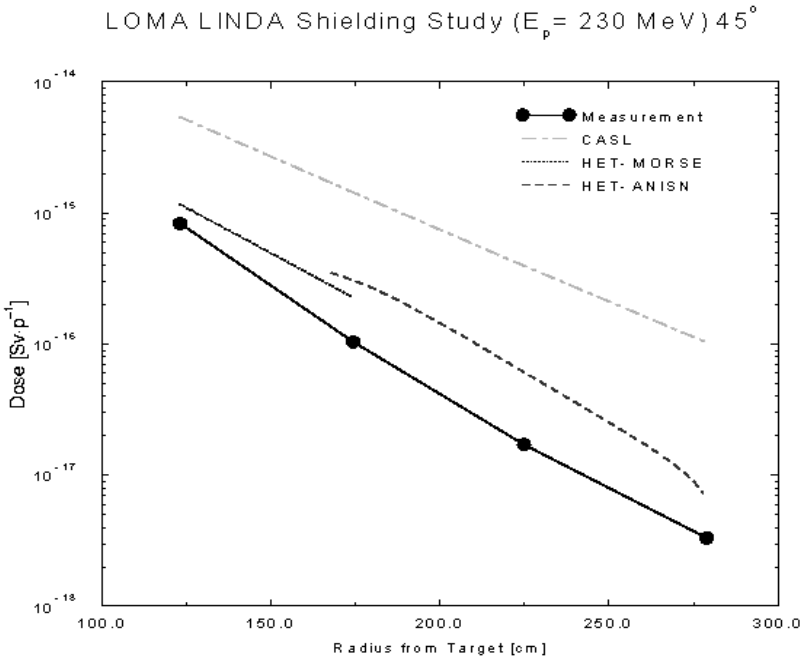

Figure 9. Dose rates of Loma Linda test shield at 90 degrees to beam direction

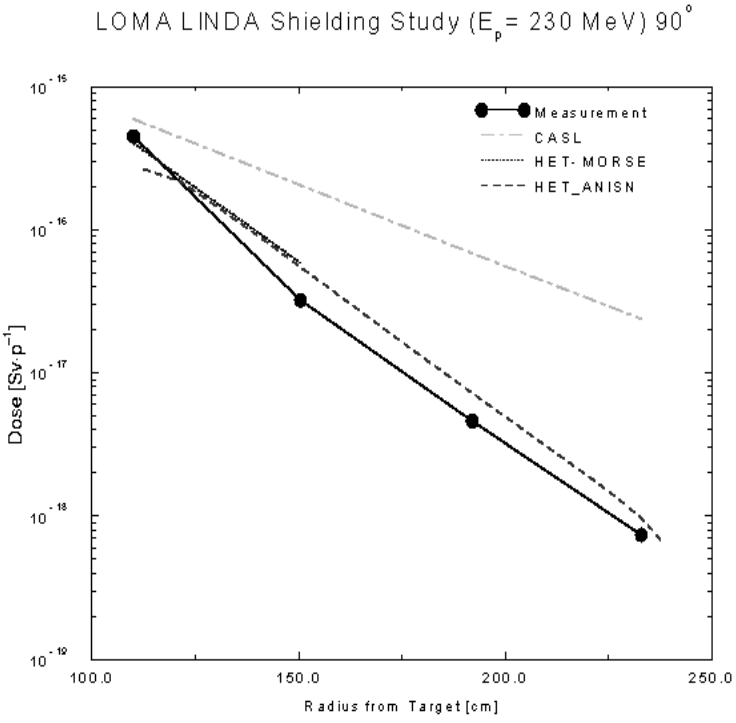

Figure 10. Schematic view of the ESS target shield

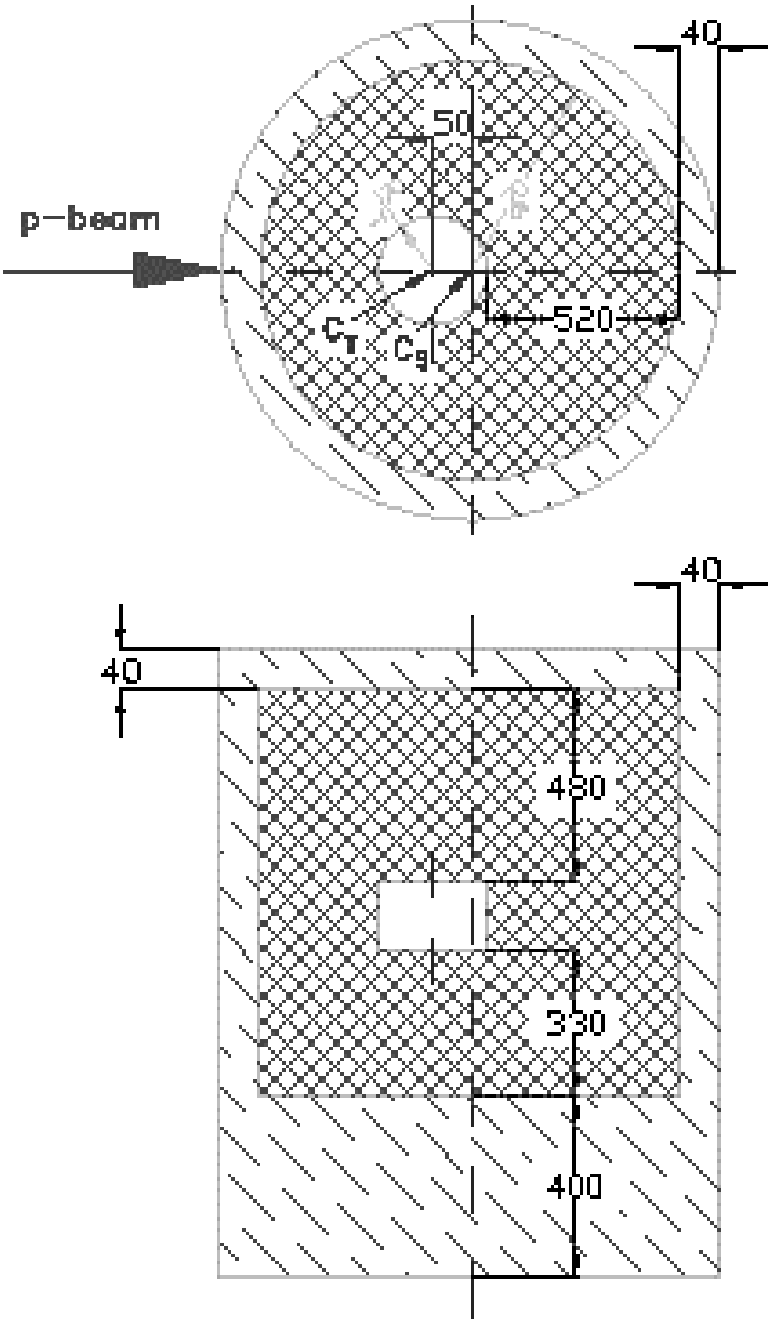

All dimensions in [cm]

Figure 11. Dose rate distribution outside tunnel shield for losses of 100 nA/m

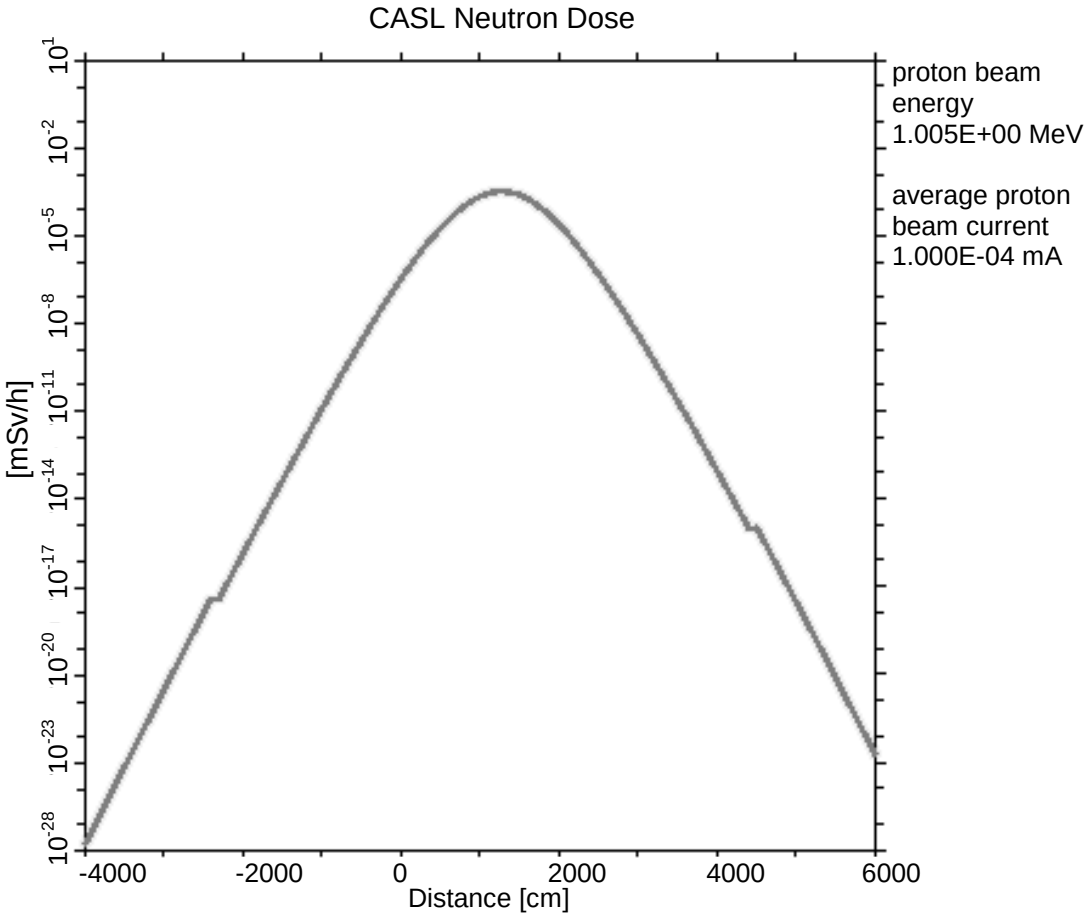

SHIELDING DESIGN OF THE SPALLATION NEUTRON SOURCE (SNS)

Jeffrey O. Johnson
Oak Ridge National Laboratory
P.O. Box 2008
Oak Ridge, Tennessee 37831-6364
Phone: 423/574-5262
Fax: 423/574-9619
E-mail: joj@ornl.gov

Abstract

The shielding design is important for the construction of an intense high-energy accelerator facility like the proposed Spallation Neutron Source (SNS) due to its impact on conventional facility design, maintenance operations and since the cost for the radiation shielding shares a considerable part of the total facility costs. A calculational strategy utilising coupled high energy Monte Carlo calculations and multi-dimensional discrete ordinates calculations, along with semi-empirical calculations, was implemented to perform the conceptual design shielding assessment of the proposed SNS. Biological shields have been designed and assessed for the proton beam transport system and associated beam dumps, the target station, and the target service cell and general remote maintenance cell. Shielding requirements have been assessed with respect to weight, space, and dose-rate constraints for operating, shutdown, and accident conditions. A discussion of the proposed facility design, conceptual design shielding requirements, calculational strategy, source terms, preliminary results and conclusions, and recommendations for additional analyses are presented.

Introduction

The Department of Energy initiated a conceptual design study [1] for the Spallation Neutron Source (SNS) and has given preliminary approval for the proposed facility to be built at Oak Ridge National Laboratory. The conceptual design of the SNS consists of an accelerator system capable of delivering a 1 GeV proton beam with 1 MW of beam power in an approximate 0.5 μs pulse at a 60 Hz frequency into a single target station. The SNS will be upgraded in stages to a 4 MW facility with two target stations (a 60 Hz station and a 10 Hz station). The radiation transport analysis, which includes the accelerator and target station neutronics, shielding and activation analyses, is important for the construction of the SNS because of its impact on conventional facility design, maintenance operations, and because the costs associated with incorporating the results of the radiation transport analysis comprise a significant part of the total facility costs. A strategy utilising coupled Monte Carlo and multi-dimensional discrete ordinates calculations, along with semi-empirical calculations has been implemented to perform the conceptual design shielding analysis.

SNS facility description

The complete accelerator system consists of a front end ion source, a linac, an accumulator ring and the associated transfer lines required to link the complete system together. The primary function of the front end systems is to produce a beam of H^- ions to be injected into the linac at 2.5 MeV. This facility consists of the ion source, the low energy beam transport (LEBT) line, and the medium energy beam transport (MEBT) line. Details of the front end systems design can be found in Section 2 of Ref. [1].

The linac is coupled to the MEBT, accepts beam from the front end system, and accelerates it from 2.5 MeV to 1.0 GeV. The linac consists of a drift-tube linac (DTL) that accelerates the H^- beam to 20 MeV, a coupled-cavity drift-tube linac (CCDTL) that further accelerates the H^- beam to 93 MeV, and a coupled-cavity linac (CCL) that accelerates the H^- beam to 1.0 GeV. The total length of the linac is approximately 492 meters. A detailed discussion of the considerations that went into the design choices and the operating parameters for the various linac components is given in Section 3 of Ref. [1].

The remainder of the accelerator system is made up of the high energy beam transport (HEBT) system from the linac to the ring, the accumulator ring and the ring to target beam transport (RTBT) system. The lengths of these three components are 165 m (HEBT), 221 m (ring) and 167 m (RTBT). The HEBT system provides the beam transport between the linac and the accumulator ring. The ring accumulates beam pulses from the linac and bunches them into intense short pulses for delivery to the target. A 1 millisecond pulse of H^- ions is delivered to the ring, passed through a stripping foil to convert it to protons, wrapped around the ring circumference approximately 1200 turns, kicked out in a single turn making a sharp pulse of approximately 0.5 μs to be delivered to the mercury target. This process is repeated 60 times per second. The RTBT accepts the extracted beam from the accumulator ring and transports it to the mercury target. A detailed discussion of considerations leading to design choices and design parameters for the beam transport and accumulator rings can be found in Section 4 of Ref. [1].

The SNS target system has the basic function of converting the short pulse (<1 μs, 60 Hz, 17 kJ/pulse), high-average power (1 MW), 1 GeV proton beam delivered via the RTBT into 18 lower-energy (<1 eV), short-pulsed (~ tens of μs) neutron beams optimised for use by neutron scattering instruments. The proton beam target is liquid mercury flowing inside a stainless steel

container. The proton beam enters horizontally at two meters above the floor level. The target is positioned within a layered iron and concrete shielding monolith approximately 12 meters in diameter. Two ambient water moderators are positioned under the target and two supercritical hydrogen cryogenic moderators are positioned above the target. The moderators are surrounded by a heavy water cooled beryllium reflector region. The core region which includes the target, moderators and beryllium reflector, is contained inside a two-meter diameter vessel filled with nickel and a helium atmosphere. Water cooling is used to cool the mercury, shielding, vessels, reflectors, and other assemblies inside the shielding monolith. The target is designed to be installed and removed horizontally using an adjacent service cell. The target service cell is located behind the target assembly and measures 10 meters wide by 17.8 meters long by 7.5 meters high. Work will normally be performed via remote handling techniques behind a one meter thick heavy concrete wall. The other core components are designed to be removed vertically and serviced in a second service maintenance cell adjacent to the target service cell. The general maintenance cell will be used to maintain the moderator/reflector/plug, proton beam window, neutron guide tubes and shutters. This cell measures 10 meters wide, 10.9 meter long and 9.5 meters high. There are 18 neutron beam lines viewing the moderators, nine on each side, and equally spaced in angle. Each beam line has an independently operable shielding shutter controlled by the experimentalists. The beam lines are located at two levels; nine lines directed at the ambient water moderators under the target, and nine at the cryogenic hydrogen moderators above the target. The shielding extends to a radius of eight meters at the beam line level to provide a region for the neutron beam choppers with a vertical access hatch positioned at a radius of seven meters. More detailed discussions of the selection criteria and design considerations for the target systems in general are contained in Section 5 of Ref. [1].

Conceptual design shielding criteria

The conceptual design phase of a project typically includes preliminary data on requirements for instruments and equipment that have safety-related functions. During this design phase, potential hazards are identified and mitigation procedures are described. Also, the hazard level for each major part of the facility (e.g. linac, ring, target station, etc.) is determined. The top level document for accelerator safety regulation, DOE Order 5480.25 – Safety of Accelerator Facilities [2], provides a framework for evaluating the safety of the SNS and the initial shielding assessment. More specifically, this document provides guidance in preparing the preliminary and final safety assessment documents (PSAD and FSAD), determining the facility hazard categorisation (low, moderate, or high), and the possibility of segmenting the facility to allow for an optimum graded approach to hazard mitigation.

The preliminary safety assessment of the SNS recognises the unique nature of accelerator safety hazards. This assessment indicates the SNS has no credible potential to affect public safety, and that the greatest hazard to worker safety will be prompt radiation during operation of the proton beam. Furthermore, the SNS target station does not have sufficient decay heat to drive the release of spallation and/or activation products and consequently represents a minimal risk to the environment and public health. To insure a low hazard rating for the SNS and potentially have the SNS evaluated as an “accelerator” facility versus a “nuclear” facility, the design of the SNS will rely on passive safety features (shielding) to as large an extent as economically feasible.

With that as a goal, and using DOE Order 5480.25, the following shielding/radiation policy was set for the conceptual design analysis. During normal operation the shielding should be designed such that the dose rate on accessible outside surfaces of the shield is less than 0.05 mrem/h in non-controlled areas and less than 0.125 mrem/h in areas under access control. Furthermore, beam control/focus requirements will be designed to keep activation of structure low enough to allow

hands-on maintenance in the linac and ring tunnels. During postulated beam control accidents, the shield thickness should reduce the dose rate on accessible outside surfaces of the shield to less than 1 rem/h in non-controlled areas of the facility and less than 25 rem/h in areas under access control. Shielding requirements relating to meeting or extending equipment lifetimes are determined on a case by case basis and typically within personnel shielding requirements. Achieving these accident shielding goals without reliance on automatic beam shut-off systems will justify a "low hazard" category rating for the SNS accelerator.

Calculational methodology

The CALOR [3] code system was the main calculational tool used for the radiation shielding studies. The three-dimensional, multimedia, high-energy nucleon-meson transport code HETC96 was used to obtain a detailed description of the nucleon-meson cascade. This Monte Carlo code takes into account the slowing down of charged particles via the continuous slowing-down approximation; the decay of charged pions and muons; and inelastic nucleon-nucleus and charged-pion-nucleus (excluding hydrogen) collisions through the use of a multitude of high energy physics models. The MCNP Monte Carlo transport code [4] was coupled to HETC96 to obtain the proper source for the low energy ($E < 20$ MeV) neutron transport. MCNP is a general purpose, continuous-energy, generalised geometry, time-dependent, coupled neutron-photon-electron Monte Carlo transport code system. For the shielding design of high power spallation targets and hadron accelerators with energies up to 1 GeV, it is beneficial to use deterministic methods for the calculations instead of Monte Carlo methods because deep penetration problems require very high particle numbers to obtain good statistics, and high particle numbers typically lead to high computational times. For the SNS conceptual design shielding analyses, three approaches were implemented.

One approach, shown in Figure 1, was to couple HETC96 with the ANISN one-dimensional discrete ordinates deterministic transport code [5] to analyse the deep penetration shielding requirements. In this analysis, the HILO86 coupled 66-neutron, 22-gamma-ray cross-section library [6] was used. A second approach (Figure 2) used the Computer Aided Shield Layout (CASL) code [7] developed at KFA Julich. The HETC96 and MCNP codes have the advantage of containing state-of-the-art physics treatments and cross-section data. However, they require considerable set-up and computing times. The CASL code has general source, material, and geometry capabilities but needs minimal computer and set-up time. CASL uses approximate, semi-empirical physics treatments to provide sufficient accuracy in the SNS conceptual design for many of the practical shielding problems. Finally, to address the shielding for shutdown activation sources, the procedure shown in Figure 3 was adopted. The HETC and MCNP codes provide the required input data for the isotope generation and depletion code, ORIHET95 [8], which utilises a matrix-exponential method to study the build-up and decay of activity for any system for which the nuclide production rates are known. The combination of these two sources yield the radionuclide concentrations, radioactivity, and time dependent decay gamma source spectra, as a function of generation (build-up) time and depletion (decay), for input into the ANISN or DORT discrete ordinates deterministic transport codes.

Geometry models

To perform the shielding and activation analysis on the linac and ring tunnels, klystron building and linac service road, a simplified model was constructed. For the linac components, a section of the tunnel was modelled as a cylindrical shell of concrete 2 300 mm in radius, 460 mm thick, and 20 m long. The tunnel was filed with air and surrounded by approximately 9 m of earth berm for shielding.

Figure 1. Schematic diagram of the coupled HETC96 and ANISN shielding analysis procedure

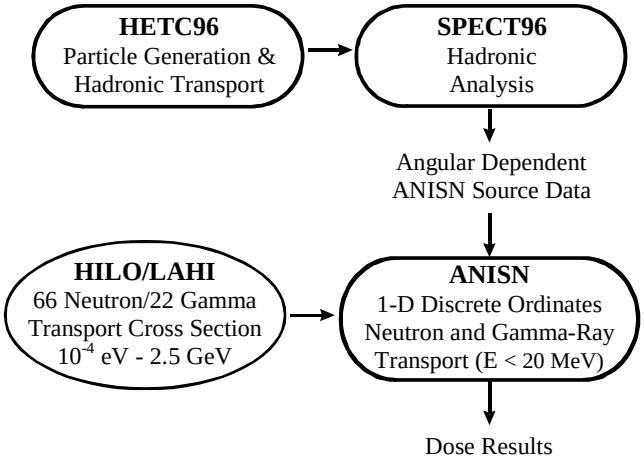

Figure 2. Schematic diagram of the CASL code system shielding analysis procedure

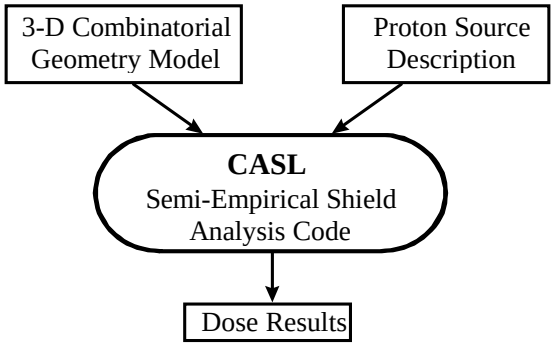

Figure 3. Schematic diagram of the shutdown activation source shielding analysis procedure

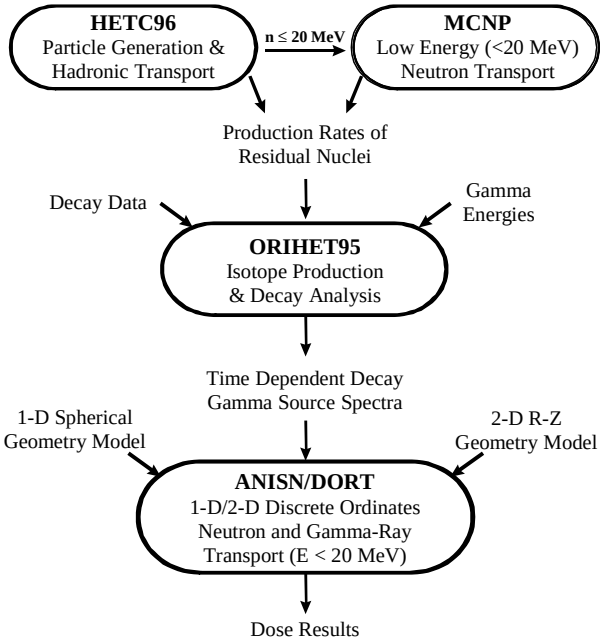

A 150 mm diameter by 1 000 mm cylinder of copper was modelled in the centre of the geometry to simulate the interaction of the proton beam with accelerator components. An equivalent model for the ring tunnel was constructed except the radius of the concrete shell was 3 200 mm. Activation analyses were performed with these models to assess the potential radioactive by-products generated as a function of normal operation of the SNS facility and shielding calculations were performed using the methodology discussed in the section entitled *Calculational methodology* to determine earth berm shielding thickness requirements for normal operation and design basis accident scenarios.

A geometry model of the target station design (Section 5, Ref. [1]) was constructed to determine the energy deposition, material damage, activation, radiation flux spectra and shielding requirements for the entire target station including the biological shielding. In this geometry, the mercury target was represented with a simplified model and the moderator assemblies and associated neutron beam tube design from an earlier target assembly model was incorporated. All core components were modelled in sufficient detail to determine the component activation, cooling requirements and bulk shielding requirements.

The initial design of the SNS employs three beam dumps. All three beam dumps use an 80% copper/20% water target approximately 600 mm in diameter and 750 mm in length. The central target is surrounded by a water cooled steel central core, followed by a sufficient amount of slab steel shielding to prevent significant activation of the surrounding soil or groundwater. The steel monolith is encased in a steel lined 460-mm-thick concrete enclosure to contain leaks. The linac tune dump, ring tune dump, and ring injection dump are all to be shielded to operate at 200 kW. This power level and the required groundwater and soil activation constraints will determine the required amount of steel shielding for each dump.

For the target service cell and general maintenance cell, the rooms were typically modelled using a one-dimensional spherical model. The mercury spill case was modelled with a two-dimensional cylindrical model. The models were comprised of spherical or cylindrical room equivalent volumes surrounded by one-meter-thick concrete walls. A candidate decay gamma radiation source term was placed in the centre of the models. The models contain representative volumes of the different components from which the gamma-ray sources were derived so as to take into account attenuation by the components.

Shielding analysis

Shielding a spallation neutron source is more difficult than shielding a reactor neutron source because spallation neutrons have higher energies than fission neutrons. For a spallation neutron source, the highest-energy cascade neutrons approach the energy of the incident proton beam. These high-energy neutrons are extremely penetrating, and well-designed shielding is needed to prevent them from causing excessive biological dose rates.

For spallation reactions, energy effects are divided into two regions: low-energy (< 20 MeV) and high-energy (> 20 MeV). This energy cut-off is convenient because the continuous-energy cross-section libraries used by MCNP have evaluated cross-sections up to 20 MeV. Low-energy neutron production from a target is the low-energy spallation neutron production plus the net production from low-energy "(n,xn)" reactions. These low-energy neutrons are emitted isotropically and cause shielding problems similar to that of fission reactors. High-energy neutrons resulting from nucleon-nucleon reactions have a strong angular dependence. At 0° to the proton beam direction, high-energy neutrons can have energies up to the incident proton energy. As the angle increases with respect to the proton beam, the high-energy neutron spectrum softens significantly.

The presence of these high-energy neutrons and their strong angle-dependence complicate spallation source shielding. Shielding a spallation source is further complicated by the fact that different neutron leakage spectra are produced depending on target thickness and material. Furthermore, in a spallation neutron source, high-energy neutron attenuation generates more low energy neutrons and creates an additional secondary gamma-ray source, i.e. the shield itself becomes a neutron source. Typically, the high-energy neutrons plus their progeny dominate the dose at the shield surface. Iron combined with concrete is required to shield the high-energy neutron component at a spallation neutron source, whereas, concrete or water is an effective neutron shield for a fission neutron source. Consequently, the iron-concrete high-energy neutron shield at a spallation source is also an effective shield for the low-energy spallation neutron component.

Shielding design calculations have been performed for all sections of the SNS facility. Biological shields have been designed and assessed for the proton beam transport system and associated beam dumps, the target station, and the target service cell, general remote maintenance cell, and utility vault. Calculations have been performed for normal operation, catastrophic accident scenarios, and shutdown activation sources. The appropriate shielding design criteria outlined in the first section of this report were utilised for the sequence of calculations to be performed for each SNS facility component.

A summary of the shielding analyses, source terms, and calculational methodologies used to support the conceptual design of the SNS is given in Table 1. For each analysis, a summary of the dose criteria, SNS conceptual shield design, calculated minimum required shielding and representative dose rate results are presented in Table 2. These results were extracted from tabulated shielding data used to support the SNS conceptual design and represent the calculation of maximum dose or minimum required shielding to meet the SNS shielding criteria specified in the first section of this report. Detailed discussions of the analysis assumptions and preliminary results are presented in each of the following subsections. From this sequence of calculations, preliminary shield designs have been integrated into the overall facility design and optimised to achieve as low as reasonably achievable dose to the facility personnel, visiting experimentalists, and sensitive electronic equipment. The intention is to build the SNS facility in stages and each stage will approximately double the delivered beam power. To ensure that there will be no fundamental impediments in the design for the later stages of the project, all calculations in support of the SNS conceptual design were based on the final maximum beam power of 4 MW unless otherwise noted.

Linac, ring, klystron building and linac service road shielding analyses

For the purpose of determining the dose rates associated with normal operation and postulated catastrophic design basis accidents of the accelerator system, the linac and ring models described in the section entitled *Geometry models* were employed in coupled HETC-ANISN calculations and semi-empirical CASL calculations using the shielding policy guidelines discussed in the first section of this report. HETC directionally dependent sources were generated for the high energy neutrons leaking out of the simulated copper accelerator component. One-dimensional traverses through the concrete tunnel structure and earth berm were analysed for the anticipated normal operational loss terms and design base accident loss terms for the maximum anticipated maximum operating levels of the SNS.

The results of the linac shielding analyses indicate the conceptual design of the SNS accelerator system has sufficient shielding to meet both normal operation dose rates and postulated catastrophic beam loss accident dose rates. In all cases, the shielding analyses were performed to a dose rate

constraint approximately equal to one-half of the required maximum dose rate to allow for a factor of two uncertainty in the modelling assumptions and calculational methodology. In the klystron gallery and linac service road analyses, the shielding berm thickness was chosen equal to the calculated minimum required shielding thickness for the 1 GeV linac tunnel catastrophic beam loss accident.

Target station shielding analyses

For the purpose of determining the dose rate at the biological shield surface, the target station, described in detail in Section 5 of Ref. [1], was modelled using the shielding guidelines outlined in the introductory section and the section entitled *Calculational methodology*. The amount of shielding above the target was fixed by limiting the biological dose rate in the high bay area of the target station building while the accelerator is operating. Equipment activation above the target is also a concern. However, a shield that is sufficiently thick enough to protect personnel will generate negligible equipment activation. The shielding beneath the target station was governed by nuclear heating in the concrete support structure. In future design efforts, other criteria may dominate the SNS target station shield design such as component activation (which affects maintenance and plant availability) or soil and groundwater activation. One-dimensional traverses through the bulk shielding were analysed for the forward, backward, transverse (side), upward and downward directions of the target station relative to the incident proton beam direction. In the forward direction, one traverse was modelled through the mercury target plug assembly, and a second traverse was modelled through the bulk shielding adjacent to the target plug. Corresponding CASL calculations were also performed for each of the ANISN calculations.

The results of the analyses indicate the target station model shield design satisfies the shielding requirements by a factor of two or more except in the downward direction. In this direction, the results show more bulk iron shielding is needed to reduce the amount of energy being deposited in the concrete and ultimately the ground. This has resulted in additional iron shielding being added below the target and increasing the thickness of the concrete. It should be noted that beam line penetration streaming through the bulk shield is beyond the scope of this analysis and has not been calculated.

Linac and ring beam dump shielding analyses

The SNS accelerator ring proton transport system will require three beam dumps for normal operation of the facility. The linac tune dump will be located at the end of the linac beyond the linac to ring transfer tunnel. This beam dump will be required to operate at 100 kW incident proton beam power. The ring facility will require two beam dumps. The ring tune dump will be required to operate at 50 kW incident proton beam power, and the ring injection dump will be capable of 200 kW of power operation. The proton beam footprint on the linac tune dump and ring injection dump will be approximately 50 to 60 mm in diameter with a Gaussian distribution. The proton beam footprint of the ring tune dump will be equivalent to the footprint for the target station, i.e. 70 mm $\times$ 200 mm parabolic with a 2 to 1 peaking factor.

For the preliminary shielding analysis, all three dumps are assumed to operate at 200 kW incident proton beam power and are to be similar in design. Furthermore, the beam dumps should be capable of sustaining full beam power for a few pulses without catastrophic failure. Since beam dumps are basically low power target stations, a similar analysis was initiated for the three beam dumps as that performed on the target station models. Within this analysis, the steel shielding

required to obtain a dose rate of 0.125 mrem/h on the outside of the concrete encasement was determined. This stringent dose rate criterion was established to ensure the beam dumps did not make a significant contribution to the ground and/or groundwater activation.

The results for the beam dump analysis indicate all three dumps require approximately 8.2-8.7 meters of steel per side to obtain dose rates on the external surface of the concrete of approximately 0.125 mrem/h. This low dose rate insures insignificant activation in the ground due to beam dump operations, and the length per side is within the SNS conceptual design of nine meters.

Target service cell, general maintenance cell and miscellaneous shielding analyses

For the purpose of determining the dose rates associated with normal operation and postulated catastrophic design basis accidents for the target service cell, general maintenance cell and utility vault, the models described above were employed in coupled HETC-ANISN calculations and semi-empirical CASL calculations using the shielding policy guidelines discussed in the first section of this report. Candidate decay gamma radiation source terms were placed in the centre of the models. The models contain representative volumes of the different components from which the gamma-ray sources were derived so as to take into account attenuation by the components. The source terms were determined from the ORIHET95 activation and were calculated for 4 MW operation of the target station for one year. The gamma-ray spectra calculated for immediately after the facility shutdown was used as the source term. For most source terms, this yields an approximate equilibrium spectrum.

For the target service cell, the target SS-316 jacket, which holds the mercury target, was selected as a source term to simulate a repair or replacement operation of this component, while the target mercury source was used for the analysis of the mercury spill case. Utilising these sources, the required concrete wall thickness was determined. The results further indicate the heavy concrete thickness of one meter satisfies the dose rate limit for normal operation scenarios. In the case of a catastrophic accident like the mercury spilling out onto the floor, the heavy concrete thickness of one meter, however, does not satisfy the shielding requirement and 1.20 meters of heavy concrete will be required.

The two most activated components from the inner reflector assembly, i.e. the beryllium/D_2O reflector assembly, and the nickel inner reflector plug assembly, were modelled in the centre of the general maintenance cell, in separate calculations, and the dose rate was determined at the external surface of the concrete wall. The results indicate at least 1.20 m of heavy concrete is required for the most activated component, the Be/D_2O reflector. This shielding thickness is greater than the conceptual design thickness of one meter. It should be noted that standard operations will involve lifting the entire safety vessel and all the interior components and placing this assembly in the remote maintenance cell for servicing. The dose rate associated with this assembly will be significantly greater than the dose rates from either of the two components analysed individually in this study. Additional analyses to seek possible alternative procedures in the general maintenance cell operations may be required to reduce the dose rates for more realistic operations. Multi-dimensional analyses using multi-component sources will also be necessary for further design of the cell shielding.

The shielding analyses for the utility vault and the transfer cask were performed in a manner similar to that used in the target and general maintenance cell calculations. The results for determining the amount of steel shielding for the target station inner reflector process water loop in the utility vault indicate approximately 0.63 m of steel shielding is required to meet the 0.5 mrem/h dose requirement. If space constraints limit the shielding, options for declaring this area a “high” or “extremely high” radiation zone will relax the dose requirements and reduce the shielding. In the

gamma-ray spectrum for the water coolant, high energy gamma rays from ^{16}N, which are produced by the $^{16}O(n,p)^{16}N$ reaction, and whose half life is 7.12 seconds, are dominant. If the target water coolant could be stored in a shielded tank for ~1 minute, the required additional steel thickness would be reduced to approximately 0.42 m for a source 1 minute after shutdown. For determination of the steel thickness for the transfer cask for activated target components, the Be/D_2O reflector assembly was used as a source term to demonstrate the shielding requirement. The results indicate 0.44 m of steel is required to obtain 77.2 mrem/h at the surface of the transfer cask. The dose rate requirement for the transfer cask is 100 mrem/h at the surface of the cask.

Conclusions and recommendations

A preliminary shielding analysis of the proposed SNS was performed for the target station and associated maintenance cells and utility areas, accelerator and ring tunnels and the accelerator system beam dumps. Analyses were performed utilising coupled HETC-ANISN calculations and CASL calculations for both normal operating conditions and catastrophic design base accident scenarios. Results of the present analysis demonstrate the bulk shielding of the SNS conceptual design meets the shielding requirements specified in DOE Order 5480.25 for almost all scenarios. Design modifications have been made to address those areas of concern. Future analyses need to refine the shielding models to account for penetrations and streaming gaps in the bulk shield, and determine mitigation measures to reduce and/or eliminate the dose from these penetrations. Furthermore, alternative procedures for operations of the general maintenance cell, will be required for a more detailed design of the maintenance systems for the construction phase of the NSNS project.

REFERENCES

[1] Oak Ridge National Laboratory, “National Spallation Neutron Source (SNS) Conceptual Design Report,” Volume 1, NSNS/CDR-2/V1.

[2] US Department of Energy, *Safety of Accelerator Facilities, DOE Order 5480.25*, US DOE, Washington DC, (1992).

[3] T.A. Gabriel *et al*., “CALOR: A Monte Carlo Program Package for the Design and Analysis of Calorimeter Systems”, Oak Ridge National Laboratory, ORNL/TM-5619 (1977).

[4] J.F. Briesmeister, ed. “MCNP – A General Purpose Monte Carlo Code for Neutron and Photon Transport”, LASL Report LA-7396-M, Rev. 2 (Sept. 1986).

[5] W.W. Engle, Jr., “A User’s Manual for ANISN: A One-Dimensional Discrete Ordinates Transport Code with Anisotropic Scattering”, Union Carbide Nuclear Division Report K-1693 (1967).

[6] R.G. Alsmiller, Jr. and J. Barish, “HILO Neutron-Photon Multi-Group Cross-Sections for Neutron Energies < 400 MeV”, Oak Ridge National Laboratory, ORNL/TM-7818 (June 1981).

[7] T.W. Armstrong, “CASL – A Computer Aided Shield Layout Code”, unpublished, (1985).

[8] P. Cloth *et al*., “HERMES, A Monte Carlo Program System for Beam Material Interaction Studies”, KFA Jülich, Report Jul-2203 (1988).

Table 1. Summary of shielding analyses, source terms and calculational methodologies used to support the conceptual design of the SNS proton beam transport and target station facility components

SNS Facility	Shielding Analysis	Source Term	Calculational Methodologies
Linac Tunnel			
333 MeV	Normal Operation	10 nA/m Beam Loss	HETC/ANISN, CASL
	Catastrophic Accident	4 MW Point Loss	HETC/ANISN, CASL
	Component Activation	Activated Copper	HETC/MCNP/ORIHET/ANISN
667 MeV	Normal Operation	10 nA/m Beam Loss	HETC/ANISN, CASL
	Catastrophic Accident	4 MW Point Loss	HETC/ANISN, CASL
	Component Activation	Activated Copper	HETC/MCNP/ORIHET/ANISN
1 GeV	Normal Operation	10 nA/m Beam Loss	HETC/ANISN, CASL
	Catastrophic Accident	4 MW Point Loss	HETC/ANISN, CASL
	Component Activation	Activated Copper	HETC/MCNP/ORIHET/ANISN
Klystron Building			
333 MeV	Normal Operation	10 nA/m Beam Loss	HETC/ANISN, CASL
	Catastrophic Accident	4 MW Point Loss	HETC/ANISN, CASL
667 MeV	Normal Operation	10 nA/m Beam Loss	HETC/ANISN, CASL
	Catastrophic Accident	4 MW Point Loss	HETC/ANISN, CASL
1 GeV	Normal Operation	10 nA/m Beam Loss	HETC/ANISN, CASL
	Catastrophic Accident	4 MW Point Loss	HETC/ANISN, CASL
Linac Service Road			
333 MeV	Normal Operation	10 nA/m Beam Loss	HETC/ANISN, CASL
	Catastrophic Accident	4 MW Point Loss	HETC/ANISN, CASL
667 MeV	Normal Operation	10 nA/m Beam Loss	HETC/ANISN, CASL
	Catastrophic Accident	4 MW Point Loss	HETC/ANISN, CASL
1 GeV	Normal Operation	10 nA/m Beam Loss	HETC/ANISN, CASL
	Catastrophic Accident	4 MW Point Loss	HETC/ANISN, CASL
Ring Tunnel			
1 GeV	Normal Operation	1 nA/m Beam Loss	HETC/ANISN, CASL
	Catastrophic Accident	2 MW Point Loss	HETC/ANISN, CASL
	Component Activation	Activated Copper	HETC/MCNP/ORIHET/ANISN
Beam Dumps			
Linac Tune	Normal Operation	100 kW Beam Power	HETC/ANISN, CASL
Ring Injection	Normal Operation	200 kW Beam Power	HETC/ANISN, CASL
Ring Tune	Normal Operation	50 kW Beam Power	HETC/ANISN, CASL
Target Station			
	Normal Operation	4 MW Beam Power	HETC/ANISN, CASL
Target Service Cell			
	Normal Operation	Activated Target SS-316	HETC/MCNP/ORIHET/ANISN
	Target Mercury Loop	Activated Mercury	HETC/MCNP/ORIHET/ANISN
	Target Cooling Loop	Activated Water	HETC/MCNP/ORIHET/ANISN
	Hg Spill Accident	Activated Mercury	HETC/MCNP/ORIHET/DORT
	Beam Trip Failure	1 MW Proton Beam	CASL
General Maintenance Cell			
	Normal Operation	Activated Be Reflector	HETC/MCNP/ORIHET/ANISN
	Normal Operation	Activated Ni Reflector	HETC/MCNP/ORIHET/ANISN
Utility Vault Pipe Chase			
	Normal Operation	Activated Cooling Water	HETC/MCNP/ORIHET/ANISN

Table 2. Summary of dose criteria, minimum required shielding and dose rate analysis results used to support the conceptual design of the SNS proton beam transport and target station facility components

SNS Facility	Shielding Analysis	Dose Criteria	CDR Shield Design	Calc. Min. Req. Shielding	Dose Rate or Comment
Linac Tunnel					
333 MeV	Normal Op.	0.125 mrem/h	9.14 m berm	6.40 m berm	0.060 mrem/h
	Catst. Acc.	25 rem/h	9.14 m berm	5.99 m berm	12.29 rem/h
667 MeV	Normal Op.	0.125 mrem/h	9.14 m berm	7.47 m berm	0.056 mrem/h
	Catst. Acc.	25 rem/h	9.14 m berm	6.93 m berm	12.18 rem/h
1 GeV	Normal Op.	0.125 mrem/h	9.14 m berm	7.92 m berm	0.077 mrem/h
	Catst. Acc.	25 rem/h	9.14 m berm	7.49 m berm	12.00 rem/h
	Comp. Act.	NA	NA	NA	264 rad/h at 1 m
Klystron Bldg.					
333 MeV	Normal Op.	0.125 mrem/h	9.14 m berm	7.49 m berm	4.24e-03 mrem/h
	Catst. Acc.	25 rem/h	9.14 m berm	7.49 m berm	0.334 rem/h
667 MeV	Normal Op.	0.125 mrem/h	9.14 m berm	7.49 m berm	2.62e-02 mrem/h
	Catst. Acc.	25 rem/h	9.14 m berm	7.49 m berm	2.520 rem/h
1 GeV	Normal Op.	0.125 mrem/h	9.14 m berm	7.49 m berm	6.29e-02 mrem/h
	Catst. Acc.	25 rem/h	9.14 m berm	7.49 m berm	5.680 rem/h
Linac Srvc. Rd.					
333 MeV	Normal Op.	0.05 mrem/h	9.14 m berm	7.49 m berm	2.02e-03 mrem/h
	Catst. Acc.	1 rem/h	9.14 m berm	7.49 m berm	0.082 rem/h
667 MeV	Normal Op.	0.05 mrem/h	9.14 m berm	7.49 m berm	1.76e-02 mrem/h
	Catst. Acc.	1 rem/h	9.14 m berm	7.49 m berm	0.711 rem/h
1 GeV	Normal Op.	0.05 mrem/h	9.14 m berm	7.49 m berm	4.14e-02 mrem/h
	Catst. Acc.	1 rem/h	9.14 m berm	7.49 m berm	1.640 rem/h
Ring Tunnel					
1 GeV	Normal Op.	0.125 mrem/h	9.14 m berm	7.92 m berm	0.068 mrem/h
	Catst. Acc.	25 rem/h	9.14 m berm	8.61 m berm	12.15 rem/h
	Comp. Act.	NA	NA	NA	25.3 rad/h at 1 m
Beam Dumps					
Linac Tune	Normal Op.	0.125 mrem/h	9 m Steel	8.48 m Steel	0.123 mrem/h
Ring Injection	Normal Op.	0.125 mrem/h	9 m Steel	8.70 m Steel	0.124 mrem/h
Ring Tune	Normal Op.	0.125 mrem/h	9 m Steel	8.22 m Steel	0.122 mrem/h
Tgt. Station					
	Normal Op.	0.125 mrem/h	5 m Steel + 1 m Conc.	5 m Steel + 1 m Concrete	6.26e-02 mrem/h
Tgt. Srvc. Cell					
	Act. Tgt. SS316	0.125 mrem/h	1 m Hvy Conc	1 m Hvy Conc	4.98e-10 mrem/h
	Tgt. Hg Lp.	10 rad/h at 0.5 m	To Be Determined	0.20 m Steel	9.70 rad/h
	Tgt. H2O Lp.	10 rad/h at 0.5 m	To Be Determined	0.10 m Steel	9.94 rad/h
	Hg Spill Acc.	0.125 mrem/h	1 m Hvy Conc	1 m Hvy Conc	1.82e-04 mrem/h
	Bm. Trp. Fail.	25 rem/h	1 m Hvy Conc	1 m Hvy Conc	Redesign Target Plug
Gen. Maint. Cell					
	Act. Be Refl.	0.125 mrem/h	1 m Hvy Conc	1.20 m Hvy Conc	0.08 mrem/h
	Act. Ni Refl.	0.125 mrem/h	1 m Hvy Conc	1.08 m Hvy Conc	0.07 mrem/h
Utility Vault					
	Normal Op.	0.5 mrem/h at 0.3 m	To Be Determined	0.42 m steel	0.469 mrem/h with 1 min Decay Source

SHIELDING DESIGN OF THE SPALLATION NEUTRON SOURCE IN JAPAN

Masayoshi Kawai
High Energy Accelerator Research Organisation (KEK)
1-1 Oho, Tsukuba-shi, Ibaraki-ken 305-0801, Japan

Abstract

There are two projects involving spallation neutron sources in Japan: JHF of KEK and NSP of JAERI. Brief descriptions of these projects and shielding designs are given in this paper while concentrating on the conceptual designs of the target station of the JHF neutron source. Parameter studies were made using the LAHET-2.7 and MARS codes to confirm the design methodology and to obtain data for designing the target and reflector system from the view point of shielding.

Introduction

Neutrons are very powerful as a probe for condensed matter and have great promise for the development of material science and life science. It is also expected to be beneficial for such technological applications as the transmutation of radioactive nuclides, i.e. actinides and long-lived fission products generated in nuclear power plants, and material irradiation tests. Recently, it has become very important to develop intense spallation neutron sources by considering the circumstances of the inevitable shutdown of nuclear reactors which have served as thermal and cold neutron sources. There have been several proposals to construct spallation neutron sources around the world. Representative projects are the SNS in the US and the ESS in the EC. In Japan, there are two projects: one is the Japan Hadron Facility Project (JHF) at KEK, having an initial 600 kW/upgraded 1.2 MW with a beam energy of 3 GeV; the other is the Neutron Science Project (NSP) at JAERI of 1.5 MW (Phase 1)/5 MW (Phase 2) with a 1.5 GeV proton beam. In both projects, the conceptual design work is progressing along with the research and development of such component technology as intense beam accelerators, a target facility, instruments for neutron spectroscopy and so on. In the present paper, outlines of the project and the designs are briefly given while concentrating on the shielding design.

In the conceptual shielding design, empirical formulas were employed, though it is important to apply sophisticated design methods such as a three-dimensional radiation transport code with the Monte Carlo method to precisely evaluate the neutron distributions in the complicated geometry around the target assembly, the target train and the beam lines, where the narrow gaps will provide paths for radiation streaming. Particularly, the neutron source of JHF will utilise a high-energy proton beam which has never been nor will be used in other facilities. Further, in the present work, parameter studies were made to clarify the calculation technique and to obtain some kinds of instructive information for designing the target and reflector system from the view point of shielding.

Japanese projects involving the Neutron Spallation Source

The Japan Hadron Facility Project (JHF) aims to advance such multi-disciplinary research fields as material science, life science, nuclear physics and particle physics by using various secondary particles and nuclei produced by an intense high-energy proton beam supplied to the four facilities in the project by a proton accelerator complex, as shown in Figure 1.

The accelerator complex consists of a 200 MeV linac, a 3 GeV proton synchrotron (PS) with 200 μA proton beams and a 50 GeV PS with 10 μA proton. The pulsed spallation neutron source facility, called N-arena, is one of four facilities at JHF. It will utilise a proton beam from the 3 GeV PS, which has a time-averaged beam power of 0.6 MW in about 1 μs width at a repetition rate of 25 Hz. It will be upgraded to 1.2 MW or more in the future. A schematic layout of the N-arena is shown in Figure 2. In the N-arena, nearly thirty spectrometers will be installed, such as small-angle scattering instruments, reflectrometers, diffractometers, inelastic spectrometers, polarisation instruments and so on. We have employed a horizontal proton beam-injection scheme and horizontal extraction of the neutron-generation target.

At the 3 GeV PS, two other experimental facilities also will be located. The first one will utilise muons for atomic, nuclear and solid-state physics, muon-catalysed fusion as well as particle physics such as a μ-e conversion experiment (M-arena). The second one will be devoted to nuclear physics research by using an ISOL post-accelerator type radioactive beams (E-arena). At the 50 GeV PS,

various types of intermediate-energy nuclear physics will be extended by using kaons, pions, antiprotons and primary beams, including heavy ions (K-arena). At this facility, experiments of kaon rare decays and other symmetry tests, such as an experiment concerning neutrino oscillation using the Super-Kamiokande will be also carried out.

In advance of the JHF project, we have already reconstructed our laboratory (KEK) in which two institutes were established in April 1997. The JHF project is a five-year project. KEK already submitted a budgetary request for JHF starting from FY1999 and finishing construction in FY2003 to the Japanese government, and waiting for its decision, by setting up construction of a part of the linear accelerator as an promising injector to the 3 GeV PS with a supplementary budget provided this year.

The Neutron Science Project (NSP) is planning to construct intense spallation neutron sources having a total of 8 MW as its final goal. There will be several utility facilities, as shown in Figure 3, for fundamental sciences as well as transmutation technology and industrial applications of a neutron source, with the establishment of the Neutron Science Project Centre in April 1997.

The proton accelerator of about 800 m length comprising the RFQ, DTL and Superconducting Linac will supply a proton beam of 1.5 GeV and 5.3 mA (8 MW) at maximum with both modes of pulse and CW operation. An accumulator ring will be installed to feed a short-pulsed beam. In this project, five main facilities are planned for using the pulsed and/or CW proton beam. The neutron scattering facility will generate a pulsed neutron source with a pulse width of 1 μs to 3.7 ms and a 50 Hz repetition rate for structural biology and material science with 30 neutron beam lines. The facility will be constructed in two steps: an initial 1.5 MW source with a solid-type target cooled by water, and finally a 5 MW source with a liquid metal target of mercury.

The Nuclear Transmutation Research Facilities with a beam power of 1-7 MW will be constructed for multi-purpose research such as studies using nuclear transmutation, nuclear transmutation of radwaste which is produced in nuclear power plants, muon utilisation and the research and development of materials tolerable to neutron irradiation, by mainly using an intense CW beam. The facility will also be utilised for industrial applications, such as non-destructive testing with neutron radiography and prompt gamma-ray analysis. At the Neutron Nuclear Physics Facility, research for high-energy neutron nuclear reactions will be made together with reactor physics experiments for the incineration of radwaste. The Spallation RI Beam Facility will be utilised to study the nuclear chemistry of transactinide elements and do research on unstable heavy nuclei as well as super-heavy elements and their synthesis. The RI Production Facility will contribute to both medicine and life science.

The project is scheduled to provide for the research and development of components technology, such as accelerators, solid targets and remote maintenance techniques up to FY2001, to construct a Phase 1 research facility with a beam current of 1 mA from FY2001 to about FY2004 and finally to complete the construction of the project at 8 MW in about FY2007.

Shielding design of the Spallation Neutron Source Facility

A preliminary shielding design study for the NSP of JAERI has already been carried out based on the Moyer Model, yielding the required shield thickness of a proposed accelerator facility.

In addition, some information about the activation of air in the accelerator tunnel and the soil surrounding the facility was acquired, and the dose equivalent at the site boundary due to skyshine was estimated using Stapleton's equation.

At present, the calculation methods to be used for the shielding design are not yet fixed. The investigation so far suggests the following. The NMTC/JAERI code will be applied to determine the source neutron intensity for shielding calculations and for neutronics calculations in and around the target/moderator/reflector system. As for deep-penetration calculations, the ANISN code will be used with a revised HILO86R library, together with partial usage of a newly developed kernel code, called PKN-H. An activity calculation code, called SPCHAIN, is being revised to calculate the decay heat and gamma-ray spectrum due to induced radioactivity for analysing induced radioactivity inside and outside of the facility.

As for the N-arena of JHF, a conceptual design of the target station and the proton beam line was made by Itoh, as mentioned below. At KEK, detailed shielding analyses will be made using the computer codes (LAHET and MCNP) for shielding calculations in and around the target/moderator/reflector system, and for radiation-streaming problems of the target train and the neutron beam lines. MARS, developed at FNAL, and the ANISN codes will be employed to analyse the deep-penetration problems for a very thick biological shield of steel (total amount of about 6 000 tonnes) in the target station. An activation calculation of materials in the facility will be made using CINDER90, developed at LANL.

Conceptual shielding designs of the N-arena were made by considering an upgrade of the beam power to 1.2 MW. Figure 4 shows a bird's-eye view of the target station of the N-arena. The annual operation duration is assumed to be 4 000 hours. The N-arena will be constructed in the present East Counter Hall, from which the nearest site boundary is 330 m, as shown in Figure 1. The design for such a facility should be considered with a radiation-safety assessment. The design method is as follows.

The dose rate at the experimental hall has been evaluated using Moyer's model for the point loss:

$$H = 2H_{\mathrm{o}} I E_{\mathrm{p}} \exp(-\beta\theta) \exp\left(-\sum_i d_i/\lambda_i\right)/r^2 \qquad (1)$$

where $H_{\mathrm{o}} = 3.2 \times 10^{-4}$ (μSv/h)m^{2}s/GeV, I is the loss current of the proton beam, $\beta = 2.5$ rad^{-1}, θ is the angle from the proton beam direction, r is the distance from the loss point, and d_i and λ_i are the thickness and the attenuation length of the ith material. H_{o}, β and the attenuation lengths for steel and concrete are obtained by the measurement at KEK-PS with $E_{\mathrm{p}} = 12$ GeV [1], where $\rho\lambda$ is 188 g/cm^2 and 143 g/cm^2 for steel and concrete, respectively (ρ is the density of the material).

In the design of the N-arena, the density of steel is assumed to be 7.2 g/cm^3 for the target station and 7.8 g/cm^3 for the beam-line shielding. The density of concrete is assumed to be 2.2 g/cm^3. Therefore, the attenuation lengths are 26.1 cm for steel in the target station, 24.1 cm for the beam line magnets, and 65.0 cm for concrete. The beam loss at the target station is assumed to be 100% of I_{p}. At the beam line, point losses occur at the Q-magnets, and the total beam loss is assumed to be 1×10^{-4}/100 m (40 nA for $I_{\mathrm{p}} = 400$ μA), which is distributed to each Q-magnet proportionally to the distance between the Q-magnets. Therefore, for four Q-magnets from the kicker magnet to the experimental hall, the beam loss is 2.8 nA/magnet, and is 2.0 nA/magnet for 14 magnets in the experimental hall.

The dose rate at the site boundary due to sky shine is estimated by using the attenuation in air as being 850 m. The dose rate in the upper part of the target station and the beam line shielding is considered to estimate the dose at the site boundary. The annual dose at the site boundary from KEK is limited to 50 μSv/y, which is shared with all facilities at KEK.

For activation of the soil under the facility, the conversion factor from the dose rate has been experimentally obtained to be 0.161 Bq/g/(mSv/h) [2]. In designing the shielding in the N-arena, the dose rate in the experimental hall is limited to 8 μSv/h, and activation of the soil under the facility is limited to 2.0 Bq/g.

The designed sectional plan of the target station and the beam line shielding is shown in Figure 5. The estimated dose rate is 7.3 μSv/h at the sides of the target station and the beam line shielding. The activation of the soil under the facility is estimated to be 1.9 Bq/g under the target station. The annual contributions to sky shine at the site boundary are 14.5 μSv/y, 3.1 μSv/y and 2.2 μSv/y from the target station, the beam line shown in the figure and the beam line near to the kicker magnet, respectively. The total annual dose from the N-arena is estimated to be approximately 20 μSv/y.

Parameter study of the shielding calculation

The JHF will use a higher energy proton beam than that of other spallation neutron sources. Accordingly, the computer codes, such as LAHET and MARS, should be verified as being feasible to design the JHF. It is also important to establish the shielding design method and to understand the general trend of the radiation distributions, especially of the fast neutrons above 100 MeV entering the shields, in order to optimise the designs of the target/reflector/shields system. In the present work, the calculations were made using both the LAHET-2.7 and MARS codes to analyse the high-energy source neutron distributions.

LAHET-2.7 can construct a complicated three-dimensional geometry with the same geometry module of MCNP. The one defect of the code is the need for a huge amount of data volume for memorising the histories of particles to be analysed after the LAHET computation. The limitation of the disk volume sometimes enforces us to stop the computation, even if the statistical error of Monte Carlo calculation would not become small enough. In the worse case, no neutrons reach the places of interest of the shielding design. In such a case, MARS will be very helpful in spite of simplifying the calculation model. Therefore, in the present work, a parameter study was made to analyse the neutron distributions in the vicinity of the target, although thick shields were considered in the actual model. The calculation model was a simple one which could be modelled with cylinder geometry.

The variable parameters are the kinds of target and reflector materials, the target size and the incident proton energy. As for the reference of the target material, we selected a lead metal and tungusten-D_2O mixture. The former is the most popular material for studying a spallation neutron source. The latter is a candidate as a material of the solid target for the N-arena. The target materials are listed in Table 1.

Table 1. Target material and its size

Target material	ρ (g/cc)	Size (dia. × length)	Ep (MeV)
Pb	11.34	20 × 60, 20 × 65, 20 × 70	3 GeV, 800 MeV
W + D_2O	16.26	10 × 55, 10 × 60, 10 × 65	3 GeV
Ta + D_2O	14.17	10 × 55	3 GeV, 800 MeV
Hg	13.59	10 × 55	3 GeV
Ta + D_2O (ISIS)	14.65	10 × 42	800 MeV

N.B. Length 55 cm of W target is near optimum, which was tentatively selected in a neutronics calculation of the target system.

Calculations by LAHET were carried out with 100 000-500 000 histories. The results are as follows:

1) *Reference calculations with bare lead target*

Figure 6 shows the polar-angle distributions of neutron fluxes integrated over energy intervals of between 20-100 MeV, 100-400 MeV and 400-3 000 MeV near the surface of the steel shields surrounding the target. The neutron flux decreases with the angle. The anisotropy of the flux is prominent for the highest energy group due to neutron generation by the spallation reaction. Below 100 MeV, the distribution becomes relatively flat, since the contribution from the evaporation neutrons is dominant. In the designs, the amplitude of the forward component relative to the perpendicular one is important. The ratio of the fluxes integrated over the broad energy intervals are 2.5 to 362, as shown in Figure 7. The value of the flux scored with a small energy bin increases monotonously with neutron energy from 240 up to 600 MeV. However, this increase is mainly due to a decrease in the perpendicular components. Accordingly, the actual value may remain within several tens in the case of a long target, which absorbs both protons and neutrons penetrating through.

It is also noted that neutrons could be transmitted through the shields by only two meters in our calculation, even with 100 000 histories. Especially, fast neutrons above 400 MeV diminished at positions of larger polar angles. The attenuation length was derived based on the neutron degradation within one meter of steel, where the neutron spectrum did not produce an asymptotic shape which would occur in deep penetration. The values are 187 g/cm^2 in the forward direction and 111 in the perpendicular direction. The former value is very similar to the experimental value of 188 g/cm^2 measured at the KEK 12 GeV PS by Ban *et al*.

2) *Effect of target materials*

High-energy protons generate more neutrons and form a broad plateau of neutron flux in the target. The broad plateau gives a flexibility as regards the number and location of moderators and reduces a severe problem of heat removal. However, increases in the stopping power with the proton energy raises the problem of excess neutrons and heat generation leaking from the target in the shield. Accordingly, the design of the target system should be made from the view point of not only characteristics of cold-and-thermal neutrons, such as brightness and sharpness, but also excess neutron and heat generation in the materials behind the target. In the present work, four kinds of materials were tested as a target.

Figure 8 compares the axial distributions of neutron current on the target surface. In the figure, 87%Ta of 10 cm diameter and 33 cm in length means the ISIS-like target, bombarded with a 800 MeV protons. The neutron currents are converted to absolute values at 1 MW proton power. It can be seen in the figure that an ISIS-like target with an 800 MeV beam generate a high top of neutron flux, compared to that of others with a 3 MeV proton beam. The next high top is those of the tungsten target. It shows a faster decrease with the longitudinal distance (z) than those of other materials lighter than tungsten. The degree of flux degradation in mercury is smaller, and the neutron current at the tail of target is about a factor of two higher than that of a tungsten target. This difference influences the neutron fluxes in the shields in the forward direction, as shown in Figure 9, comparing the polar angle distributions of the neutron fluxes. Near 0°, the flux increases in the cases of mercury, tantalum and lead with a 3 GeV proton beam, while it shows a dip in the cases of tungsten and tantalum with 800 MeV protons. The former cases seem to be influenced by neutron generation by high-energy protons leaking from the target. The latter case means that the portion of the target near to the end works as a shield against protons and neutrons.

Accordingly, a denser material is preferable as a target material in the case of higher energy proton incidence from the view point of shielding. It will also produce higher neutron fluxes in the target.

3) *Effect of reflector*

A reflector is important to enhance the flux level of thermal and cold neutrons in the moderators. In the present work, three kinds of materials, beryllium, lead and stainless steel, were tested as reflector candidates. The reflector is a box of $100\ \text{cm} \times 100\ \text{cm} \times 135\ \text{cm}$. It maintains a thickness of 40 cm around the target at minimum. Calculations were made for a tungsten target. Since no moderators were considered in the model, neutron reflection effect on thermal and cold neutron fluxes has not been considered so far.

Figure 10 shows the neutron spectra in the steel shield near its surface in the forward direction. The spectra of the lead and stainless steel reflectors resemble each other, and are much smaller than that of a bare target. The shield effect of the reflector is expressed by the flux ratios, as shown in Figure 11. It is about one decade in the case of lead and stainless steel reflectors at almost all energies. However, the shielding effect of a beryllium reflector is very small.

Accordingly, the choice of the reflector material is also important from the view point of radiation shielding. Even if a beryllium reflector is needed for proper thermal and cold neutron sources, supplementary reflectors of lead or stainless steel could be effective to reduce transmitted neutrons.

4) *Other effects*

The target-size effect was also tested by changing the length of the lead and tungsten target. The effect was observed in the forward direction of the neutron fluxes, but were not very large in the perpendicular direction. The diameter of a beryllium target influenced the neutron fluxes on the target. The parameter is more important to the neutronics designs than the shielding aspect.

Deep penetration calculation with MARS

In the present parameter study with LAHET-2.7, fast neutrons above 20 MeV reached places within a depth of about two meters in a steel shield, even using 500 000 histories at maximum. In order to continue the computation, many more devices to store the data of particle histories will be needed. We believe that the code should be improved to accelerate the Monte Carlo simulation by means of a variance reduction technique and/or to score the fluence into the tallies by itself, in order to overcome such a problem. Then, the applicability of the MARS code was examined for a simple problem by roughly modelling the target station of the N-arena. The model comprised cylinders of which the main axis was taken to be on the proton beam axis.

Two cases were tested, bare and lead-reflected targets of tungsten. The calculations were made with 100 000 histories for the bare target and 300 000 histories for the lead-reflected target. The calculated results were compared with those by LAHET.

1) *Bare target case*

   Figure 12 shows the results for the neutron-flux distributions in the perpendicular direction, where LAHET has difficulty to estimate high-energy neutrons above 1 GeV. Since the model of the MARS calculation neglected the portions in front of the target, the calculated results were taken for two planes at Z = 2.5 cm (very near the boundary) and Z = 27.5 cm in the intermediate region of a target of 55 cm in length. The results of LAHET are given at two positions in steel (ranging from r = 100 cm to 500 cm), i.e. r = 105 cm and 195 cm. The LAHET results agree well with those of MARS.

   A similar comparison was made for the neutron spectra in Figure 13. In this figure, a general agreement is observed, while LAHET underestimates the neutron flux at r = 100 cm in the neutron energy range above 300 MeV. As for the axial distribution, similar good results were obtained.

2) *Lead reflector case*

   Figure 14 compares the axial distribution of the neutron fluxes. MARS gives the values in the overall range up to 720 cm. An agreement can be seen at the position of the target edge and inside of the shield. At 200 cm, there is slight discrepancy between LAHET and MARS. The values calculated by MARS abruptly decrease beyond 450 cm because of worse Monte Carlo statistics. This problem can be easily resolved by continuing the computation until good statistics are obtained.

   Figure 15 contains the results for the dose rate distributions. The shape of the distributions in both directions are very similar to each other. This means that the high-energy protons, which determined the isotropy of the neutron flux distributions, must be well shielded by the thick lead reflector. The distributions show a steep decrease at a distance beyond 400 cm, where the statistical errors are almost 100%.

Conclusion

In the present paper, brief descriptions of the project involving spallation neutron sources in Japan are given. The conceptual design of the target station of the JHF neutron source is also reported to be effectively made with simplified methods, such as Moyer's Model.

A parameter study LAHET-2.7 indicates that a dense target, such as tungsten, is desirable in the case of high-energy proton beams to reduce the neutron flux in the forward direction. In such a case, lead and stainless steel reflectors are very effective to reduce neutrons bombarding the shields.

The MARS code is suitable for shielding designs, although some type of model simplification will be needed.

Although LAHET-2.7 is adequate for target/moderato/reflector system calculations, some improvements for saving data storage and accelerating the computation by means of a variance reduction technique are needed for large shielding problems. The new version, LAHET-2.8, is in the testing stage, and allows some variance reduction techniques.

A benchmark study of design codes is expected to investigate the calculation accuracy. Now, however, the attenuation length is not yet considered to be confirmed.

REFERENCES

[1] S. Ban *et al*., *Nucl. Instr. Meth*. 174 (1980) 271.

[2] M. Numajiri *et al*., KEK Internal 96-1 (1996), and the related work.

Figure 1. Location of the JHF Site

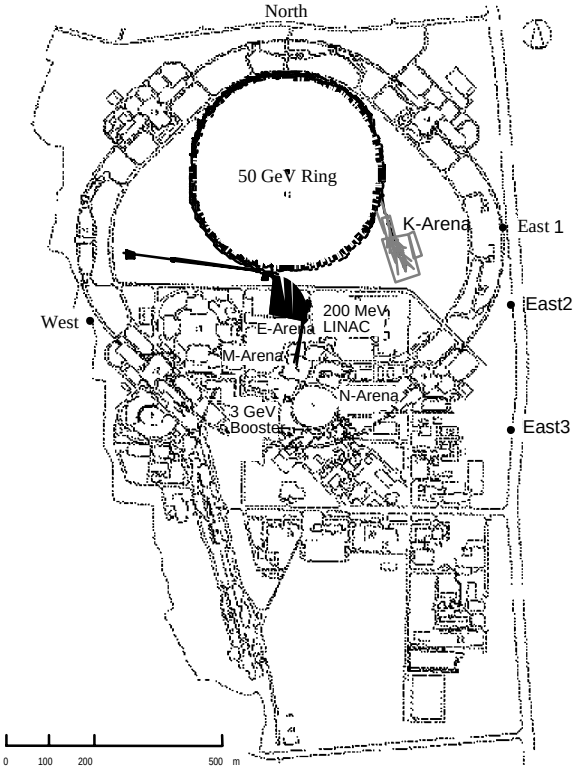

Figure 2. Schematic layout of the N-arena

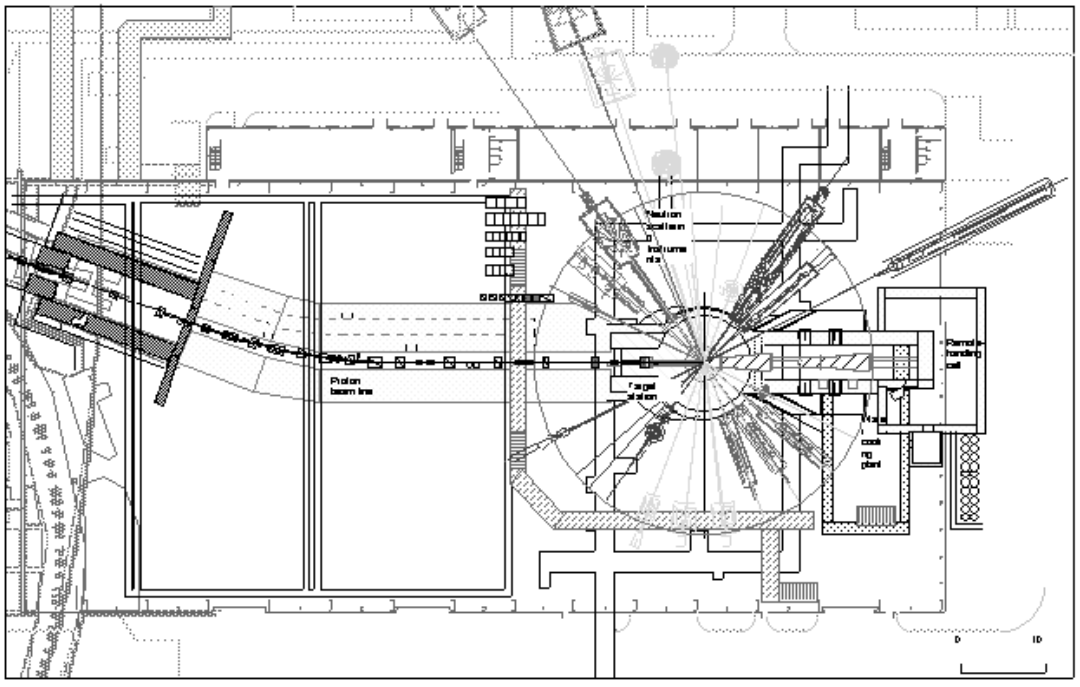

Figure 3. Planned research facility complex for neutron science

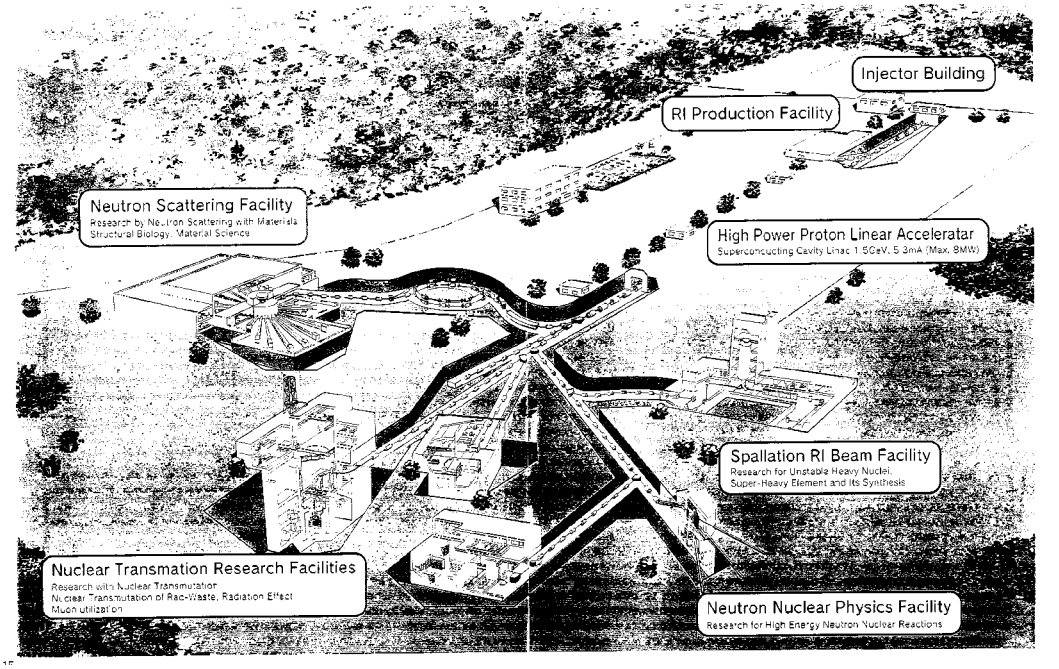

Figure 4. Bird's eye view of the N-arena target station

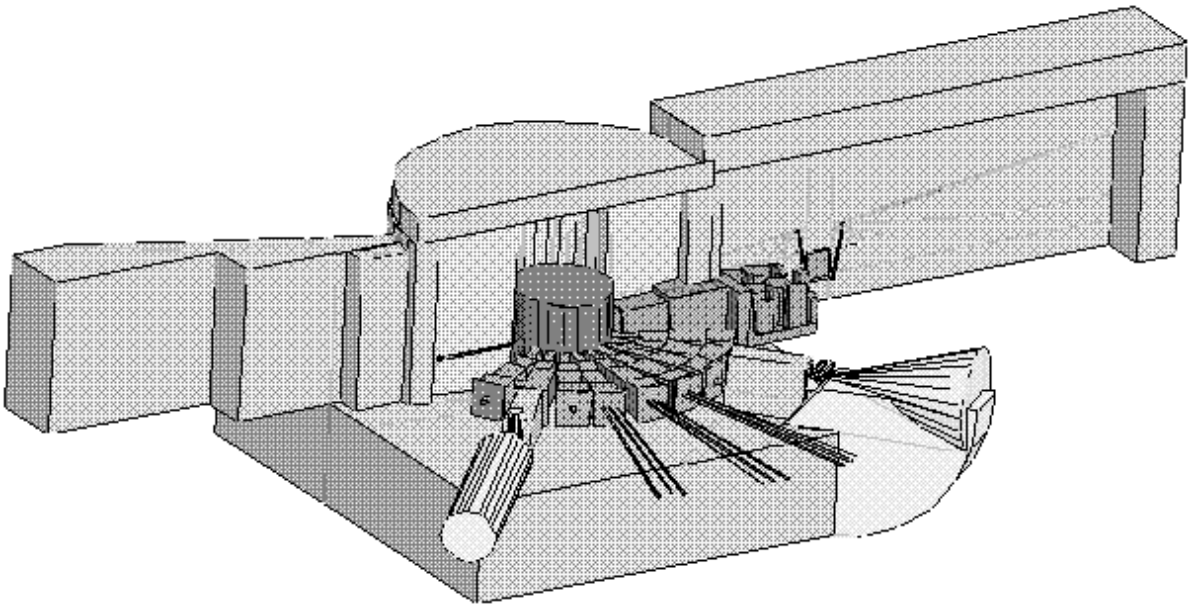

Figure 5. Sectional plan of the target station and beam line shielding of the N-arena

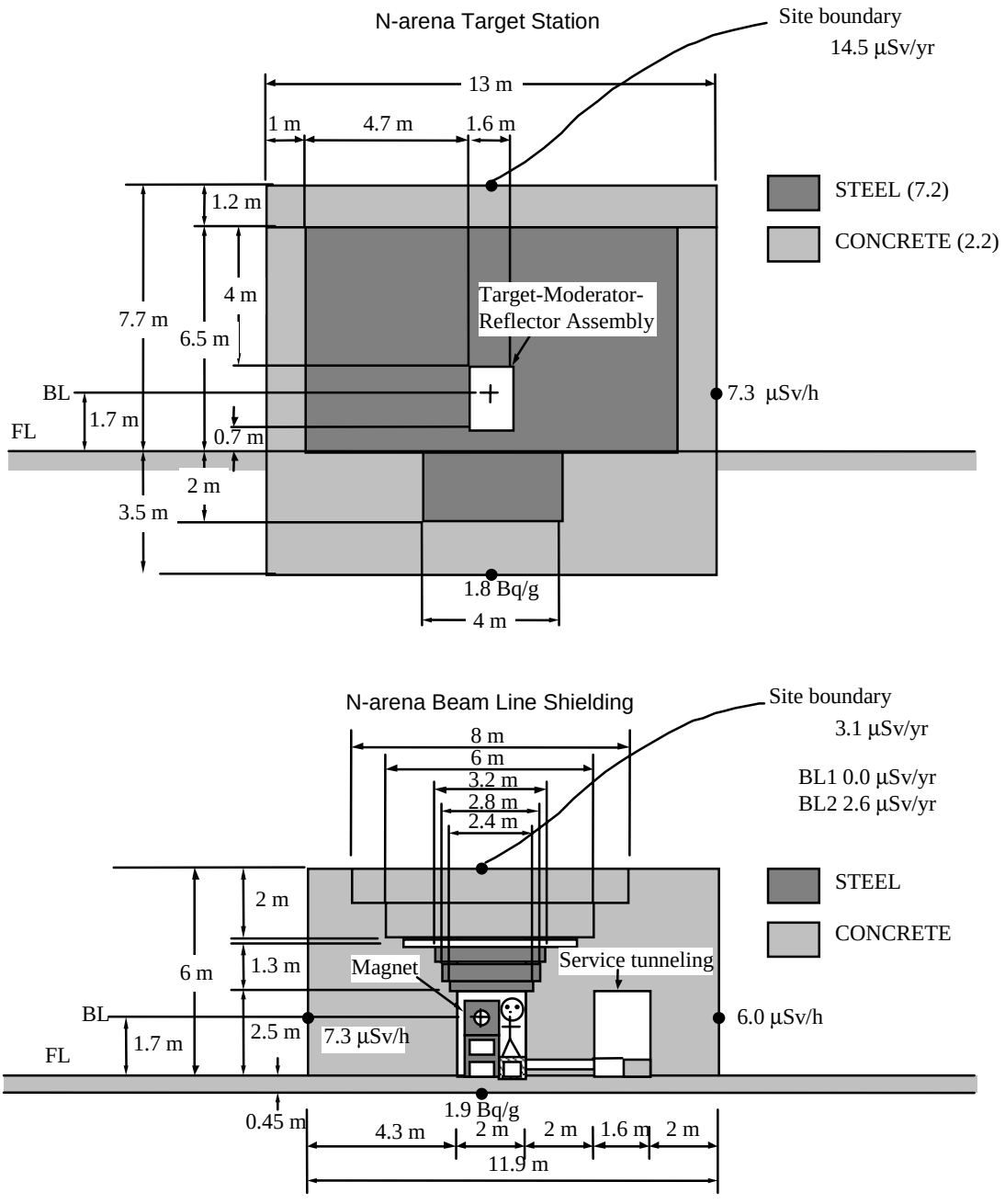

Figure 6. Polar-angle distribution of neutron fluxes in a steel shield

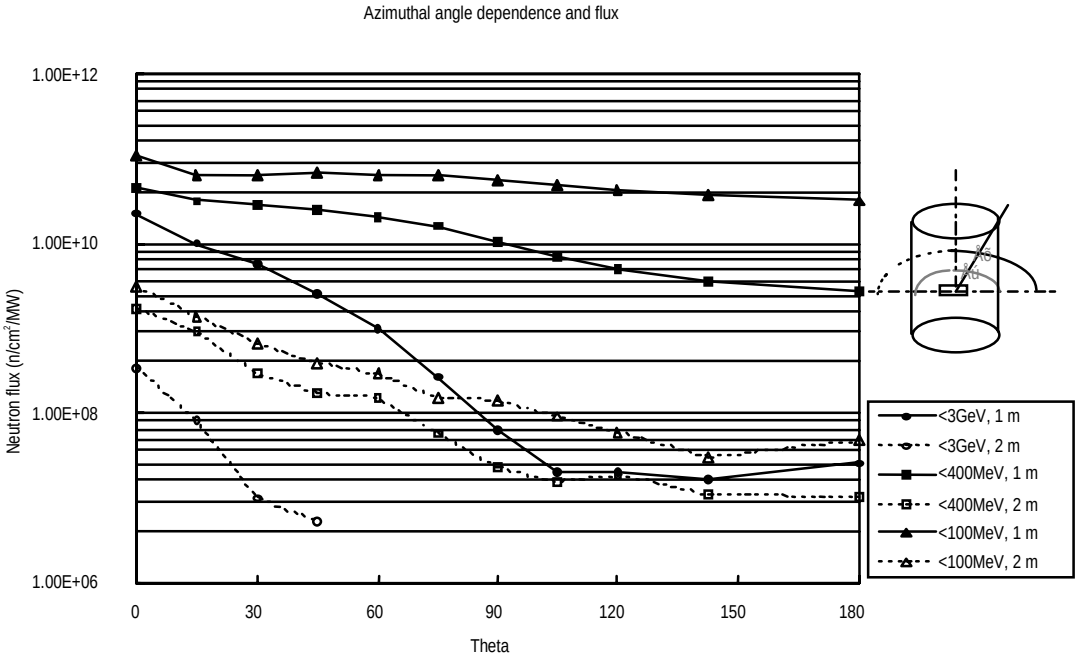

Figure 7. Ratio of the forward-to-perpendicular fluxes near to the steel-shield surface

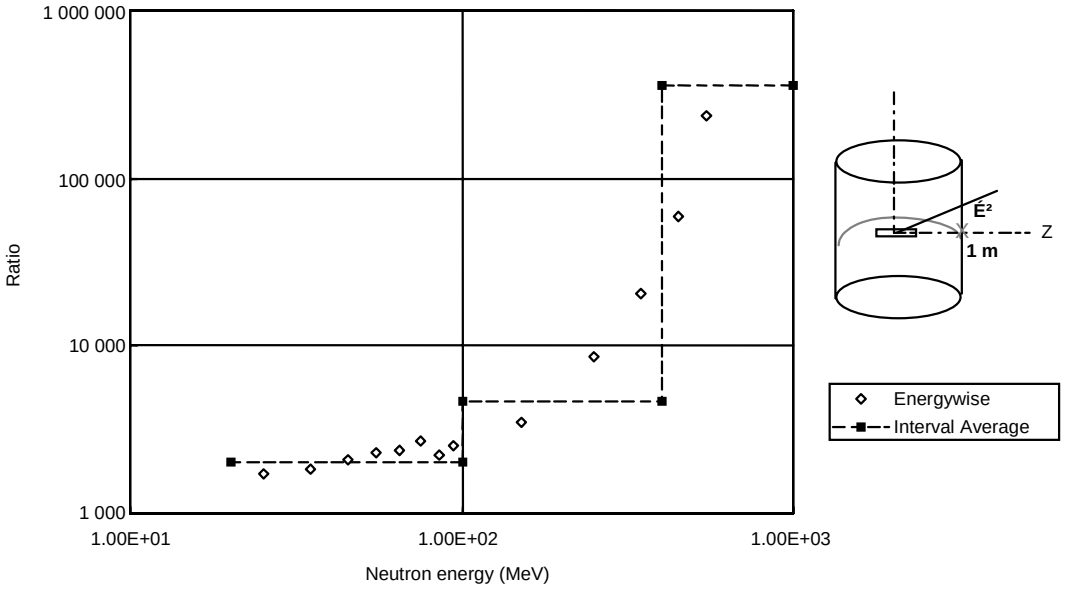

Figure 8. Axial distribution of the neutron current on the target

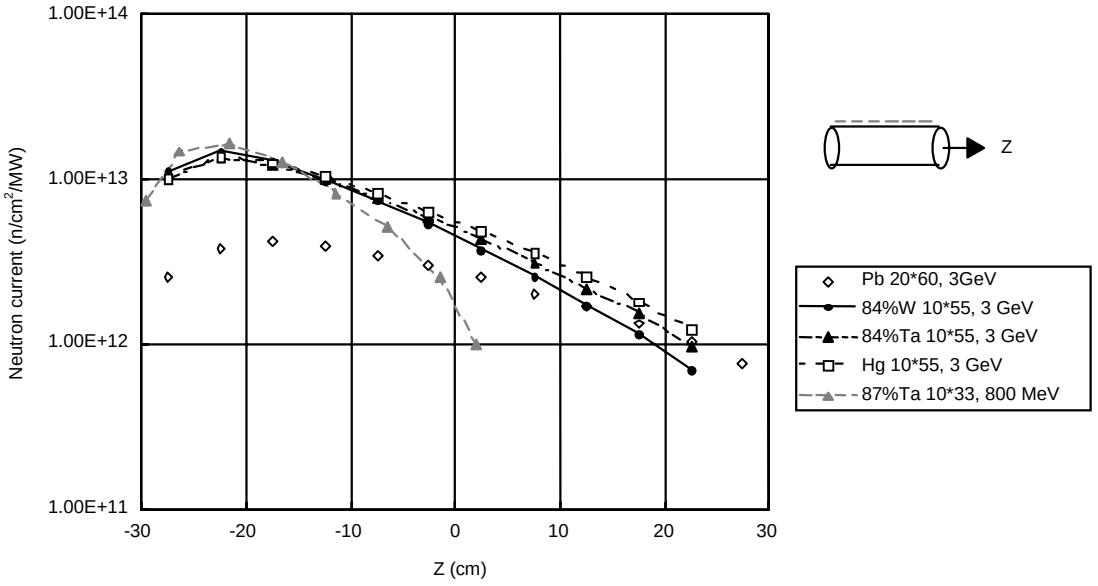

Figure 9. Polar-angle distributions of the neutron fluxes in the energy range between 100 and 400 MeV near to the steel-shield surface

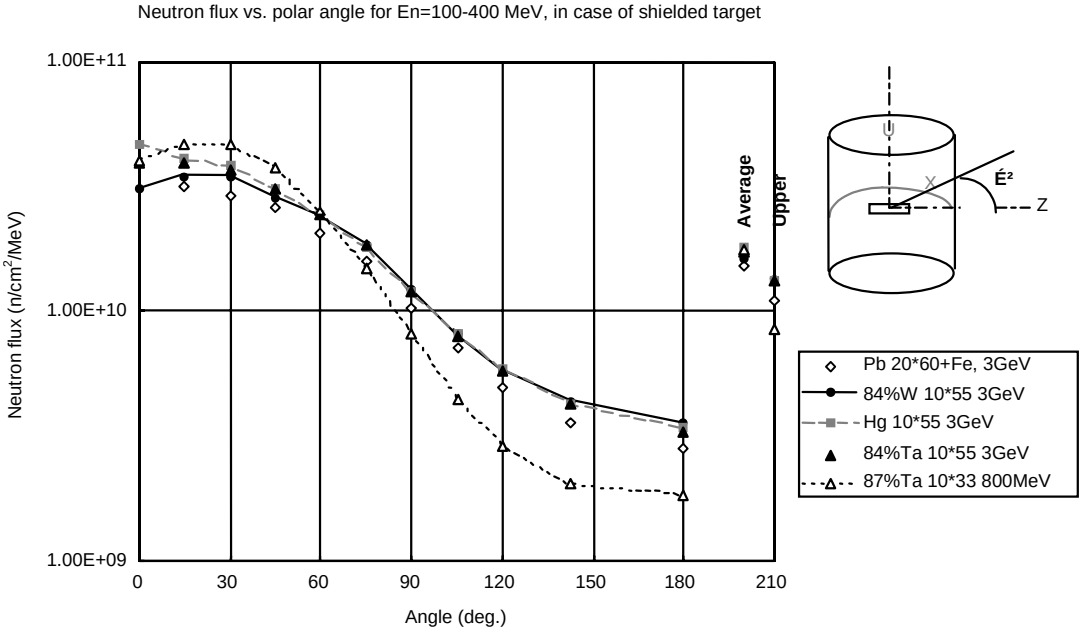

Figure 10. Comparison of the neutron spectra calculated for reflected tungsten-targets with the one for a bare target

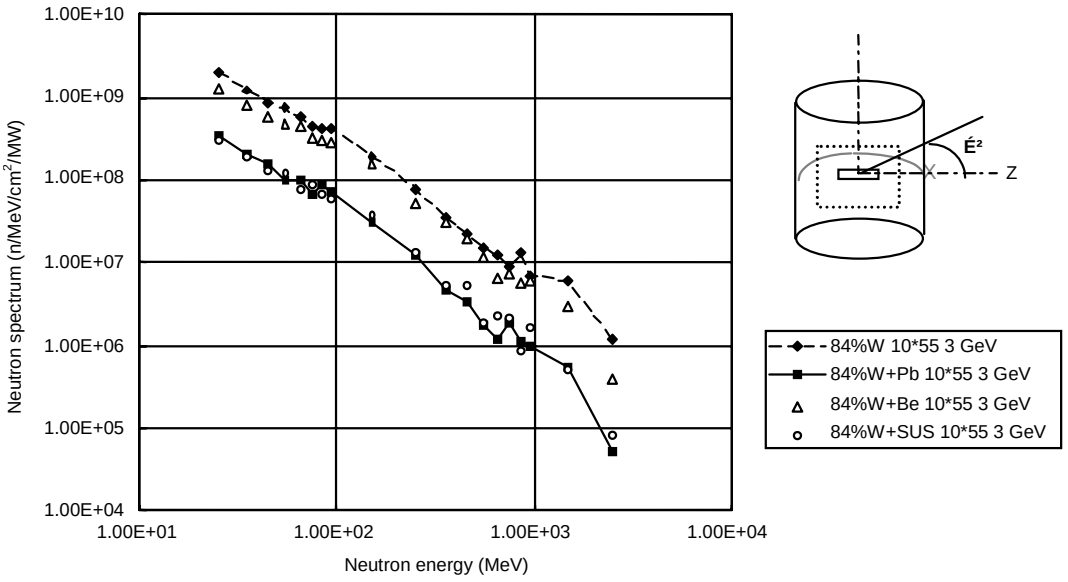

Figure 11. Reflector effect on the neutron fluxes in the forward direction

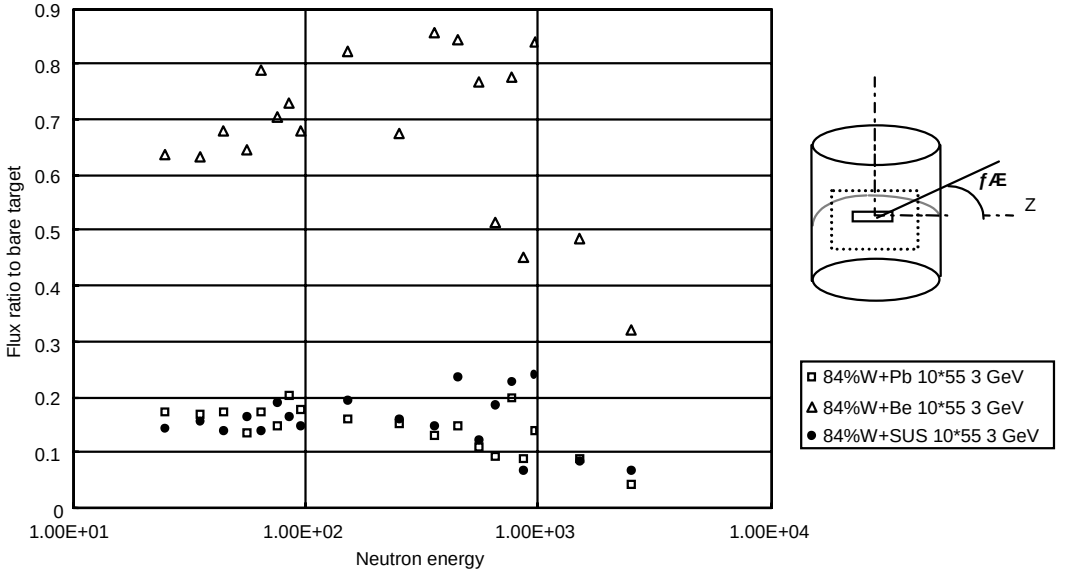

Figure 12. Comparison of the neutron flux distributions in the perpendicular direction, calculated by MARS with those by LAHET in the case of a bare tungsten target

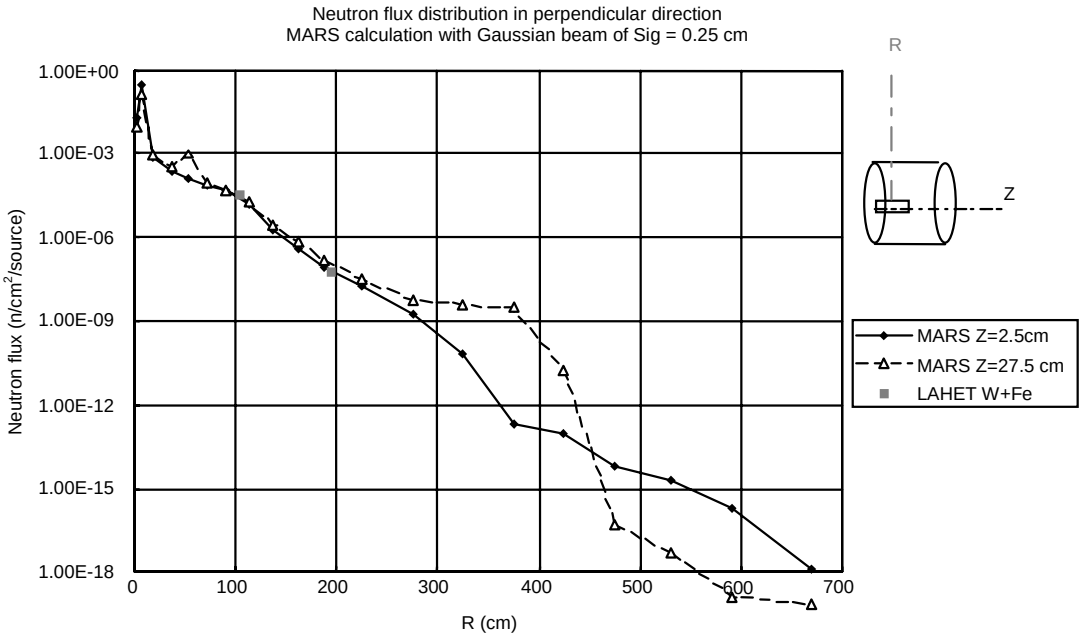

Figure 13. Comparison of the neutron spectra at positions in the perpendicular direction, calculated by MARS with those by LAHET in the case of a bare tungsten target

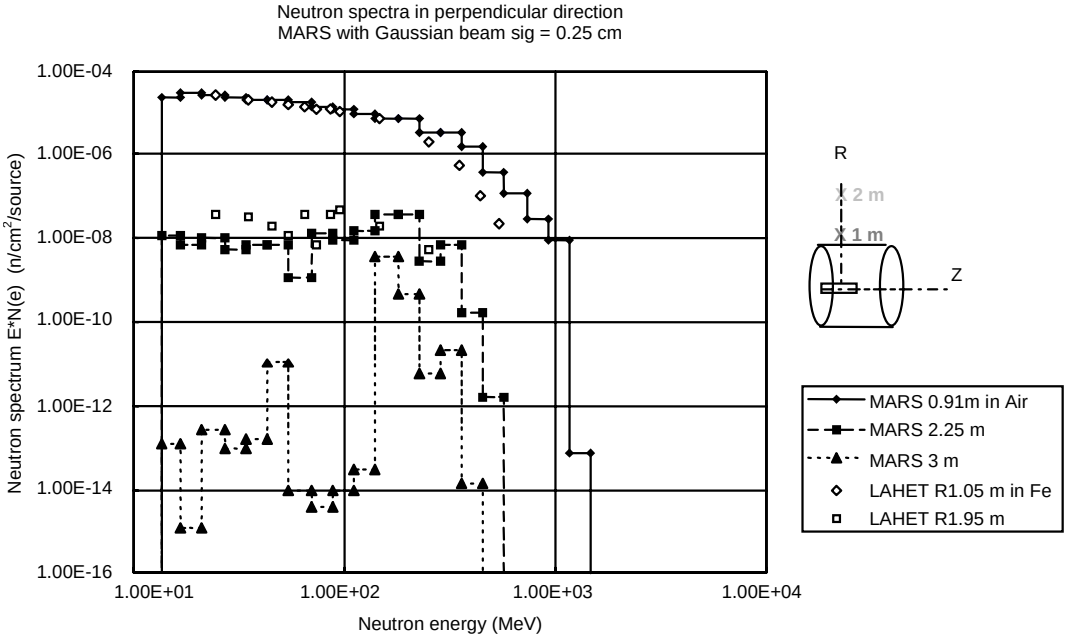

Figure 14. Comparison of the neutron flux distributions in the forward direction, calculated by MARS with those by LAHET in the case of a lead-reflected tungsten target

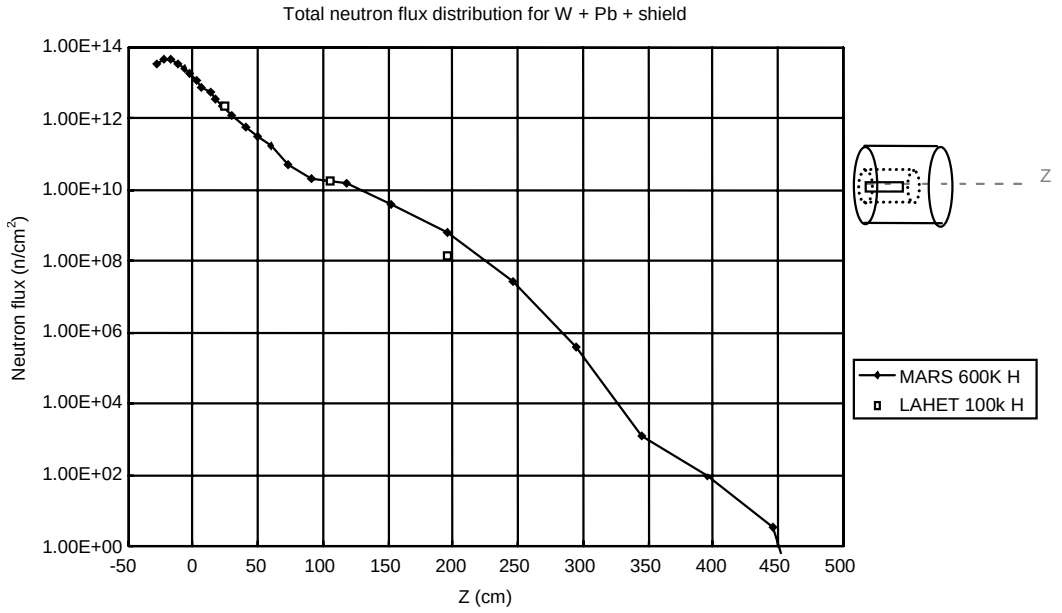

Figure 15. Dose-rate distributions calculated with MARS in the case of a lead-reflected tungsten target

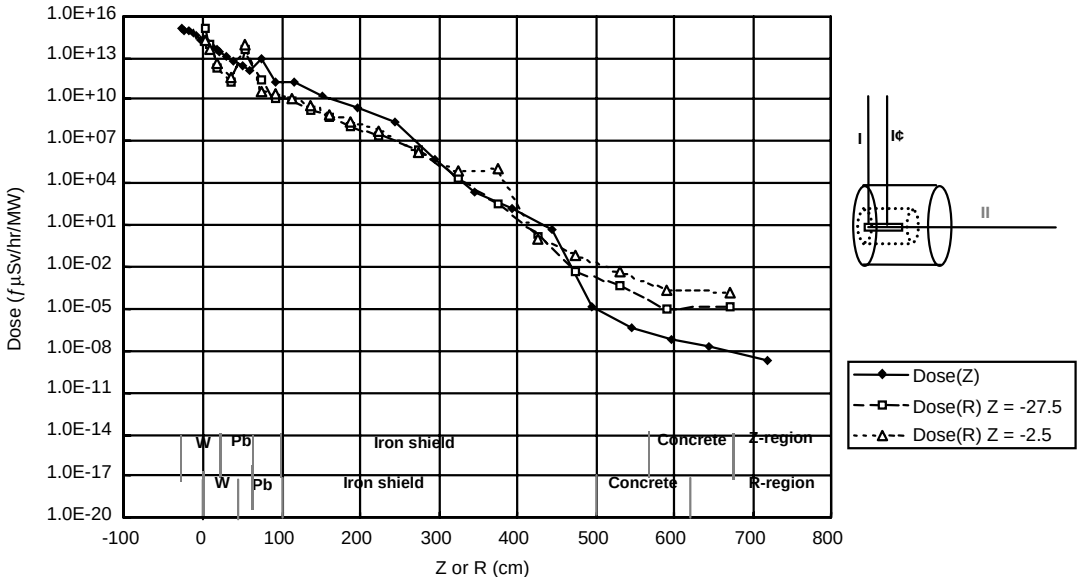

SHIELDING DESIGN OF RIKEN RI BEAM FACTORY

Yoshitomo Uwamino, Nobuhisa Fukunishi
The Institute of Physical and Chemical Research (RIKEN)
2-1, Hirosawa, Wako, Saitama 351-0198 Japan

Abstract

Construction of RIKEN RI Beam Factory is started, and the first phase will be finished by the end of March 2003. Two ring cyclotrons including one superconducting machine and two Big RIPSs (RIKEN Projectile Fragment Separator) will be constructed during the first phase. Heavy ions of proton to uranium will be accelerated up to 400 MeV/u (A < 40) and 150 MeV/u for uranium at an intensity of 10^{13}-pps.

Neutron production by the 400 MeV/u ^{20}Ne beam was measured at HIMAC of NIRS and it was used for the source term of the shielding calculations. The deep penetration of high-energy neutrons was calculated by using the ANISN code with the DLC-119/HILO86R group constants and also by using the HETC code. The ANISN results were modified on the HETC results and the shielding experiment at ISIS, and they were fitted by a simple formula for practical use. The concrete thicknesses of the building walls, ceilings and floors were decided by using these data.

High-energy neutron penetrations of slantwise injection and the reflection probabilities of iron slab were calculated with the HETC code, and these results were used for the estimation of the thicknesses for the iron local shielding of Big RIPSs. Skyshine effect and its height distribution were estimated by using simple formula, and the present design was found to meet the regulation.

The RI Beam Factory

The RIKEN RI (Radioactive Isotope) Beam Factory (RIBF) which is a facility expanding project has been started for the construction. A bird's eye view of the facility is shown in Figure 1. The left side of the image is the existing facility, and the facility in the right has yet to be constructed.

Figure 1. A bird's eye view of the RIKEN RI Beam Factory

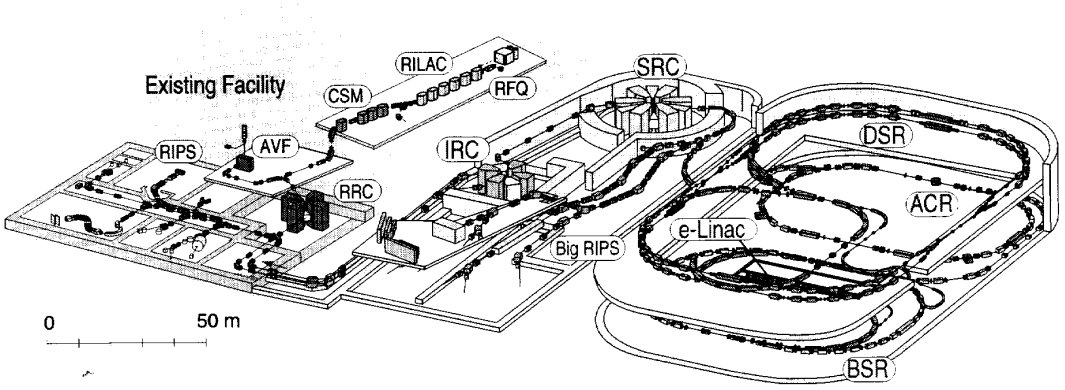

The existing facility consists of a heavy ion linear accelerator, RILAC, an AVF cyclotron, and a four-sector ring cyclotron, RRC. RILAC and AVF are mainly used as the injectors of RRC. The maximum energy of the existing facility is 210 MeV for protons, 135 MeV/u for light-heavy ions ($A < 40$), and 15 MeV for uranium ion, however, we have not yet obtained the license for uranium.

The expanding facility consists of two ring cyclotrons, IRC and SRC. SRC is of superconducting, projectile fragment separators which is the RI beam production devices, Big RIPSs (RIKEN Projectile Fragment Separator), an accumulation cooler ring, ACR, double storage ring, DSR, and a booster synchrotron ring, BSR. The maximum beam energy of SRC is 400 MeV/u for ions lighter than Ar and 150 MeV/u for uranium ions of the high charge state, and this energy makes the projectile fragmentation possible up to uranium. The beam intensity will be 10^{13} particle(s) for any element. The maximum beam power will be 24 kW for uranium ions.

The construction schedule of the RIBF is divided into three phases. IRC, SRC and Big RIPSs will be constructed in the first phase, which is already approved. ACR and DSR will be built in the second stage, and BSR in the third stage. Phase one will be finished by March 2003, phase two by 2007 and phase three by 2010.

Dose limit criteria

The Japanese legislation for radiation safety will be changed to meet the ICRP-60 recommendation soon. The dose limit criteria for RIBF were fixed taking this revision into consideration, as shown in Table 1.

Beam loss

The beam loss is the most ambiguous parameter in the accelerator shielding design, here, however it was assumed as Table 2. The low beam loss rate, total 2% at SRC, for example, must be kept by the beam loss monitoring.

Table 1. Criteria of effective dose for safety design of RIKEN RI Beam Factory

Item (boundary)	External radiation	Air concentration	Water concentration
Non-restricted area in radiation controlled area	25 μSv/h (1 mSv/w)	DAC (50 mSv/y)	
Radiation controlled area	2.6 μSv/h (1.3 mSv/3m)	DAC (1 mSv/y)	DWC (1 mSv/y)
Office in-site	0.5 μSv/h (250 μSv/3m)		
Site	50 μSv/y	DAC (1 mSv/y) × 0.05	DWC (1 mSv/y) × 0.05

Table 2. The assumed beam loss rate at RIBF

Position	IRC	SRC	Big RIPS
Loss	2 [%]	2 [%]	100 [%]

High-energy neutron production by heavy ions

The high-energy neutron production is the most fundamental data for the safety design of RIBF. High-energy heavy ion beams are available at HIMAC facility of the National Institute of Radiological Sciences, and the neutron production at thick graphite, aluminium, copper and lead targets bombarded by the 400 MeV/u ^{20}Ne beam were measured [1]. The data of the copper target are shown in Figure 2. The neutron energy spreads to very high energy, and the angular distribution of high-energy neutrons have a strong forwardness.

Figure 2. The measured neutron production at a thick Cu target bombarded by 400 MeV/u ^{20}Ne beam

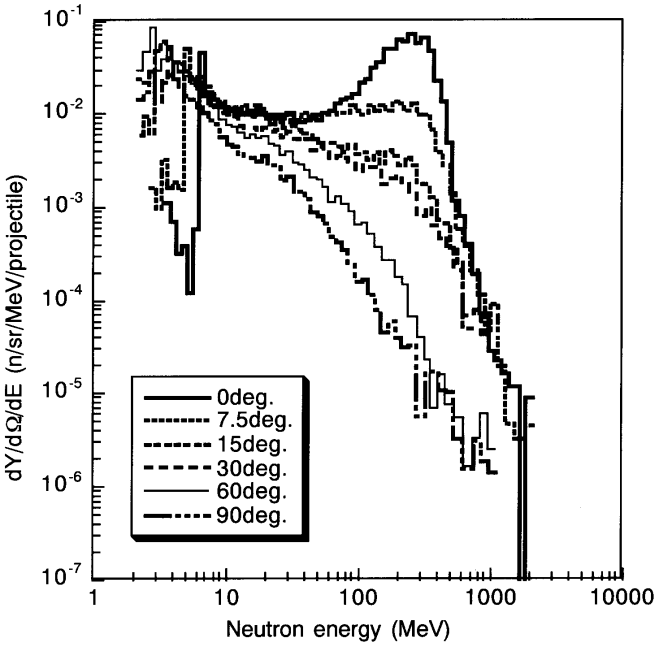

RIBF will accelerate all the elements, and we must know which element will produce the largest amount of high-energy neutrons. This estimation was performed on the assumption that the neutron yield is in proportion to $[E^2 \cdot A]$, where E is the beam energy in MeV/u and A is the mass number. The results are shown in Table 2 on the relative value.

In Table 3 the neutron production is highest for the $^{84}Kr^{30+}$ beam, and the result of the ^{20}Ne beam was corrected by multiplying a factor of 2.5 $[=(300/400)^2 \cdot (84/20)]$.

Table 3. Neutron yield by the SRC beam

Ion	Energy (MeV/u)	Intensity (pμA)	Relative neutron yield
$^{16}O^{7+}$	400	1	1.00
$^{40}Ar^{17+}$	400	1	2.50
$^{84}Kr^{30+}$	300	1	2.95
$^{129}Xe^{38+}$	200	1	2.02
$^{238}U^{49+}$	100	1	0.93
$^{238}U^{58+}$	150	0.2	0.42

Deep penetration of high-energy neutrons

HETC calculation

A several-meter thick iron slab is necessary for the 0-degree shielding at a dump of an 1-particle μA heavy ion beam. The neutrons very heavily attenuate after such a thick shield, and some biasing method must be incorporated into a Monte Carlo transport calculation.

The "multi-layer" method was incorporated into HETC-3STEP [2] and the one-dimensional transportation was calculated. The "multi-layer" method is explained in the following.

When a neutron penetration through a 3-m thick iron slab is calculated, the slab is separated into three one-meter slabs. The source neutrons are generated at the centre of the left surface of the first one-meter slab, and the neutron penetration is calculated. The energy-angular distribution of the leakage neutrons, protons and negative pions from the right surface is obtained. The particle penetration through the second one-meter slab is calculated by using the point directional source placed at the centre of the left surface, which was obtained from the leakage particle distributions of the previous slab. The deep penetration is calculated by repeating this procedure.

ANISN calculation

ANISN is the most powerful code for practical shielding design because of its short calculation time, and was used with the DLC-119/HILO86R [3].

Correction and fitting of the calculated results

The shielding experiment at ISIS [4] showed that the HETC and the ANISN codes give considerable underestimation for the high-energy neutron transport. The ANISN results were corrected by using some typical calculations with HETC at first, which seems to give more reliable

results, and the corrected results were secondly corrected by using the C/E (calculation/experiment) value of the ISIS benchmark experiment. We obtained the following correction formula for the ANISN results:

$$H_{\text{corrected}} = He^{Rt} \tag{1}$$

where R is $1.21\times10^{-3}\text{g}^{-1}\,\text{cm}^2$.

The calculated results of the iron-concrete slabs were corrected with Eq. (1), and the dose distributions in the concrete backing were fitted by using the following exponential formula:

$$Hr^2 = H_0 e^{-t/\lambda} \tag{2}$$

Figure 3 shows the ANISN result, the corrected results with Eq. (1), and the fitting of Eq. (2) for the case of 1-m iron and concrete shield. The H_0 and λ parameters as functions of primary iron shield thickness are shown for the various emission angle of the secondary neutrons in Figures 4 and 5. Eq. (2) was used in the practical shielding design and, for example, the result of the effective dose distribution on the SRC roof is shown in Figure 6.

Figure 3. Effective dose distribution in a 1-m thick iron and 12-m thick ordinary concrete slab calculated with the ANISN code, its corrected result with Eq. (1), and the fitting with Eq. (2)

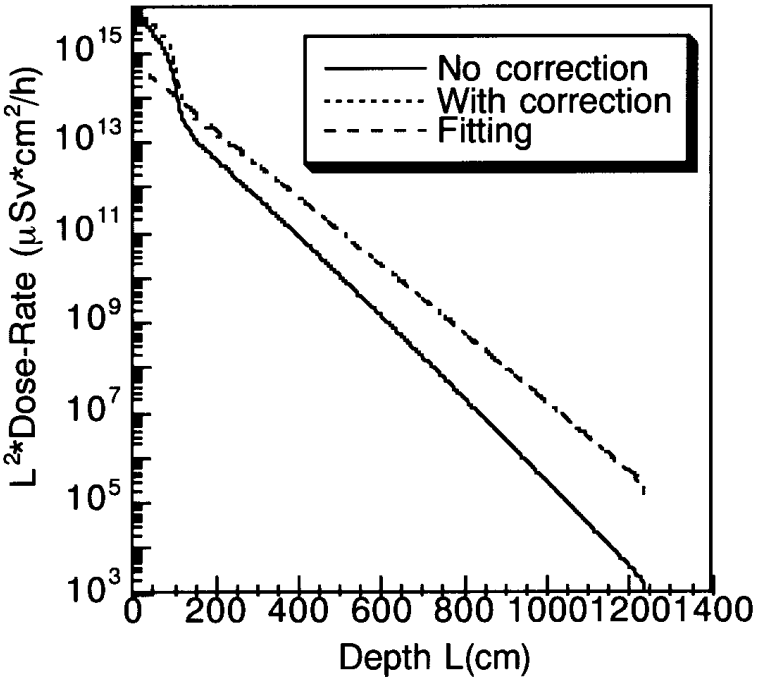

Figure 4. H_0 parameters as functions of primary iron shield thickness

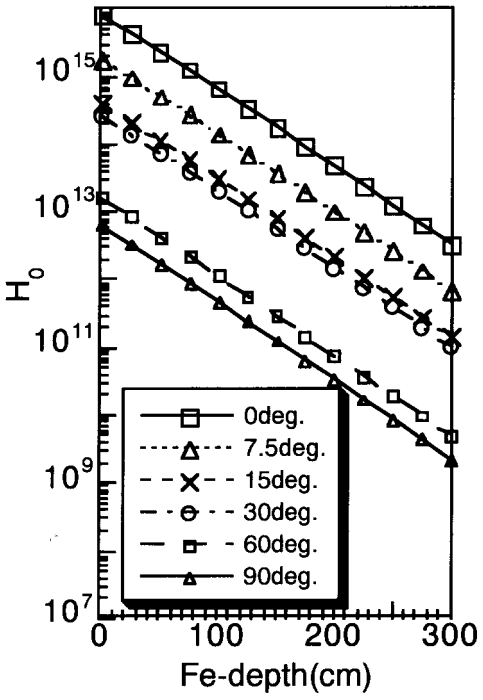

Figure 5. λ parameters as functions of primary iron shield thickness

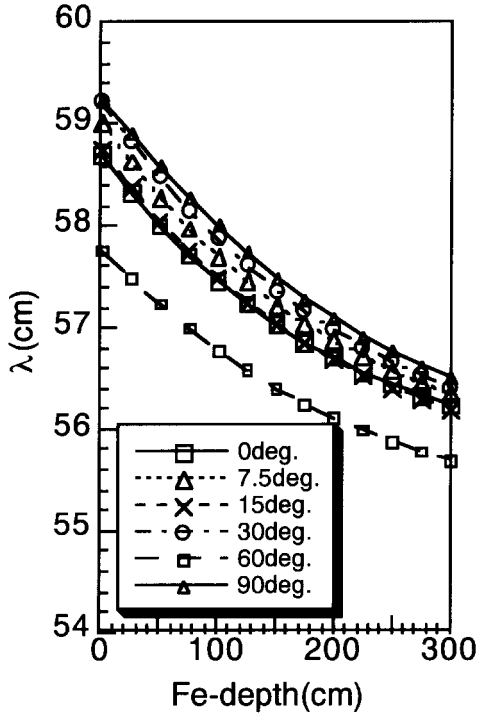

Figure 6. Effective dose distribution on the SRC room. R is the distance from the roof centre, and the abscissa is the angle from the BIG RIPS side direction

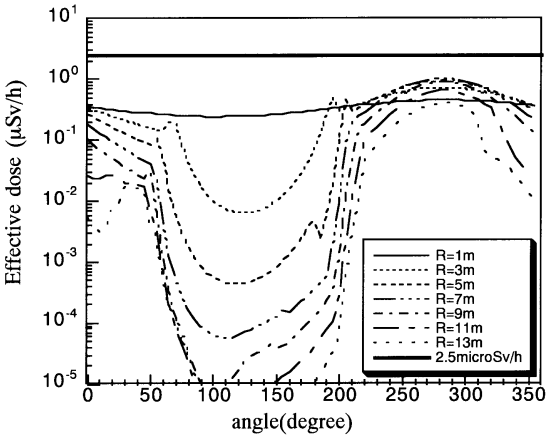

Shielding of Big RIPS

Direct ray shielding

The beam loss at Big RIPS is 100% and the shielding design is most difficult. In the Big RIPS, 20% beam is lost at the fragmentation target, and the residual beam is lost in the first dipole magnet. Moreover, about 1.6% beam will be stopped at the first focusing point. The local iron shielding for Big RIPS likes a square tunnel.

The fast neutrons irradiate the inner surface of the tunnel with large angles in the area far from the beam loss point. The neutrons scattered many times in iron, and the direction is diffused. In this condition, the shielding thickness cannot be estimated with the factor of $1/\cos\theta$.

The effective dose attenuation to the slatwise-injecting source neutrons was calculated with the HETC-3STEP code, and the results are shown in Figure 7. The attenuation is slower than the $1/\cos\theta$ correction.

Figure 7. Effective dose attenuation to the slantwise-injecting source neutrons

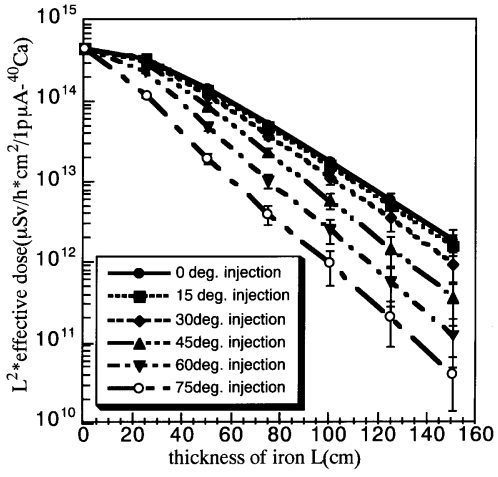

Scattered ray shielding

The backscattered neutrons hit against the local shielding wall and also go out through the tunnel. To estimate this effect the angular differential albedo function was calculated with the HETC-3STEP code, and the result is shown in Figure 8. By using the data of Figures 7 and 8, the thicknesses of iron local shielding and the "barrier" in the tunnel were obtained.

Figure 8. Angular differential effective-dose albedo function of iron

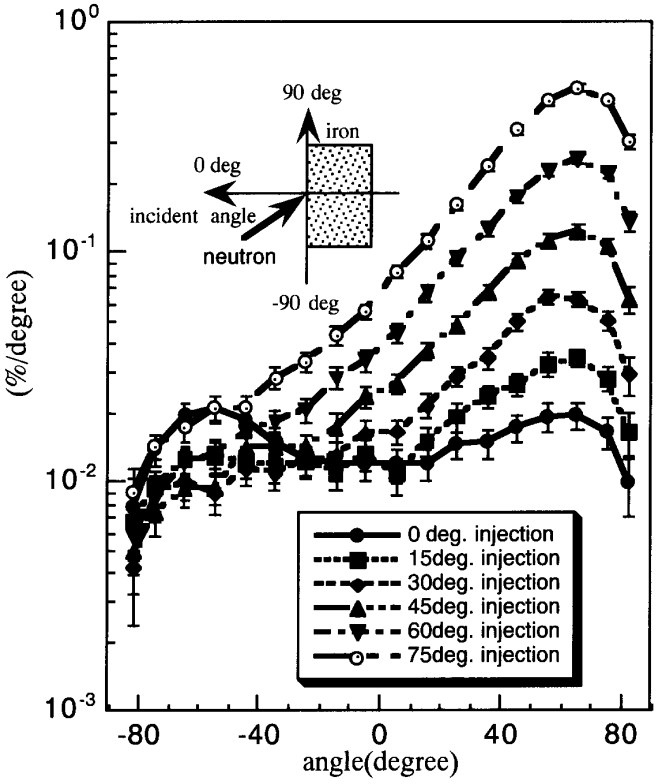

Air activation

The high-energy and thermal neutron fluxes in the cyclotron rooms, the Big RIPS tunnel, and the experimental rooms were obtained by using the ANISN code. The activation cross-sections of air was quoted from Ref. [5]. The air ventilation duct of the room where the beam is on is closed, and it is opened two hours later from the beam off. The ventilation rate is 0.5 replacement per hour. The air concentration was estimated on these conditions.

Skyshine

The whole building of RIBF is below ground level, and only the roof can be seen from the exterior. The skyshine radiation is the main component to the dose rate at the site boundary. The area of RIKEN is not large and it is surrounded by houses and buildings. A simple exponential fitting of the skyshine radiation distribution gives a considerable overestimation at short distances, and the following equation was obtained by using the data of Ref. [6].

$$H(r) = \frac{3.7 \times 10^{-2} hs}{r^2} e^{-2.38 \times 10^{-3} r} \left(1 - e^{-1.7 \times 10^{-2} r}\right) \quad [\mu\mathrm{Sv/h}] \tag{3}$$

The dose rate above the ground becomes larger than that on the ground [6], and the correction factor can be obtained by Eq. (4):

$$\frac{H(z)}{H(0)} = 0.094\theta + 1 \tag{4}$$

where θ is elevation angle in degree, and θ = 14 was adopted for RIBF.

Conclusion

A primary safety design work was performed for RIKEN RI Beam Factory. Many local shielding and thick ordinary concrete roof of 3.5 m at SRC, for example, will keep the radiation level and induced radioactivity level in the air below the criteria.

REFERENCES

[1] T. Kurosawa *et al*., "Measurement of Secondary Neutrons Produced from Thick Targets Bombarded by Heavy Ions", Int. Conf. Nucl. Data for Sci. and Technol., Trieste (May 1997).

[2] N. Yoshizawa *et al*., "Development of High Energy Transport Code HETC-3STEP Applicable to Nuclear Reaction with Incident Energies Above 20 MeV", *J. Nucl. Sci. Technol*., 32, 601 (1995).

[3] H. Kotegawa *et al*., "Neutron-Photon Multigroup Cross-Sections for Neutron Energies Up to 400 MeV: HILO86R", JAERI-M 93-020, Japan Atomic Energy Research Institute (1993).

[4] Y. Uwamino *et al*., "Shielding Experiment for High-Energy Neutrons at ISIS", Genshikaku Kenkyu, 41 No. 3, 89 (1996), *in Japanese*.

[5] A.H. Sullivan, "A Guide to Radiation and Radioactivity Levels Near High-Energy Particle Accelerators", Nuclear Technology Publishing, Kent (1992), p. 138.

[6] Y. Uwamino and T. Nakamura, Particle Accelerators, 21, 157 (1987).

Session IV

Shielding Benchmark Calculations and Results

Chairs: A. Fassò and L. Waters

BEEP: THE BENCHMARK EXERCISE FOR ELECTRONS AND PHOTONS

William P. Ballard
Sandia National Laboratories
Albuquerque, USA

Alex F. Bielajew (Chairman)
The University of Michigan
Ann Arbor, USA

Dermott E. Cullen
Lawrence Livermore National Laboratory
USA

Alberto Fassò
Stanford Linear Accelerator Centre
USA

Detlef Filges
Institut fur Kernphysik
Jülich, Deutschland

Hideo Hirayama
KEK, High Energy Accelerator Research Centre,
Tsukuba, Japan

H. Grady Hughes III
Los Alamos National Laboratory
Los Alamos, USA

Iwan Kawrakow
National Research Council of Canada
Ottawa, Canada

Ronald P. Kensek
Sandia National Laboratories
Albuquerque, USA

Bernadette L. Kirk (Observer)
Radiation Safety Information Computational Centre,
Oak Ridge, USA

Francesc Salvat
Universitat de Barcelona
Barcelona, Spain

Stephen M. Seltzer
National Institute of Standards and Technology,
Gaithersburg, USA

Pedro Vaz (Secretary)
OECD/NEA Data Bank
Issy-les-Moulineaux, France

Abstract

The purpose of this exercise is to gather together a group of experts in general-purpose electron/photon Monte Carlo methods to design a benchmark suite for comparison of existing public-domain Monte Carlo codes, or ones that are due to be released by the date of the release of this report – the fourth quarter of the year 2000. Through use of results of the benchmark suite, the community will have unprecedented knowledge of the dynamic range of a given code, its range of applicability and its accuracy in comparison to experimental and theoretical benchmarks. A user will also be able to gain some idea as to how efficient a code may be for certain applications and some information as to the computing resources required for certain broad classes of problems.

Introduction

It is a very interesting time for code and algorithm development in electron and photon Monte Carlo methods and a very propitious time for doing an intercomparison of codes. Historically, the hard-core $e^{\pm}$-γ Monte Carlo world is divided up among public-domain EGS, ITS and MCNP. Most of the development of electron and photon algorithms are developed within these code systems. These stand-alone codes are sometimes attached to more comprehensive integrator codes increasing their utility to the client community. We are also seeing recent development of new codes such as PENELOPE and the introduction of new electron transport physics in the FLUKA code.

The external active client community of the EGS, ITS and MCNP codes probably numbers in the vicinity of a thousand or so, and the time-integrated community probably numbers in the tens of thousands. Interestingly, the client communities are nearly orthogonal to each other despite versions of these codes being in the public domain for decades. Therefore, a secondary but equally important motivation is to stimulate discussion among the various code and algorithm developers, to become familiar with one another's applications and to stimulate new development or consolidation of existing ideas. It is hoped that a sharper focus on one's own applications can be obtained through this benchmark exercise with increased awareness of the broader spectrum of application.

In view of this, a benchmarking effort is being undertaken that involves some of the major players in electromagnetic Monte Carlo code and algorithm development. It is possible that certain interests are underrepresented. If such is the case, any concerns should be brought to the attention of the Secretary and/or chairman of BEEP. We plan to be as comprehensive as possible subject to the constraints of efficiency and productivity. The remainder of this report describes the initial efforts in this exercise.

Participating codes

The participant codes in this exercise were selected because the laboratories that produce them are deeply involved in the development of Monte Carlo transport methods for electrons and photons and have expressed an interest in this effort. Only codes that will be distributed publicly will be employed. The following general-purpose codes will participate in this exercise:

- *EGS*: The EGS [1,2] code is released by the Stanford Linear Accelerator Centre (SLAC, USA), the High Energy Accelerator Research Centre (KEK, Japan) and the National Research Council of Canada (NRCC). EGS is the least "controlled" code that we shall consider. Many additions have been made by numerous groups [3]. The KEK focuses primarily on photon transport improvements [4-8] and the NRCC develops electron transport [9-15].

- *FLUKA*: FLUKA [16,17] is a high-energy code with some new electromagnetic physics.

- *ITS*: The ITS system of codes [18-20] is developed by Sandia. Elements of the ETRAN code [21-23] are integrated in the ITS code system.

- *MCNP*: The MCNP code system is developed by Los Alamos National Laboratory [24-26]. Elements of ITS and ETRAN are incorporated in MCNP.

- *PENELOPE*: PENELOPE [27-37] is being developed by the University of Barcelona. It is a new code that embodies a careful consideration of low-energy phenomena.

- *TART*: TART [38-40] is being developed by Lawrence Livermore National Laboratory. At the present time it does not model electron transport. However, this capability may be introduced by the time the final report of this committee is issued.

Benchmarks

In this section we describe a subset of the benchmarks that may be attempted. These fall into two categories, experimental and theoretical.

Experimental benchmarks

The ultimate test of a Monte Carlo code is its performance relative to a well-described and well-understood measurement. Measurements are selected as experimental benchmarks because they measure a physical quantity that can be related unambiguously to some fundamental physical phenomenon.

An initial part of the exercise is to search the literature for benchmark-quality data. The initial effort in this regard resulted in the following:

- catalogues of existing experimental benchmarks [33,36,41-44];
- photon detector response functions [45,46];
- electron detector response functions [47];
- photon energy deposition [48-50];
- electron energy deposition [51,52];
- bremsstrahlung and bremsstrahlung effects [53-62];
- response of ion chambers [63];
- electron transmission and reflection [64-70];
- low energy photon scattering [8];
- absorbed dose distribution inside phantoms [71];
- electron impact ionisation [41,72];
- k X-ray yield [73];
- energy deposition by electron sources [51,52,74-79];
- charge deposition by electron sources [80,81];
- photon effects [82-90].

Theoretical benchmarks

A theoretical benchmark is an important consideration in the evaluation of Monte Carlo codes, supplementary and complementary to comparisons with measurements. Theoretical benchmarks are absolute (no normalisations are required), clean (sources are "ideal") and differences between the codes can be maximised through careful design of computer experiments. Theoretical experiments can explore physical realms that can not be approached experimentally and the limits of the codes can be exercised. In some cases, the results are known from independent theory.

There is a two-fold object to this benchmark exercise. One is to show the community what our Monte Carlo codes can do and the other is to show what they can not do. In the case of the latter, the differences should be related to either the algorithm structure of the code (for example, a failing of the condensed history or CSDA modelling), a spatial resolution problem, or a shortcoming in cross-section modelling. No Monte Carlo code system should aspire to solve every problem. However, every Monte Carlo code system should be distributed with an indication of its weaknesses as well as its strengths.

The following list presents an initial set of theoretical benchmark trials:

- Electron energy-deposition profiles, both axial and radial. Monoenergetic beams incident normally and at an angle on 1-D semi-infinite targets of various composition.

- Electron transmission and backscatter. Monoenergetic beams incident normally and at an angle on targets of various composition and thickness.

- Simulation of ionisation chambers. This is a demanding application that can test transport across boundaries where the density and the atomic composition can change significantly. The response of certain ionisation chambers can be predicted theoretically to within a few per cent.

- Spatial, angular and space-angle correlations. Monte Carlo results can be compared with the theoretical predictions of Lewis [91] and Goudsmit and Saunderson [92, 93].

- The broomstick simulation. This tallies the path-length distribution of electrons incident on the end of narrow cylindrical tubes of material. In the limit that the diameter of the tube goes to zero, the average path-length theoretically should approach the mean free path to an angular scattering event. This is an extremely severe test of the condensed history technique and every code we will consider should be expected to fail this test.

The report

There will be a text-based hard copy report associated with this effort. In addition, the NEA and the RSICC have agreed to "publish" the report on their web sites along with supplementary material. The supplementary material will include the data that were used to generate the figures and enough detail to enable an interested reader to repeat the benchmark using the input files and/or user codes supplied with the benchmark. The target date for release of the report is Q4/2000.

REFERENCES

[1] R.L. Ford and W.R. Nelson, The EGS Code System – Version 3, Stanford Linear Accelerator Center, Report SLAC-210, 1978.

[2] W.R. Nelson, H. Hirayama and D.W.O. Rogers, The EGS4 Code System, Report SLAC-265, Stanford Linear Accelerator Center, Stanford, California, 1985.

[3] A.F. Bielajew, H. Hirayama, W.R. Nelson and D.W.O. Rogers, History, Overview and Recent Improvements of EGS4, National Research Council of Canada, Report PIRS-0436, 1994.

[4] Y. Namito and H. Hirayama, Improvement of Low Energy Photon Transport Calculation by EGS4 – Electron Bound Effect in Compton Scattering, Japan Atomic Energy Society, Osaka, p. 401, 1991.

[5] Y. Namito, S. Ban and H. Hirayama, Implementation of Linearly-Polarized Photon Scattering into the EGS4 Code, *Nuclear Instruments and Methods*, A322:277-283, 1993.

[6] H. Hirayama, Y. Namito and S. Ban, Effects of Linear Polarisation and Doppler Broadening on the Exposure Build-Up Factors of Low-Energy Gamma Rays, National Laboratory for High Energy Physics, Report KEK Pre-Print 93-186 (KEK, Japan), 1994.

[7] H. Hirayama, Y. Namito and S. Ban, Implementation of an L-Shell Photoelectron and an L-Shell X-Ray for Elements into the EGS4 Code, National Laboratory for High Energy Physics, Report KEK Pre-Print 96-10 (KEK, Japan), 1996.

[8] Y. Namito, H. Hirayama and S. Ban, Improvements of Low-Energy Photon Transport in EGS4, in Proceedings of the First International Workshop on EGS4 (Technical Information and Library, Laboratory for High Energy Physics, Japan), pp. 32-50, 1997.

[9] A.F. Bielajew and D.W.O. Rogers, PRESTA: The Parameter Reduced Electron-Step Transport Algorithm for Electron Monte Carlo Transport, *Nuclear Instruments and Methods*, B18:165-181, 1987.

[10] A.F. Bielajew and D.W.O. Rogers, PRESTA: The Parameter Reduced Electron-Step Transport Algorithm for Electron Monte Carlo Transport, National Research Council of Canada, Report PIRS-0042, 1986.

[11] A.F. Bielajew and I. Kawrakow, The EGS4/PRESTA-II Electron Transport Algorithm: Tests of Electron Step-Size Stability, in Proceedings of the XII Conference on the Use of Computers in Radiotherapy (Medical Physics Publishing, Madison, Wisconsin), pp. 153-154, 1997.

[12] A.F. Bielajew and I. Kawrakow, From “Black Art” to “Black Box”: Towards a Step-Size Independent Electron Transport Condensed History Algorithm Using the Physics of EGS4/PRESTA-II, in Proceedings of the Joint International Conference on Mathematical Methods and Supercomputing for Nuclear Applications (American Nuclear Society Press, La Grange Park, Illinois, USA), pp. 1289-1298, 1997.

[13] A.F. Bielajew and I. Kawrakow, PRESTA-I ⇒ PRESTA-II: The New Physics, in Proceedings of the First International Workshop on EGS4 (Technical Information and Library, Laboratory for High Energy Physics, Japan), pp. 51-65, 1997.

[14] I. Kawrakow and A.F. Bielajew, On the Representation of Electron Multiple Elastic-Scattering Distributions for Monte Carlo Calculations, *Nuclear Instruments and Methods*, B134:325-336, 1998.

[15] I. Kawrakow and A.F. Bielajew, On the Condensed History Technique for Electron Transport, *Nuclear Instruments and Methods*, B142:253-280, 1998.

[16] A. Ferrari, P.R. Sala, R. Guaraldi and F. Padoani, An Improved Multiple Scattering Model for Charged Particle Transport, *Nucl. Inst. Meth.*, B71:412-416, 1992.

[17] A. Fassò, A. Ferrari, J. Ranft and P.R. Sala, FLUKA: Present Status and Future Developments, in Proceedings of the 4th Conference on Calorimetry in High Energy Physics, *World Sci.*, Singapore: 493-502, 1994.

[18] J.A. Halbleib and T.A. Mehlhorn, ITS: The Integrated TIGER Series of Coupled Electron/Photon Monte Carlo Transport Codes, Sandia Report SAND84-0573, 1984.

[19] J. Halbleib, Structure and Operation of the ITS Code System, in T.M. Jenkins, W.R. Nelson, A. Rindi, A.E. Nahum and D.W.O. Rogers, eds., Monte Carlo Transport of Electrons and Photons, pp. 249-262, Plenum Press, New York, 1989.

[20] J.A. Halbleib, R.P. Kensek, T.A. Mehlhorn, G.D. Valdez, S.M. Seltzer and M.J. Berger, ITS Version 3.0: The Integrated TIGER Series of Coupled Electron/Photon Monte Carlo Transport Codes, Sandia Report SAND91-1634, 1992.

[21] M.J. Berger, Monte Carlo Calculation of the Penetration and Diffusion of Fast Charged Particles, *Methods in Comput. Phys.*, 1:135-215, 1963.

[22] S.M. Seltzer, An Overview of ETRAN Monte Carlo Methods, in T.M. Jenkins, W.R. Nelson, A. Rindi, A.E. Nahum and D.W.O. Rogers, eds., Monte Carlo Transport of Electrons and Photons, pp. 153-182, Plenum Press, New York, 1989.

[23] S.M. Seltzer, Electron-Photon Monte Carlo Calculations: The ETRAN Code, *Intl. J. of Appl. Radiation and Isotopes*, 42:917-941, 1991.

[24] J. Briesmeister, MCNP – A General Purpose Monte Carlo Code for Neutron and Photon Transport, Version 3A, Los Alamos National Laboratory, Report LA-7396-M (Los Alamos, NM), 1986.

[25] J.F. Briesmeister, MCNP – A General Monte Carlo N-Particle Transport Code, Los Alamos National Laboratory, Report LA-12625-M (Los Alamos, NM), 1993.

[26] J.F. Briesmeister, MCNP – A General Monte Carlo N-Particle Transport Code, Los Alamos National Laboratory, Report LA-12625-M, Version 4B (Los Alamos, NM), 1997.

[27] F. Salvat and J.M. Fernández-Varea, Semiempirical Cross-Sections for the Simulation of the Energy Loss of Electrons and Positrons in Matter, *Nuclear Instruments and Methods*, B63:255-269, 1992.

[28] J.M. Fernández -Varea, R. Mayol, J. Baró and F. Salvat, On the Theory and Simulation of Multiple Elastic Scattering of Electrons, *Nuclear Instruments and Methods*, B73:447-473, 1993.

[29] J.M. Fernández -Varea, F. Salvat and R. Mayol, Cross-Sections for Elastic Scattering of Fast Electrons and Positron by Atoms, *Nuclear Instruments and Methods*, B82:39-45, 1993.

[30] F. Salvat and R. Mayol, Elastic Scattering of Electrons and Positrons by Atoms: Schrodinger and Dirac Partial Wave Analysis, *Comput. Phys. Commun*., 74:358-374, 1993.

[31] J. Baró, M. Roteta, J.M. Fernández-Varea and F. Salvat, Analytical Cross-Sections for Monte Carlo Simulation of Photon Transport, *Radiation Physics and Chemistry*, 44:531-552, 1994.

[32] J. Baró, J. Sempau, J.M. Fernández-Varea and F. Salvat, Simplified Monte Carlo Simulation of Elastic Electron Scattering in Limited Media, *Nuclear Instruments and Methods*, B84:465-483, 1994.

[33] J. Baró, J. Sempau, J.M. Fernández-Varea and F. Salvat, PENELOPE: An Algorithm for Monte Carlo Simulation of the Penetration and Energy Loss of Electrons and Positrons in Matter, *Nuclear Instruments and Methods*, B100:31-46, 1995.

[34] F. Salvat, J.M. Fernández-Varea, J. Baró and J. Sempau, PENELOPE, An Algorithm and Computer Code for Monte Carlo Simulation of Electron-Photon Showers, University of Barcelona CIEMAT (Contro de Investigaciones Energéticas, Medioambientales y Tecnolgicas), Report 799, 1996.

[35] D. Brusa, G. Stutz, J.A. Riveros, J.M. Fernández-Varea and F. Salvat, Fast Sampling Algorithm for the Simulation of Photon Compton Scattering, *Nuclear Instruments and Methods*, A379:167-175, 1996.

[36] J. Sempau, E. Acosta, J. Baró, J.M. Fernández-Varea and F. Salvat, An Algorithm for Monte Carlo Simulation of Coupled Electron-Photon Showers, *Nuclear Instruments and Methods*, B132:377-390, 1997.

[37] F. Salvat, PENGEOM2, A Modular Quadric Geometry Package for Monte Carlo Simulation of Radiation Transport with PENELOPE, University of Barcelona Report, 1998.

[38] D.E. Cullen, A.L. Edwards and E.F. Plechaty, TART95: A Coupled Neutron-Photon Monte Carlo Transport Code, Lawrence Livermore National Laboratory, Report UCRL-MA-121319 (Livermore, California), 1995.

[39] D.E. Cullen, TART96: A Coupled Neutron-Photon, 3-D, Combinatorial Geometry Monte Carlo Transport Code, Lawrence Livermore National Laboratory, Report UCRL-ID-126455 (Livermore, California), 1996.

[40] D.E. Cullen, TART97: A Coupled Neutron-Photon, 3-D, Combinatorial Geometry Monte Carlo Transport Code, Lawrence Livermore National Laboratory, Report UCRL-ID-126455, Rev. 1 (Livermore, California), 1997.

[41] M.J. Berger, ETRAN – Experimental Benchmarks, in T.M. Jenkins, W.R. Nelson, A. Rindi, A.E. Nahum and D.W.O. Rogers, eds., Monte Carlo Transport of Electrons and Photons, pp. 183-219, Plenum Press, New York, 1989.

[42] D.W.O. Rogers and A.F. Bielajew, Experimental Benchmarks of EGS, in T.M. Jenkins, W.R. Nelson, A. Rindi, A.E. Nahum and D.W.O. Rogers, eds., Monte Carlo Transport of Electrons and Photons, pp. 307-322, Plenum Press, New York, 1989.

[43] S.M. Seltzer, Applications of ETRAN Monte Carlo Codes, in T.M. Jenkins, W.R. Nelson, A. Rindi, A.E. Nahum and D.W.O. Rogers, eds., Monte Carlo Transport of Electrons and Photons, pp. 221-246, Plenum Press, New York, 1989.

[44] J. Halbleib, Applications of the ITS Codes, in T.M. Jenkins, W.R. Nelson, A. Rindi, A.E. Nahum, and D.W.O. Rogers, eds., Monte Carlo Transport of Electrons and Photons, pp. 263-284, Plenum Press, New York, 1989.

[45] R.L. Heath, Scintillation Spectrometry – Gamma-Ray Spectrum Catalogue, USAEC Report IDO-16880-1, 1964.

[46] D.W.O. Rogers, More Realistic Monte Carlo Calculations of Photon Detector Response Functions, *Nucl. Instrum. Meth*., 199:531-548, 1982.

[47] M.J. Berger, S.M. Seltzer, H. Eisen and J. Silverman, Response of Silicon Detectors to Monoenergetic Electrons With Energies Between 0.15 and 5.0 MeV, *Nucl. Instrumm. Meth.*, 69:181-193, 1969.

[48] H. Mach and D.W.O. Rogers, A Measurement of Absorbed Dose to Water per Unit Incident 7 MeV Photon Fluence, *Physics in Medicine and Biology*, 29:1555-1570, 1984.

[49] P.D. Higgins, C.H. Sibata and B.R. Paliwal, Determination of Contaminant-Free Build-Up for ^{60}Co, *Phys. Med. Biol*., 16:153-162, 1985.

[50] O.T. Ogunleye, F.H. Attix and B.R. Paliwal, Comparison of Burlin Cavity Theory with LiF TLD Measurements for Cobalt-60 Gamma Rays, *Phys. Med. Biol*., 25:203, 1980.

[51] G.J. Lockwood, L.E. Ruggles, G.H. Miller and J.A. Halbleib, Calorimetric Measurement of Electron Energy Deposition in Extended Media – Theory Versus Measurement, Sandia Report SAND79-0414, 1980.

[52] K.R. Shortt, C.K. Ross, A.F. Bielajew and D.W.O. Rogers, Electron Beam Dose Distributions Near Standard Inhomogeneities, *Phys. Med. Biol*., 31:235-249, 1986.

[53] T.W.L. Sanford, J.A. Halbleib and W. Beezhold, Experimental Check of Bremsstrahlung Dosimetry Predictions for 0.75 MeV Electrons, *IEEE Transactions on Nuclear Science*, 32:4410, 1985.

[54] J.A. Halbleib, T.W.L. Sanford and W. Beezhold, Experimental Verification of Bremsstrahlung Dosimetry Predictions for 0.75 MeV Electrons, Sandia Report SAND85-1517, 1986.

[55] T.W.L. Sanford, J.A. Halbleib, W. Beezhold and L.J. Lorence, Experimental Verification of Non-Equilibrated Bremsstrahlung Dosimetry Predictions for 0.75 MeV Electrons, *IEEE Transactions on Nuclear Science*, 33:1261, 1986.

[56] D.E. Beutler, J.A. Halbleib and D.P. Knott, Comparison of Experimental Pulse-Height Distributions in Germainium Detectors with Integrated TIGER Series-Code Predictions, *IEEE Transactions on Nuclear Science*, 36:1912, 1989.

[57] B.A. Faddegon, C.K. Ross and D.W.O. Rogers, Forward Directed Bremsstrahlung of 10-30 MeV Electrons Incident on Thick Targets of Al and Pb, *Medical Physics*, 17:773-785, 1990.

[58] B.A. Faddegon, C.K. Ross and D.W.O. Rogers, Angular Distribution of Bremsstrahlung from 15 MeV Electrons Incident on Thick Targets of Be, Al and Pb, *Medical Physics*, 18:727-739, 1991.

[59] T.W.L. Sanford, D.E. Beutler, J.A. Halbleib and D.P. Knott, Experimental Verification of Bremsstrahlung Production and Dosimetry Predictions for 15.5 MeV Electrons, *IEEE Transactions on Nuclear Science*, 38, 1991.

[60] T.W.L. Sanford, J.A. Halbleib, D.E. Beutler and D.P. Knott, Experimental Verification of Dosimetry Predictions of Bremsstrahlung Attenuation as a Function of Material and Electron Energy, *IEEE Transactions on Nuclear Science*, 40, 1993.

[61] B.A. Faddegon and D.W.O. Rogers, Comparisons of Thick-Target Bremsstrahlung Calculations by EGS4 and ITS, *Nucl. Inst. Meth*., A327:556-565, 1993.

[62] D.E. Beutler, J.A. Halbleib, T.W.L. Sanford and D.P. Knott, Experimental Verification of Bremsstrahlung Production and Dosimetry Predictions as a Function of Energy and Angle, *IEEE Transactions on Nuclear Science*, 41, 1994.

[63] B. Nilsson, A. Montelius, P. Andreo and B. Sorcini, Perturbation Correction Factors in Ionization Chamber Dosimetry, in Dosimetry in Radiotherapy (IAEA, Vienna), Vol. 1, pp. 175-185, 1988.

[64] H. Frank, Zur Vielfachstreuung und Ruckdiffusion schneller Elektronen nach Durchgang durch dicke Schichten, *Z. Naturforsch*, 14a:247, 1959.

[65] H. Drescher, L. Reimer, H. Seider and Z. Agnew, Rückstreukoeffizient und Sekundärelektronen-Ausbeute von 10-100 keV-Elektronen und Beziehungen zur Raster-Elektronenmikroskopie, *Physik*, 29:331, 1970.

[66] H.K. Hunger and L. Küchler, Measurements of the Electron Backscattering Coefficient for Quantitative EPMA in the Energy Range of 4 to 40 keV, *Phys. Stat. Sol*., A56:45, 1979.

[67] G. Neubert and S. Rogaschewski, Backscattering Coefficient Measurements of 15 to 60 keV Electrons for Solids at Various Angles of Incidence, *Phys. Stat. Sol*., A59:35, 1980.

[68] G. Soum, A. Mouselli, F. Arnal and P. Verdier, Etude de la transmission et de la rétrodiffusion d'électrons d'énergie 0,05 à 3 MeV dans le domaine de la diffusion multiple, *Rev. Phys. Appl*., 22:1189, 1987.

[69] G.J. Lockwood, L.E. Ruggles, G.H. Miller and J.A. Halbleib, Electron Energy and Charge Albedos – Calorimetric Measurement Versus Monte Carlo Theory, Sandia Report SAND84-0912, 1984.

[70] R. Wang, S. Duane and A.F. Bielajew, A New Scheme for Monte Carlo Electron and Photon Transport, NRC Report PIRS-0355, 1993.

[71] N. Nariyama, S. Tanaka, Y. Nakane, Y. Namito, H. Hirayama, S. Ban and H. Nakasima, Absorbed Dose Measurements and Calculations in Phantom for 1.5 to 50 keV Photons, *Health Physics*, 68:253-260, 1995.

[72] R. Placious, Dependence of 50- and 100-keV Bremsstrahlung on Target Thickness, Atomic Number, and Geometric Factors, *J. Appl. Phys*., 38:2030-2038, 1967.

[73] C.E. Dick, A.C. Lucas, J.M. Motz, R.C. Placious and J.H. Sparrow, Large-Angle L X-Ray Production by Electrons, *J. Appl. Phys*., 44:815-826, 1973.

[74] W.L. McLaughlin and E.K. Hussmann, The Measurement of Electron and Gamma-Ray Dose Distributions in Various Media, in Large Radiation Sources for Industrial Processes, Intl. Atomic Energy Agency Publication IAEA SM-123/43, 1969.

[75] H. Eisen, M. Rosenstein and J. Silverman, 2.0-MeV Electron Depth-Dose Measurements in Aluminum, Copper and Tin Absorbers Using a Radiochromic Dye Film, *Intl. J. of Appl. Radiation and Isotopes*, 23:97-108, 1972.

[76] H. Eisen, M. Rosenstein and J. Silverman, Electron Depth-Dose Distribution Measurements in Two-Layer Slab Absorbers, *J. Radiat. Res*., 52:429, 1972.

[77] E. Farley, K. Crase and D. Selway, 500-MeV Electron Beam Benchmark Experiments and Calculations, Lawrence Livermore National Laboratory Report UCRL-52871 (Livermore, California), 1979.

[78] S.G. Miller, 500-MeV Electron Beam Benchmark Experiment Revisited, Lawrence Livermore National Laboratory, Report DDV-88-0010 (Livermore, California), 1988.

[79] D.E. Weiss, W.C. Johnson and R.P. Kensek, Dose Distributions in Tubing Irradiated by Electron Beam: Monte Carlo Simulation and Measurement, *Radiat. Phys. Chem.*, 50:475-485, 1997.

[80] A.R. Frederickson and S. Woolf, Electron Beam Current Penetration in Semi-Infinite Slabs, *IEEE Transactions on Nuclear Science*, 28:4186, 1981.

[81] T. Tabata, R. Ito, S. Okabe and Y. Fujita, Charge Distributions Produced by 4 to 24 MeV Electrons in Elemental Materials, *Phys. Rev*., B3:572, 1971.

[82] J.A. Wall and E.A. Burke, Dose Distributions at and Near the Interface of Different Materials Exposed to Cobalt-60 Gamma Radiation, AFCRL-TR-75-004, 1974.

[83] K.W. Dolan, X-Ray-Induced Electron Emission from Metals, *J. Appl. Phys*., 46:2456, 1975.

[84] M.Ya. Grudskii, A.V. Malyshenkov and V.V. Smirnov, Electron Yield from Metals Under the Action of 30 to 90 keV Photon Radiation, *Sov. Phys. Tech. Phys*., 21:172-176, 1976.

[85] M.Ya. Grudskii, N.N. Roldugin, V.V. Smirnov, A.F. Adadurov and V.T. Lazurik, Experimental Investigation and Monte Carlo Calculation of Photo-Induced Electron Emission from Solids, *Nucl. Inst. Meth. Phys. Res*., 227:26-134, 1984.

[86] W.P. Ballard, L.J. Lorence Jr., D.P. Snowden, V.A.J. van Lint and E.S. Beale, A Comparison of Experiment, CEPXS/ONETRAN, TIGERP and TIGER Net Electron Emission Coefficients for Various Bremsstrahlung Spectra, *IEEE Transactions on Nuclear Science*, 34:1569-1574, 1987.

[87] J.A. Meli, A.S. Meigooni and R. Nath, On the Choice of Phantom Material for the Dosimetry of ^{192}Ir Sources, *Intl. J. Radiation Oncology Biol. Phys*., 14:587-594, 1988.

[88] A.S. Meigooni, J.A. Meli and R. Nath, A Comparison of Solid Phantoms with Water for Dosimetry of ^{125}I Brachytherapy Sources, *Med. Phys*., 15:695-701, 1988.

[89] A.S. Meigooni and R. Nath, Tissue Inhomogeneity Correction for Brachytherapy Sources in a Heterogeneous Phantom with Cylindrical Symmetry, *Med. Phys*., 19:401-407, 1992.

[90] J.C. Garth, K.L. Critchfield, J.R. Turinetti and D.E. Beutler, A Comprehensive Comparison of CEPXS/ONELD Calculations of Dose Enhancement with the ^{60}Co Data Set of Wall and Burke, *IEEE Transactions on Nuclear Science*, 43, 1996.

[91] H.W. Lewis, Multiple Scattering in an Infinite Medium, *Phys. Rev*., 78:526-529, 1950.

[92] S.A. Goudsmit and J.L. Saunderson, Multiple Scattering of Electrons, *Phys. Rev*., 57:24-29, 1940.

[93] S.A. Goudsmit and J.L. Saunderson, Multiple Scattering of Electrons, II, *Phys. Rev*., 58:36-42, 1940.

INTERCOMPARISON OF MEDIUM-ENERGY NEUTRON ATTENUATION IN IRON AND CONCRETE

H. Hirayama
KEK, High Energy Accelerator Research Organisation
1-1 Oho, Tsukuba, Ibaraki, 305-0801 Japan
E-mail: hideo.hirayama@kek.jp

Attenuation Length Sub-Working Group
Japan

Abstract

Neutron attenuation of medium energy below 1 GeV has not been well understood until now. It is desired to obtain common agreements concerning the behaviours of neutrons inside various materials. This is necessary in order to agree on definitions of the attenuation length, which is very important for shielding calculations involving high energy accelerators. As one attempt, it was proposed by Japanese attendants of SATIF-2 to compare the attenuation of medium-energy neutrons inside iron and concrete shields between various computer codes and data, and was cited as a suitable action for SATIF. The first results from three groups were presented at SATIF-3 [1]. It has become clear that neutrons above 20 MeV are important for understanding the attenuation inside materials and that the geometry, planar or spherical, does not affect the results very much. Considering the CPU times required for Monte Carlo calculations and this result, revised problems to be calculated were prepared by the Japanese Working Group and sent to the participants of this action. The geometry is only plane, and calculations are required only for neutrons above 20 MeV. The secondary neutrons from high energy protons, which were calculated by H. Nakashima [2], are also included in the problem. The results from four groups were sent to the organiser at the end of August. This paper presents a comparison between groups concerning the attenuation length together with the neutron spectrum and the future themes which come from this intercomparison.

Introduction

Neutron attenuation of medium energy below 1 GeV has not been well understood until now. It is desired to obtain common agreements concerning the behaviours of neutrons inside various materials. This is necessary in order to agree on definitions of the attenuation length, which is very important for shielding calculations involving high energy accelerators. As one attempt, it was proposed by Japanese attendants of SATIF-2 to compare the attenuation of medium-energy neutrons inside iron and concrete shields between various computer codes and data, and was cited as a suitable action for SATIF. The first results from three groups were presented at SATIF-3 [1]. It has become clear that neutrons above 20 MeV are important for understanding the attenuation inside materials and that the geometry, planar or spherical, does not affect the results very much. Considering the CPU times required for Monte Carlo calculations and this result, revised problems to be calculated were prepared by the Japanese Working Group and sent to the participants of this action. The geometry is only plane, and calculations are required only for neutrons above 20 MeV. The secondary neutrons from high energy protons, which were calculated by H. Nakashima [2], are also included in the problem. The results from four groups were sent to the organiser at the end of August. This paper presents a comparison between groups concerning the attenuation length together with the neutron spectrum and the future themes which come from this intercomparison.

Problems for an intercomparison (2)

Considering the results presented at SATIF-3 [1] and the CPU times necessary for Monte Carlo calculations, the following revised problems were proposed to be calculated by various codes with their own databases. In addition to the first problems, secondary neutrons produced by high energy protons toward lateral directions were added. These data were calculated by H. Nakashima [2] using FLUKA [3,4].

Source neutron energy

(a) Source neutrons are uniformly distributed within the following energy regions:

A. 40- 50 MeV
B. 90-100 MeV
C. 180-200 MeV
D. 375-400 MeV

(b) Secondary neutrons (see Figure 1):

A. from 200 MeV protons
B. from 500 MeV protons
C. from 1 GeV protons

Geometry

Plane (6 m thick) with normal-incident parallel beams.

Figure 1. Secondary neutron at 90° from an iron target bombarded by protons (FLUKA calculations)

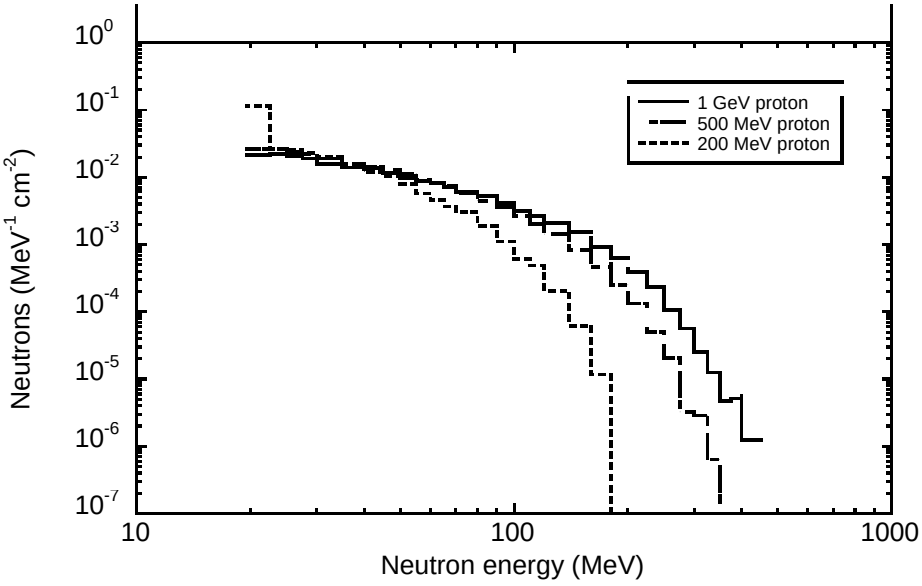

Shielding material

As typical shielding materials, iron and concrete were selected. The densities of two materials and the composition of concrete are also presented (Table 1).

(a) Iron (density 7.87 g cm^{-3})

(b) Concrete (density 2.27 g cm^{-3}) [Type 02-a, ANL-5800, 660(1963)]

Table 1. Composition of concrete

Element	Atomic number density	Weight per cent
	(10^{24}/cm^{-3})	
H	1.3851E–2	1.02
C	1.1542E–4	1.00
O	4.5921E–2	53.85
Mg	1.2388E–4	0.22
Al	1.7409E–3	3.44
Si	1.6621E–2	34.21
K	4.6205E–4	1.32
Ca	1.5025E–3	4.41
Fe	3.4510E–4	1.41

Energy group and fluence to dose-equivalent conversion factor

The energy group in Table 2 is presented as the standard one; it is required that the neutron spectra be presented in this energy group if possible.

Table 2. Upper energy of 66 neutron energy groups (MeV)

4.00E+2	3.75E+2	3.50E+2	3.25E+2	3.00E+2	2.75E+2	2.50E+2	2.25E+2
2.00E+2	1.80E+2	1.60E+2	1.40E+2	1.20E+2	1.10E+2	1.00E+2	9.00E+1
8.00E+1	7.00E+1	6.50E+1	6.00E+1	5.50E+1	5.00E+1	4.50E+1	4.00E+1
3.50E+1	3.00E+1	2.75E+1	2.50E+1	2.25E+1	2.00E+1		

In dose calculations, it is recommended to use the neutron flux-to-dose equivalent conversion factor given in Table 3 so as to avoid any ambiguity due to the conversion factor used. The values given in Table 3 are conversion factors to the neutron energy corresponding to that given in Table 2.

Table 3. Neutron flux-to-dose conversion factor[(Sv/hr)/(n/sec/cm^2)]
(ICRP51 (1987) [5], 20-400 MeV, Table 23)

2.25E–6	2.20E–6	2.15E–6	2.10E–6	2.05E–6	1.99E–6	1.93E–6	1.86E–6
1.82E–6	1.79E–6	1.77E–6	1.74E–6	1.72E–6	1.70E–6	1.68E–6	1.67E–6
1.65E–6	1.64E–6	1.63E–6	1.62E–6	1.61E–6	1.60E–6	1.59E–6	1.58E–6
1.57E–6	1.56E–6	1.55E–6	1.54E–6	1.53E–6	1.52E–6		

Quantities to be calculated

The following quantities must be calculated for intercomparisons:

(a) dose equivalent due to neutrons above 20 MeV at 50, 100, 150, 200, 250, 300, 350, 400, 450 and 500 cm;

(b) neutron spectrum in n/cm^2/MeV/source neutron at 100, 200, 300, 400 and 500 cm.

Summary of contributors

Four groups sent the results to Hideo Hirayama at KEK before the end of August. Table 4 lists the participants, the name of the computer code used and the name of database used in the computer code.

The "multi-layer" method [6][1] was incorporated into the HETC-3 step calculation.

[1] When the neutron penetration through a thick iron or concrete slab is calculated one-dimensionally, the slab is separated into several one-meter slabs. The source neutrons are generated at the center of the left surface of the 1st one-meter slab, and the neutron penetration is calculated. The energy-angular distribution of the leakage neutrons, protons, and negative pions from the right surface is obtained. The particle penetration through the 2nd one-meter slab is calculated by using a point particle source placed at the center of the left surface, which was obtained from the leakage particle distributions of the previous slab.

Table 4. Summary of contributors

Name of participants and organisation	Name of computer code used for calculations	Name of database used in the computer code
Yoshitomo Uwamino (RIKEN)	HETC-3STEP	Library data in HETC
Yukio Sakamoto (JAERI)	ANISN-JR	HILO86R
Yukio Sakamoto (JAERI)	MCNP-4B	HILO86 and 100XS
Hiroyuki Handa, etc.[2] (Hitachi Engineering Co., Ltd., JAERI and Business Automation, Co., Ltd)	NMTC/JAERI97	Library data in NMTC
Nikolai Mokhov (FNAL)	MARS13(98)	Library data in MARS

Results and discussion

Attenuation of dose equivalents

The attenuations of the dose equivalents inside iron and concrete are given in Figures 2 and 3, respectively. The dose equivalents of neutrons above 20 MeV decrease almost exponentially along with an increase in the thickness for all of the results. Clear differences, however, can be seen in the attenuation length. The differences become larger with a decrease of the source neutron energy.

Although the same differences were also seen in comparisons presented at SATIF-3, the degrees of the differences were smaller than this time. The total dose equivalents were compared at SATIF-3. The large differences in Figures 2 and 3, therefore, are supposed to be the differences in the cross-section data above 20 MeV. This assumption is verified by comparisons of the attenuation of source neutrons shown in Figures 4 and 5. Comparisons between ANISN-JR and MCNP-4B with HILO86 or 100XS in Figure 6 also show the effects of the cross-section data used.

The attenuation of the dose equivalent for secondary neutrons from protons shows a similar tendency with that for mono-energetic neutrons.

Neutron spectrum

Neutron energy spectra at various depths inside iron and concrete for 400 MeV source neutrons are shown in Figures 7 and 8, respectively. The shape of the spectrum varies with the thickness and the portion of source-neutrons decreases with the increase of the thickness. Although general tendencies are similar between each results, clear differences exits at the source-energy region and below 200 MeV.

Figures 9 and 10 show similar comparisons of the neutron energy spectrum of secondary neutrons from 1 GeV protons for iron and concrete, respectively.

---

[2] Nobuo Sasamoto, Hiroshi Nakashima, Yukio Sakamoto (JAERI)
Hiroyuki Handa, Katsumi Hayashi (Hitachi Eng. Co., Ltd.)
Koubun Yamada, Teruo Abe (Business Automation Co., Ltd.)

Figure 2. Attenuation of dose equivalent inside iron

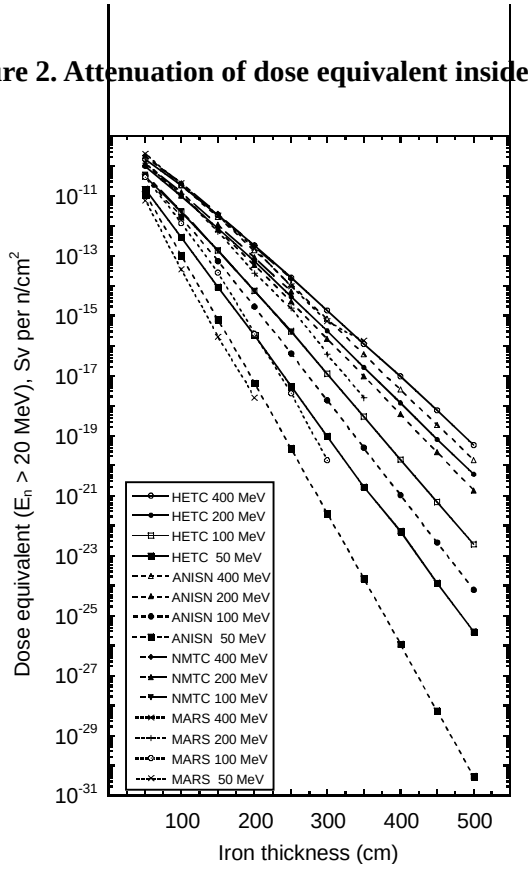

Figure 3. Attenuation of dose equivalent inside concrete

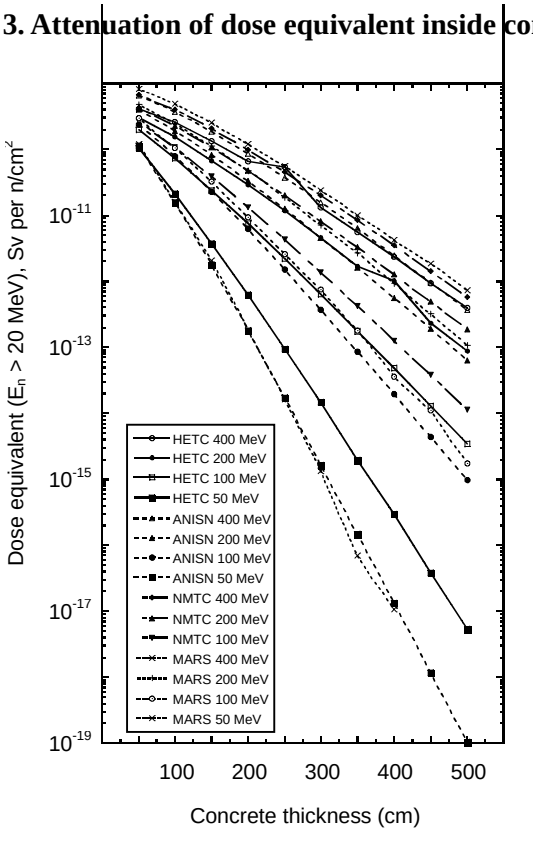

Figure 4. Attenuation of source neutron inside iron

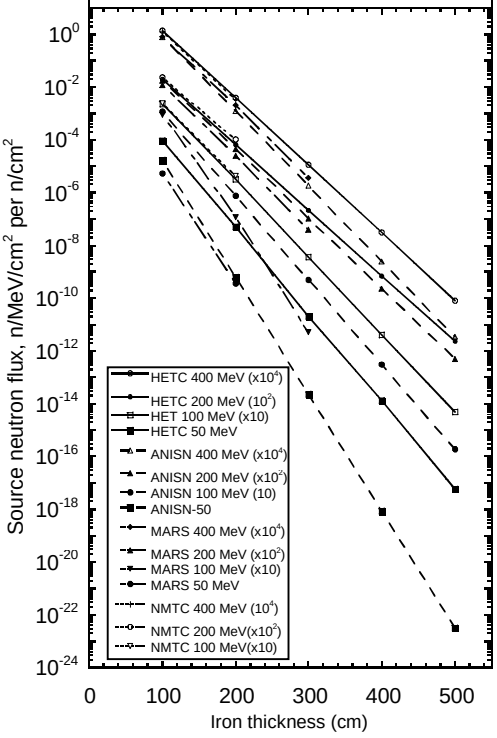

Figure 5. Attenuation of source neutron inside concrete

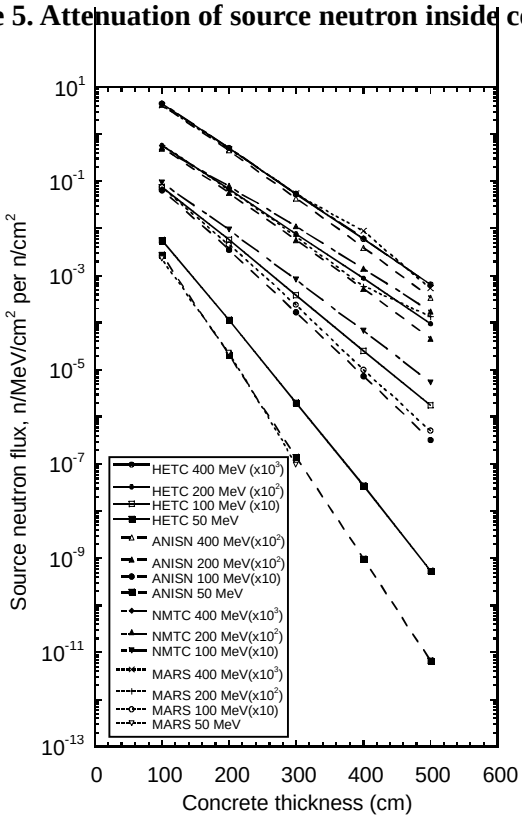

Figure 6. Comparison between ANISN-JR (HILO86R), MCNP-4B (HILO86) and MCNP-4B (100XS)

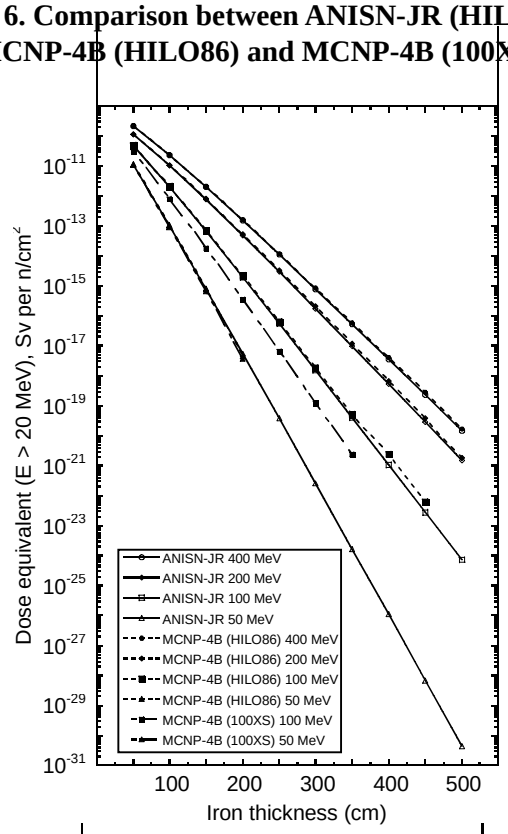

Figure 7. Neutron spectrum inside iron for 400 MeV source neutron

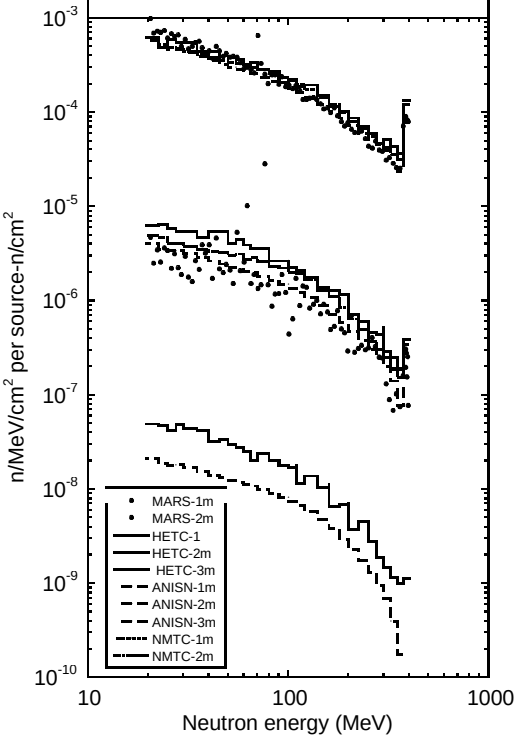

Figure 8. Neutron spectrum inside concrete for 400 MeV source neutron

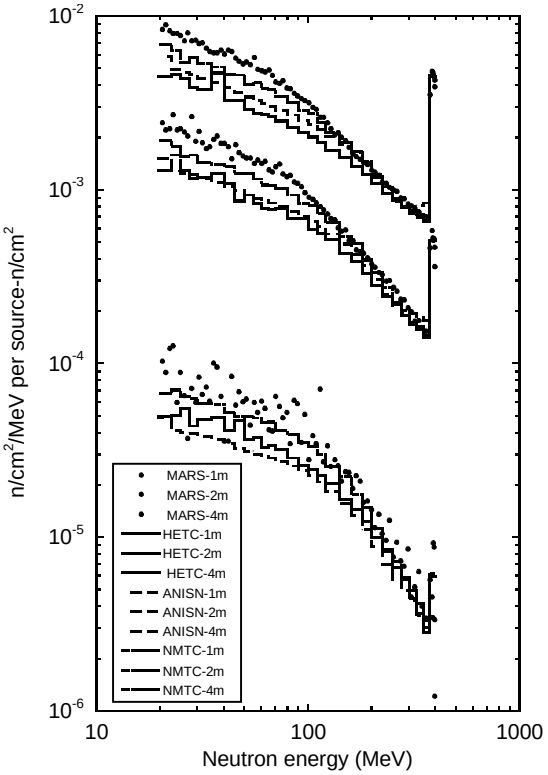

Figure 9. Neutron spectrum inside iron for secondary neutrons from 1 GeV proton

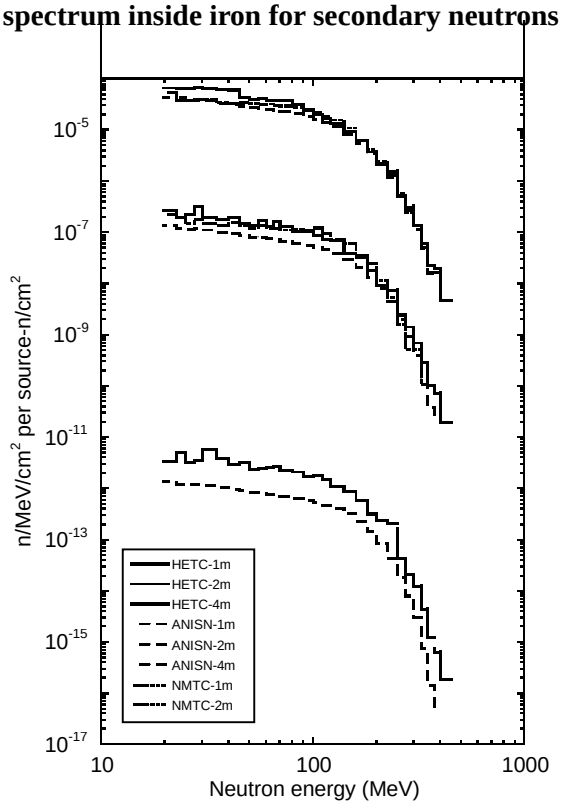

Figure 10. Neutron spectrum inside concrete for secondary neutrons from 1 GeV proton

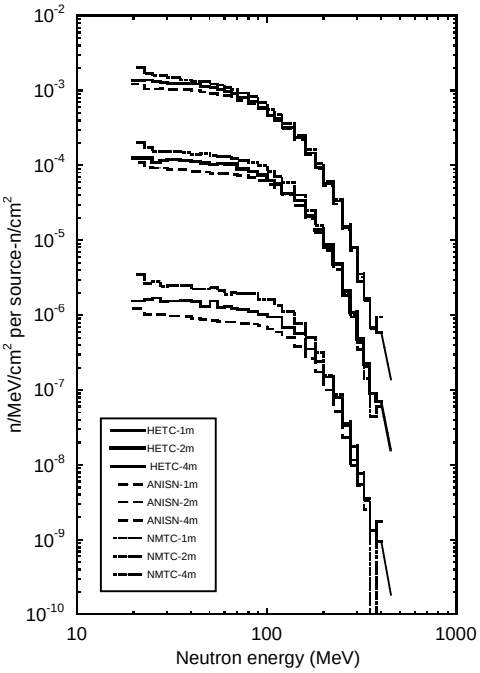

Attenuation length

The attenuation length (λ; g cm^{-2}) for each case was obtained by a least-squares fitting. The thus-obtained attenuation lengths for iron and concrete are shown in Figures 11 and 12, respectively. In the case of secondary neutrons, the average neutron energy above 20 MeV was used for plotting. The same tendency to increase along with an increase in the source neutron energy was presented at SATIF-3, but differences between each result were larger, reflecting the differences in Figures 3 and 4.

Figure 11. Comparison of the attenuation length of iron

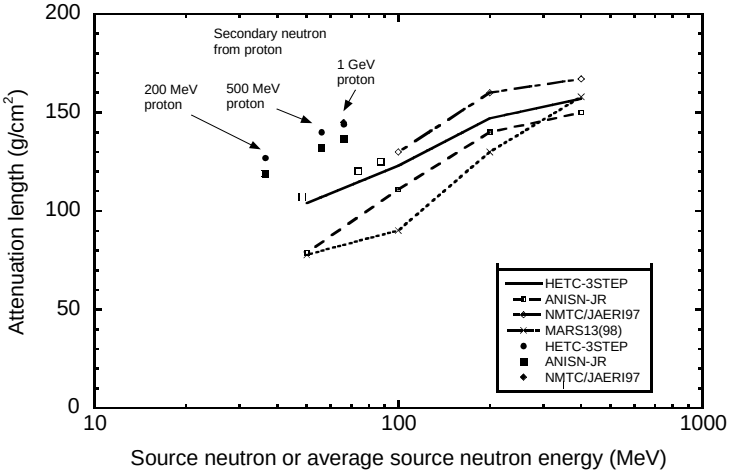

Figure 12. Comparison of the attenuation length of concrete

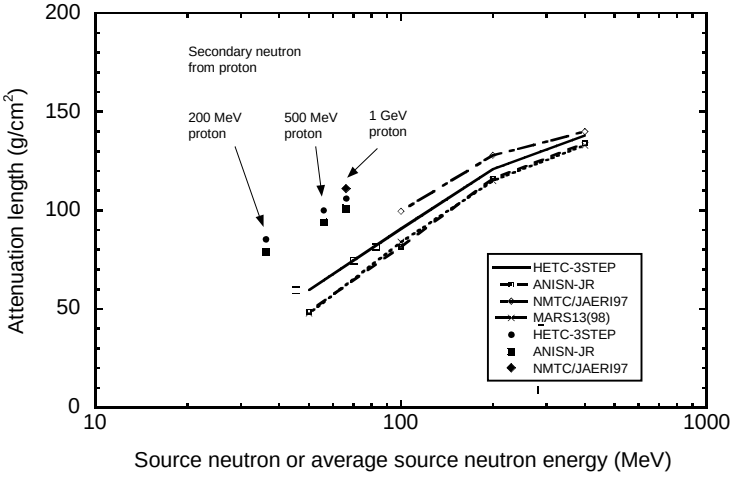

The effective neutron energy, estimated from the attenuation length, for secondary neutrons from protons, is larger than its average energy, and increases slightly along with an increase in the proton energy. It is about 180 MeV and 140 MeV for secondary neutrons from 1 GeV protons for iron and concrete, respectively. These tendencies show the necessity to use the energy-dependent attenuation length in the shielding calculation for secondary neutrons including other particles from protons up to several GeVs.

Future themes

From the comparisons mentioned above, it is necessary to perform the following intercomparisons as the next step:

(a) Comparisons of cross-section data above 20 MeV. The way to make comparisons must be discussed. It is important to compare the elastic and inelastic scattering cross-sections directly, if possible.

(b) Neutron dose equivalent attenuation up to a several GeVs in order to confirm whether the attenuation length reaches to a constant value or not.

(c) Neutron dose equivalent attenuation of secondary neutrons (or particles) from high energy protons up to a several tenth GeVs.

Currently, hadron cascade Monte Carlo codes can only perform calculations for (b) and (c). It is, therefore, desired that other groups will attend this intercomparison using the other Monte Carlo codes.

REFERENCES

[1] H. Hirayama *et al*., "Intercomparison of the Medium-Energy Neutron Attenuation in Iron and Concrete", Proceedings of the Third Specialists Meeting on Shielding Aspects of Accelerators, Targets and Irradiation Facilities, Tohoku University 12-13 May, 1997, pp. 185-195.

[2] H. Nakashima, private communication.

[3] A. Fasso, A. Ferrari, J. Ranft and P.R.Sala, "FLUKA: Present Status and Future Developments", Proc. IV Intl. Conf. On Calorimetry in High Energy Physics, La Biodola (Isolad'Elba), 20-25 Sept. 1993. ed. A. Menzione and A. Scribano, *World Scientific*, p. 493.

[4] A. Fasso, A. Ferrari, J. Ranft and P.R. Sala, "FLUKA: Performances and Applications in the Intermediate Energy Range", Specialists Meeting on Shielding Aspects of Accelerators, Targets and Irradiation Facilities. Arlington, Texas, 28-29 April 1994.

[5] ICRP Publication 51, "Data for Use in Protection Against External Radiation", Annals of the ICRP 17(2/3)}(1987).

[6] Y. Uwamino, N. Fukunishi, T. Kurosawa, S. Furihata, N. Yoshizawa, N. Nakanishi and S. Ito, "Safety Design of RIKEN RI Beam Factory", SARE3, KEK Proc. 97-5, p. 209 (1997).

[7] H.W. Paterson and R.H. Thomas, "Accelerator Health Physics", Academic Press, New York and London 1973.

SESSION V

Miscellaneous Topics

Chairs: B.L. Kirk and M. Silari

Radioactive Ion Beam Facilities

RADIOACTIVE ION BEAM FACILITIES: NEW THICK TARGETS, HIGHLIGHTS AND CHALLENGES

F. Clapier, N. Pauwels, J. Proust
Institut de Physique Nucléaire
91406 Orsay Cedex France

Abstract

Light and heavy ion projectiles are being tested for radioactive ion beam production by both projectile-like fragments impinging on dedicated targets and by fast neutron induced reactions. The beam power density and/or the use of neutrons require new generations of target-source configurations for ion on-line separation for post-acceleration. Programmes are dedicated to exotic beam making by new facilities. Radioactivity and radiation data are becoming available and requirements for further developments for residue and neutron distributions should be considered for the achievement of pertinent simulations.

Comments on experimental data and simulation of exotic nuclei production

Secondary beams obtained through the interaction of 95 MeV/u ^{36}Ar ions with various targets thanks to the use of the LISE spectrometer at GANIL show that the available simulation codes are in disagreement with experimental data by 1 to 4 orders of magnitude for ^{16}O and close to 6 orders when the fairly exotic ^{18}O are considered at a given velocity.

When inverse kinematic reactions are produced with heavy projectiles such as ^{197}Au 0.6 GeV/u on protons at GSI the best simulations can approach experimental data by two fold to ten fold.

Secondary neutrons produced by 100 MeV/u deuterons on Be thick targets were simulated by the LCS (LAHET) code for very large angle intervals but were not able to provide precise predictions. Both LAHET and FLUKA codes still need to be improved by building-in the physics of a deuteron impinging on a thick target.

The residual dose rate from deuterons at 100 MeV/u hitting a thick uranium target has been controlled at LNS (Saclay) and can be fit by one of A.H. Sullivan's formulae. The neutron spectra from thick U, Be thick targets for 100 MeV/u deuterons and ^{36}Ar ions at 95 MeV/u on C thick targets were measured by an activation detectors set-up. The fast neutron component of the spectra can be fit by Serber's pioneer simulation within a factor of two.

For shielding purposes our experimental data have been plotted for the sets of projectile-thick target couples we were able to combine at GANIL and LNS. Deuterons are the most neutron productive projectiles regardless of the mass number of the target.

Other experimental attempts, ^{238}U + ^{208}Pb at 750 MeV/u show that more than 100 new neutron rich exotic isotopes were evidenced and that the maximum yields are found for 8 to 10 neutrons away from the valley of stability and that A/Z = 2.8 ratio appears to be a new limit for exotic nuclei.

Most recently mass and element distribution observed in nuclear fission remaining unexplained for the moment.

Furthermore, through electromagnetic excitation, fission fragments as a function of neutron and proton numbers of the fissioning Ac, Th, Pa and U nuclei are explored but not yet understood.

In summary the use of neutron induced fission as a process to produce residues with high A/Z ratios, or neutron rich nuclei to prepare radioactive beams to explore the limits of nuclei stability (terra incognita) can be tested in parallel of the very fine experiments presented above despite further physics understanding is expected but not yet available.

PARRNE (Production d'Atomes Radioactifs Riches en NEutrons)

Given the short presentation of the background information, PARRNE is intended for R&D efforts to test the main features of the feasibility and optimisation of neutron rich isotope production and on-line separation.

The scenario comprises a several-stage process:

i. a deuteron impinging on a heavy target to produce neutrons and absorb the energy transfer according to the Bragg peak behaviour;

ii. a fission target in which the best use of the forward direction neutrons is explored thanks to the geometry and density of a ^{238}U heated compound;

iii. a fission target and ion source combination compatible with short half-life isotope effusion and transport, separation and post acceleration;

iv. determining the best cost-effective combination of the main parameters for production and minimisation of radiation safety aftermath (neutrons, activation, contamination, radiation resistance of materials, etc...).

This programme is driven by IPN and CSNSM at Orsay and is funded by CNRS/IN2P3.

PARRNE set-ups and outcomes

PARRNE 0 consists in a break-up target followed by an uranium foil.

PARRNE 1 display is made to fit in a neutron production target at different distances from UC_x or molten uranium target, the noble gases produced are transported to a cold finger behind an appropriate shield. These two set-ups can be bombarded at any site where deuterons are available at given energies (16 to 200 MeV).

PARRNE 2 is an target-source ensemble built in a ISOL configuration i.e. an on-line mass separator.

Several figures show the corresponding schemes, productions and fits of experimental data and simulations. A comparison of different tests are plotted for PARRNE 1. Condensable elements such as ^{136}I were evidenced. Additionally neutron spectra produced by deuterons on, Be, C and U targets (converters) are measured for projectile energies ranging from 16 to 200 MeV at different facilities.

Conclusion

During and after tests the activation and radioactive contamination are controlled for radiation protection purpose, the outcomes depending on each isobar considered matching with the neutron-rich species produced.

The R&D programme briefly described here is supported by the European programme SPIRAL 2.

The laboratories joining their efforts are IPN and CSNSM at ORSAY (FR), GANIL (FR), KVI (NL), Louvain-La-Neuve (B), Jyväskylä (FI) and ISOLDE at CERN. Yearly, reports will be issued to describe the optimisation of the production process and the radiation safety data obtained.

REFERENCES

[1] "Nuclear Physics in Europe: Highlights and Opportunities", NuPECC Report, edited by J. Vervier, *et al*., (Munich, FR Germany), 1997, http://www.e12.physik.tu-muenchen.de/nupecc/.

[2] Nuclear Science: A Long-Range Plan, DOE/NSF Nuclear Science Advisory Committee (1996), US Government Printing Office 1996-711-218, and "Scientific Opportunities with an Advanced ISOL Facility", NSAC report (1997), htpp//www.er.doe.gov/production/henp/isolpaper.pdf.

[3] Report of the Japanese Nuclear Science Committee (1998), in preparation.

[4] Report of the Working Group on Nuclear Physics, OECD Megascience Forum (1998), to be published.

[5] H.L. Ravn and B. Allardyce, in Treatise on Heavy Ion Science, Allan Bromley, ed. (Plenum Press, New York, 1989), Vol. 8, p. 363.

[6] C. Engelmann, *et al.*, *Z. Phys.* A 352, 351 (1995).

[7] B. Fogelberg, *et al.*, *Nucl. Ins. Meth*., B 70, 137 (1992).

[8] J.A. Pinston, *et al*. in International Workshop on Research with Fission Fragments, Benediktbeuern, 1996, T. Von Egidy, *et al.*, eds., (World Scientific, Singapore, 1997), p. 22-25.

[9] D. Habs, *et al*., *Nucl. Phys.* A616, 39c-47c (1997).

[10] J.A. Nolen, in Radioactive Nuclear Beams, D.J. Morrissey, ed. (Editions Frontières, Gif-sur-Yvette, 1993), p. 111.

[11] Concept for an Advanced Exotic Beam Facility Based on ATLAS, working paper, Physics Division, Argonne National Laboratory, February, 1995.

[12] J.M. Lagniel, S. Joly, J.L. Lemaire, A.C. Mueller, "The IPHI Project at Saclay", Proc. 1997 Particle Accelerator Conference and International Conference on High-Energy Accelerators, 12-16 May 1997, Vancouver, BC, Canada, in press.

[13] M. Lefort, La chimie nucléaire (Dunod, Paris, 1976).

[14] F. Clapier, *et al.*, Exotic Beams Produced by Fast Neutrons, *Phys. Rev*. Spec. Topics-AB, Vol. 1, 1998.

[15] J. Lettry, *et al.*, *Nucl. Ins. Meth*., B126, 130 (1997).

[16] S. Kandri-Rody, *et al*., submitted to *Nucl. Ins. Meth*.

[17] A.H.M. Evensen, *et al.*, *Nucl. Ins. Meth*., B126, 160 (1997).

[18] M. Mirea and F. Clapier, Fine Structure in Superasymmetric Fission, *Europhysics Letters* (Nov. 97).

[19] M. Mirea, *et al*., Kr and Xe Neutron-Rich Nuclei Production Through ^{238}U Fission, IL NUOVO CIMENTO, Vol. 11 A, N.3, March 1998.

[20] S. Ménard, *et al.*, Fast Neutron Forward Distributions from C, Be and U Thick Targets Bombarded by Deuterons, IPNO 98-12, to be published in *Phys. Rev*. Spec. Topics-AB.

[21] N. Pauwels, *et al.*, Neutrons produits dans des cibles épaisses de Be et ^{238}U par des deutons de 100 MeV/A et de C par des ^{36}Ar de 95 MeV/A: Débit de dose résultant de l'activation de l'uranium, IPNO 98-04, submitted to *Radioprotection*.

[22] O. Bajeat, M. Mirea et F. Clapier, Géométrie convertisseurs-cibles de fission: Calculs de l'épaisseur équivalente des cibles, IPNO 98-03.

[23] R. Antoni, Mesures physiques et radioprotection, autour du projet PARRNE, Rapport de stage D.E.S.S. de Radioprotection, Université Joseph FOURRIER-Grenoble, (1998).

Figure 1

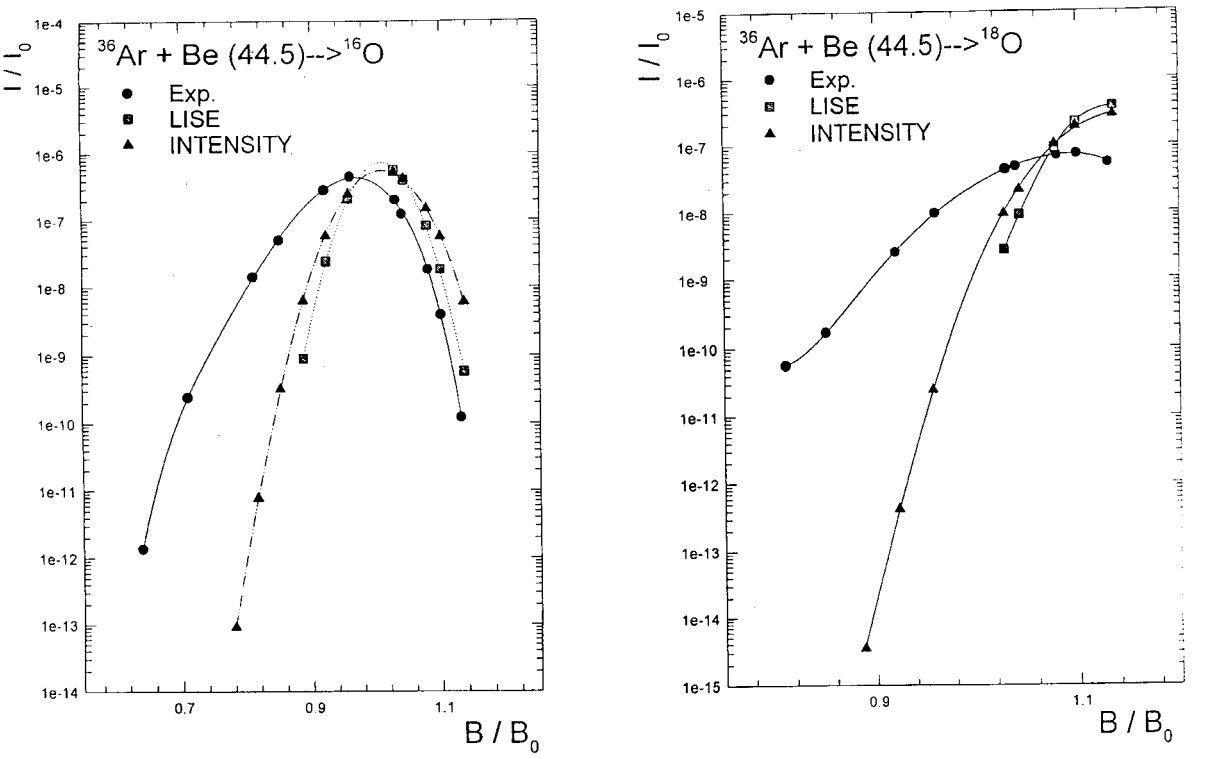

Figure 2

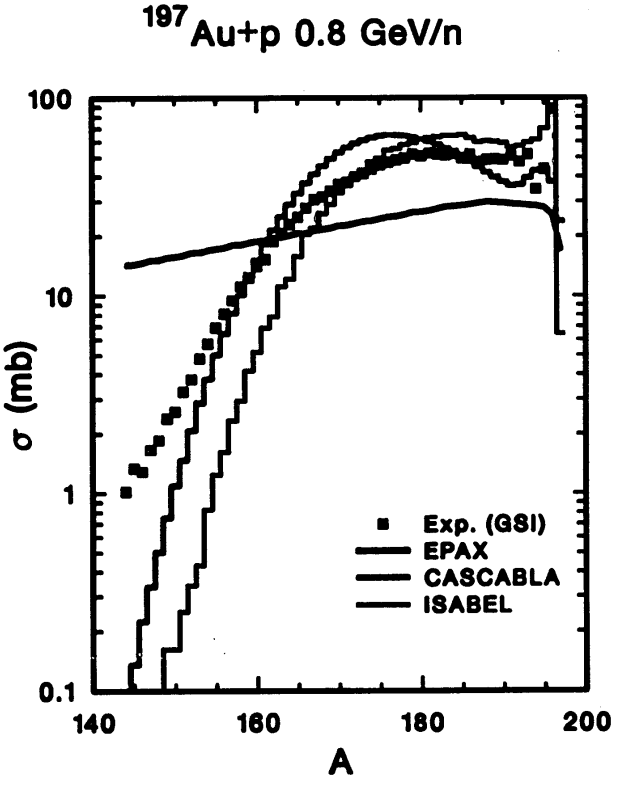

Figure 3. Angle integrated spectra (dσ/dE) of the neutrons emitted from a primary beryllium target bombarded with 200 MeV deuterons

The dashed line represents the differential cross-section integrated from 0 to 25 degrees.
The dotted line represents the differential cross-section integrated from 25 to 60 degrees.
The dot-dashed line represents the differential cross-section integrated from 60 to 90 degrees.
The simulation was performed with the LCS.

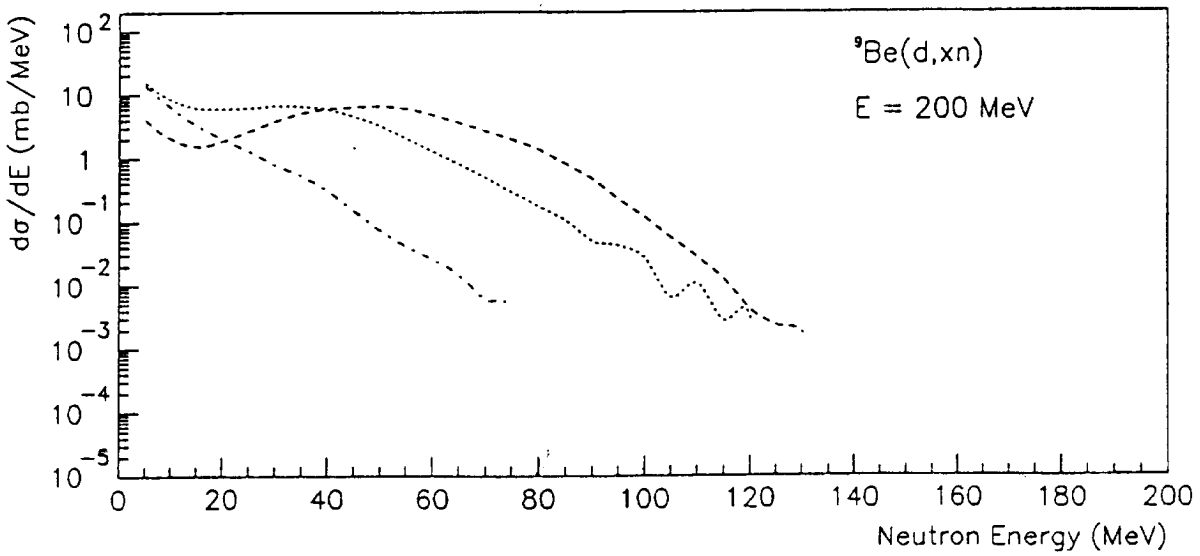

Figure 4. Energy integrated differential cross-section of the neutrons emitted from a primary beryllium target bombarded with 200 MeV deuterons

The simulation was performed with the LCS.

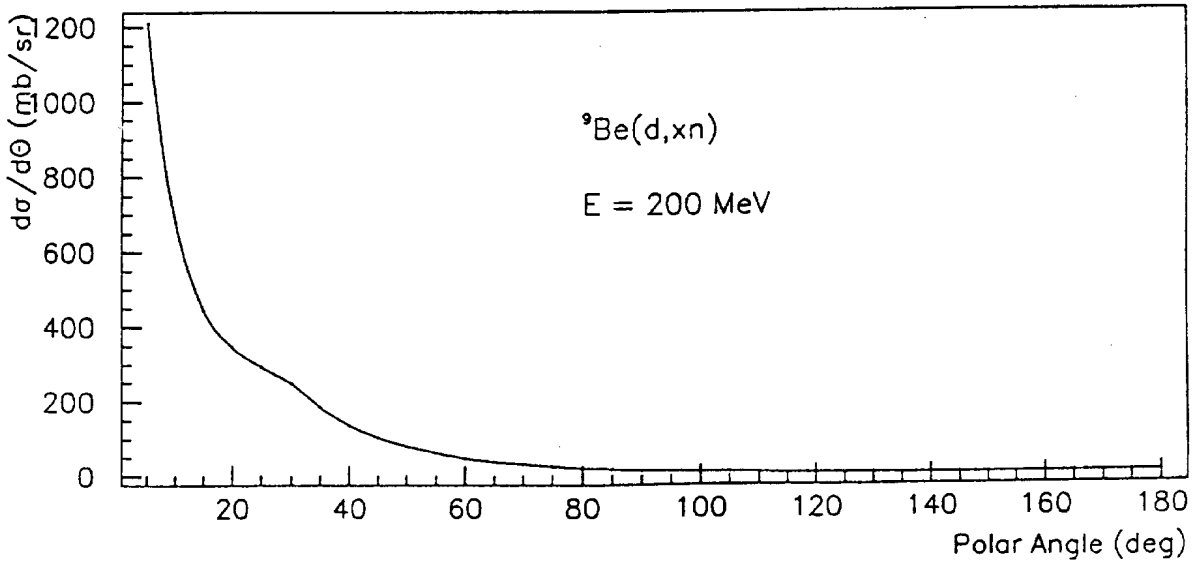

Figure 5

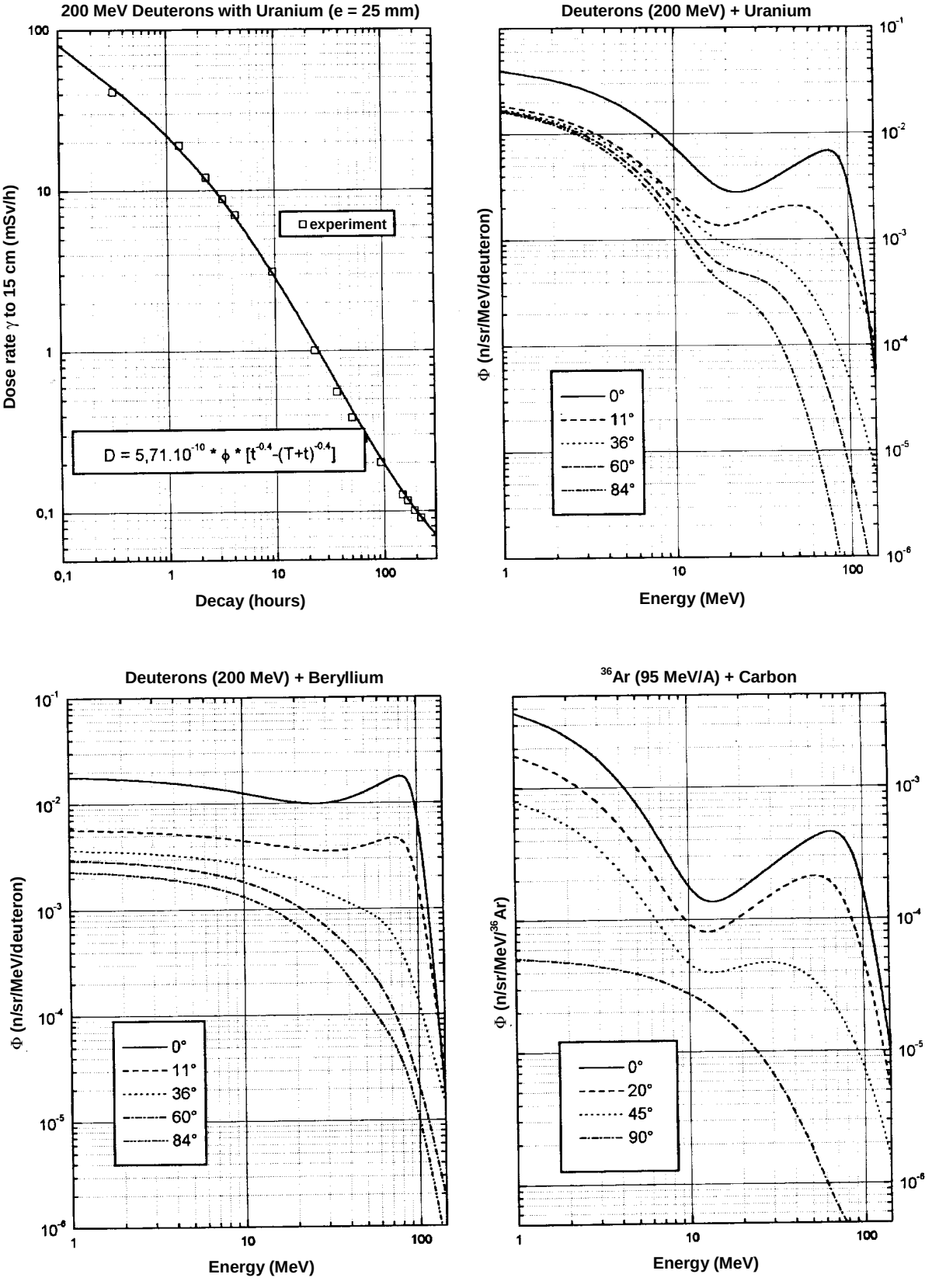
200 MeV Deuterons with Uranium (e = 25 mm)
Dose rate γ to 15 cm (mSv/h)
Decay (hours)
experiment
D = 5,71.10^-10 * ϕ * [t^-0.4 -(T+t)^-0.4]
Deuterons (200 MeV) + Uranium
Φ (n/sr/MeV/deuteron)
Energy (MeV)
0°
11°
36°
60°
84°
Deuterons (200 MeV) + Beryllium
Φ (n/sr/MeV/deuteron)
Energy (MeV)
0°
11°
36°
60°
84°
36Ar (95 MeV/A) + Carbon
Φ (n/sr/MeV/36Ar)
Energy (MeV)
0°
20°
45°
90°

Figure 6

Solid line: experimental result, dotted line: simulation based on Serber's model

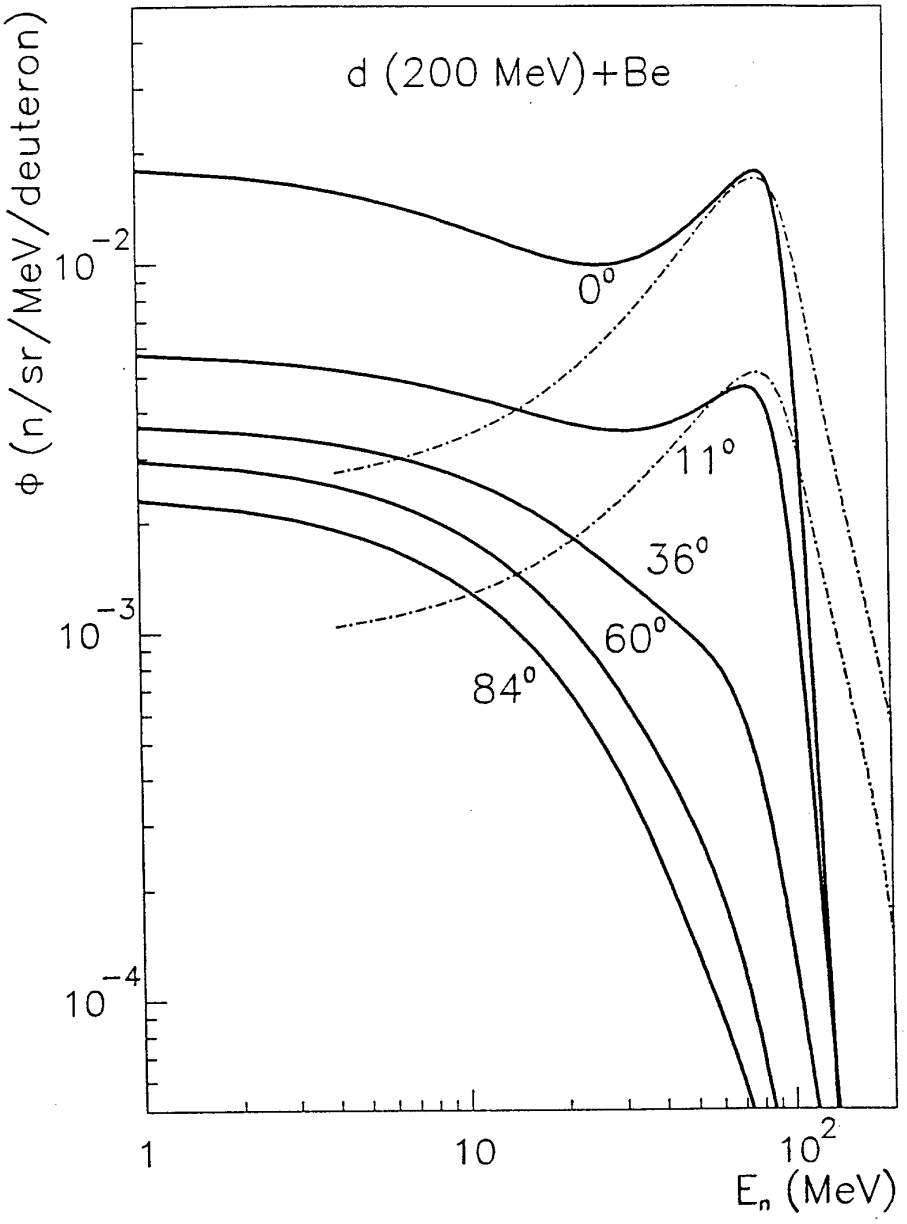

Figure 7. Projectile + thick target → neutrons

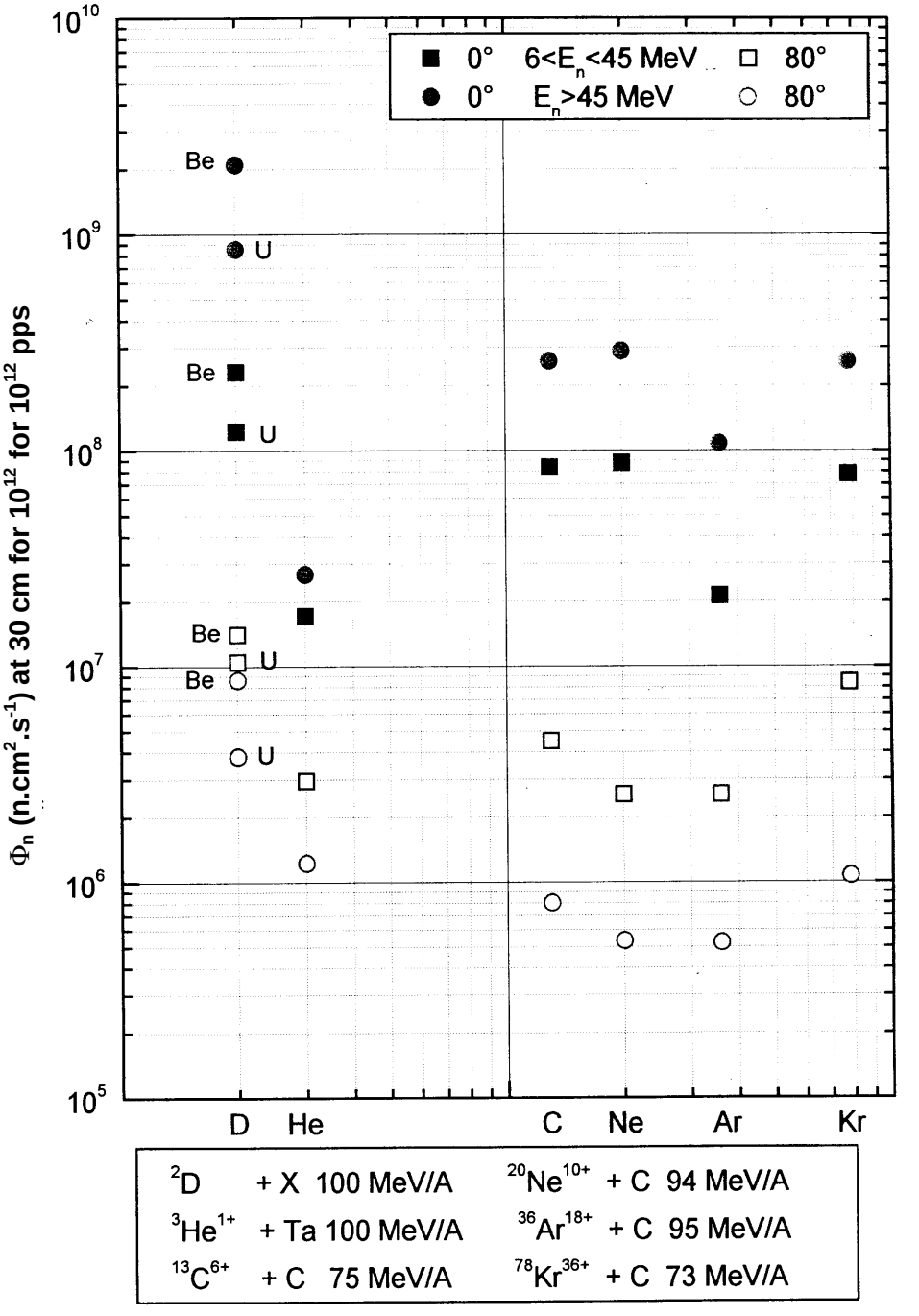

Figure 8. 750 MeV/amv. $^{238}U + ^{208}Pb$ (M. Bernas, *et al.*)

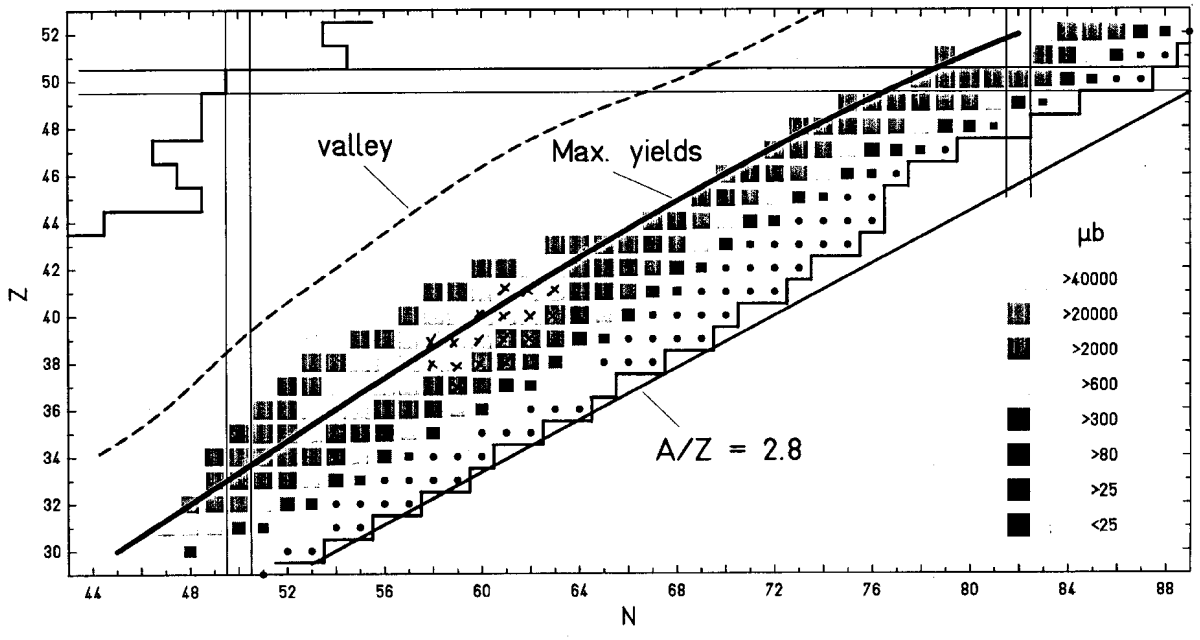

Figure 9. Mass and element distribution observed in nuclear fission

Overview of mass and element distributions for low energy fission. Circles represent nuclei whose mass distributions were previously measured at excitation energies less than 10 MeV above the fission barrier. Exemplary mass distributions are given for several nuclei. Crosses mark nuclei investigated in recent fission studies with the help of secondary beams from the GSI fragment separator.

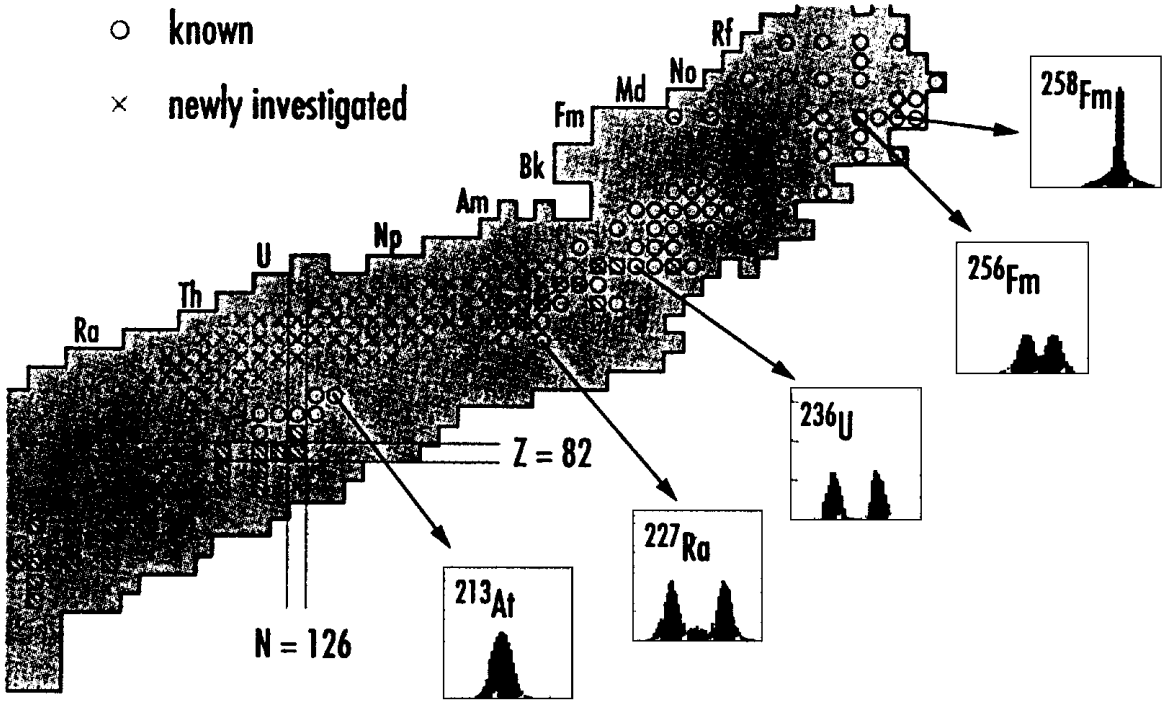

Figure 10. Distribution of fragments

Element distributions of fission fragments after electromagnetic excitation of secondary projectiles, shown as a function of the neutron and proton numbers of the fissioning nuclei

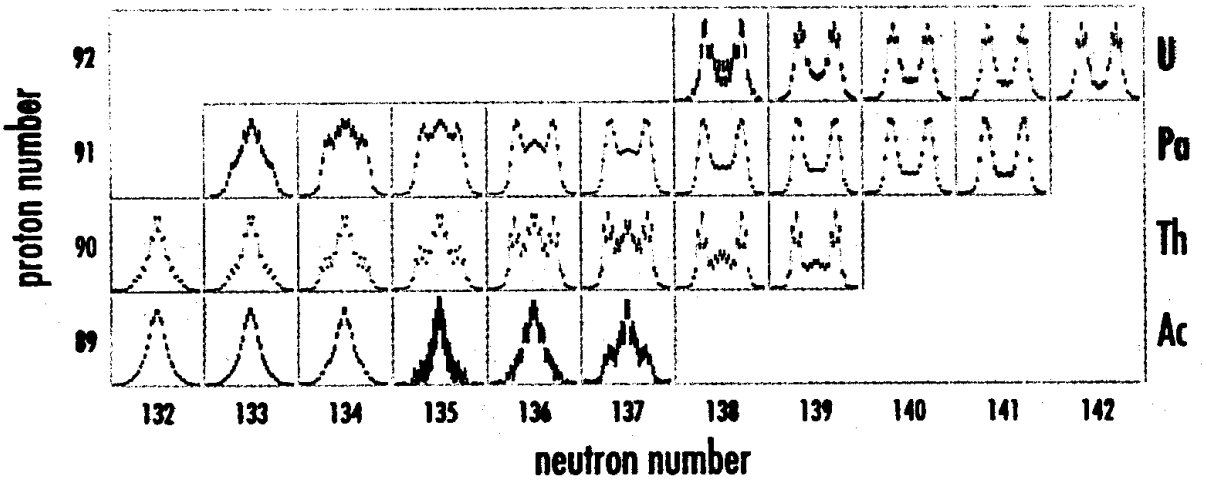

Figure 11. Nuclear landscape

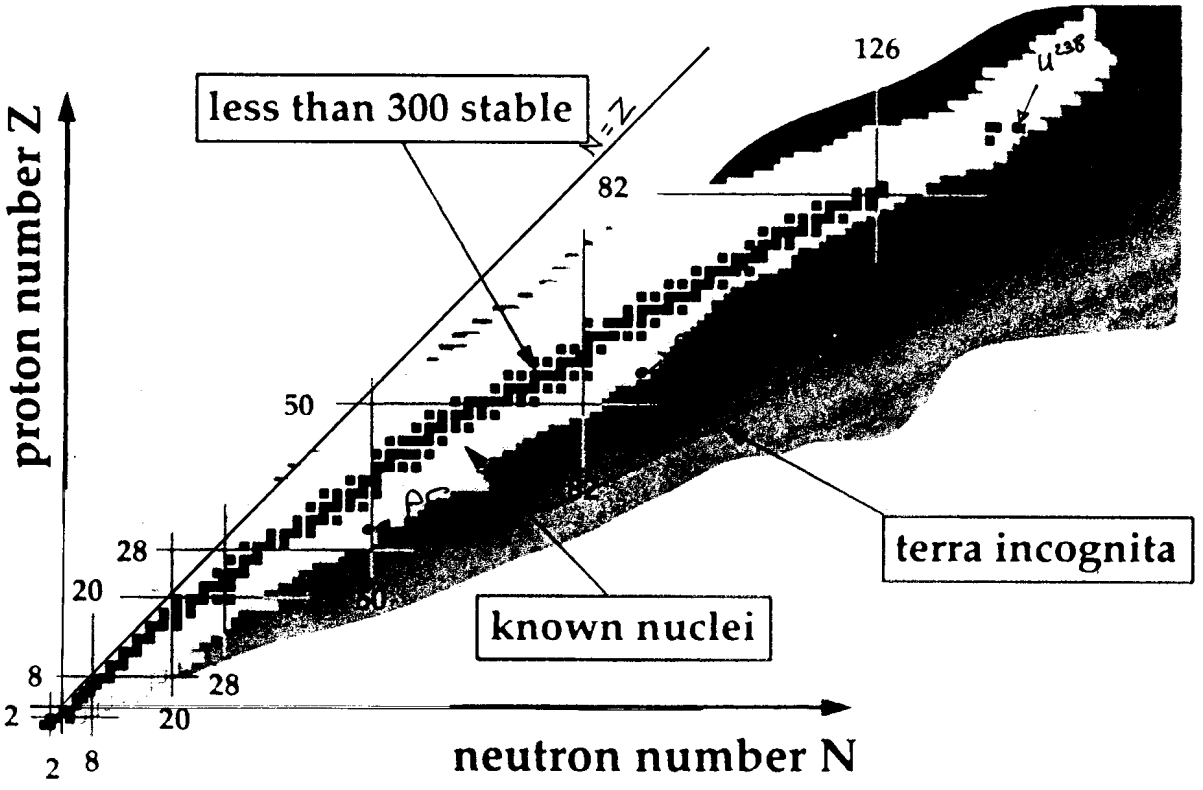

Figure 12

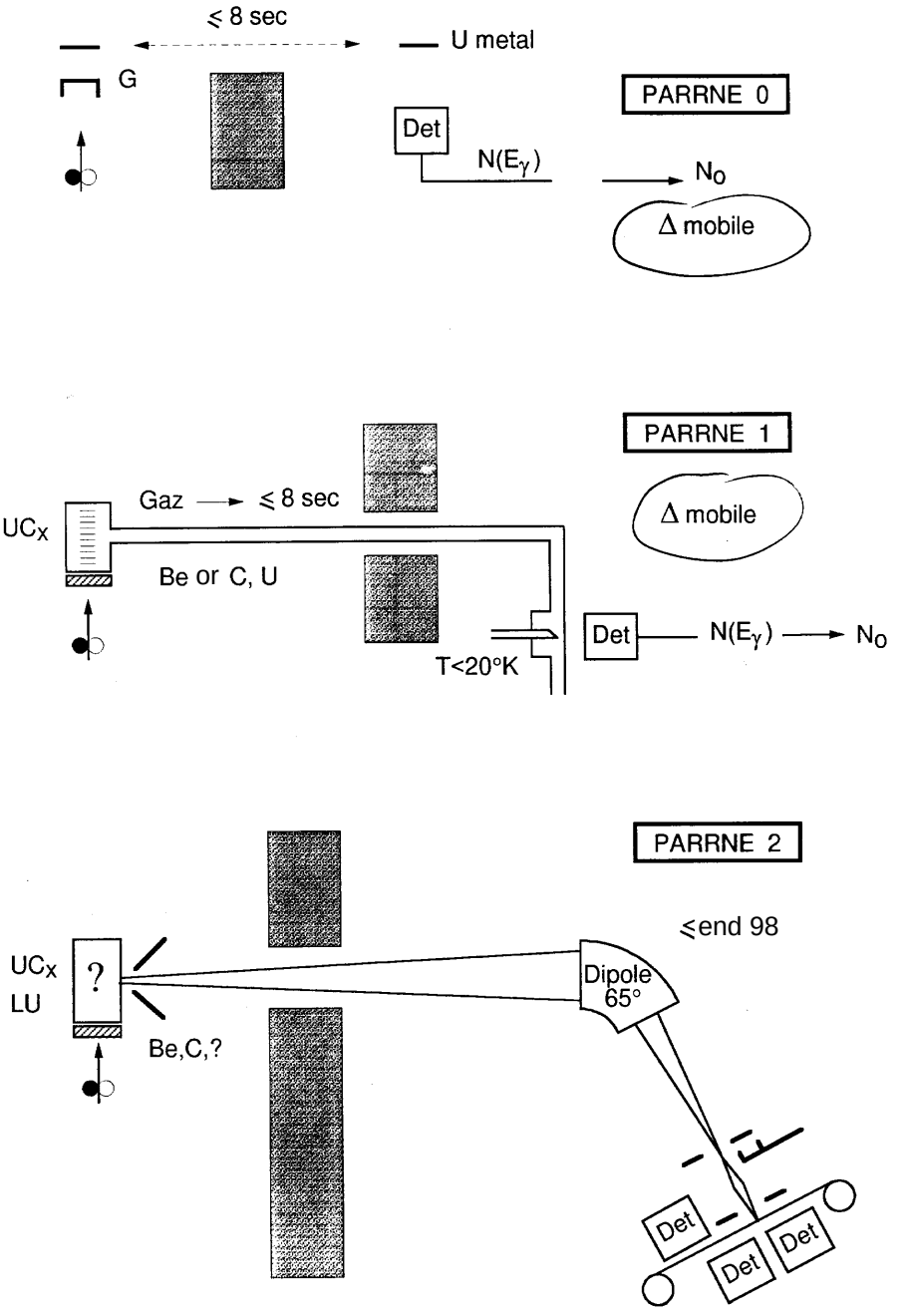
≲ 8 sec
U metal
G
PARRNE 0
Det
N(Eγ)
No
Δ mobile
PARRNE 1
Δ mobile
Gaz
≲ 8 sec
UCx
Be or C, U
Det
N(Eγ)
No
T<20°K
PARRNE 2
≲end 98
UCx
LU
?
Be,C,?
Dipole
65°
Det
Det
Det

Figure 13. PARRNE (Production d'Atomes Radioactifs Riches en NEutrons)

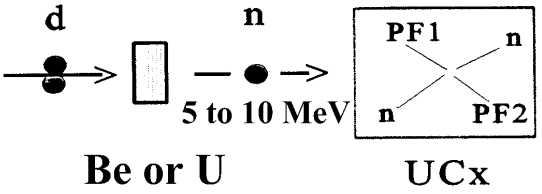

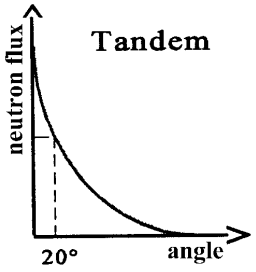

PRODUCTION RUNS

Phase 1: GARRNE
GAz Rares Riches en NEutrons
(Neutron rich rare gases)
Set-up in progress

Phase 2: PARRNE
Other elements with mass separation on-line

Phase 3: PARRNE
Optimise the target

OPTIONS Ed = 100 MeV/A * i pps
Ed < 100 MeV/A * I pps

R & D: Target source system, performances

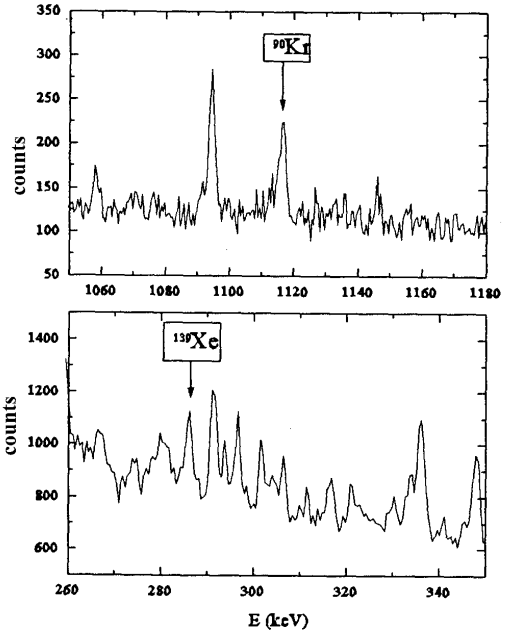

Deuterons from 20 MeV: 100 nA x 120 seconds

REA	T	N_0(*10^6)	Δn
^{89}Kr	3.07 min	4.14	3
^{90}Kr	32.32 s	1.6	4
^{91}Kr	8.6 s	PARRNE1	5
^{92}Kr	1.84 s	PARRNE1	6
^{132}Sn	40 s	0.46	8
^{133}Sb	2.3 min	3	10
^{136a}I	1.38 min	2.28	9
^{136b}I	46 s	0.76	9
^{137}Xe	3.83 min	6.58	1
^{138}Xe	14.1 min	PARRNE1	2
^{139}Xe	39.5 s	1.45	3
^{140}Xe	13.6 s	PARRNE1	4

Figure 14. PARRNE (Production d'Atomes Radioactifs Riches en NEutrons)

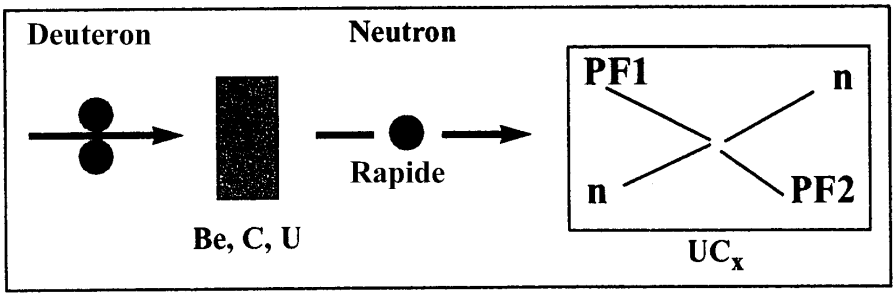

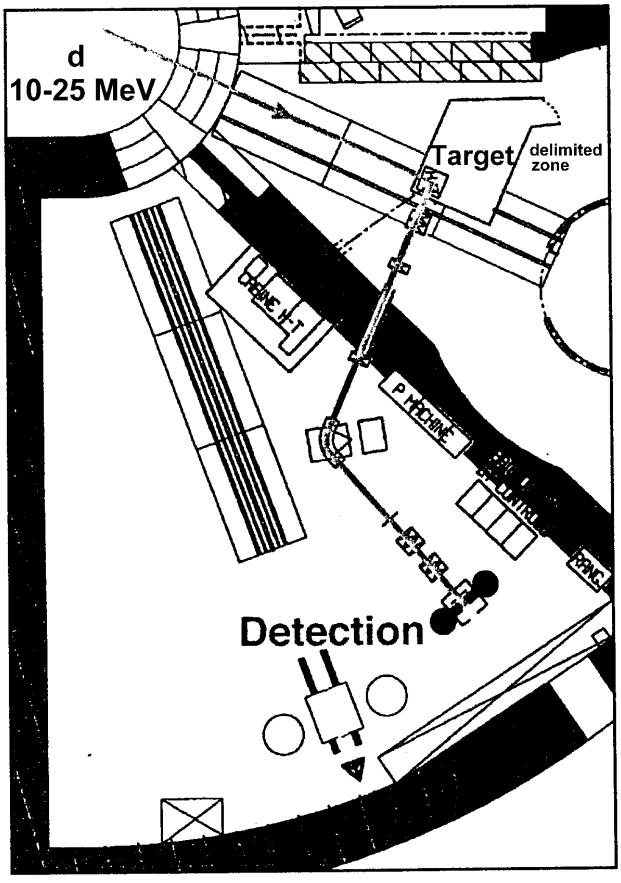

TANDEM installation at Orsay

Generated nuclei
PARRNE 0

REA	T	R (10^3/μg)	Δn
^{89}Kr	3.07 min	30	3
^{90}Kr	32.32 s	25	4
^{132}Sn	40 s	6.2	8
^{133}Sb	2.3 min	23	10
^{136a}I	1.38 min	20.8	9
^{136b}I	46 s	9.7	9
^{137}Xe	3.83 min	45.2	1
^{139}Xe	39.5 s	20.1	3

PARRNE 1

REA	T	Yield (10^4/μC)	Δn
^{90}Kr	32.3 s	20	4
^{91}Kr	8.6 s	4	5
^{92}Kr	1.8 s	1	6
^{139}Xe	39.7 s	20	3

Figure 15. Simulation of neutron-rich nuclei production through ^{239}U fission at intermediate energies

Filled squares: the experimental yields obtained for $^{90-92}$Kr and ^{139}Xe; empty squares: the theoretical values of $^{87-95}$Kr and $^{133-146}$Xe normalised to the ^{91}Kr experimental value; empty circles: theoretical values belonging to $^{90-92}$Br and $^{139-142}$I; stars: hypothetical values for ^{147,148}Xe; E = 10 MeV.*

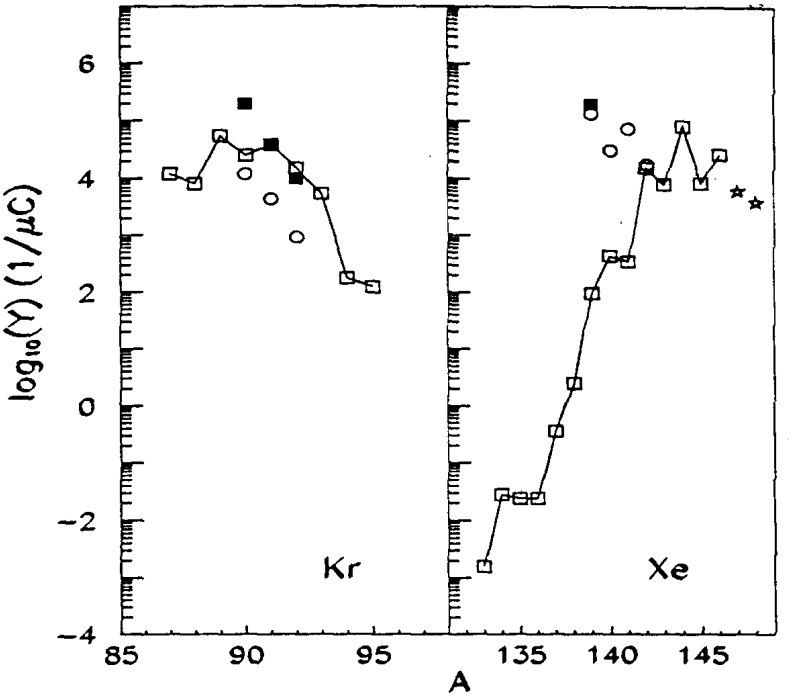

Figure 16. Comparison between experimental and theoretical values obtained after the evaporation of one nucleon

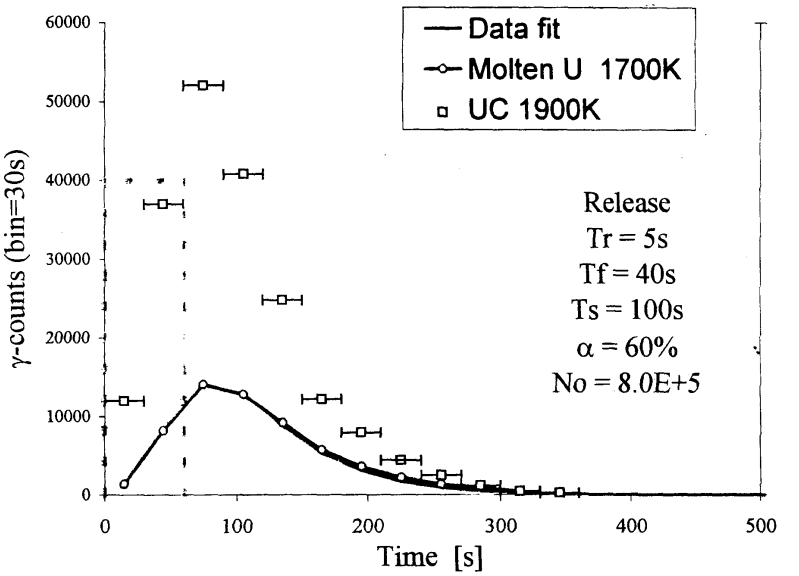

Figure 17. UC vs. molten U target; krypton release and transport

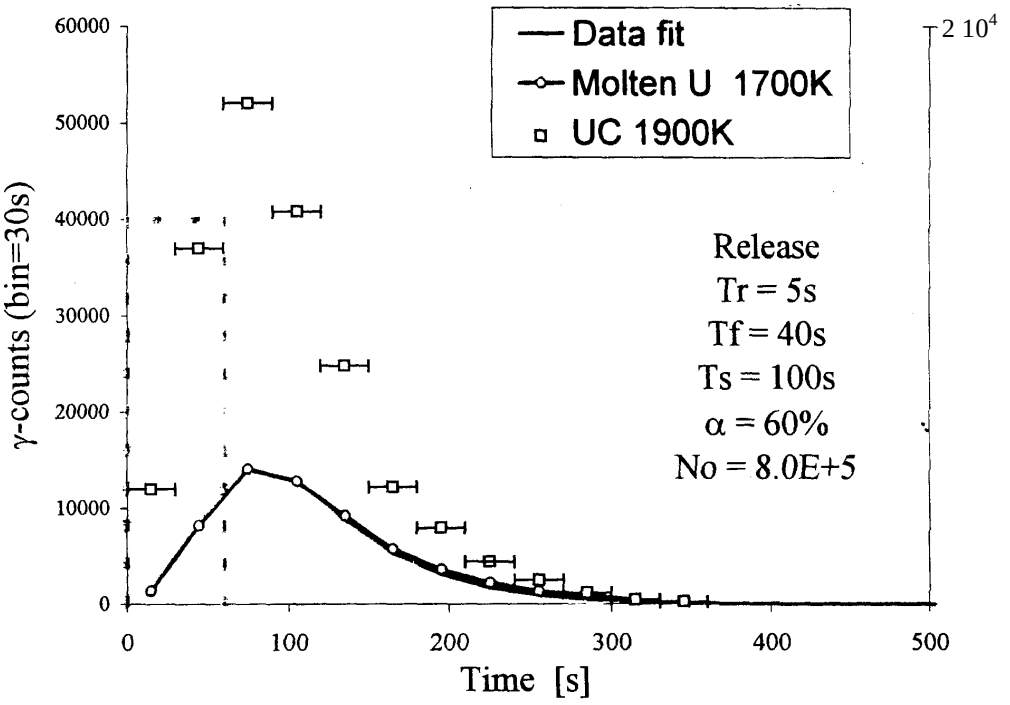

Figure 18. UC vs. molten U target; xenon release and transport

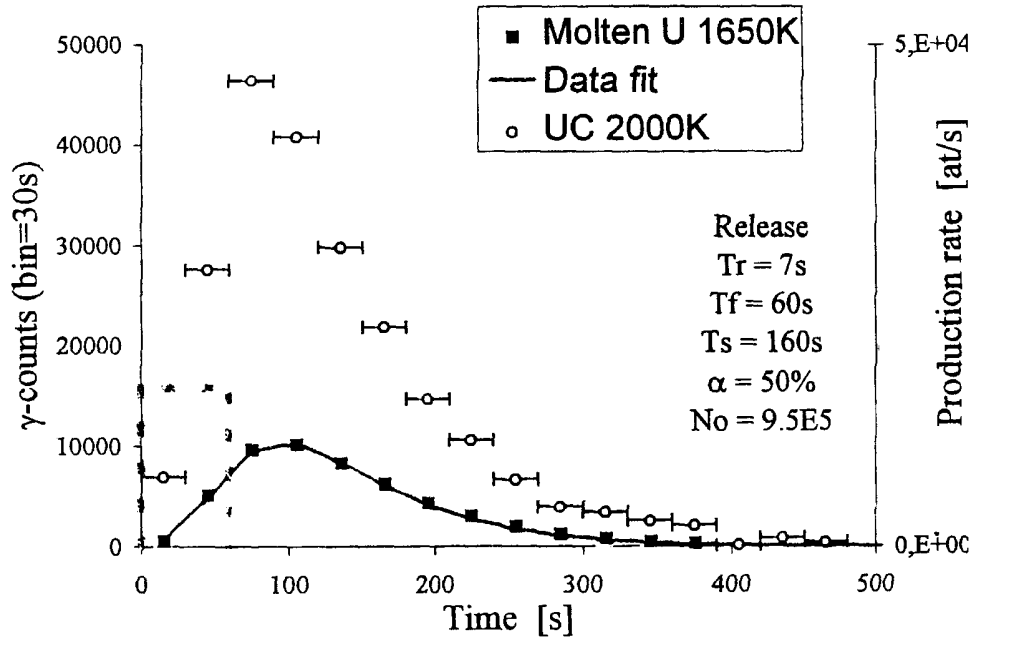

Figure 19. Preliminary noble gases production comparison

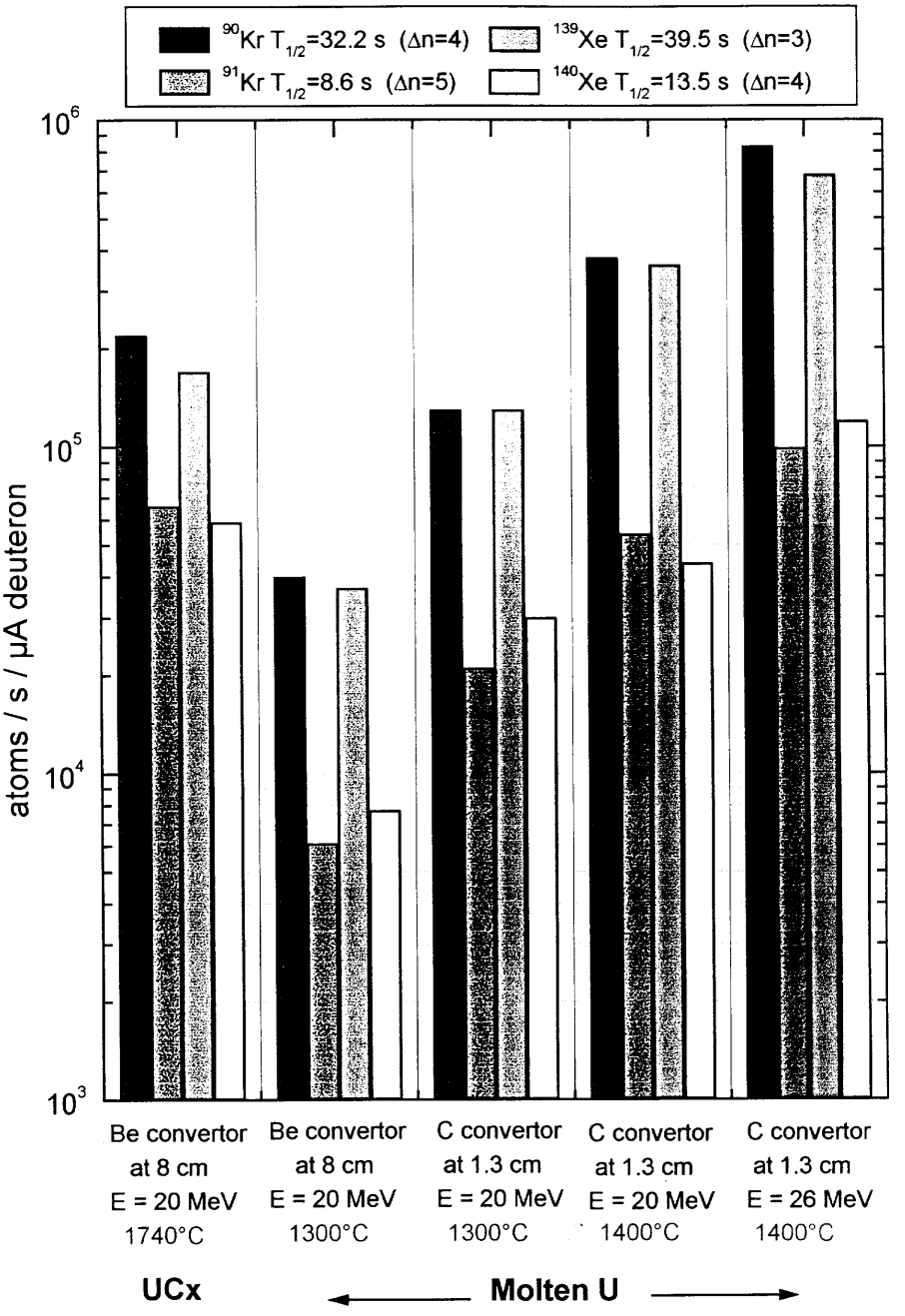

Dose Conversion Coefficient

RADIATION WEIGHTING FACTORS AND CONVERSION COEFFICIENTS FOR HIGH-ENERGY RADIATION

M. Pelliccioni
INFN, 00044 Frascati, Italy

Abstract

In accordance with the list of actions decided at the SATIF-3 meeting, fluence-to-effective dose conversion coefficients for charged pions and kaons have been computed. Calculations have been carried out using the FLUKA Monte Carlo transport code, for various geometrical conditions of irradiation of an anthropomorphic computational model. The calculated results are given for twelve incident energies from 1 MeV to 10 TeV.

In order to assign appropriate values to the radiation weighting factors in the high-energy region, several criteria have been analysed. Modifications of the recommended values are proposed for high-energy neutrons and protons and for charged pions.

Introduction

As is well known, the radiation protection system recommended in ICRP Publication 60 [1] is based on limits expressed in terms of equivalent dose and effective dose. The effective dose, E, is the sum of the weighted equivalent doses, H_T, in the tissues and organs of the body:

$$E = \sum_T w_T \cdot H_T \tag{1}$$

where w_T is the weighting factor for tissue T.

The equivalent dose, H_T, is the absorbed dose in one organ or tissue multiplied by the relevant radiation weighting factor, w_R:

$$H_T = \sum_R w_R \cdot D_{T,R} \tag{2}$$

where $D_{T,R}$ is the absorbed dose averaged over the tissue or organ T due to radiation R.

Table 1 gives the values of the radiation weighting factors used for radiological protection purposes as now recommended by ICRP.

Table 1. Values for radiation weighting factors recommended in ICRP Publication 60

Radiation	w_R
Photons	1
Electrons and muons	1
Neutron energy	
< 10 keV	5
10 keV - 100 keV	10
100 keV - 2 MeV	20
2 MeV - 20 MeV	10
> 20 MeV	5
Protons, other than recoils protons, energy > 2 MeV	5
Alpha particles, fission fragments, heavy nuclei	20

For radiation types and energy that are not included in Table 1, the ICRP stated in Paragraph (A14) of ICRP Publication 60 that an approximation of w_R can be obtained by calculation of $\overline{Q}$ at a depth of 10 mm in the ICRU sphere:

$$\overline{Q} = \frac{1}{D_L} \int Q(L) D(L) dL \tag{3}$$

where D(L)dL is the absorbed dose at 10 mm between linear energy transfer L and L+dL and Q(L) the corresponding quality factor.

Conversion coefficients from particle fluence to effective dose for high-energy radiation, calculated by the FLUKA Monte Carlo transport code, have been presented at the SATIF-3 meeting for photons, electrons, positrons, protons, neutrons and muons [2]. In accordance with the list of actions decided at the meeting, conversion coefficients for charged pions and kaons have been computed and the calculated results are made available in the present paper.

In addition, since the values recommended by ICRP for high-energy radiation are inconsistent with the Q-L relationship and the application in the high-energy region of the rule in Paragraph (A14) of the ICRP Publication 60 is quite questionable, more appropriate criteria for the determination of the w_R values have been investigated.

Therefore the present paper has two main objectives. First, the presentation of the calculated results of the conversion coefficients fluence-to-effective dose for charged pions. Second, a proposal for a revision of the radiation weighting factors is formulated.

Conversion coefficients for charged pions

The calculations of the conversion coefficients have been performed for monoenergetic negatively and positively charged pions and kaons of energy between 1 MeV and 10 TeV, incident on an anthropomorphic computational model in various geometrical conditions of irradiation. The latest version of the FLUKA code has been used [3]. The model was hermaphrodite and included the gonads and breasts of both sexes. Parallel beams and a fully isotropic radiation incidence have been considered. The directions of incidence of the parallel beams were anterior-posterior (AP), posterior-anterior (PA) and right lateral (LAT). The isotropic irradiation (ISO) has been obtained by the use of an inward-directed, biased cosine source on a spherical surface. The medium surrounding the phantom was assumed to be vacuum. The details of the calculations are described in a paper dedicated to pion dosimetry [4].

As pions and kaons are not included in Table 1, in accordance with the statement of Paragraph (A14) of ICRP Publication 60, an approximation of their radiation weighting factors has been obtained by calculation of effective quality factors has been obtained by calculation of effective quality factor at 10 mm depth in the ICRU sphere [5]. Figures 1 and 2 show the obtained values as a function of incident particle energy, for both charged pions and kaons, respectively.

Tables 2, 3, 4 and 5 summarise the calculated conversion coefficients fluence to effective dose for the particles here considered. In the case of kaons, only two geometries irradiation (AP and ISO) have been considered. A graphical presentation of the calculated results is displayed in Figures 3, 4, 5 and 6. In the figures, the conversion coefficients are plotted as a function of incident pion or kaon energy for the various geometrical conditions of irradiation investigated. A discussion of the obtained results for pions can be found in Ref. [4].

No other calculations of effective dose for pions and kaons are known to the author. Therefore comparisons are restricted to the operational quantity ambient dose equivalent. Values of ambient dose equivalent for pions are shown in Figures 3 and 4, according to the results of calculations described in Ref. [5]. On the basis of a comparison with the calculated values of the effective doses, the ambient dose equivalent appears a conservative predictor of the limiting quantity only at 1 and 10 MeV. This fact could be partially explained by the low values attributed to the pion radiation weighting factors at these energies, on the basis of the effective quality factor at the depth of 10 mm.

Table 2. Calculated effective quality factors at 10 mm depth in the ICRU sphere and conversion coefficients fluence to ambient dose equivalent and fluence to effective dose equivalent, as a function of the incident negative pion energy

Energy (GeV)	Q at 10 mm	H*(10) ($Sv \cdot cm^2$)	E (AP) ($Sv \cdot cm^2$)	E (PA) ($Sv \cdot cm^2$)	E (LAT) ($Sv \cdot cm^2$)	E (ISO) ($Sv \cdot cm^2$)
1.0E-03	3.7	1.13E-09	3.49E-10	2.04E-10	1.13E-10	2.93E-10
1.0E-02	2.9	1.81E-09	7.21E-10	2.70E-10	2.25E-10	3.56E-10
5.0E-02	1.6	9.75E-10	1.88E-09	1.61E-09	7.28E-10	7.71E-10
1.0E-01	1.9	8.97E-10	9.53E-10	9.98E-10	1.14E-09	9.51E-10
2.0E-01	2.3	1.08E-09	1.08E-09	1.05E-09	9.44E-10	9.49E-10
5.0E-01	1.9	7.12E-10	8.29E-10	8.35E-10	7.79E-10	7.98E-10
1.0E+00	1.8	7.34E-10	8.95E-10	9.18E-10	8.95E-10	9.00E-10
5.0E+00	1.8	7.43E-10	1.11E-09	1.19E-09	1.19E-09	1.25E-09
1.0E+01	1.8	7.40E-10	1.10E-09	1.27E-09	1.41E-09	1.38E-09
1.0E+02	1.7	7.13E-10	1.43E-09	1.54E-09	2.15E-09	2.15E-09
1.0E+03	1.7	7.88E-10	2.19E-09	2.68E-09	4.22E-09	4.18E-09
1.0E+04	1.8	9.53E-10	3.70E-09	4.63E-09	7.93E-09	9.63E-09

Table 3. Calculated effective quality factors at 10 mm depth in the ICRU sphere and conversion coefficients fluence to ambient dose equivalent and fluence to effective dose equivalent, as a function of the incident positive pion energy

Energy (GeV)	Q at 10 mm	H*(10) ($Sv \cdot cm^2$)	E (AP) ($Sv \cdot cm^2$)	E (PA) ($Sv \cdot cm^2$)	E (LAT) ($Sv \cdot cm^2$)	E (ISO) ($Sv \cdot cm^2$)
1.0E-03	1.0	2.24E-10	7.13E-11	3.75E-11	1.97E-11	6.58E-11
1.0E-02	1.0	5.28E-10	2.48E-10	1.05E-10	7.05E-11	1.16E-10
5.0E-02	1.2	8.19E-10	1.30E-09	1.00E-09	5.34E-10	5.79E-10
1.0E-01	1.7	9.79E-10	9.83E-10	9.42E-10	1.05E-09	8.85E-10
2.0E-01	1.9	1.08E-09	1.29E-09	1.28E-09	1.07E-09	1.11E-09
5.0E-01	1.9	7.74E-10	9.18E-10	9.24E-10	8.86E-10	8.75E-10
1.0E+00	1.8	7.80E-10	9.80E-10	1.03E-09	9.17E-10	9.65E-10
5.0E+00	1.8	7.50E-10	1.14E-09	1.20E-09	1.24E-09	1.24E-09
1.0E+01	1.8	7.56E-10	1.11E-09	1.28E-09	1.58E-09	1.43E-09
1.0E+02	1.7	7.12E-10	1.29E-09	1.63E-09	2.06E-09	2.17E-09
1.0E+03	1.6	7.76E-10	2.04E-09	2.60E-09	3.92E-09	4.23E-09
1.0E+04	1.6	8.38E-10	3.15E-09	4.12E-09	7.01E-09	7.72E-09

Table 4. Calculated effective quality factors at 10 mm depth in the ICRU sphere and conversion coefficients fluence to ambient dose equivalent and fluence to effective dose equivalent, as a function of the incident negative kaon energy

Energy (GeV)	Q at 10 mm	H*(10) ($Sv \cdot cm^2$)	E (AP) ($Sv \cdot cm^2$)	E (ISO) ($Sv \cdot cm^2$)
1.0E-03	1.97	1.39E-09	1.02E-10	3.58E-10
1.0E-02	1.80	1.45E-09	3.58E-10	4.66E-10
5.0E-02	1.11	1.92E-09	9.12E-10	5.44E-10
1.0E-01	1.23	1.22E-09	1.18E-09	9.02E-10
2.0E-01	1.32	7.26E-10	6.94E-10	7.65E-10
5.0E-01	1.52	6.32E-10	6.18E-10	6.41E-10
1.0E+00	1.42	5.11E-10	5.60E-10	5.82E-10
5.0E+00	1.69	6.59E-10	8.71E-10	9.66E-10
1.0E+01	1.96	8.20E-10	1.06E-09	1.31E-09
1.0E+02	1.60	6.82E-10	1.09E-09	1.75E-09
1.0E+03	2.02	8.89E-10	2.04E-09	4.58E-09
1.0E+04	1.80	9.11E-10	2.82E-09	9.30E-09

Table 5. Calculated effective quality factors at 10 mm depth in the ICRU sphere and conversion coefficients fluence to ambient dose equivalent and fluence to effective dose equivalent, as a function of the incident positive kaon energy

Energy (GeV)	Q at 10 mm	H*(10) ($Sv \cdot cm^2$)	E (AP) ($Sv \cdot cm^2$)	E (ISO) ($Sv \cdot cm^2$)
1.0E-03	1.55	E-09	E-11	2.87E-10
1.0E-02	1.52	E-09	E-10	4.03E-10
5.0E-02	1.07	E-09	E-10	5.22E-10
1.0E-01	1.17	E-09	E-09	8.78E-10
2.0E-01	1.14	E-10	E-10	6.47E-10
5.0E-01	1.26	E-10	E-10	5.19E-10
1.0E+00	1.30	E-10	E-10	5.12E-10
5.0E+00	1.61	E-10	E-10	8.77E-10
1.0E+01	1.83	E-10	E-10	1.08E-09
1.0E+02	1.65	E-10	E-09	1.66E-09
1.0E+03	1.75	E-10	E-09	3.60E-09
1.0E+04	2.17	E-09	E-09	9.52E-09

As far as kaons are concerned, the ambient dose equivalent is shown in Figures 5 and 6 as a function of the incident particle energy. The operational quantity appears a conservative predictor of the limiting quantity up to about 50 MeV for positive kaons and up to about 100 MeV for negative kaons.

Radiation weighting factors

In principle several effective quality factors can be selected in order to determine w_R values. The following are considered in the present paper:

1) the effective quality factor at 10 mm depth in the ICRU sphere, $\overline{Q}_{10}$, in accordance with the statement in Paragraph (A14) of ICRP Publication 60;

2) the effective quality factor at depth, along the principal diameter of the ICRU sphere, at which the maximum of the depth-dose distribution occurs, $\overline{Q}_{max}$;

3) the ratio of the effective dose equivalent to the effective absorbed dose for AP (front) irradiation, calculated using the organs and the weights as specified for the effective dose, $\overline{Q}_E$:

$$\overline{Q}_E = \frac{\sum_T w_T Q_T D_T}{\sum_T w_T D_T} \tag{4}$$

where D_T is the mean absorbed dose in the tissue or organ T;

4) the mean organ quality factor, weighted on the organ absorbed dose for AP (front) irradiation, $\overline{Q}_{ORG}$:

$$\overline{Q}_{ORG} = \frac{\sum_T Q_T D_T}{\sum_T D_T} \tag{5}$$

where D_T is the organ dose.

The calculated values of $\overline{Q}_{ORG}$ are assumed here as the most representative basis in order to assign appropriate values to the radiation weighting factors of high-energy radiation. The other calculated quality factors provide additional elements of judgement. The details of the calculations of the various effective quality factors are described in Ref. [6].

Figures 7-10 show the calculated results as a function of incident particle energy, for high-energy neutrons, protons, negative pions and positive pions, respectively.

Inspection of these figures shows that:

- the values of $\overline{Q}_{ORG}$ and $\overline{Q}_E$ are practically the same for all kinds of radiation considered;
- in the case of neutrons of energy above 50 MeV, both $\overline{Q}_{ORG}$ and $\overline{Q}_E$ are lower than $\overline{Q}_{10}$, which seems to represent therefore a very conservative approximation of the radiation weighting factor; conversely, $\overline{Q}_{max}$ always appears lower than $\overline{Q}_{ORG}$;

- for protons, all of the investigated effective quality factors assume values of between 1 and 2 whatever the incident energy may be, except at 10 MeV ($\overline{Q}_{ORG} = \overline{Q}_E = 3$);
- the values of $\overline{Q}_{10}$ for negative pions appear to be equal to those of $\overline{Q}_{ORG}$ from 100 MeV;
- for positively charged pions, whatever the incident energy may be, the values of $\overline{Q}_{10}$ are very close to the ones of $\overline{Q}_{ORG}$.

As with incident muons, a summary of the obtained results is given in Table 6 [6].

Table 6. Calculated effective quality factors as a function of muon energy

Energy	Negative muons				Positive muons			
(GeV)	$\overline{Q}_{10}$	$\overline{Q}_{max}$	$\overline{Q}_E$	$\overline{Q}_{ORG}$	$\overline{Q}_{10}$	$\overline{Q}_{max}$	$\overline{Q}_E$	$\overline{Q}_{ORG}$
1.0E-03	1.1	3.6	1.2	1.6	1.0	1.9	1.0	1.2
1.0E-02	1.1	2.0	1.3	1.2	1.0	1.4	1.0	1.1
5.0E-02	1.0	1.2	1.1	1.1	1.0	1.1	1.0	1.0
> 1.03-01	1.0	1.0	1.0	1.0	1.0	1.0	1.0	1.0

In the case of kaons, all calculated values of $\overline{Q}_{ORG}$ lie between 1.5 and 1.8 for negatively charged kaons, or between 1.2 and 1.7 for positively charged kaons. However the effective quality factor at the maximum gives values between 3 and 5 at the lowest energies (1 and 10 MeV) for both kinds of particles.

A proposal of revision of the w_R values

On the basis of the present results it is evident that the recommended w_R values should be revised. The properties of the weighted organ quality factor given by Eq. (5) make it of interest as a possible quantity upon which to base the adoption of a new set of w_R values. To this aim the calculated values of this factor have been rounded and grouped as reported in Table 7.

Table 7. Proposed radiation weighting factors for high-energy radiation

Radiation	Energy (GeV)	Radiation weighting factor
Neutrons	0.05-0.1	5
	0.1-0.5	4
	0.5-10	3
	> 10	2
Protons	> 0.01	2
Negative pions	<0.05	5
	≥ 0.05	2
Positive pions	< 0.1	1
	≥ 0.1	2
Negative and positive muons	10^{-3}-10^{4}	1
Negative and positive kaons	10^{-3}-10^{4}	2

The proposed rounded values are systematically higher than the calculated values of $\overline{Q}_{ORG}$ for protons, negative pions of energy over 50 MeV, positive pions over 100 MeV and kaons.

Since the proposed values generally are lower than those recommended by the ICRP, the lack of conservatism of the ambient dose equivalent with respect to the effective dose is expected to be consequently mitigated.

Future actions

On the basis of the present results (see Table 7), actions of the SATIF scientific community towards the International Commission on Radiological Protection, aimed to obtain a revision of the w_R values for high-energy radiation, would be highly recommended.

REFERENCES

[1] International Commission on Radiological Protection, *1990 Recommendations of the International Commission on Radiological Protection*, ICRP Publication 60, Annals of ICRP, **21** (1-3) (1991).

[2] M. Pelliccioni, *Conversion Coefficients for High-Energy Radiation*, SATIF-3, Tohoku University, Sendai, Japan, 12-13 May 1997, OECD Proceedings, pp. 289-298, 1998.

[3] A. Fassò, A. Ferrari, J. Ranft and P.R. Sala, *An Update About FLUKA*, Proceedings of Second Workshop on Simulating Accelerator Radiation Environments, CERN, 8-11 October 1995, pp. 158-170 (1997).

[4] A. Ferrari, M. Pelliccioni and M. Pillon, *Fluence-to-Effective Dose Conversion Coefficients for Negatively and Positively Charged Pions*, submitted to *Rad. Prot. Dosim.*

[5] M. Pelliccioni, *Conversion Coefficients Data and Radiation Weighting Factors for High-Energy Radiation*, accepted for publication in *Rad. Prot. Dosim.*

[6] M. Pelliccioni, *Radiation Weighting Factors and High-Energy Radiation*, accepted for publication in *Rad. Prot. Dosim*.

Figure 1. Effective quality factors at 10 mm depth in the ICRU sphere as a function of pion energy

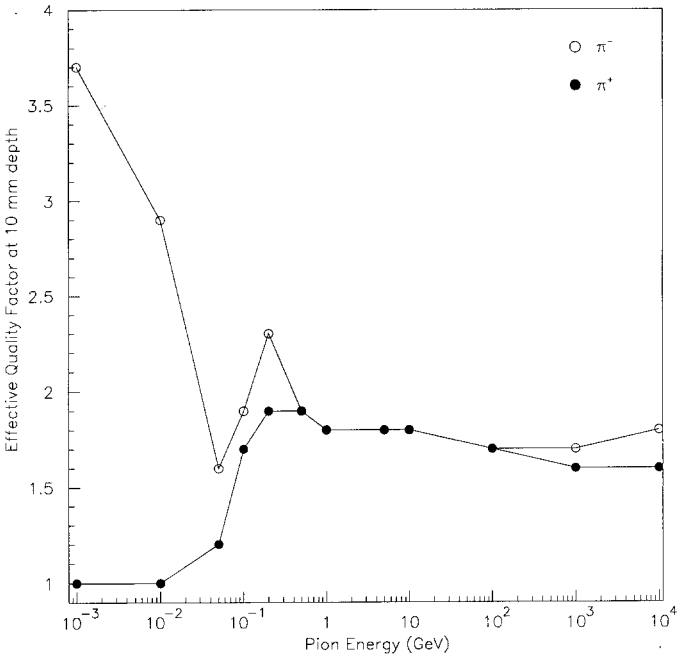

Figure 2. Effective quality factors at 10 mm depth in the ICRU sphere as a function of kaon energy

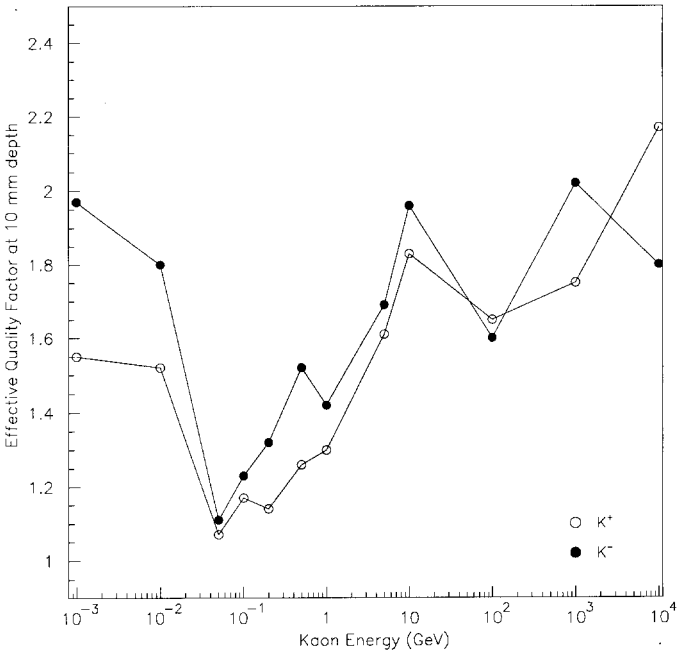

Figure 3. Effective dose and ambient dose equivalent per unit of fluence as a function of negative pion energy, for various irradiation geometries

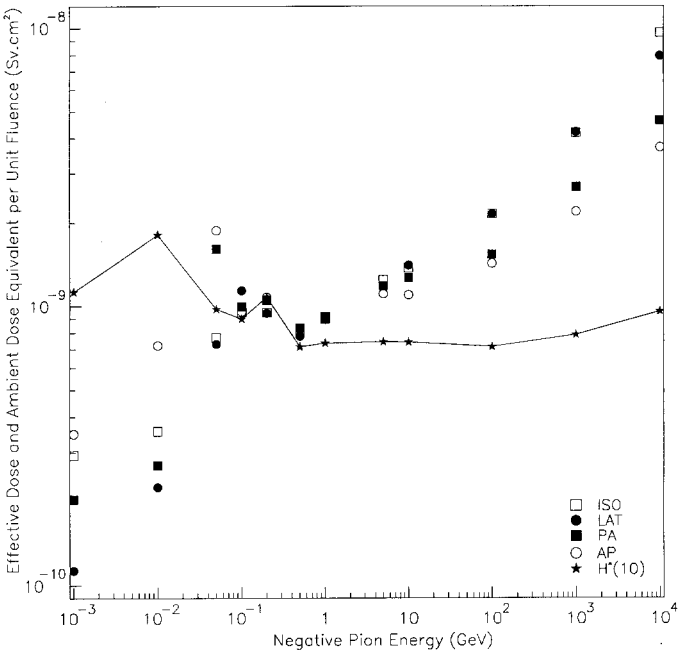

Figure 4. Effective dose and ambient dose equivalent per unit of fluence as a function of positive pion energy, for various irradiation geometries

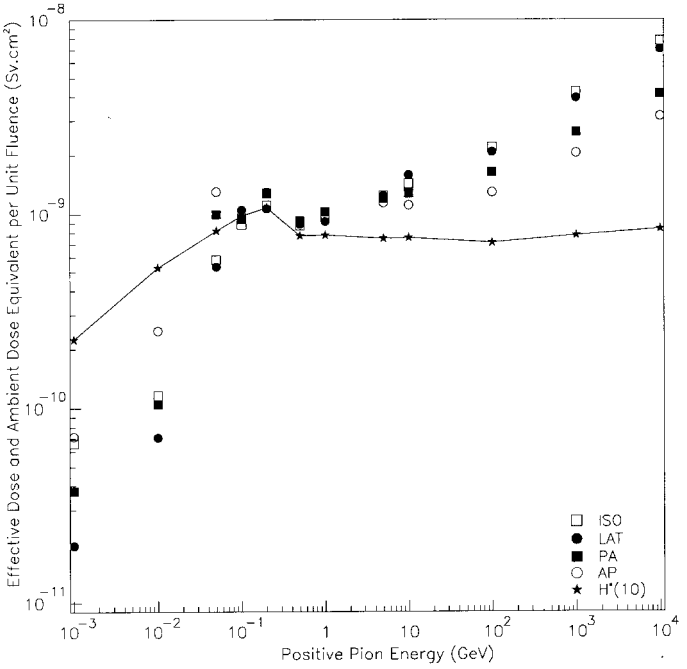

Figure 5. Effective dose and ambient dose equivalent per unit of fluence as a function of negative kaon energy, for AP and ISO irradiation geometries

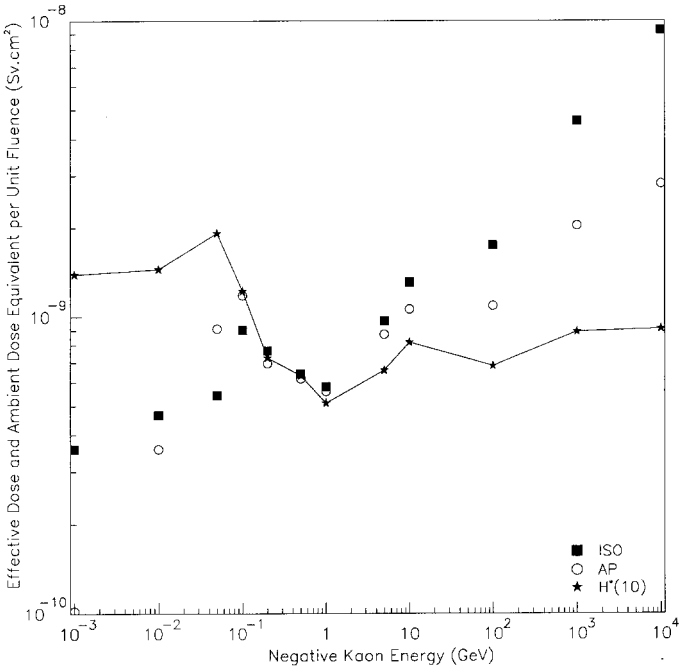

Figure 6. Effective dose and ambient dose equivalent per unit of fluence as a function of positive kaon energy, for AP and ISO irradiation geometries

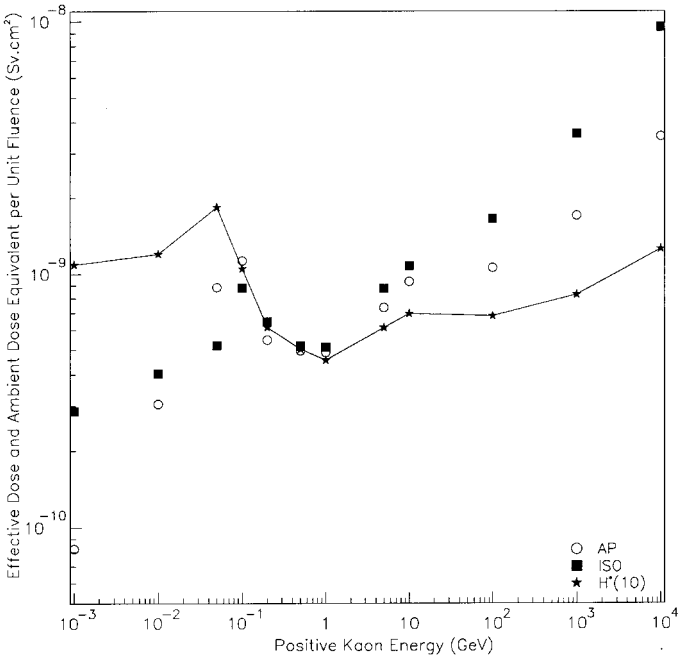

Figure 7. Calculated effective quality factors as a function of neutron energy

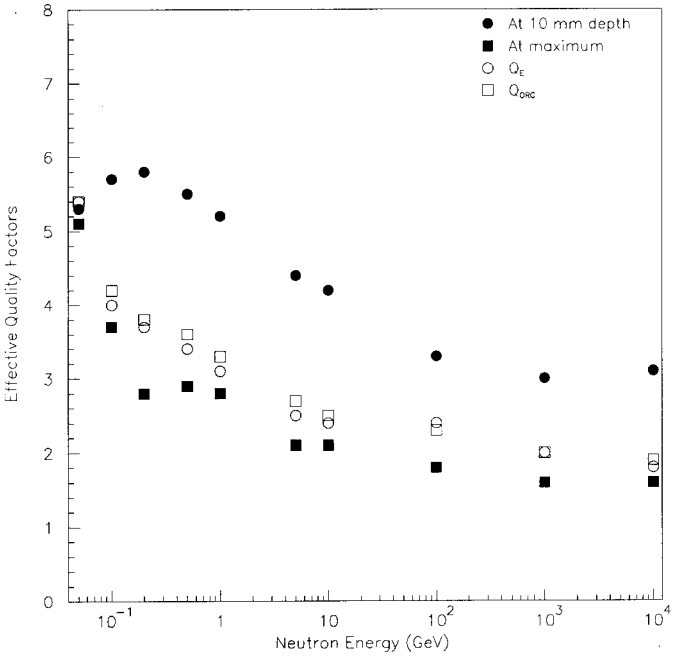

Figure 8. Calculated effective quality factors as a function of proton energy

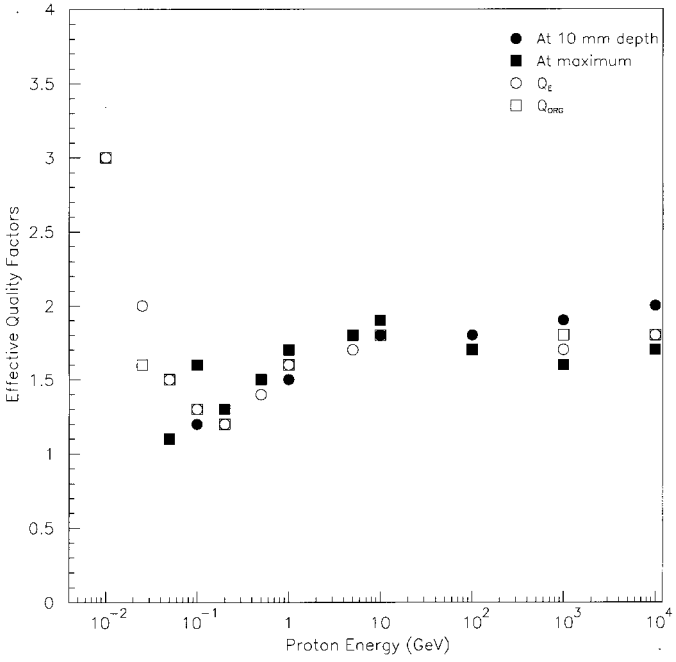

Figure 9. Calculated effective quality factors as a function of negative pion energy

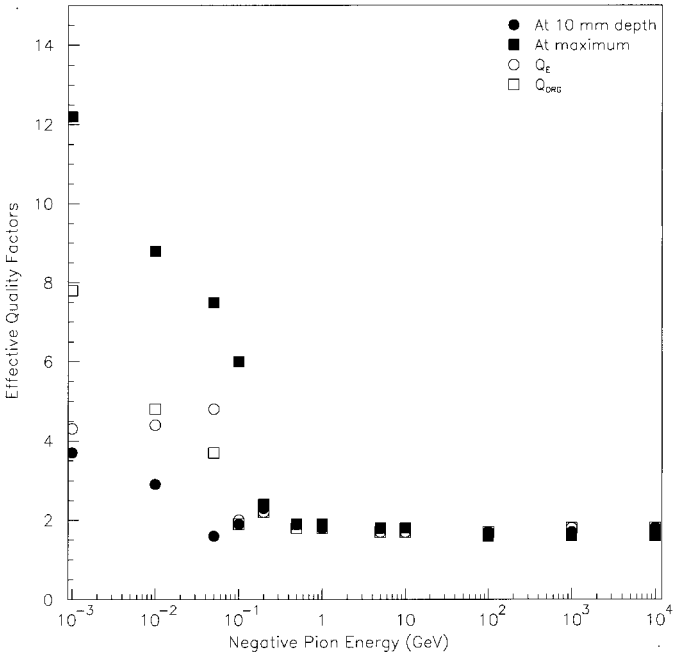

Figure 10. Calculated effective quality factors as a function of positive pion energy

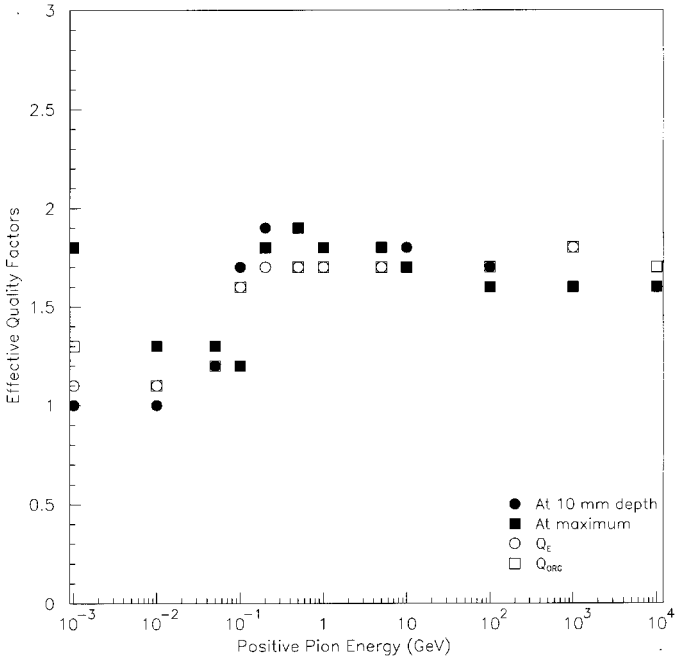

OVERVIEW OF FLUENCE TO DOSE EQUIVALENT CONVERSION COEFFICIENTS FOR HIGH-ENERGY RADIATIONS: CALCULATIONAL METHODS AND RESULTS OF TWO KINDS OF EFFECTIVE DOSES PER UNIT PARTICLE INFLUENCE

Satoshi Iwai*, Takashi Uehara*
Mitsubishi Heavy Industries, Ltd.
1-297, Kitabukuro-cho, Omiya-city, Saitama, Japan
** Present address: Nuclear Development Corporation*
1-297, Kitabukuro-cho, Omiya-city, Saitama, Japan

Osamu Sato, Nobuaki Yoshizawa, Shiori Furihata, Shunji Takagi
Mitsubishi Research Institute, Inc.
2-3-6 Ohtemachi, Chiyodo-ku, Tokyo, Japan

Shun-ichi Tanaka
Japan Atomic Research Institute, Planning Office
2-2-2 Uchisaiwai-cho, Chiyoda-ku, Tokyo, Japan

Yukio Sakamoto
Japan Atomic Research Institute, Accelerator Radiation Laboratory
Centre for Neutron Science, Tokai-mura, Naka-gun, Ibaraki, Japan

Abstract

In and around high-energy accelerator facilities, high-energy radiation dose estimation is important for the radiological protection of workers. The contribution of high-energy protons and neutrons to the radiation exposure of astronauts can also not be disregarded inside a spacecraft. This report provides an overview of calculational methodologies and estimated results of effective doses and effective dose equivalents for high-energy radiations such as photons, neutrons, protons, electrons, muons and pions in several groups. These data will be helpful to establish authoritative dose equivalent conversion coefficients for high-energy radiations up to 10 GeV.

Introduction

Due to the increase of high-energy accelerator facilities and space missions, high-energy radiation has come to be an important issue with regard to radiological protection.

Effective doses or effective dose equivalents are adequate radiological protection quantities to evaluate radiation risks of individuals exposed to radiations not only of low and intermediate energy but also of high energy. In 1987, ICRP51 [1] showed the conversion coefficients of effective dose equivalents based on ICRP26 [2] for photons from 10 keV to 10 MeV and for neutrons from 2.5×10^{-2} eV to 14 MeV. In 1996, ICRP74 [3] demonstrated the conversion coefficients of effective dose for photons from 10 keV to 10 MeV and for neutrons from 1×10^{-3} eV to 180 MeV, but conversion coefficients above 180 MeV have not been specified for all kinds of particles in any publication of the ICRP or the ICRU.

This work summarises the comparisons of calculational methodologies and results of dose conversion coefficients of effective dose and effective dose equivalents for high-energy neutrons, photons, protons and electrons up to maximum 10 GeV.

Maximum energy limit of conversion coefficients

The maximum energy investigated depends on the radiation environment of interest, and the energy of 10 GeV is adopted as the maximum energy limit of conversion coefficients calculated in this work. This value was derived from the radiation environment inside space vehicles in low earth orbits such as US space shuttles and the Russian space station MIR.

Figure 1 shows one of the typical radiation environments inside a space vehicle of 70 mm thickness of aluminium in the low earth orbit of 400 km altitude and 5.16° inclination. In this figure, radiation integral spectra[1] were calculated by use of space radiation environment models and a high-energy radiation code system; the former are AP8 [4] (proton radiation belt model), AE8 [6] (electron radiation belt model) and CREME [5] (galactic cosmic ray model), and the latter is the HERMES code system [7], which calculates high-energy radiation transports and secondary particle productions.

The proton component above 10 GeV is estimated to contribute less than 5% of proton effective doses of the crews inside space crafts in the low earth orbit, from the calculated result of the proton effective dose conversion coefficient [8] and the proton integral spectra shown in Figure 1. This result leads to the finding that the energy of 10 GeV is a sufficient upper limit to evaluate the dose equivalents of space crews inside vehicles of low earth orbit. This energy limit is also suited to the radiation environments in and around high-energy accelerator facilities of the maximum projectile energy of up to 10 GeV.

Definitions of effective dose and effective dose equivalent

ICRP26 [2] introduced the averaged organ dose equivalent H_T expanded from the dose equivalent at a point in an organ or tissue T. In 1978, by use of $\hat{H}_T$ this publication defined the effective dose

[1] Integral flux $\phi(E)$ is expressed as: $f(E) = \int_E^\infty f(e)de$, where $\phi(e)$ is a particle energy spectrum.

equivalent H_E which is the weighted sum of the dose equivalents of six specified organs and a remainder consisting of five organs at most:

$$H_E = \sum_T W_{T,26} \hat{H}_T \tag{1}$$

where $W_{T,26}$ is the tissue weighting factor specified in ICRP26.

In 1990, ICRP60 [9] recommended new quantities used for radiological protection: equivalent dose H_T is defined as the average organ-absorbed-dose multiplied by a radiation weighting factor W_R; the ICRP recommended radiation weighting factors in place of effective quality factor Q because of the uncertainties in the radio-biological information for the high LET part of the Q-L relationship specified in ICRP60. Although the radiation weighting factors are presented for the first time in ICRP60, the theoretical background on the derivation of the factors is not explained in any documents.

The effective dose E is defined as the weighted sum of the equivalent dose of twelve specified organs[2] and of the remainder consisting of ten organs additionally specified in ICRP60.

$$E = \sum_T W_{T,60} H_T \tag{2}$$

where $W_{T,60}$ is the appropriate tissue weighting factor shown in ICRP60.

In 1993, ICRU51 [11] re-defined the effective dose equivalent H_E by use of Eq. (3) so as to remain consistent with ICRP26, ICRP60 and ICRP67 [10].

$$H_E = \sum_T W_{T,60} D_T Q_T = \sum_T W_{T,60} \hat{H}_T \tag{3}$$

where D_T and Q_T are the mean absorbed dose and the man quality factor in a specified tissue (or organ) T, respectively. In Eq. (3) D_T and Q_T are defined as follows:

$$D_T = \frac{1}{m_T} \int_{m_T} D\,dm \tag{4}$$

$$Q_T = \frac{1}{m_T D_T} \int_{m_T} \int_L Q(L) \bullet D(L)\,dL\,dm$$

where m_T is the mass of the tissue or organ T, D is the absorbed dose in the mass element dm, D(L) denotes an absorbed dose distribution in the tissue (or organ) T as a function of L (unrestricted linear energy transfer in water), and Q(L) denotes the Q-L relationship of ICRP60. $\hat{H}_T$ is the averaged dose equivalent in the tissue (or organ) T.

[2] The equivalent dose to the colon – one of the twelve specified organs – Hcolon is given as: Hcolon = $0.57H_{ULI} + 0.47H_{LLI}$, where H_{ULI} and H_{LLI} are the equivalent doses to the ULI (upper large intestine) and the LLI (lower large intestine), according to ICRP67 [10].

"Effective dose equivalent, H_E" of Eq. (1) defined in ICRP26 is defined again as "effective dose equivalent" in ICRP74 [3] in 1995 and in ICRU57 [43] in 1998. These definitions have led to the confusion of the term of "effective dose equivalent, H_E" again.

In this paper, the following terms and symbols are used:

- E_{WR}, effective dose using radiation weighting factor W_R

$$E_{WR} = E = \sum_T W_{T,60} H_T \tag{5}$$

- $E_{Q\text{-}L}$, effective dose using Q(L) specified in ICRP60

$$E_{Q\text{-}L} = \sum_T W_{T,60} D_T Q_T = \sum_T W_{T,60} \hat{H}_T \tag{6}$$

- H_E, effective dose equivalent defined in ICRP26, 74 and ICRU57

$$H_E = \sum_T W_{T,26} \hat{H}_T \tag{7}$$

Calculational methodologies and conditions for effective dose and effective dose equivalent

This section provides methodologies and conditions calculating conversion coefficients from unit particle fluence to effective doses E_{WR}, $E_{Q\text{-}L}$ and effective dose equivalent H_E. Table 1 summarises the protection quantities, emitted particles, energy ranges, Q(L) data, physical databases, application of kerma factors, anthropomorphic phantoms and irradiation geometries used for the calculation of the dose conversion coefficients in each group of authors. The purpose of this study is an overview of conversion coefficients of particle fluence to effective doses and effective dose equivalent. Therefore in this table, data corresponding to effective doses E_{WR}, $E_{Q\text{-}L}$ and effective dose equivalent H_E appear, except the reference of ambient dose equivalent of Sannikov *et al.* [14]. The conversion coefficients of ambient dose equivalent H*(10) and the ICRU sphere depth dose calculated in each group are eliminated in principle, because these data are out of the scope of this report.

Comparison of conversion coefficients of effective dose and effective dose equivalent per unit particle fluence calculated in each group

Conversion coefficients for neutrons

Figure 2 shows the comparison of conversion coefficients of E_{WR} calculated by the four groups, for AP, PA and ISO geometries with the reference of h*(10), ambient dose equivalent conversion coefficient for ICRP60 Q(L) dependence, calculated by Sannikov *et al.* [14] and the conversion coefficients specified in ICRP74. Estimated E_{WR} values are in fairly good agreement below 500 MeV in spite of several kinds of differences in computer codes, physical databases and anthropomorphic phantom geometries. But the maximum difference of about 30% can be observed around 2 GeV. The ambient dose equivalent conversion coefficient h*(10) does not show conservative values above 50 MeV.

Figure 3 provides the comparison of estimates of $E_{Q\text{-}L}$ calculated by the three groups. The h*(10) values are shown for reference. There is good agreement between the data of Nabelssi *et al*. [15,16] and those of Yoshizawa *et al*. [27]. The estimates of Mares *et al*. [19] show 30% larger values than the former two kinds of data [15,16,27], especially at 100 MeV. For a detailed analysis of the differences, comparison of organ doses will be required among the three groups. The h*(10) of Sannikov *et al*. shows a fairly good agreement with the $E_{Q\text{-}L}$ for AP geometry of Ref. [27] above 50 MeV. But the h*(10) is also a little lower than the estimates of $E_{Q\text{-}L}$ for PA within a difference of 5%, although the h*(10) shows about 50% smaller values than E_{WR} above 50 MeV at maximum difference.

Conversion coefficients for photons

The comparison of estimates of E calculated by two groups are shown for AP geometry in Figure 4, for PA geometry in Figure 5, for LAT geometry in Figure 6 and for ISO geometry in Figure 7. These data are in good agreement except some data within maximum 20% difference, despite the use of different computer codes, databases and phantom geometries. The analysis of these differences are discussed in detail in Ref. [12].

Conversion coefficients for protons

High-energy protons inside space shuttles are estimated to be the major component of astronauts' whole body dose equivalents. Nevertheless proton dose conversion coefficients of fluence to E_{WR} and $E_{Q\text{-}L}$ are not shown in any document except Refs. [8,27,45]. ICRP51 [1] provides the maximum dose equivalent and 10 mm depth dose equivalent in 30 cm thick semi-infinite slab phantom for proton incidence up to 10 GeV.

Figure 8 represents the comparisons of E_{WR} for AP, PA and ISO irradiation geometries calculated in the two groups, with the reference data of the maximum dose equivalent and the 10 mm depth dose equivalent in the 30 cm thickness semi-infinite slab phantom in ICRP51. The E_{WR} shown in Ref. [8] is also exhibited for R-LAT geometries in Figure 8. Above 50 MeV, there is good agreement between the data of Yoshizawa *et al*. [27] and those of Ferrari *et al*. [8] for AP, PA and ISO geometries. Above 200 MeV, good agreement can be observed among the effective doses E_{WR} for the three irradiation geometries. The estimated E_{WR} represent slightly larger values than the maximum dose equivalents shown in ICRP51 for the energy rangeof 200 MeV to 10 GeV.

Figure 9 shows the comparisons of $E_{Q\text{-}L}$ for AP, PA and ISO irradiations and the maximum dose equivalent and the 10 mm depth dose equivalent in ICRP51. The estimates of Yoshizawa *et al*. [27,45] for $E_{Q\text{-}L}$ show fairly good agreement with the 10 mm depth dose in ICRP51 above 200 MeV.

Summary

1) Dose equivalent conversion coefficients from particle fluence to effective dose were overviewed for high-energy neutron, proton, photon, electron and charge muon and pions. Comprehensive comparisons were performed for the methodologies and conditions adopted in the four different groups calculating dose conversion coefficients from fluence to two kinds of effective dose, E_{WR} and $E_{Q\text{-}L}$ of high-energy neutrons, photons, protons.

2) Comparisons of high-energy neutron conversion coefficients of E_{WR} and E_{Q-L} were performed in the four groups. The estimates of E_{WR} in the four groups show fairly good agreement below 500 MeV. The estimates of E_{WR} agree well with one exception of 30% difference.

3) Ambient dose equivalent h*(10) of high-energy neutron shows less than 50% lower values than E_{WR} above 50 MeV. The quantity of h*(10) agrees well with E_{Q-L} especially for AP irradiation geometry above 50 MeV, but for PA and ISO irradiation geometries it shows slightly smaller values than E_{Q-L} within the maximum difference of 30%.

4) Comparisons were performed for the dose conversion coefficients of high-energy photons calculated in the two groups. These data agree well within the maximum difference of 20% for the irradiation geometries of AP, PA, R-LAT and ISO conditions.

5) Comparisons of high-energy proton conversion coefficients of E_{WR} were performed between the two groups from 20 MeV to 10 GeV. Good agreement can be observed for AP, PA and ISO geometries above 50 MeV. The estimated E_{WR} represent slightly larger values than the maximum dose equivalents in the slab phantom of ICRP51 from 200 MeV to 10 GeV.

6) The estimated E_{Q-L} of high-energy protons show fairly good agreement with the 10 mm depth dose in the slab phantom in ICRP51 above 200 MeV.

REFERENCES

[1] ICRP Publication 51, “Data for Use in Protection Against External Radiation”, Annals of the ICRP 17 (2/3) (1987).

[2] ICRP Publication 26, “Recommendations of the ICRP”, Annals of the ICRP 1 (3) (1997), reprinted (with additions) in 1987 (Stockholm statement).

[3] ICRP Publication 74, “Conversion Coefficients for Use In Radiological Protection Against External Radiation”, Annals of the ICRP 26 (3/4) (1996).

[4] D.M. Sawyer and J.I Vette, AP-8 Trapped Proton Environment for Solar Maximum and Solar Minimum, NSSDC/WDC-A-R & S 76-06 (1976).

[5] J.I. Vette, The AE-8 Trapped Electron Model Environment, NASA-WDC-A-R & S 91-24 (1991).

[6] J.H. Adams Jr., R. Silberberg and C.H. Tsao, Cosmic Ray Effects on Microelectronics. Part I – The Near-Earth Particle Environment. NRL Memo. Rep. 4506-Pt. I, US Navy, August (1981). (Available from DTIC as AD A103 897.) Cosmic Ray Effects on Microelectronics, Part IV.

[7] P. Cloth, D. Filges, R.D. Neef, G. Sterzenbach, Ch. Ruel, T.W. Armstrong, B.L. Colbom, B. Anders and H. Bruckman, "HERMES: A Monte Carlo Program System for Beam Materials Interaction Studies", FA-IRE-E AN/12/88 (1988).

[8] A. Ferrari, M. Pelliccioni and M. Pillon, Fluence to Effective Dose Conversion Coefficients for Protons from 5 MeV to 10 TeV, *Radiat. Prot. Dosim.* 71 (1997) 85.

[9] ICRP Publication 60, "1990 Recommendations of the International Commission on Radiological Protection", Annals of the ICRP 21 (1-3) (1991).

[10] ICRP Publication 67, "Age-Dependent Doses to Members of the Public from Intake of Radionuclides: Part 2, Ingestion Dose Coefficients", Annals of the ICRP 23 (3/4) (1993).

[11] ICRU Report 51, "Quantities and Units in Radiation Protection Dosimetry", International Commission on Radiation Units and Measurements (1993).

[12] A. Ferrari, M. Pelliccioni and M. Pillon, Fluence to Effective Dose and Effective Dose Equivalent Conversion Coefficients for Photons from 50 keV to 10 GeV, *Radiat. Prot. Dosim*. 67 (1996) 245.

[13] A. Ferrari, M. Pelliccioni and M. Pillon, Fluence to Effective Dose and Effective Dose Equivalent Conversion Coefficients for Electrons from 50 keV to 10 GeV, *Radiat. Prot. Dosim*. 69 (1996) 97.

[14] A.V. Sannikov and E.N. Savitskaya, Ambient Dose Equivalent Conversion Factor for High-Energy Neutrons Based on the ICRP60 Recommendations, *Radiat. Prot. Dosim.* 70 (1997) 386.

[15] B.K. Nabelssi and N.E. Hertel, "Ambient Dose Equivalents, Effective Dose Equivalents and Effective Doses for Neutrons from 10 to 20 MeV", *Radiat. Prot. Dosim*. 48 (1993) 153.

[16] B.K. Nabelssi and N.E. Hertel, "Effective Dose Equivalents and Effective Doses for Neutrons from 30 to 180 MeV", *Radiat. Prot. Dosim*. 48 (1993) 227.

[17] R.E. Prael and H. Lichtenstein, User Guide to LCS: The LAHET Code System, Radiation Transport Group, LA-UR-89-3014 (Los Alamos National Laboratory) (1989).

[18] R.D. Stewart, J.E. Tanner and J.A. Lenowich, An Extended Tabulation of Effective Dose Equivalent from Neutrons Incident on a Male Anthropomorphic Phantom, accepted for publication in *Health Phys*. (1993).

[19] V. Mares, G. Leuthold and H. Schraube, Organ Doses and Dose Equivalents for Neutrons Above 20 MeV, *Radiat. Prot. Dosim*. 70 (1997) 391.

[20] J.F. Briesmeister, ed., MCNP – A General Monte Carlo N-Particle Transport Code, Version 4A, LA-12625-M (Los Alamos).

[21] P.G. Young *et al*., Transport Data Libraries for Incident Proton and Neutron Energies to 100 MeV, LANL Report LA 11753-MS (Los Alamos) (1990).

[22] J.S. Hendricks, S.C. Frankle and J.D. Court, ENDF/B-VI Data for MCNP, LANL Report LA-12891 (Los Alamos) (1994).

[23] J.H. Hubbell, W.J. Veigele, E.A. Briggs, R.T. Brown, D.T. Cramer and R.J. Howerton, Atomic Form Factor Incoherent Scattering Functions and Photon Scattering Cross-Sections, *J. Phys. Chem. Ref. Data* 4 (1975) 471.

[24] R. Kramer, M. Zankl, G. Williams and G. Drexler, The Calculation of Dose from External Photon Exposures Using Reference Human Phantoms and Monte Carlo Methods, Part I: The Male (Adam) and Female (Eva) Adult Mathematical Phantoms, GSF-Bericht S-855 (1982).

[25] M. Zankl, N. Petoussi and G. Drexler, Effective Dose and Effective Dose Equivalent – The Impact of the New ICRP Definition for External Photon Irradiation, *Health Phys.* 62 (1992) 395.

[26] S. Iwai, T. Uehara, O. Sata, N. Yoshizawa, S. Furihata, S. Takagi, S. Tanaka and Y. Sakamoto, Evaluation Fluence to Dose Equivalent Conversion Coefficients for Energy Neutrons – Calculation of Effective Dose Equivalents and Effective Dose, in Proc. 2nd Specialists Meeting on Shielding Aspects of Accelerators, Targets and Irradiation Facilities (SATIF-2), CERN, Geneva, 12-13 October 1995.

[27] N. Yoshizawa (Appendix Table) in:
S. Iwai, T. Uehara, O. Sata, N. Yoshizawa, S. Furihata, S. Tanaka and Y. Sakamoto, Overview of Fluence to Dose Equivalent Conversion Coefficients for High-Energy Radiations, in Proc. 3rd Specialists Meeting on Shielding Aspects of Accelerators, Targets and Irradiation Facilities (SATIF-3), pp. 299-331, Sendai, Japan, 12-13 May 1997.

[28] O. Sata, S. Iwai, S. Tanaka, T. Uehara, Y. Sakamoto, N. Yoshizawa and S. Furihata, “Calculations of Equivalent Dose and Effective Dose Conversion Coefficients for Photons from 1 MeV to 10 GeV”, *Radiat. Prot. Dosim*. 62 (1997) 119.

[29] N. Yoshizawa, K. Ishibashi and H. Takada, *J. Nucl. Sci. and Technol.* 32 (1995) 601.

[30] P. Cloth, D. Filges, R.D. Neef, G. Sterzenbach, Ch. Ruel, T.W. Armstrong, B.L. Colbom, B. Anders and H. Bruckman, “HERMES: A Monte Carlo Program for Beam Materials Interaction Studies”, KFA-IRE-EAN 12/88 (1988).

[31] K. Shibata, T. Nakagawa, T. Asami, T. Fukahori, T. Narita, S. Chiba, M. Mizumoto, A. Hasegawa, Y. Kikuchi, Y. Nakajima and S.I. Garashi, “Japanese Evaluated Nuclear Data Library, Version 3, JENDL-3”, JAERI 1319 (1990).

[32] W.R. Nelson, H. Hirayama and D.W.O. Rogers, “The EGS4 Code System”, Stanford Linear Accelerator Center Report SLAC-267 (Stanford, Calif.) (1985).

[33] D.K. Trubey, M.J. Berger and J.H. Hubbell, “Photon Cross-Section for ENDF/B-VI”, Advances in Nuclear Computation and Radiation Shielding, American Nuclear Society Topical Meeting (1989).

[34] ICRU, “Topping Powers for Electrons and Positrons”, Report 37, Bethesda MD (1984).

[35] M. Cristy and K.F. Eckerman, Specific Absorbed Fractions of Energy at Various Ages from Internal Photon Sources, ORNAL-TM-8381/V1-V7 (1987).

[36] Y. Yamaguchi, DEEP Code to Calculated Dose Equivalents in Human Phantom for External Photon Exposure by Monte Carlo, JAERI-M 90-235 (1990).

[37] C.A. Lewis and R.E. Ellis, Additions to the Snyder Mathematical Phantom, *Phys. Med. Biol.* 24 (1979) 1019.

[38] V.T. Golovachik, N.V. Kustarjov, E.N. Savitskaya and A.V. Sannikov, Absorbed Dose and Dose Equivalent Depth Distributions for Protons with Energies from 2 to 600 MeV, *Radiat. Prot. Dosim*. 28 (1989) 189.

[39] E.N. Savitskaya and A.V. Sannikov, High-Energy Neutron and Proton Kerma Factors for Different Elements, *Radiat. Prot. Dosim*. 60 (1995) 135.

[40] A. Ferrari, M. Pelliccioni and M. Pillon, Fluence to Effective Dose Conversion Coefficients for Neutrons Up to 10 TeV, *Radiat. Prot. Dosim*. 71 (1997) 165.

[41] A. Fassò, A. Ferrari, J. Ranft and P.R. Sala, An Update About FLUKA, in Proc. 2nd Workshop on Simulating Accelerator Radiation Environments, CERN, 8-11 October 1995.

[42] D. Garber, ed., ENDF/B-V Report BNL-17541 (ENDF-201) (National Nuclear Data Center, Brookhaven National Laboratory, Upton, NY) (1975).

[43] ICRU Report 57, “Conversion Coefficient for Use in Radiological Protection Against External Radiation”, International Commission on Radiation Units and Measurements (1998).

[44] O. Sato, N. Yoshizawa, S. Takagi, S. Iwai, T. Uehara, Y. Sakamoto, Y. Yamaguchi and S. Tanaka, Calculations of Effective Dose and Ambient Dose Equivalent Conversion Coefficients for High-Energy Photons, submitted to *J. Nucl. Sci. Technol*., 1988.

[45] N. Yoshizawa (Appendix Table) in:
S. Iwai, T. Uehara, O. Sato, N. Yoshizawa, S. Takagi, S. Tanaka and Y. Sakamoto, Overviews of Fluence to Dose Equivalent Conversion Coefficients for Energy Radiations – Calculational Methods and Results of Effective Dose and Effective Dose Equivalent Per Unit Particle Fluence, in Proc. 4th Specialists Meeting on Shielding Aspects of Accelerators, Targets and Irradiation Facilities (SATIF-4), Knoxville, 17-18 September 1998.

[46] A. Ferrari, M. Pelliccioni and M. Pillon, Fluence-to-Effective Dose Conversion Coefficients for Muon, *Radiat. Prot. Dosim.* 74 (1997) 227.

[47] A. Ferrari, M. Pelliccioni and M. Pillon, Fluence-to-Effective Dose Conversion Coefficients for Negatively and Positively Charged Pions, submitted to *Radiat. Prot. Dosim.*

Table 1(a). Summary of calculational methodologies and conditions of conversion coefficients

Group	Contributors	Particles (energy range)	Calculated dose equivalent
University of Texas at Austin	B.K. Nabelssi N.E. Hertel	Neutron [15,16] (10-180 MeV)	1) Effective dose using W_R (E_{WR}) 2) Effective dose using Q(L) ($E_{Q\text{-}L}$) 3) Effective dose equivalent (H_E)
GSF	V. Mares G. Leuthold H. Schraube	Neutron [19] (20-100 MeV)	1) Effective dose using W_R (E_{WR}) 2) Effective dose using Q(L) ($E_{Q\text{-}L}$) (Q(L),W_T:ICRP60)
Mitsubishi & JAERI	S. Iwai, T. Uehara O. Sata, N. Yoshizawa S. Furihata, S. Takagi S. Tanaka, Y. Sakamoto	Neutron [26,27,45], Proton [27,45] (20 MeV-10 GeV) Photon [28,44] (1 MeV-10 GeV)	1) Effective dose using W_R (E_{WR}) 2) Effective dose using Q(L) ($E_{Q\text{-}L}$) (Q(L),W_T:ICRP60)
INFN & EURATOM-ENEA	A. Ferrari M. Pelliccioni M. Pillon	Proton [8] (5 MeV-10 TeV) Neutron [4] (0.025 eV-10 TeV) Photon [12] (50 keV-10 GeV) Electron [13] 5 MeV-10 GeV) Muon* [46] (1 MeV-10 TeV) Pion* [47] (1 MeV-10 TeV)	1) Effective dose using W_R (E_{WR}) 2) Effective dose equivalent (H_E) (H_E,Q(L) = 1, W_T: ICRP26 for photon and electron)
IHEP	A.V. Sannikov E.N. Savitskaya V.T. Golovachik V.N. Kustarjov	Neutron [14] (20 MeV-5 GeV)	Ambient dose equivalent (h*(10))† (Q(L):ICRP60)

* *Charged (positive and negative)*

† *Reference data*

Table 1(b). Summary of calculational methodologies and conditions of conversion coefficients

Group	Application of Q(L) for calculating	Application of Kerma factor
University of Texas at Austin	p, d, t, ^{3}H, α – Q(L) of ICRP60 recoil nuclei (A > 4) – Q(L) = 20	Below 20 MeV (neutron)
GSF	q*(10) is used as neutron quality factor (q*(10) = H*(10)/D*(10) at 10 mm depth in ICRU sphere)	Below 100 MeV (neutron) (all energy ranges)
Mitsubishi & JAERI	Q(L) of ICRP60 for all charged particles	Below 15 MeV (neutron)
INFN & EURATOM-ENEA	Q(L) = 1: for photon, electron and positron W_R = H*(10)/D*(10) at 10 mm depth in ICRU sphere for charged pions	
IHEP	Q(L) of ICRP 60 for all charged particles	

Table 1(c). Summary of calculational methodologies and conditions of conversion coefficients

Group	Computer code and data library			Phantom	Irradiation geometries
The University of Texas at Austin	Above 20 MeV neutron LAHET [17]	HMCNP [17] (ENDF / B – V – n; DLC – 7E – γ) [42]		Modified PNL phantom [18] (male, female)	AP, PA, R-LAT (L-LAT)† ROT
GSF	MCNP [20] (LA100 [21]; ENDF / B - VI [22] extrapolation }n; Hubbell's data [23] ——— γ)			ADAM phantom (male) [24,25]	AP, Different angle of incidence (15°, 30°, 45°, 60°, 75°)
Mitsubishi & JAERI	Above 15 MeV neutron: Modified HERMES (HETC-3STEP [29])	Below 15 MeV neutron: MORSE-CG/ KFA [30] (JENDL-3.1 [31]) (PHOTX [33])	Photon: EGS4 [32] (PHOTX, ICRU37 [34])	Modified Christy adult phantom [26] (hermaphrodite)	(neutron, proton) AP, PA, ISO (photon) AP, PA, ISO, L-LAT, R-LAT, ROT
INFN & EURATOM-ENEA	FLUKA [41]			Modified ADAM phantom (hermaphrodite) [22,23]	AP, PA R-LAT ISO
IHEP	HADRON [38,39]			ICRU sphere	Parallel incidence

† *The conversion coefficient of the L-LAT geometry was calculated from 10-10 MeV.*

Figure 1. Radiation spectra inside a space vehicle of 70 mm thickness aluminium (solar activity is solar maximum)

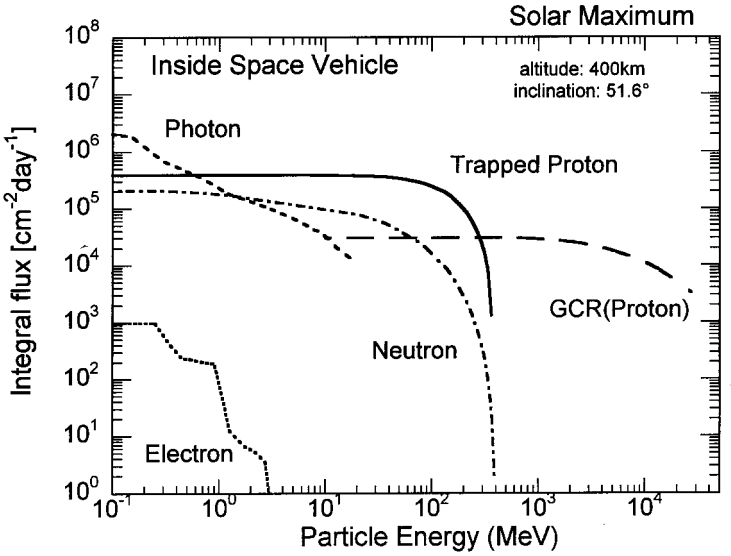

Figure 2. Comparison of effective dose using W_R (E_{WR}) for AP, PA and ISO irradiation neutron beams (the error bars are within symbols)

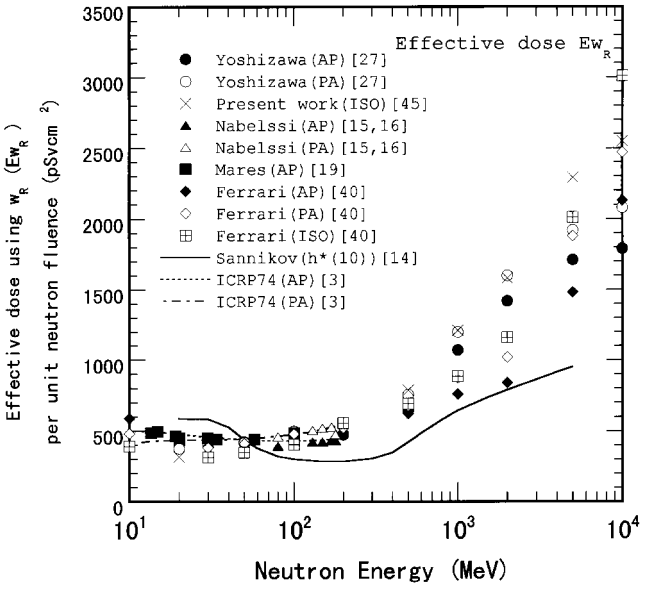

Figure 3. Comparison of effective dose using Q(L) (E_{Q-L}) for AP, PA and ISO irradiation neutron beams (the error bars are within symbols)

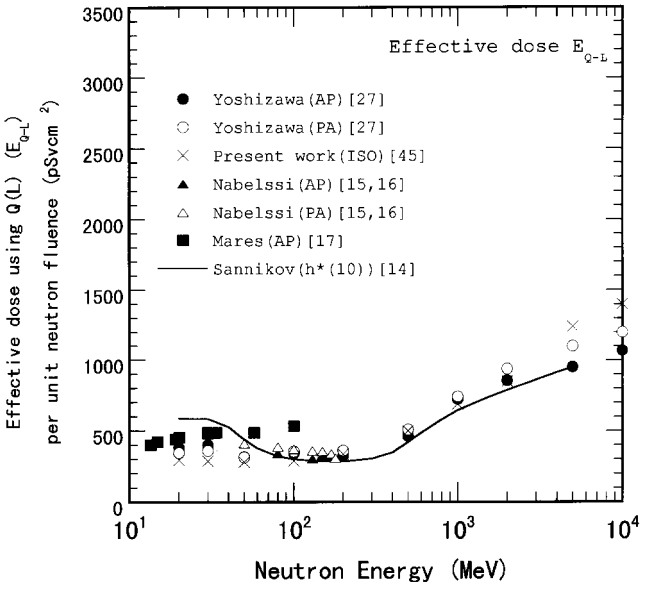

Figure 4. Comparison of effective dose E for AP irradiation photon beam (the error bars represent one-statistical deviations)

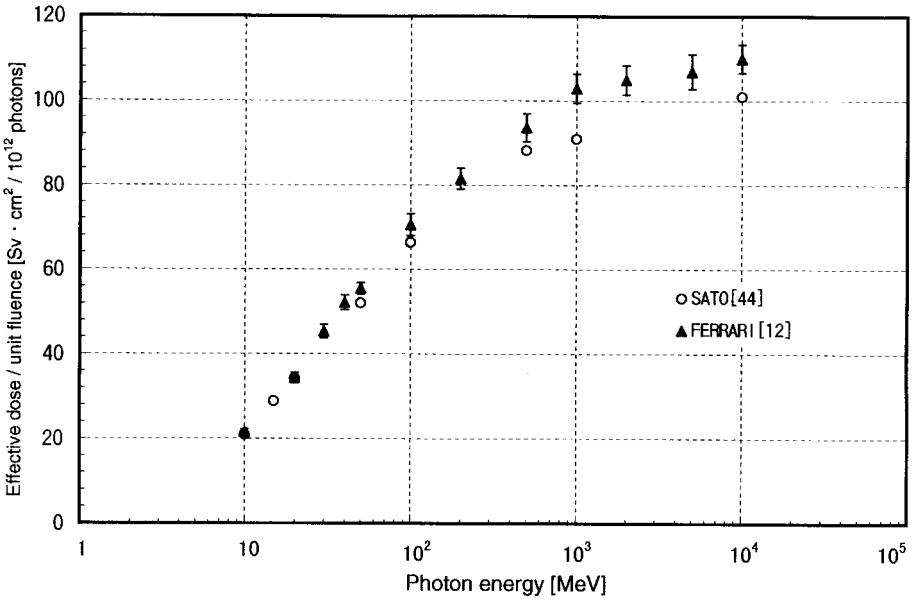

Figure 5. Comparison of effective dose E for PA irradiation photon beam (the error bars represent one-statistical deviations)

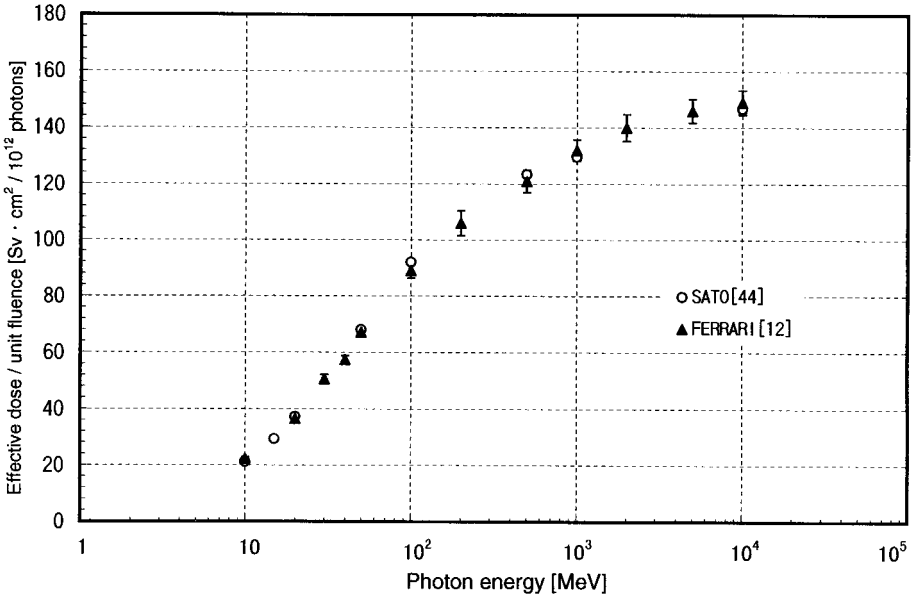

Figure 6. Comparison of effective dose E for LAT irradiation photon beam (the error bars represent one-statistical deviations)

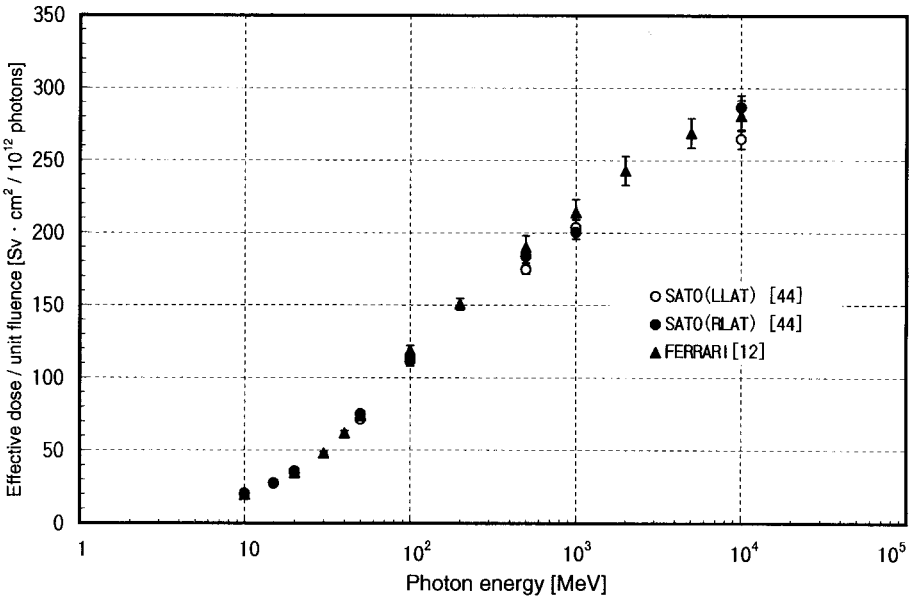

Figure 7. Comparison of effective dose E for ISO irradiation photon beam (the error bars represent one-statistical deviations)

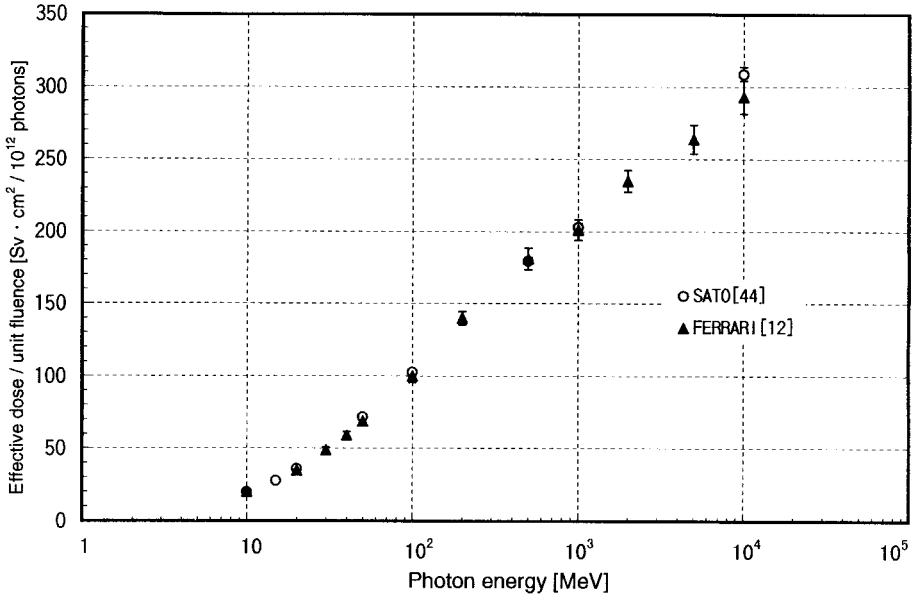

Figure 8. Comparison of effective dose using W_R (E_{WR}) for AP, PA and ISO irradiation proton beams (the error bars are within symbols)

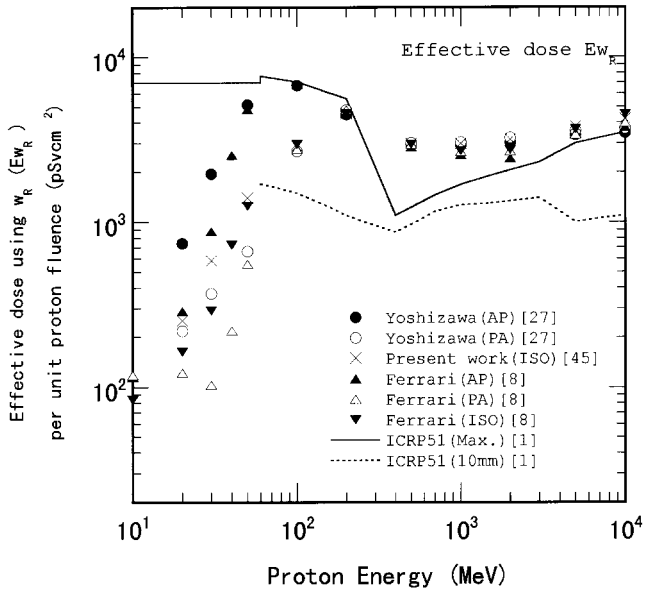

Figure 9. Comparison of effective dose using Q(L) (E_{Q-L}) for AP, PA and ISO irradiation proton beams (the error bars are within symbols)

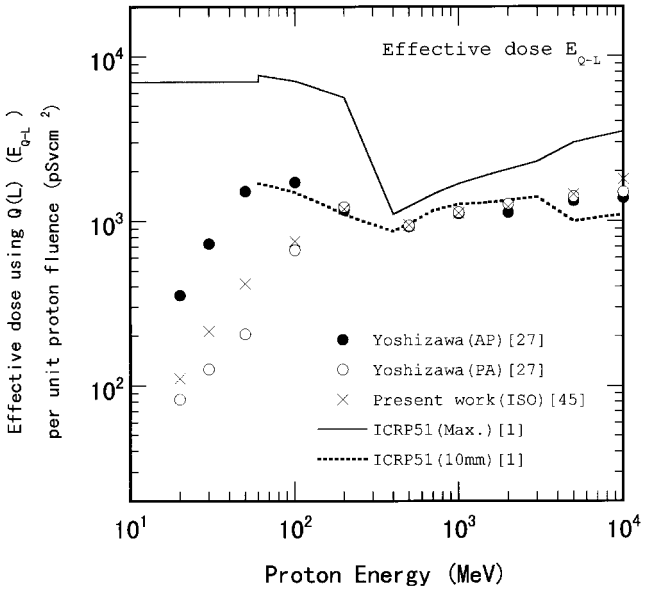

Appendix

Dose conversion coefficients from neutron and proton fluence to E_{WR}, E_Q, averaged organ absorbed dose, equivalent dose, averaged organ dose equivalent from 20 MeV to 10 GeV for ISO geometry

Table A-1. Fluence to neutron and proton effective dose conversion coefficients for ISO irradiation

Energy (MeV)	neutron					proton				
	E_{WR}* (pSVcm^2)		$E_{Q\text{-}L}$† (pSVcm^2)		$\overline{Q}_{body}$ ‡	E_{WR}* (pSVcm^2)		$E_{Q\text{-}L}$† (pSVcm^2)		$\overline{Q}_{body}$ ‡
20	3.17E+02	6.7%	2.95E+02	7.1%	6.3	2.53E+02	1.6%	1.11E+02	2.1%	2.2
30	3.49E+02	3.4%	2.87E+02	4.1%	5.0	5.82E+02	2.5%	2.15E+02	2.8%	1.8
50	3.69E+02	3.6%	2.80E+02	4.4%	4.2	1.40E+03	2.8%	4.17E+02	2.9%	1.5
100	4.55E+02	5.6%	2.88E+02	3.5%	3.3	2.88E+03	1.3%	7.55E+02	1.5%	1.3
200	5.34E+02	4.1%	3.36E+02	5.5%	3.2	4.57E+03	0.9%	1.18E+03	3.9%	1.3
500	7.87E+02	7.6%	5.02E+02	12.8%	3.2	2.97E+03	1.0%	9.45E+02	3.1%	1.6
1000	1.21E+03	3.1%	6.90E+02	3.2%	2.9	2.98E+03	1.8%	1.12E+03	5.8%	1.9
2000	1.58E+03	3.8%	8.50E+02	7.3%	2.7	3.15E+03	1.7%	1.22E+03	4.8%	1.9
5000	2.29E+03	4.0%	1.24E+03	7.9%	2.7	3.77E+03	2.2%	1.45E+03	2.8%	1.9
10000	2.55E+03	2.3%	1.40E+03	5.2%	2.7	4.20E+03	2.7%	1.79E+03	6.8%	2.1

* E_{WR}: Effective dose using W_R

† $E_{Q\text{-}L}$: Effective dose using Q-L relationship recommended in ICRP60.

‡ $\overline{Q}_{body}$: Mean quality factor for the whole body.

% value means fractional standard deviation of Monte Carlo calculation.
E+02 means $\times 10^2$.

Table A-2a. Organ absorbed dose, equivalent dose and dose equivalent per unit fluence for 20 MeV neutron for ISO irradiation

Organ or tissue	Absorbed dose*		Equivalent dose W_R = 6.76		Dose equivalent†		Mean quality factor Q-L in ICRP60
	($pGycm^2$)	error	($pSVcm^2$)	error	($pSVcm^2$)	error	
Testes	4.27E+01	14.8%	2.88E+02	14.8%	2.13E+02	17.7%	5.0
Ovaries	4.90E+01	30.5%	3.31E+02	30.5%	2.81E+02	34.3%	5.7
Red marrow	3.61E+01	1.7%	2.44E+02	1.7%	2.38E+02	2.1%	6.6
Colon	4.74E+01	2.3%	3.20E+02	2.3%	2.93E+02	2.9%	6.2
Lungs	4.77E+01	2.8%	3.22E+02	2.8%	2.79E+02	3.3%	5.9
Stomach	5.10E+01	10.4%	3.44E+02	10.4%	3.40E+02	12.8%	6.7
Bladder	5.00E+01	11.4%	3.38E+02	11.4%	3.36E+02	13.0%	6.7
Breasts	5.41E+01	6.7%	3.66E+02	6.7%	2.93E+02	8.2%	5.4
Liver	4.92E+01	3.0%	3.33E+02	3.0%	3.05E+02	3.8%	6.2
Oesophagus	3.66E+01	12.7%	2.47E+02	12.7%	2.55E+02	15.6%	7.0
Thyroid	4.20E+01	17.7%	2.84E+02	17.7%	3.14E+02	20.7%	7.5
Skin	4.30E+01	1.4%	2.91E+02	1.4%	2.64E+02	1.7%	6.1
Bone surface	3.72E+01	1.1%	2.52E+02	1.1%	2.42E+02	1.3%	6.5
Adrenals	6.14E+01	18.8%	4.15E+02	18.8%	5.00E+02	19.9%	8.1
Brain	5.33E+01	3.1%	3.61E+02	3.1%	3.28E+02	4.0%	6.2
Small intestine wall	4.35E+01	3.8%	2.94E+02	3.8%	2.81E+02	4.6%	6.5
Kidneys	4.74E+01	6.6%	3.20E+02	6.6%	2.77E+02	8.1%	5.8
Muscle	4.95E+01	0.6%	3.34E+02	0.6%	3.02E+02	0.7%	6.1
Pancreas	4.99E+01	8.7%	3.38E+02	8.7%	3.19E+02	10.9%	6.4
Spleen	3.49E+01	12.4%	2.36E+02	12.4%	2.14E+02	14.9%	6.1
Thymus	6.37E+01	16.1%	4.31E+02	16.1%	3.79E+02	17.5%	6.0
Uterus	4.37E+01	13.4%	2.96E+02	13.4%	2.65E+02	16.1%	6.1
Remainder	4.94E+01	0.5%	3.34E+02	0.5%	3.02E+02	0.7%	6.1

* Averaged absorbed dose in organ or tissue.

† Averaged dose equivalent in organ or tissue based on Q(L) in ICRP60.

Table A-2b. Organ absorbed dose, equivalent dose and dose equivalent per unit fluence for 30 MeV neutron for ISO irradiation

Organ or tissue	Absorbed dose*		Equivalent dose W_R = 6.04		Dose equivalent†		Mean quality factor Q-L in ICRP60
	($pGycm^2$)	error	($pSVcm^2$)	error	($pSVcm^2$)	error	
Testes	5.19E+01	15.4%	3.13E+02	15.4%	2.02E+02	19.7%	3.9
Ovaries	4.52E+01	32.9%	2.73E+02	32.9%	1.25E+02	26.7%	2.8
Red marrow	4.87E+01	1.6%	2.94E+02	1.6%	2.73E+02	2.2%	5.6
Colon	5.94E+01	2.3%	3.59E+02	2.3%	3.08E+02	3.2%	5.2
Lungs	5.92E+01	2.6%	3.58E+02	2.6%	2.84E+02	3.7%	4.8
Stomach	5.67E+01	9.8%	3.42E+02	9.8%	2.79E+02	14.1%	4.9
Bladder	6.10E+01	10.5%	3.68E+02	10.5%	3.72E+02	17.5%	6.1
Breasts	6.89E+01	6.5%	4.16E+02	6.5%	3.17E+02	9.1%	4.6
Liver	6.18E+01	2.4%	3.73E+02	2.4%	3.19E+02	3.4%	5.2
Oesophagus	6.24E+01	11.5%	3.77E+02	11.5%	2.76E+02	14.1%	4.4
Thyroid	7.45E+01	17.9%	4.50E+02	17.9%	4.68E+02	24.8%	6.3
Skin	4.99E+01	1.4%	3.01E+02	1.4%	2.79E+02	2.3%	5.6
Bone surface	4.90E+01	1.0%	2.96E+02	1.0%	2.72E+02	1.4%	5.6
Adrenals	6.38E+01	20.1%	3.85E+02	20.1%	3.40E+02	28.9%	5.3
Brain	6.57E+01	2.7%	3.97E+02	2.7%	3.41E+02	3.9%	5.2
Small intestine wall	5.79E+01	3.2%	3.50E+02	3.2%	3.11E+02	4.7%	5.4
Kidneys	6.11E+01	5.8%	3.69E+02	5.8%	3.19E+02	8.6%	5.2
Muscle	6.28E+01	0.5%	3.79E+02	0.5%	3.23E+02	0.7%	5.2
Pancreas	6.64E+01	7.0%	4.01E+02	7.0%	3.49E+02	9.9%	5.3
Spleen	4.45E+01	12.9%	2.69E+02	12.9%	2.43E+02	16.8%	5.5
Thymus	6.76E+01	17.2%	4.08E+02	17.2%	2.91E+02	25.8%	4.3
Uterus	4.84E+01	12.3%	2.92E+02	12.3%	2.42E+02	14.6%	5.0
Remainder	6.27E+01	0.5%	3.79E+02	0.5%	3.23E+02	0.7%	5.2

* Averaged absorbed dose in organ or tissue.

† Averaged dose equivalent in organ or tissue based on Q(L) in ICRP60.

Table A-2c. Organ absorbed dose, equivalent dose and dose equivalent per unit fluence for 50 MeV neutron for ISO irradiation

Organ or tissue	Absorbed dose*		Equivalent dose W_R = 5.50		Dose equivalent†		Mean quality factor Q-L in ICRP60
	($pGycm^2$)	error	($pSVcm^2$)	error	($pSVcm^2$)	error	
Testes	6.51E+01	15.6%	3.58E+02	15.6%	2.69E+02	18.1%	4.1
Ovaries	4.21E+01	34.5%	2.32E+02	34.5%	1.47E+02	46.2%	3.5
Red marrow	6.10E+01	1.5%	3.36E+02	1.5%	2.72E+02	2.0%	4.5
Colon	7.17E+01	2.2%	3.94E+02	2.2%	2.87E+02	2.9%	4.0
Lungs	7.12E+01	2.8%	3.91E+02	2.8%	2.63E+02	3.7%	3.7
Stomach	6.12E+01	10.9%	3.37E+02	10.9%	2.81E+02	14.4%	4.6
Bladder	7.23E+01	9.9%	3.98E+02	9.9%	4.37E+02	20.1%	6.0
Breasts	6.30E+01	8.0%	3.46E+02	8.0%	2.57E+02	10.1%	4.1
Liver	7.29E+01	2.5%	4.01E+02	2.5%	2.99E+02	3.7%	4.1
Oesophagus	6.08E+01	12.6%	3.34E+02	12.6%	2.41E+02	16.2%	4.0
Thyroid	7.94E+01	18.1%	4.37E+02	18.1%	2.39E+02	18.0%	3.0
Skin	5.04E+01	1.5%	2.77E+02	1.5%	2.27E+02	2.2%	4.5
Bone surface	6.07E+01	1.0%	3.34E+02	1.0%	2.69E+02	1.3%	4.4
Adrenals	7.21E+01	21.4%	3.97E+02	21.4%	3.03E+02	22.3%	4.2
Brain	7.50E+01	2.7%	4.12E+02	2.7%	3.01E+02	3.8%	4.0
Small intestine wall	7.07E+01	3.3%	3.89E+02	3.3%	3.07E+02	4.4%	4.3
Kidneys	6.83E+01	6.0%	3.76E+02	6.0%	2.67E+02	8.1%	3.9
Muscle	7.24E+01	0.5%	3.98E+02	0.5%	2.97E+02	0.7%	4.1
Pancreas	6.76E+01	7.0%	3.72E+02	7.0%	3.04E+02	9.7%	4.5
Spleen	6.17E+01	11.8%	3.39E+02	11.8%	3.64E+02	16.0%	5.9
Thymus	7.34E+01	21.6%	4.04E+02	21.6%	3.20E+02	28.4%	4.4
Uterus	8.04E+01	10.9%	4.42E+02	10.9%	2.73E+02	13.6%	3.4
Remainder	7.24E+01	0.5%	3.98E+02	0.5%	2.97E+02	0.6%	4.1

* Averaged absorbed dose in organ or tissue.

† Averaged dose equivalent in organ or tissue based on Q(L) in ICRP60.

Table A-2d. Organ absorbed dose, equivalent dose and dose equivalent per unit fluence for 100 MeV neutron for ISO irradiation

Organ or tissue	Absorbed dose*		Equivalent dose W_R = 5.16		Dose equivalent†		Mean quality factor Q-L in ICRP60
	($pGycm^2$)	error	($pSVcm^2$)	error	($pSVcm^2$)	error	
Testes	8.05E+01	14.7%	4.15E+02	14.7%	2.00E+02	17.0%	2.5
Ovaries	9.11E+01	25.4%	4.70E+02	25.4%	1.39E+02	25.1%	1.5
Red marrow	7.99E+01	1.6%	4.12E+02	1.6%	3.07E+02	2.0%	3.8
Colon	8.82E+01	2.2%	4.55E+02	2.2%	3.43E+02	3.4%	3.9
Lungs	9.18E+01	2.8%	4.74E+02	2.8%	3.04E+02	3.7%	3.3
Stomach	8.59E+01	9.8%	4.43E+02	9.8%	2.75E+02	13.7%	3.2
Bladder	1.01E+02	9.9%	5.20E+02	9.9%	3.05E+02	16.4%	3.0
Breasts	6.67E+01	8.6%	3.44E+02	8.6%	2.87E+02	10.9%	4.3
Liver	9.79E+01	2.6%	5.05E+02	2.6%	3.60E+02	3.3%	3.7
Oesophagus	9.07E+01	10.7%	4.68E+02	10.7%	2.93E+02	19.3%	3.2
Thyroid	8.92E+01	20.6%	4.60E+02	20.6%	2.36E+02	25.1%	2.6
Skin	5.64E+01	1.4%	2.91E+02	1.4%	2.63E+02	2.5%	4.7
Bone surface	7.92E+01	1.1%	4.09E+02	1.1%	3.07E+02	1.3%	3.9
Adrenals	9.96E+01	18.2%	5.14E+02	18.2%	2.86E+02	27.4%	2.9
Brain	8.72E+01	3.2%	4.50E+02	3.2%	3.43E+02	4.1%	3.9
Small intestine wall	9.45E+01	3.3%	4.88E+02	3.3%	3.54E+02	4.0%	3.7
Kidneys	8.52E+01	6.2%	4.40E+02	6.2%	2.51E+02	7.5%	2.9
Muscle	8.49E+01	0.5%	4.38E+02	0.5%	3.27E+02	0.7%	3.8
Pancreas	7.62E+01	7.9%	3.93E+02	7.9%	3.03E+02	11.2%	4.0
Spleen	8.45E+01	11.7%	4.36E+02	11.7%	3.40E+02	17.3%	4.0
Thymus	7.61E+01	19.4%	3.93E+02	19.4%	3.75E+02	22.1%	4.9
Uterus	1.07E+02	10.6%	5.52E+02	10.6%	5.01E+02	14.3%	4.7
Remainder	8.51E+01	0.5%	4.93E+02	0.5%	3.27E+02	0.6%	3.8

* Averaged absorbed dose in organ or tissue.

† Averaged dose equivalent in organ or tissue based on Q(L) in ICRP60.

Table A-2e. Organ absorbed dose, equivalent dose and dose equivalent per unit fluence for 200 MeV neutron for ISO irradiation

Organ or tissue	Absorbed dose*		Equivalent dose W_R = 5.04		Dose equivalent†		Mean quality factor Q-L in ICRP60
	($pGycm^2$)	error	($pSVcm^2$)	error	($pSVcm^2$)	error	
Testes	8.68E+01	13.5%	4.37E+02	13.5%	1.86E+02	18.5%	2.1
Ovaries	1.05E+02	18.9%	5.31E+02	18.9%	2.82E+02	27.3%	2.7
Red marrow	9.89E+01	1.5%	4.99E+02	1.5%	3.40E+02	2.0%	3.4
Colon	1.17E+02	1.9%	5.88E+02	1.9%	3.63E+02	3.4%	3.1
Lungs	9.89E+01	2.6%	4.98E+02	2.6%	3.18E+02	4.3%	3.2
Stomach	1.17E+02	7.5%	5.92E+02	7.5%	3.86E+02	12.5%	3.3
Bladder	1.28E+02	8.3%	6.46E+02	8.3%	4.02E+02	20.1%	3.1
Breasts	7.29E+01	8.1%	3.67E+02	8.1%	2.40E+02	12.6%	3.3
Liver	1.11E+02	2.7%	5.58E+02	2.7%	3.47E+02	3.3%	3.1
Oesophagus	1.18E+02	10.3%	5.95E+02	10.3%	3.93E+02	17.2%	3.3
Thyroid	8.02E+01	19.1%	4.04E+02	19.1%	2.68E+02	28.9%	3.3
Skin	6.91E+01	1.3%	3.48E+02	1.3%	2.83E+02	2.7%	4.1
Bone surface	9.41E+01	1.0%	4.74E+02	1.0%	3.27E+02	1.3%	3.5
Adrenals	1.13E+02	15.7%	5.70E+02	15.7%	4.35E+02	30.9%	3.8
Brain	8.93E+01	3.6%	4.50E+02	3.6%	3.06E+02	4.2%	3.4
Small intestine wall	1.20E+02	3.2%	6.03E+02	3.2%	3.74E+02	4.0%	3.1
Kidneys	1.08E+02	5.5%	5.43E+02	5.5%	3.40E+02	7.9%	3.2
Muscle	9.86E+01	0.6%	4.97E+02	0.6%	3.36E+02	0.7%	3.4
Pancreas	1.16E+02	7.1%	5.83E+02	7.1%	3.71E+02	8.4%	3.2
Spleen	1.32E+02	9.3%	6.65E+02	9.3%	5.46E+02	13.9%	4.1
Thymus	1.39E+02	16.6%	6.99E+02	16.6%	4.78E+02	20.4%	3.4
Uterus	1.10E+02	10.1%	5.52E+02	10.1%	3.41E+02	15.6%	3.1
Remainder	9.89E+01	0.6%	4.98E+02	0.6%	3.36E+02	0.7%	3.4

* Averaged absorbed dose in organ or tissue.

† Averaged dose equivalent in organ or tissue based on Q(L) in ICRP60.

Table A-2f. Organ absorbed dose, equivalent dose and dose equivalent per unit fluence for 500 MeV neutron for ISO irradiation

Organ or tissue	Absorbed dose*		Equivalent dose W_R = 5.01		Dose equivalent†		Mean quality factor Q-L in ICRP60
	($pGycm^2$)	error	($pSVcm^2$)	error	($pSVcm^2$)	error	
Testes	1.54E+02	11.1%	7.73E+02	11.1%	4.49E+02	17.9%	2.9
Ovaries	2.08E+02	28.1%	1.04E+03	28.1%	5.16E+02	60.4%	2.5
Red marrow	1.40E+02	1.3%	7.03E+02	1.3%	4.90E+02	2.0%	3.5
Colon	1.68E+02	1.6%	8.43E+02	1.6%	5.79E+02	3.1%	3.4
Lungs	1.31E+02	2.4%	6.57E+02	2.4%	4.68E+02	3.8%	3.6
Stomach	1.47E+02	6.6%	7.35E+02	6.6%	4.69E+02	12.4%	3.2
Bladder	1.61E+02	6.6%	8.06E+02	6.6%	4.29E+02	14.1%	2.7
Breasts	1.01E+02	7.6%	5.08E+02	7.6%	3.48E+02	11.2%	3.4
Liver	1.53E+02	2.3%	7.66E+02	2.3%	4.89E+02	3.0%	3.2
Oesophagus	1.41E+02	8.4%	7.08E+02	8.4%	5.01E+02	17.7%	3.5
Thyroid	1.64E+02	16.2%	8.20E+02	16.2%	6.37E+02	30.4%	3.9
Skin	9.66E+01	1.2%	4.84E+02	1.2%	3.76E+02	2.5%	3.9
Bone surface	1.34E+02	0.9%	6.72E+02	0.9%	4.73E+02	1.2%	3.5
Adrenals	1.89E+02	13.9%	9.46E+02	13.9%	4.50E+02	20.1%	2.4
Brain	1.29E+02	3.1%	6.44E+02	3.1%	4.64E+02	3.6%	3.6
Small intestine wall	1.59E+02	2.8%	7.95E+02	2.8%	4.89E+02	3.7%	3.1
Kidneys	1.53E+02	4.6%	7.65E+02	4.6%	5.23E+02	7.1%	3.4
Muscle	1.38E+02	0.6%	6.92E+02	0.6%	4.70E+02	0.6%	3.4
Pancreas	1.45E+02	6.5%	7.28E+02	6.5%	4.56E+02	10.2%	3.1
Spleen	1.37E+02	8.5%	6.84E+02	8.5%	4.52E+02	16.0%	3.3
Thymus	1.40E+02	16.4%	7.01E+02	16.4%	2.64E+02	23.6%	1.9
Uterus	1.74E+02	8.3%	8.70E+02	8.3%	7.09E+02	12.9%	4.1
Remainder	1.38E+02	0.6%	6.94E+02	0.6%	4.70E+02	0.6%	3.4

* Averaged absorbed dose in organ or tissue.

† Averaged dose equivalent in organ or tissue based on Q(L) in ICRP60.

Table A-2g. Organ absorbed dose, equivalent dose and dose equivalent per unit fluence for 1000 MeV neutron for ISO irradiation

Organ or tissue	Absorbed dose*		Equivalent dose $W_R = 5.00$		Dose equivalent†		Mean quality factor Q-L in ICRP60
	($pGycm^2$)	error	($pSVcm^2$)	error	($pSVcm^2$)	error	
Testes	2.00E+02	10.0%	2.00E+02	10.0%	5.22E+02	14.3%	2.6
Ovaries	2.54E+02	13.5%	2.54E+02	13.5%	4.81E+02	29.8%	1.9
Red marrow	2.29E+02	1.2%	2.29E+02	1.2%	7.56E+02	1.7%	3.3
Colon	2.61E+02	1.3%	2.61E+02	1.3%	7.76E+02	2.4%	3.0
Lungs	2.18E+02	2.0%	2.18E+02	2.0%	7.03E+02	3.3%	3.2
Stomach	2.89E+02	6.2%	2.89E+02	6.2%	8.43E+02	11.2%	2.9
Bladder	2.68E+02	6.3%	2.68E+02	6.3%	7.66E+02	13.9%	2.9
Breasts	1.59E+02	5.5%	1.59E+02	5.5%	5.13E+02	9.7%	3.2
Liver	2.55E+02	2.0%	2.55E+02	2.0%	7.78E+02	2.4%	3.1
Oesophagus	2.35E+02	6.3%	2.35E+02	6.3%	6.04E+02	13.5%	2.6
Thyroid	2.18E+02	11.3%	2.18E+02	11.3%	6.94E+02	23.4%	3.2
Skin	1.61E+02	1.1%	1.61E+02	1.1%	5.91E+02	2.1%	3.7
Bone surface	2.19E+02	0.8%	2.19E+02	0.8%	7.18E+02	1.1%	3.3
Adrenals	2.55E+02	13.8%	2.55E+02	13.8%	6.83E+02	31.4%	2.7
Brain	2.01E+02	2.6%	2.01E+02	2.6%	6.54E+02	3.2%	3.2
Small intestine wall	2.75E+02	2.3%	2.75E+02	2.3%	8.19E+02	3.1%	3.0
Kidneys	2.46E+02	3.8%	2.46E+02	3.8%	7.01E+02	5.9%	2.9
Muscle	2.23E+02	0.5%	2.23E+02	0.5%	7.00E+02	0.5%	3.1
Pancreas	2.41E+02	5.4%	2.41E+02	5.4%	7.47E+02	7.6%	3.1
Spleen	2.58E+02	6.9%	2.58E+02	6.9%	8.18E+02	12.6%	3.2
Thymus	2.43E+02	11.0%	2.43E+02	11.0%	8.50E+02	21.5%	3.5
Uterus	2.61E+02	6.6%	2.61E+02	6.6%	7.09E+02	11.1%	2.7
Remainder	2.23E+02	0.5%	2.23E+02	0.5%	7.01E+02	0.5%	3.1

* Averaged absorbed dose in organ or tissue.

† Averaged dose equivalent in organ or tissue based on Q(L) in ICRP60.

Table A-2h. Organ absorbed dose, equivalent dose and dose equivalent per unit fluence for 2000 MeV neutron for ISO irradiation

Organ or tissue	Absorbed dose*		Equivalent dose $W_R = 5.00$		Dose equivalent†		Mean quality factor Q-L in ICRP60
	($pGycm^2$)	error	($pSVcm^2$)	error	($pSVcm^2$)	error	
Testes	3.17E+02	9.3%	1.59E+03	9.3%	7.74E+02	18.3%	2.4
Ovaries	3.40E+02	16.6%	1.70E+03	16.6%	8.14E+02	36.5%	2.4
Red marrow	3.09E+02	1.1%	1.55E+03	1.1%	9.15E+02	1.4%	3.0
Colon	3.46E+02	1.2%	1.73E+03	1.2%	9.28E+02	2.2%	2.7
Lungs	2.85E+02	1.9%	1.43E+03	1.9%	8.18E+02	3.1%	2.9
Stomach	3.36E+02	5.9%	1.68E+03	5.9%	7.06E+02	10.2%	2.1
Bladder	3.87E+02	5.3%	1.93E+03	5.3%	1.09E+03	11.5%	2.8
Breasts	2.09E+02	6.4%	1.05E+03	6.4%	6.17E+02	10.3%	3.0
Liver	3.19E+02	1.9%	1.60E+03	1.9%	8.87E+02	2.4%	2.8
Oesophagus	3.18E+02	6.1%	1.59E+03	6.1%	9.36E+02	12.3%	2.9
Thyroid	2.52E+02	9.9%	1.26E+03	9.9%	8.24E+02	20.0%	3.3
Skin	2.09E+02	1.0%	1.05E+03	1.0%	6.70E+02	2.1%	3.2
Bone surface	2.93E+02	0.7%	1.47E+03	0.7%	8.81E+02	1.0%	3.0
Adrenals	3.07E+02	10.0%	1.54E+03	10.0%	7.57E+02	21.7%	2.5
Brain	2.63E+02	2.4%	1.32E+03	2.4%	7.96E+02	2.9%	3.0
Small intestine wall	3.69E+02	2.1%	1.84E+03	2.1%	1.02E+03	2.8%	2.8
Kidneys	3.17E+02	3.6%	1.59E+03	3.6%	8.36E+02	6.0%	2.6
Muscle	2.94E+02	0.5%	1.47E+03	0.5%	8.48E+02	0.5%	2.9
Pancreas	3.16E+02	4.7%	1.58E+03	4.7%	7.84E+02	7.2%	2.5
Spleen	3.53E+02	6.0%	1.76E+03	6.0%	8.89E+02	10.2%	2.5
Thymus	3.29E+02	9.8%	1.64E+03	9.8%	1.06E+03	17.7%	3.2
Uterus	3.86E+02	6.5%	1.93E+03	6.5%	1.16E+03	11.0%	3.0
Remainder	2.96E+02	0.5%	1.48E+03	0.5%	8.50E+02	0.5%	2.9

* Averaged absorbed dose in organ or tissue.

† Averaged dose equivalent in organ or tissue based on Q(L) in ICRP60.

Table A-2i. Organ absorbed dose, equivalent dose and dose equivalent per unit fluence for 5000 MeV neutron for ISO irradiation

Organ or tissue	Absorbed dose*		Equivalent dose $W_R = 5.00$		Dose equivalent†		Mean quality factor Q-L in ICRP60
	($pGycm^2$)	error	($pSVcm^2$)	error	($pSVcm^2$)	error	
Testes	3.98E+02	8.1%	1.99E+03	8.1%	9.39E+02	13.0%	2.4
Ovaries	5.37E+02	16.6%	2.69E+03	16.6%	1.54E+03	30.3%	2.9
Red marrow	4.44E+02	0.9%	2.22E+03	0.9%	1.22E+03	1.4%	2.8
Colon	4.92E+02	1.1%	2.46E+03	1.1%	1.33E+03	2.0%	2.7
Lungs	3.86E+02	1.7%	1.93E+03	1.7%	1.06E+03	2.7%	2.7
Stomach	4.74E+02	4.4%	2.37E+03	4.4%	1.18E+03	8.1%	2.5
Bladder	4.71E+02	5.1%	2.35E+03	5.1%	1.28E+03	10.9%	2.7
Breasts	3.06E+02	6.0%	1.53E+03	6.0%	8.74E+02	8.8%	2.9
Liver	4.59E+02	1.7%	2.29E+03	1.7%	1.20E+03	2.1%	2.6
Oesophagus	4.37E+02	5.4%	2.19E+03	5.4%	9.43E+02	12.1%	2.2
Thyroid	4.11E+02	9.4%	2.05E+03	9.4%	7.70E+02	16.8%	1.9
Skin	2.82E+02	1.0%	1.41E+03	1.0%	8.35E+02	1.9%	3.0
Bone surface	4.04E+02	0.7%	2.02E+03	0.7%	1.14E+03	0.9%	2.8
Adrenals	4.96E+02	9.3%	2.48E+03	9.3%	1.19E+03	22.3%	2.4
Brain	3.39E+02	2.3%	1.69E+03	2.3%	9.36E+02	2.9%	2.8
Small intestine wall	4.95E+02	1.9%	2.48E+03	1.9%	1.27E+03	2.6%	2.6
Kidneys	4.60E+02	3.2%	2.30E+03	3.2%	1.23E+03	5.0%	2.7
Muscle	4.02E+02	0.4%	2.01E+03	0.4%	1.09E+03	0.5%	2.7
Pancreas	4.50E+02	4.0%	2.25E+03	4.0%	1.22E+03	7.0%	2.7
Spleen	5.52E+02	5.2%	2.76E+03	5.2%	1.29E+03	8.8%	2.3
Thymus	5.24E+02	14.4%	2.62E+03	14.4%	2.36E+03	39.2%	4.5
Uterus	5.10E+02	5.4%	2.55E+03	5.4%	1.40E+03	9.1%	2.8
Remainder	4.03E+02	0.4%	2.01E+03	0.4%	1.09E+03	0.5%	2.7

* Averaged absorbed dose in organ or tissue.

† Averaged dose equivalent in organ or tissue based on Q(L) in ICRP60.

Table A-2j. Organ absorbed dose, equivalent dose and dose equivalent per unit fluence for 10000 MeV neutron for ISO irradiation

Organ or tissue	Absorbed dose*		Equivalent dose $W_R = 5.00$		Dose equivalent†		Mean quality factor Q-L in ICRP60
	($pGycm^2$)	error	($pSVcm^2$)	error	($pSVcm^2$)	error	
Testes	4.17E+02	8.0%	2.08E+03	8.0%	1.18E+03	17.5%	2.8
Ovaries	5.26E+02	10.1%	2.63E+03	10.1%	1.36E+03	24.9%	2.6
Red marrow	5.02E+02	1.0%	2.51E+03	1.0%	1.39E+03	1.6%	2.8
Colon	5.30E+02	1.0%	2.65E+03	1.0%	1.39E+03	1.9%	2.6
Lungs	4.40E+02	1.8%	2.20E+03	1.8%	1.25E+03	2.8%	2.8
Stomach	6.05E+02	4.5%	3.02E+03	4.5%	1.81E+03	8.9%	3.0
Bladder	4.90E+02	4.0%	2.45E+03	4.0%	1.22E+03	10.3%	2.5
Breasts	3.72E+02	6.4%	1.86E+03	6.4%	1.09E+03	8.3%	2.9
Liver	5.28E+02	1.7%	2.64E+03	1.7%	1.40E+03	2.2%	2.7
Oesophagus	5.45E+02	6.8%	2.73E+03	6.8%	1.55E+03	13.6%	2.8
Thyroid	5.46E+02	9.0%	2.73E+03	9.0%	1.55E+03	15.9%	2.8
Skin	3.31E+02	1.0%	1.65E+03	1.0%	1.02E+03	2.3%	3.1
Bone surface	4.62E+02	0.7%	2.31E+03	0.7%	1.31E+03	1.0%	2.8
Adrenals	5.49E+02	7.9%	2.74E+03	7.9%	1.36E+03	16.2%	2.5
Brain	3.96E+02	2.2%	1.98E+03	2.2%	1.13E+03	2.9%	2.9
Small intestine wall	5.77E+02	2.5%	2.88E+03	2.5%	1.44E+03	2.6%	2.5
Kidneys	4.87E+02	2.9%	2.43E+03	2.9%	1.30E+03	5.0%	2.7
Muscle	4.61E+02	0.4%	2.31E+03	0.4%	1.25E+03	0.5%	2.7
Pancreas	5.59E+02	5.0%	2.80E+03	5.0%	1.55E+03	7.9%	2.8
Spleen	5.82E+02	5.1%	2.91E+03	5.1%	1.48E+03	8.4%	2.5
Thymus	5.08E+02	10.0%	2.54E+03	10.0%	1.61E+03	20.6%	3.2
Uterus	5.54E+02	5.0%	2.77E+03	5.0%	1.38E+03	8.5%	2.5
Remainder	4.63E+02	0.4%	2.31E+03	0.4%	1.26E+03	0.4%	2.7

* Averaged absorbed dose in organ or tissue.

† Averaged dose equivalent in organ or tissue based on Q(L) in ICRP60.

Table A-2k. Organ absorbed dose, equivalent dose and dose equivalent per unit fluence for 20 MeV proton for ISO irradiation

Organ or tissue	Absorbed dose*		Equivalent dose $W_R = 5$		Dose equivalent†		Mean quality factor Q-L in ICRP60
	($pGycm^2$)	error	($pSVcm^2$)	error	($pSVcm^2$)	error	
Testes	1.98E+01	16.7%	9.92E+01	16.7%	6.82E+01	15.5%	3.4
Ovaries	–	–	–	–	–	–	–
Red marrow	2.50E+01	1.4%	1.25E+02	1.4%	7.43E+01	1.3%	3.0
Colon	8.00E-02	43.0%	4.00E-01	43.0%	8.00E-02	43.0%	1.0
Lungs	–	–	–	–	–	–	–
Stomach	–	–	–	–	–	–	–
Bladder	–	–	–	–	–	–	–
Breasts	3.77E+02	2.3%	1.88E+03	2.3%	9.65E+02	2.2%	2.6
Liver	–	–	–	–	–	–	–
Oesophagus	–	–	–	–	–	–	–
Thyroid	–	–	–	–	–	–	–
Skin	2.04E+03	0.2%	1.02E+04	0.2%	2.87E+03	0.3%	1.4
Bone surface	2.43E+01	1.0%	1.22E+02	1.0%	7.07E+01	0.9%	2.9
Adrenals	–	–	–	–	–	–	–
Brain	–	–	–	–	–	–	–
Small intestine wall	–	–	–	–	–	–	–
Kidneys	–	–	–	–	–	–	–
Muscle	9.03E+01	0.3%	4.51E+02	0.3%	2.35E+02	0.3%	2.6
Pancreas	–	–	–	–	–	–	–
Spleen	–	–	–	–	–	–	–
Thymus	–	–	–	–	–	–	–
Uterus	–	–	–	–	–	–	–
Remainder	8.51E+01	0.3%	4.26E+02	0.3%	2.21E+02	0.3%	2.6

* Averaged absorbed dose in organ or tissue.

† Averaged dose equivalent in organ or tissue based on Q(L) in ICRP60.

Table A-2l. Organ absorbed dose, equivalent dose and dose equivalent per unit fluence for 30 MeV proton for ISO irradiation

Organ or tissue	Absorbed dose*		Equivalent dose $W_R = 5$		Dose equivalent†		Mean quality factor Q-L in ICRP60
	($pGycm^2$)	error	($pSVcm^2$)	error	($pSVcm^2$)	error	
Testes	1.63E+02	8.6%	8.17E+02	8.6%	3.54E+02	8.1%	2.2
Ovaries	–	–	–	–	–	–	–
Red marrow	1.28E+02	0.9%	6.41E+02	0.9%	2.60E+02	0.8%	2.0
Colon	4.90E-01	39.6%	2.45E+00	39.6%	3.68E+00	52.2%	7.5
Lungs	1.20E-01	58.6%	6.00E-01	58.6%	2.50E-01	57.8%	2.1
Stomach	1.10E-01	100.0%	5.50E-01	100.0%	7.50E-01	100.0%	6.8
Bladder	–	–	–	–	–	–	–
Breasts	8.42E+02	2.1%	4.21E+03	2.1%	1.49E+03	2.1%	1.8
Liver	1.00E-02	71.6%	5.00E-02	71.6%	1.20E-01	75.7%	12.0
Oesophagus	–	–	–	–	–	–	–
Thyroid	–	–	–	–	–	–	–
Skin	1.50E+03	0.3%	7.50E+03	0.3%	1.78E+03	0.4%	1.2
Bone surface	1.18E+02	0.6%	5.88E+02	0.6%	2.37E+02	0.6%	2.0
Adrenals	–	–	–	–	–	–	–
Brain	3.00E-02	76.7%	1.50E-01	76.7%	1.50E-01	73.7%	5.0
Small intestine wall	1.90E-01	59.5%	9.50E-01	59.5%	2.67E+00	50.8%	14.1
Kidneys	3.00E-02	71.0%	1.50E-01	71.0%	3.60E-01	71.8%	12.0
Muscle	2.09E+02	0.2%	1.05E+03	0.2%	3.76E+02	0.2%	1.8
Pancreas	2.50E-01	100.0%	1.25E+00	100.0%	5.00E-01	100.0%	2.0
Spleen	–	–	–	–	–	–	–
Thymus	–	–	–	–	–	–	–
Uterus	1.20E-01	73.8%	6.00E-01	73.8%	1.36E+00	70.8%	11.3
Remainder	1.98E+02	0.2%	9.88E+02	0.2%	3.54E+02	0.2%	1.8

* Averaged absorbed dose in organ or tissue.

† Averaged dose equivalent in organ or tissue based on Q(L) in ICRP60.

Table A-2m. Organ absorbed dose, equivalent dose and dose equivalent per unit fluence for 50 MeV proton for ISO irradiation

Organ or tissue	Absorbed dose*		Equivalent dose $W_R = 5$		Dose equivalent†		Mean quality factor Q-L in ICRP60
	($pGycm^2$)	error	($pSVcm^2$)	error	($pSVcm^2$)	error	
Testes	6.46E+02	5.9%	3.23E+03	5.9%	9.94E+02	5.9%	1.5
Ovaries	–	–	–	–	–	–	–
Red marrow	3.08E+02	0.6%	1.54E+03	0.6%	4.45E+02	0.7%	1.4
Colon	4.60E-01	17.3%	2.30E+00	17.3%	1.18E+00	15.7%	2.6
Lungs	2.16E+01	4.5%	1.08E+02	4.5%	4.83E+01	4.8%	2.2
Stomach	1.01E+00	46.1%	5.05E+00	46.1%	1.24E+01	48.1%	12.3
Bladder	2.69E+00	35.0%	1.35E+01	35.0%	1.16E+01	33.2%	4.3
Breasts	1.30E+03	2.3%	6.51E+03	2.3%	1.76E+03	2.4%	1.4
Liver	3.25E+00	6.3%	1.63E+01	6.3%	1.12E+01	7.7%	3.4
Oesophagus	8.70E-01	99.3%	4.35E+00	99.3%	1.92E+00	93.0%	2.2
Thyroid	2.72E+02	11.0%	1.36E+03	11.0%	4.76E+02	10.7%	1.8
Skin	1.05E+03	0.3%	5.23E+03	0.3%	1.14E+03	0.5%	1.1
Bone surface	3.16E+02	0.5%	1.58E+03	0.5%	4.65E+02	0.5%	1.5
Adrenals	–	–	–	–	–	–	–
Brain	7.20E+01	2.1%	3.60E+02	2.1%	1.62E+02	2.1%	2.2
Small intestine wall	3.50E-01	47.3%	1.75E+00	47.3%	4.53E+00	56.0%	12.9
Kidneys	2.45E+01	6.7%	1.23E+02	6.7%	6.35E+01	6.3%	2.6
Muscle	4.02E+02	0.2%	2.01E+03	0.2%	5.84E+02	0.2%	1.5
Pancreas	2.00E-02	60.3%	1.00E-01	60.3%	3.60E-01	59.5%	18.0
Spleen	2.90E-01	70.5%	1.45E+00	70.5%	2.17E+00	70.5%	7.5
Thymus	2.40E+01	24.4%	1.20E+02	24.4%	7.57E+01	21.8%	3.1
Uterus	–	–	–	–	–	–	–
Remainder	3.81E+02	0.2%	1.91E+03	0.2%	5.55E+02	0.2%	1.5

* Averaged absorbed dose in organ or tissue.

† Averaged dose equivalent in organ or tissue based on Q(L) in ICRP60.

Table A-2n. Organ absorbed dose, equivalent dose and dose equivalent per unit fluence for 100 MeV proton for ISO irradiation

Organ or tissue	Absorbed dose*		Equivalent dose $W_R = 5$		Dose equivalent†		Mean quality factor Q-L in ICRP60
	($pGycm^2$)	error	($pSVcm^2$)	error	($pSVcm^2$)	error	
Testes	6.56E+02	4.9%	3.28E+03	4.9%	8.18E+02	5.9%	1.2
Ovaries	6.25E+00	100.0%	3.13E+01	100.0%	4.39E+01	100.0%	7.0
Red marrow	5.83E+02	0.6%	2.91E+03	0.6%	7.58E+02	0.7%	1.3
Colon	2.26E+02	1.5%	1.13E+03	1.5%	3.40E+02	1.8%	1.5
Lungs	9.13E+02	1.0%	4.56E+03	1.0%	1.22E+03	1.1%	1.3
Stomach	3.76E+02	4.8%	1.88E+03	4.8%	5.24E+02	6.1%	1.4
Bladder	4.36E+02	4.8%	2.18E+03	4.8%	5.85E+02	6.6%	1.3
Breasts	8.42E+02	2.7%	4.21E+03	2.7%	9.70E+02	3.4%	1.2
Liver	5.94E+02	1.2%	2.97E+03	1.2%	8.04E+02	1.3%	1.4
Oesophagus	6.40E+01	14.8%	3.20E+02	14.8%	1.04E+02	14.3%	1.6
Thyroid	7.64E+02	6.6%	3.82E+03	6.6%	1.03E+03	7.9%	1.3
Skin	7.85E+02	0.4%	3.93E+03	0.4%	1.03E+03	0.6%	1.3
Bone surface	6.98E+02	0.4%	3.49E+03	0.4%	9.18E+02	0.4%	1.3
Adrenals	4.92E+02	8.3%	2.46E+03	8.3%	6.44E+02	10.0%	1.3
Brain	1.02E+03	1.2%	5.08E+03	1.2%	1.35E+03	1.2%	1.3
Small intestine wall	1.77E+02	2.1%	8.87E+02	2.1%	2.72E+02	2.4%	1.5
Kidneys	6.69E+02	2.2%	3.35E+03	2.2%	8.48E+02	2.6%	1.3
Muscle	7.25E+02	0.2%	3.62E+03	0.2%	9.26E+02	0.2%	1.3
Pancreas	5.74E+02	3.5%	2.87E+03	3.5%	8.02E+02	3.9%	1.4
Spleen	4.73E+01	13.1%	2.37E+02	13.1%	8.40E+01	12.5%	1.8
Thymus	6.91E+02	6.5%	3.45E+03	6.5%	8.48E+02	7.4%	1.2
Uterus	1.12E+02	10.9%	5.58E+02	10.9%	1.99E+02	13.0%	1.8
Remainder	7.11E+02	0.2%	3.56E+03	0.2%	9.10E+02	0.2%	1.3

* Averaged absorbed dose in organ or tissue.

† Averaged dose equivalent in organ or tissue based on Q(L) in ICRP60.

Table A-2o. Organ absorbed dose, equivalent dose and dose equivalent per unit fluence for 200 MeV proton for ISO irradiation

Organ or tissue	Absorbed dose*		Equivalent dose $W_R = 5$		Dose equivalent†		Mean quality factor Q-L in ICRP60
	($pGycm^2$)	error	($pSVcm^2$)	error	($pSVcm^2$)	error	
Testes	9.50E+02	3.8%	4.75E+03	3.8%	1.16E+02	5.7%	1.2
Ovaries	9.49E+02	6.4%	4.75E+03	6.4%	1.34E+03	16.6%	1.4
Red marrow	8.59E+02	0.5%	4.29E+03	0.5%	1.10E+03	0.7%	1.3
Colon	8.91E+02	0.6%	4.45E+03	0.6%	1.15E+03	1.1%	1.3
Lungs	9.06E+02	0.7%	4.53E+03	0.7%	1.15E+03	1.2%	1.3
Stomach	9.45E+02	2.5%	4.73E+03	2.5%	1.21E+03	4.0%	1.3
Bladder	9.37E+02	2.5%	4.69E+03	2.5%	1.17E+03	4.0%	1.3
Breasts	8.32E+02	2.1%	4.16E+03	2.1%	1.05E+02	3.2%	1.3
Liver	8.89E+02	1.0%	4.45E+03	1.0%	1.10E+03	1.2%	1.2
Oesophagus	9.07E+02	2.7%	4.53E+03	2.7%	1.13E+02	4.8%	1.2
Thyroid	9.88E+02	4.8%	4.94E+03	4.8%	1.16E+02	7.8%	1.2
Skin	7.94E+02	0.3%	3.97E+03	0.3%	1.09E+02	0.6%	1.4
Bone surface	8.33E+02	0.3%	4.17E+03	0.3%	1.07E+03	0.5%	1.3
Adrenals	9.43E+02	4.5%	4.72E+03	4.5%	1.10E+03	7.4%	1.2
Brain	8.59E+02	1.2%	4.30E+03	1.2%	1.10E+02	1.5%	1.3
Small intestine wall	9.41E+02	1.2%	4.70E+03	1.2%	1.18E+03	1.4%	1.3
Kidneys	8.89E+02	1.7%	4.44E+03	1.7%	1.13E+03	2.4%	1.3
Muscle	8.83E+02	0.2%	4.41E+03	0.2%	1.12E+03	0.3%	1.3
Pancreas	8.62E+02	2.3%	4.31E+03	2.3%	1.10E+03	3.2%	1.3
Spleen	9.73E+02	3.0%	4.86E+03	3.0%	1.15E+03	4.3%	1.2
Thymus	9.92E+02	4.3%	4.96E+03	4.3%	1.24E+03	7.5%	1.3
Uterus	1.01E+03	3.2%	5.06E+03	3.2%	1.31E+03	4.5%	1.3
Remainder	8.83E+02	0.2%	4.42E+03	0.2%	1.12E+03	0.3%	1.3

* Averaged absorbed dose in organ or tissue.

† Averaged dose equivalent in organ or tissue based on Q(L) in ICRP60.

Table A-2p. Organ absorbed dose, equivalent dose and dose equivalent per unit fluence for 500 MeV proton for ISO irradiation

Organ or tissue	Absorbed dose*		Equivalent dose $W_R = 5$		Dose equivalent†		Mean quality factor Q-L in ICRP60
	($pGycm^2$)	error	($pSVcm^2$)	error	($pSVcm^2$)	error	
Testes	6.35E+02	4.0%	3.17E+03	4.0%	1.15E+03	11.3%	1.8
Ovaries	5.85E+02	5.6%	2.92E+03	5.6%	6.19E+02	6.2%	1.1
Red marrow	5.68E+02	0.5%	2.84E+03	0.5%	8.95E+02	1.0%	1.6
Colon	5.87E+02	0.6%	2.94E+03	0.6%	9.04E+02	1.7%	1.5
Lungs	5.82E+02	0.8%	2.91E+03	0.8%	9.04E+02	2.0%	1.6
Stomach	5.92E+02	2.6%	2.96E+03	2.6%	8.74E+02	6.8%	1.5
Bladder	6.12E+02	2.6%	3.06E+03	2.6%	9.01E+02	7.2%	1.5
Breasts	5.47E+02	2.3%	2.73E+03	2.3%	8.17E+02	5.4%	1.5
Liver	5.96E+02	1.0%	2.98E+03	1.0%	9.13E+02	1.6%	1.5
Oesophagus	5.69E+02	3.2%	2.85E+03	3.2%	7.99E+02	7.7%	1.4
Thyroid	6.13E+02	6.3%	3.06E+03	6.3%	1.07E+03	16.9%	1.7
Skin	5.27E+02	0.3%	2.63E+03	0.3%	8.14E+02	1.1%	1.5
Bone surface	5.54E+02	0.4%	2.77E+03	0.4%	8.66E+02	0.7%	1.6
Adrenals	5.50E+02	4.7%	2.75E+03	4.7%	7.53E+02	11.2%	1.4
Brain	5.67E+02	1.2%	2.84E+03	1.2%	8.55E+02	1.9%	1.5
Small intestine wall	6.12E+02	1.2%	3.06E+03	1.2%	9.36E+02	2.1%	1.5
Kidneys	5.77E+02	1.8%	2.88E+03	1.8%	8.63E+02	3.8%	1.5
Muscle	5.81E+02	0.3%	2.91E+03	0.3%	8.94E+02	0.3%	1.5
Pancreas	6.17E+02	2.4%	3.09E+03	2.4%	1.02E+03	4.6%	1.7
Spleen	6.01E+02	3.1%	3.00E+03	3.1%	8.38E+02	6.1%	1.4
Thymus	5.76E+02	5.3%	2.88E+03	5.3%	9.07E+02	14.1%	1.6
Uterus	6.50E+02	3.4%	3.25E+03	3.4%	1.09E+03	7.9%	1.7
Remainder	5.82E+02	0.2%	2.91E+03	0.2%	8.94E+02	0.3%	1.5

* Averaged absorbed dose in organ or tissue.

† Averaged dose equivalent in organ or tissue based on Q(L) in ICRP60.

Table A-2q. Organ absorbed dose, equivalent dose and dose equivalent per unit fluence for 1000 MeV proton for ISO irradiation

Organ or tissue	Absorbed dose*		Equivalent dose $W_R = 5$		Dose equivalent†		Mean quality factor Q-L in ICRP60
	($pGycm^2$)	error	($pSVcm^2$)	error	($pSVcm^2$)	error	
Testes	5.98E+02	4.2%	2.99E+03	4.2%	1.14E+03	10.5%	1.9
Ovaries	6.05E+02	8.2%	3.02E+03	8.2%	1.16E+03	27.0%	1.9
Red marrow	5.66E+02	0.6%	2.83E+03	0.6%	1.08E+03	1.2%	1.9
Colon	5.97E+02	0.7%	2.99E+03	0.7%	1.04E+03	1.7%	1.7
Lungs	5.85E+02	0.9%	2.92E+03	0.9%	1.09E+03	2.2%	1.9
Stomach	6.14E+02	3.0%	3.07E+03	3.0%	1.19E+03	7.6%	1.9
Bladder	6.33E+02	3.0%	3.17E+03	3.0%	1.21E+03	9.4%	1.9
Breasts	5.38E+02	2.6%	2.69E+03	2.6%	9.46E+02	6.1%	1.8
Liver	6.01E+02	1.1%	3.01E+03	1.1%	1.10E+03	1.8%	1.8
Oesophagus	5.60E+02	3.1%	2.80E+03	3.1%	1.13E+03	9.4%	2.0
Thyroid	6.92E+02	7.4%	3.46E+03	7.4%	1.35E+03	15.3%	1.9
Skin	5.03E+02	0.4%	2.51E+03	0.4%	9.30E+02	1.4%	1.9
Bone surface	5.51E+02	0.4%	2.75E+03	0.4%	1.05E+03	0.7%	1.9
Adrenals	5.47E+02	6.1%	2.74E+03	6.1%	8.61E+02	15.7%	1.6
Brain	5.49E+02	1.4%	2.74E+03	1.4%	1.03E+03	2.2%	1.9
Small intestine wall	6.24E+02	1.3%	3.12E+03	1.3%	1.18E+03	2.3%	1.9
Kidneys	5.98E+02	2.0%	2.99E+03	2.0%	1.10E+03	4.1%	1.8
Muscle	5.77E+02	0.3%	2.88E+03	0.3%	1.05E+03	0.4%	1.8
Pancreas	5.87E+02	2.5%	2.94E+03	2.5%	9.93E+02	5.2%	1.7
Spleen	6.33E+02	3.4%	3.16E+03	3.4%	1.17E+03	7.8%	1.8
Thymus	5.78E+02	5.9%	2.89E+03	5.9%	9.78E+02	12.4%	1.7
Uterus	5.70E+02	3.4%	2.85E+03	3.4%	1.02E+03	8.4%	1.8
Remainder	5.77E+02	0.3%	2.89E+03	0.3%	1.05E+03	0.4%	1.8

* Averaged absorbed dose in organ or tissue.

† Averaged dose equivalent in organ or tissue based on Q(L) in ICRP60.

Table A-2r. Organ absorbed dose, equivalent dose and dose equivalent per unit fluence for 2000 MeV proton for ISO irradiation

Organ or tissue	Absorbed dose*		Equivalent dose $W_R = 5$		Dose equivalent†		Mean quality factor Q-L in ICRP60
	($pGycm^2$)	error	($pSVcm^2$)	error	($pSVcm^2$)	error	
Testes	6.24E+02	4.8%	3.12E+03	4.8%	1.25E+03	9.6%	2.0
Ovaries	6.60E+02	7.4%	3.30E+03	7.4%	1.41E+03	19.7%	2.1
Red marrow	6.14E+02	0.6%	3.07E+03	0.6%	1.24E+03	1.2%	2.0
Colon	6.49E+02	0.7%	3.24E+03	0.7%	1.24E+03	1.6%	1.9
Lungs	6.07E+02	1.0%	3.04E+03	1.0%	1.14E+03	2.2%	1.9
Stomach	6.36E+02	2.9%	3.18E+03	2.9%	1.17E+03	7.9%	1.8
Bladder	6.57E+02	2.9%	3.29E+03	2.9%	1.26E+03	8.3%	1.9
Breasts	5.51E+02	2.8%	2.75E+03	2.8%	1.10E+03	6.7%	2.0
Liver	6.43E+02	1.2%	3.22E+03	1.2%	1.22E+03	1.8%	1.9
Oesophagus	6.10E+02	3.1%	3.05E+03	3.1%	1.03E+03	7.6%	1.7
Thyroid	5.95E+02	7.2%	2.97E+03	7.2%	1.00E+03	11.4%	1.7
Skin	5.18E+02	0.5%	2.59E+03	0.5%	9.86E+02	1.4%	1.9
Bone surface	5.90E+02	0.4%	2.95E+03	0.4%	1.18E+03	0.8%	2.0
Adrenals	6.48E+02	6.2%	3.24E+03	6.2%	1.48E+03	17.0%	2.3
Brain	5.84E+02	1.4%	2.92E+03	1.4%	1.13E+03	2.2%	1.9
Small intestine wall	6.79E+02	1.3%	3.40E+03	1.3%	1.28E+03	2.2%	1.9
Kidneys	6.41E+02	2.0%	3.21E+03	2.0%	1.27E+03	4.1%	2.0
Muscle	6.10E+02	0.3%	3.05E+03	0.3%	1.16E+03	0.4%	1.9
Pancreas	6.91E+02	3.0%	3.46E+03	3.0%	1.34E+03	4.8%	1.9
Spleen	6.71E+02	3.6%	3.36E+03	3.6%	1.16E+03	7.7%	1.7
Thymus	6.49E+02	6.6%	3.24E+03	6.6%	1.42E+03	14.9%	2.2
Uterus	6.64E+02	4.2%	3.32E+03	4.2%	1.30E+03	8.5%	2.0
Remainder	6.11E+02	0.3%	3.06E+03	0.3%	1.16E+03	0.4%	1.9

* Averaged absorbed dose in organ or tissue.

† Averaged dose equivalent in organ or tissue based on Q(L) in ICRP60.

Table A-2s. Organ absorbed dose, equivalent dose and dose equivalent per unit fluence for 5000 MeV proton for ISO irradiation

Organ or tissue	Absorbed dose*		Equivalent dose $W_R = 5$		Dose equivalent†		Mean quality factor Q-L in ICRP60
	($pGycm^2$)	error	($pSVcm^2$)	error	($pSVcm^2$)	error	
Testes	7.01E+02	5.1%	3.50E+03	5.1%	1.42E+03	12.0%	2.0
Ovaries	8.03E+02	9.6%	4.01E+03	9.6%	1.35E+03	17.1%	1.7
Red marrow	7.18E+02	0.6%	3.59E+03	0.6%	1.46E+03	1.1%	2.0
Colon	7.91E+02	0.8%	3.95E+03	0.8%	1.55E+03	1.6%	2.0
Lungs	7.09E+02	1.0%	3.55E+03	1.0%	1.36E+03	2.1%	1.9
Stomach	7.60E+02	2.8%	3.80E+03	2.8%	1.53E+03	7.5%	2.0
Bladder	8.04E+02	3.1%	4.02E+03	3.1%	1.65E+03	8.7%	2.1
Breasts	6.55E+02	3.5%	3.28E+03	3.5%	1.30E+03	6.7%	2.0
Liver	7.57E+02	1.2%	3.78E+03	1.2%	1.52E+03	1.8%	2.0
Oesophagus	7.32E+02	5.3%	3.66E+03	5.3%	1.30E+03	9.2%	1.8
Thyroid	7.53E+02	7.0%	3.76E+03	7.0%	1.47E+03	15.0%	2.0
Skin	5.94E+02	0.5%	2.97E+03	0.5%	1.17E+03	1.5%	2.0
Bone surface	6.95E+02	0.4%	3.47E+03	0.4%	1.41E+03	0.7%	2.0
Adrenals	8.43E+02	7.4%	4.21E+03	7.4%	1.60E+03	16.4%	1.9
Brain	6.83E+02	1.4%	3.41E+03	1.4%	1.34E+03	2.1%	2.0
Small intestine wall	7.99E+02	1.3%	3.99E+03	1.3%	1.58E+03	2.1%	2.0
Kidneys	7.69E+02	2.1%	3.85E+03	2.1%	1.49E+03	3.6%	1.9
Muscle	7.10E+02	0.3%	3.55E+03	0.3%	1.38E+03	0.4%	1.9
Pancreas	7.61E+02	3.1%	3.80E+03	3.1%	1.38E+03	5.0%	1.8
Spleen	7.40E+02	3.4%	3.70E+03	3.4%	1.40E+03	7.9%	1.9
Thymus	6.80E+02	5.5%	3.40E+03	5.5%	1.05E+03	14.5%	1.5
Uterus	8.04E+02	4.4%	4.02E+03	4.4%	1.55E+03	8.0%	1.9
Remainder	7.12E+02	0.3%	3.56E+03	0.3%	1.38E+03	0.4%	1.9

* Averaged absorbed dose in organ or tissue.

† Averaged dose equivalent in organ or tissue based on Q(L) in ICRP60.

Table A-2t. Organ absorbed dose, equivalent dose and dose equivalent per unit fluence for 10000 MeV proton for ISO irradiation

Organ or tissue	Absorbed dose*		Equivalent dose $W_R = 5$		Dose equivalent†		Mean quality factor Q-L in ICRP60
	($pGycm^2$)	error	($pSVcm^2$)	error	($pSVcm^2$)	error	
Testes	7.46E+02	4.5%	3.73E+03	4.5%	1.51E+03	9.8%	2.0
Ovaries	9.85E+02	10.9%	4.93E+03	10.9%	2.46E+03	24.3%	2.5
Red marrow	7.82E+02	0.7%	3.91E+03	0.7%	1.63E+03	1.4%	2.1
Colon	8.87E+02	0.8%	4.43E+03	0.8%	1.88E+03	1.6%	2.1
Lungs	7.80E+02	1.2%	3.90E+03	1.2%	1.58E+03	2.4%	2.0
Stomach	7.76E+02	2.9%	3.88E+03	2.9%	1.30E+03	6.4%	1.7
Bladder	8.61E+02	3.5%	4.30E+03	3.5%	1.82E+03	8.4%	2.1
Breasts	7.35E+02	5.9%	3.68E+03	5.9%	1.46E+03	7.3%	2.0
Liver	8.21E+02	1.2%	4.11E+03	1.2%	1.65E+03	1.7%	2.0
Oesophagus	8.66E+02	6.3%	4.33E+03	6.3%	1.73E+03	9.2%	2.0
Thyroid	7.72E+02	6.9%	3.86E+03	6.9%	1.78E+03	15.8%	2.3
Skin	6.45E+02	0.6%	3.23E+03	0.6%	1.28E+03	1.4%	2.0
Bone surface	7.53E+02	0.5%	3.77E+03	0.5%	1.58E+03	0.8%	2.1
Adrenals	9.19E+02	6.6%	4.60E+03	6.6%	2.12E+03	16.6%	2.3
Brain	7.26E+02	1.5%	3.63E+03	1.5%	1.47E+03	2.2%	2.0
Small intestine wall	9.14E+02	1.4%	4.57E+03	1.4%	1.88E+03	2.0%	2.1
Kidneys	8.05E+02	1.9%	4.02E+03	1.9%	1.60E+03	4.2%	2.0
Muscle	7.80E+02	0.3%	3.90E+03	0.3%	1.57E+03	0.4%	2.0
Pancreas	8.83E+02	2.8%	4.41E+03	2.8%	1.85E+03	4.8%	2.1
Spleen	7.80E+02	3.2%	3.90E+03	3.2%	1.39E+03	7.3%	1.8
Thymus	8.36E+02	5.4%	4.18E+03	5.4%	1.82E+03	12.3%	2.2
Uterus	7.89E+02	3.5%	3.95E+03	3.5%	1.50E+03	6.2%	1.9
Remainder	7.82E+02	0.3%	3.91E+03	0.3%	1.58E+03	0.4%	2.0

* Averaged absorbed dose in organ or tissue.

† Averaged dose equivalent in organ or tissue based on Q(L) in ICRP60.

Figure A-1. Comparison of effective dose E_{WR} per unit neutron fluence for AP, PA and ISO irradiation

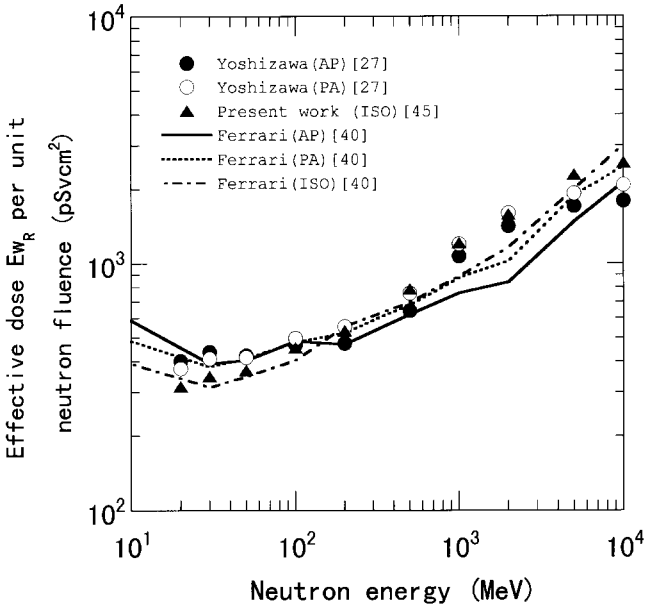

Figure A-2. Comparison of effective dose E_{WR} per unit proton fluence for AP, PA and ISO irradiation

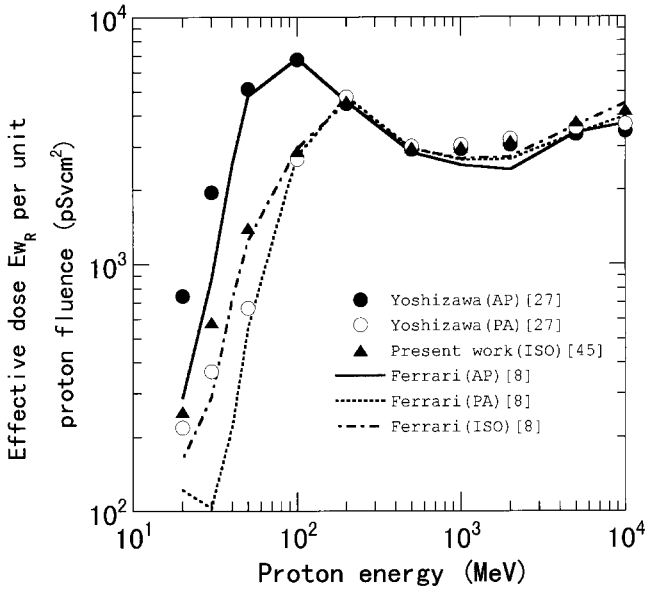

Figure A-3. Comparison of effective dose $E_{Q\text{-}L}$ per unit proton fluence for AP, PA and ISO irradiation

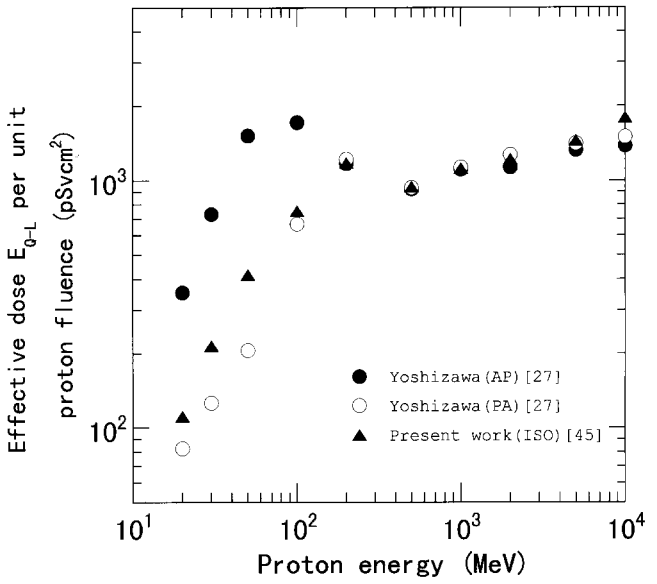

PRELIMINARY STUDY ON NARROW BEAM DOSIMETRY

Satoshi Iwai*, Takashi Uehara*
Mitsubishi Heavy Industries, Japan
** Present address: Nuclear Development Corporation, Japan*

Osamu Sato, Nobuaki Yoshizawa, Shunji Takagi
Mitsubishi Research Institute, Japan

Shun-ichi Tanaka
Japan Atomic Research Institute
Office of Planning, Japan

Yukio Sakamoto
Japan Atomic Research Institute
Accelerator Radiation Lab. Centre for Neutron Science

Abstract

This report describes a preliminary study on narrow beam dosimetric quantities used for radiological protection. The basic framework of radiological protection is intended to prevent the occurrence of deterministic effects and to ensure that all reasonable steps are taken to reduce the induction of stochastic effects. In this work, investigations were performed on adequate quantities to evaluate the occurrence of deterministic effects and the induction of stochastic effects for narrow beam exposure. From this study, effective dose was proved to be applicable to the index of stochastic effects for narrow beam. However, it is difficult to define the adequate dose indicator to evaluate the occurrence of deterministic effects for narrow beam exposure.

Introduction

Narrow beam dosimetry is required for radiation protection purposes in accelerator facilities and in diagnostic radiology. But we think narrow beam dosimetry in diagnostic radiology is out of scope for radiological protection purposes discussed here, because diagnostic medical exposures are usually performed under the control of planning.

In high-energy electron storage rings, the radiative interaction of the electron with the residual gas in vacuum chamber constitutes bremsstrahlung produced in a very small angular cone along the election beam direction [1,2]. The mean value of emission angle is $\theta = mc^2/E$, where mc^2 is the election rest mass and E is the electron beam energy [3]. This radiation is called the gas bremsstrahlung due to the production in residual gas.

In the facilities of proton or election beam accelerators, leakage radiations are not so significant, because the radiation shieldings are usually sufficient. In accelerator facilities, accidental exposure to primary beam will not occur unless failure of the interlock also occurs.

The concept of narrow beam dosimetry for radiological protection

In its Publication 60 [4], the ICRP (International Commission on Radiological Protection) distinguished between “stochastic” and “deterministic” effects for the purposes of radiological protection, suggesting that “deterministic effects” are those for which both the probability and severity of the effect vary with the dose, and for which a threshold of dose-response may occur. In contrast, it is suggested that “stochastic effects” are those for which only the probability of the occurrence effects, and not its severity, is regarded as a function of dose, without threshold.

Cancer and hereditary effects are typical stochastic effects. Representative examples of most radiosensitive deterministic effects include cataract of the lens, non-malignant damage to the skin, cell depletion of red bone marrow causing haematological deficiencies and gonadel cell damage leading to impairment of fertility [4,7].

The basic framework of radiological protection of the ICRP is to prevent the occurrence of deterministic effects by keeping doses below the thresholds, and to ensure that all steps are taken to reduce the stochastic effects [4].

Therefore, two kinds of dosimetric quantities should be controlled for the purpose of radiation protection, one for evaluating the occurrence of deterministic effects, the other for stochastic effects.

The average dose in a tissue or organ is used as an indicator of the occurrence probability of stochastic effects subsequent to exposure. This use depends on the linearity of the relationship between the probability of inducing effects and dose (the dose-response relationship) [4]. In ICRP Publication 60, this linearity is suggested to be a reasonable approximation within a limited range of dose. In the range of dose, the occurrence probability of stochastic effects has a linearity to the energy deposited in the tissue or organ, subsequent to the radiation exposure. The probability of stochastic effects does not depend on the energy distribution.

This concept will easily be understandable by the following methodologies shown below. As shown in Figure 1(a), an organ T is exposed isotropically by radiation and subsequent energy is deposited uniformly in T. The average dose in the organ T is calculated to be E/M, where E is

deposited energy and the organ M is the mass of the organ T. In contrast, the organ T is exposed by a narrow beam and the same energy E is deposited locally in a small region “t” in the organ, T shown in Figure 1(b). The dose in the exposed region by the narrow beam is calculated to be E/m, where E is the deposited energy and m is the mass of exposed region (no energy is deposited in the remainder region by the narrow beam). The average dose (E/m) in the exposed region “t” is larger than the average organ dose (E/M) of isotropic irradiation.

Figure 1. Narrow beam dosimetry for stochastic effects

(a) Isotopic irradiation

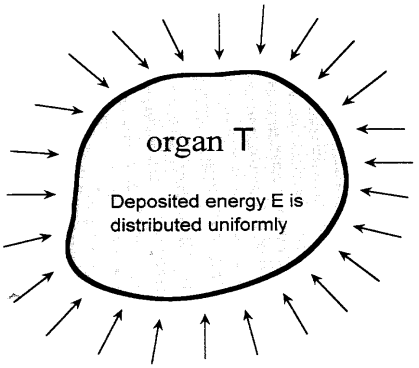

(b) Narrow beam irradiation

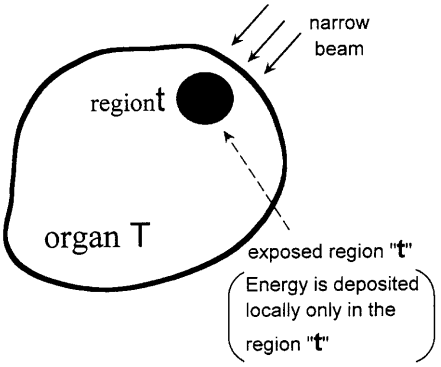

E: energy deposited in **T**
M: mass of exposed region
D = E/M: absorbed dose in exposed region
Pi: occurrence probability of stochastic effects in **T** for isotopic exposure

$$Pi = D \bullet M = \frac{E}{M} \bullet M = E$$

E: energy deposited in region **t**
m: mass of exposed region
d: absorbed dose in exposed region
Ph: occurrence probability of stochastic effects in **T** for narrow beam

$$Pn = d \bullet m = \frac{E}{m} \bullet m = E$$

The occurrence probability (Pi) of stochastic effects in T for isotopic exposure is estimated to be E as derived by Eq. (1).

$$\begin{aligned} Pi &= (\text{average dose in T}) \bullet (\text{mass of exposed region}) \\ &= D \bullet M \\ &= E/M \bullet M = E \end{aligned} \tag{1}$$

The occurrence probability (Pn) of stochastic effects in T for narrow beam exposure is also calculated to be E as derived by Eq. (2).

$$\begin{aligned} Pn &= (\text{average dose in T}) \bullet (\text{mass of exposed region}) \\ &= d \bullet m \\ &= E/m \bullet m = E \end{aligned} \tag{2}$$

From Eqs. (1) and (2), the occurrence probability (Pn) of stochastic effects in T for narrow beam is equal to Pi of isotropic exposure. This result leads to the finding that average dose in a tissue or organ can be used as an indicator of the occurrence probability of stochastic effects for narrow beam dosimetry. From this conclusion, effective dose can also be employed as an index of stochastic effects for narrow beam dosimetry, assuming that tissue weighting factors of the ICRP Publication 60 are applicable to narrow beam exposure.

Dosimetric quantity for deterministic effects

The average dose in a tissue or organ is not directly relevant to deterministic effects unless the dose is fairly uniformly distributed over the tissue or organ, because dose-response relationship is not linear for deterministic effects [4]. Therefore, the dose averaged the tissue or organ can not be used as an indicator of the occurrence of deterministic effects for narrow beam exposure, because of uniform dose distribution.

The definitions of dose calculational methods are not in agreement precisely among three groups [3,5,6] for the narrow beam dosimetry of gas bremsstrahlung produced in electron storage rings. The definition of dose for high energetic narrow beam is difficult, because of the lateral spread of electromagnetic shown along the angular cone.

The dose defined for deterministic effects must be a domestic indicator directly relevant to the occurrence of deterministic effects. For health physics purpose, occurrence of deterministic effects should be defined as a functional loss of the tissue or organ, and not as a functional loss of a small portion of the tissue or organ.

From a health physics point of view, the occurrence of deterministic effects could be observed when the following two conditions are satisfied for narrow beam:

1) the narrow beam is exposed to a portion of tissue (or organ) which would be large enough to reflect a loss of tissue function;

2) the dose in the portion exceeds a threshold of a deterministic effects.

The definition of dose for deterministic effects for narrow beam should be performed, considering the portion of a tissue which would be large enough to reflect of tissue function. Since the minimal necessary size of the portion of the tissue depends on functions and tissues (organ), more discussions would be necessary to define the region to estimating the dose for deterministic effects for narrow beam dosimetry.

A few examples of narrow beam dosimetry

Narrow beam exposure should be controlled by the following two quantities: effective dose and dose equivalent of the exposed region.

In this work, two cases are exemplified for photon narrow beam dosimetry.

1) **Case 1**

   The lens of the right eye is exposed to the narrow photon beam of monochromatic energy in the AP irradiation geometry, so as to be 5.0 Sv (the threshold dose equivalent of cataract) of the dose equivalent of lens.

   a) Beam cross-section: circle of radius of 0.2, 0.5 and 1.0 cm

   b) Photon energy: 30 keV, 100 keV and 1 GeV

2) **Case 2**

The right testis is exposed to the narrow photon beam of monochromatic energy in the AP irradiation geometry, so as to be 0.15 Sv (the threshold dose equivalent of temporary sterility) of the dose equivalent of the testis.

a) Beam cross-section: circle of radius of 0.2, 0.5 and 1.0 cm

b) Photon energy: 30 keV, 100 keV and 1 GeV

Three-dimensional Monte Carlo calculations were performed by use of the EGS4 code [4] with the anthrophormatic mathematical phantom model which appears in Ref. [9]. In these results, Monte Carlo errors were adjusted within 3%.

In a single brief exposure, the threshold for cataract in the lens in 5.0 Sv, and that for temporary sterility in testes is 0.15 Sv in adult humans.

Table 1 shows the calculational results of the effective dose, when the dose equivalents of the lens of right eye equals to the threshold (5.0 Sv) of cataract for each beam radius and energy.

Table 2 shows the effective doses, when the dose equivalents of the right testis equals to the threshold (0.15 Sv) of temporary sterility for each beam. Figure 2 shows photon and secondary particle tracks when the right testis is exposed to the narrow beam of 1 GeV photons of 0.5 cm radius.

Table 1. Effective dose exposed to the narrow beam, when the dose equivalent of the lens of right eye equals to 5.0 Sv (cataract threshold dose)

(AP geometry)

Photon energy	Beam radius = 0.2 cm	Beam radius = 0.5 cm	Beam radius = 1.0 cm
30 keV	1.08	1.08	1.09
100 keV	2.68	2.74	2.70
1 GeV	178	165	161

Table 2. Effective dose exposed to the narrow beam, when the dose equivalent of the right testis equals to 0.15 Sv (temporary sterility dose)

(AP geometry)

Photon energy	Beam radius = 0.2 cm	Beam radius = 0.5 cm	Beam radius = 1.0 cm
30 keV	30.0	30.0	30.0
100 keV	30.2	30.2	30.2
1 GeV	30.1	30.1	30.2

These results lead to the following findings:

1) The effective doses do not exceed the limit of effective dose of 20 mSv (per year) recommended in the ICRP Publication 60, even if the dose equivalent of the lens of eye equals to the cataract threshold dose for 30 keV and 100 keV photon beam.

2) The effective doses may exceed the limit of effective dose of 20 mSv, when the averaged dose equivalent of testis is below the threshold of temporary sterility.

From these findings, two kinds of dosimetric quantities (effective dose and dose equivalent of tissue or organ) are essential to the narrow beam dosimetry for the purpose of radiological protection.

Figure 2. Photon and secondary particle tracks, when the right testis is exposed to the narrow beam of 1 GeV photon of 0.5 cm radius

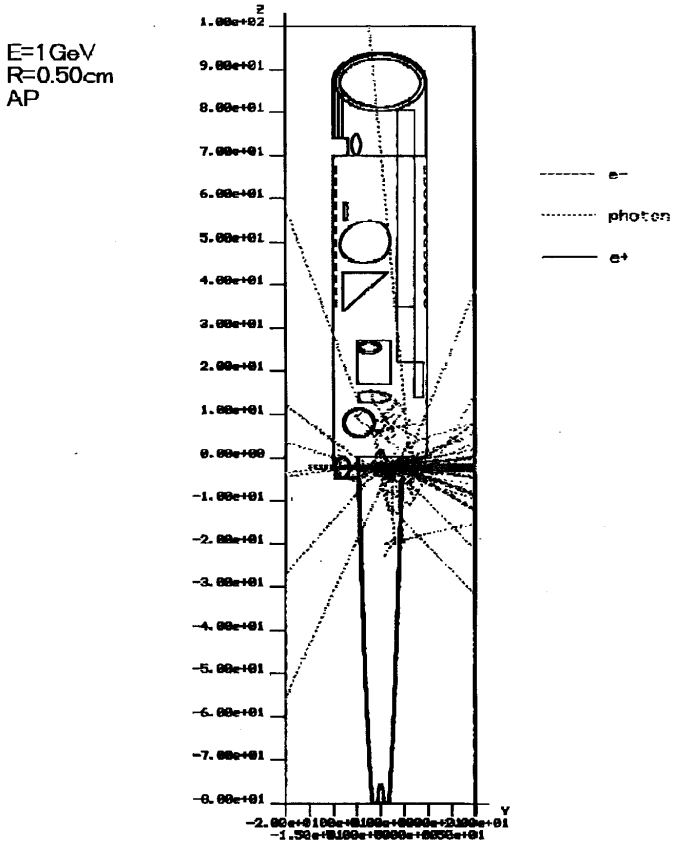

Summary

- Gas bremsstrahlung produced in election storage rings is a typical example of narrow beam. The narrow beam may represent a serious radiation hazard when the shield itself is not thick enough.

- Effective dose can be used as an indicator of the occurrence of stochastic effects of narrow beam exposure, in much the same way as isotropic exposure.

- The dose equivalent of the region exposed to narrow beam should be applied to an indicator of the occurrence of deterministic effects for narrow beam exposure. But more investigation would be essential to define *the region exposed to narrow beam*.

- Two kinds of dosimetric quantities (effective dose and equivalent of tissue or organ) are essential to narrow beam dosimetry, for the purpose of radiological protection.

- In this work, calculations were performed for the narrow beam dosimetry of the tissues or organs located near the body surface such as testes and lens. Subsequent calculations would be necessary for other radiosensitive tissues such as skin, ovaries and red bone marrows, in order to investigate other dosimetric features for narrow beam dosimetry.

REFERENCES

[1] S. Ban, Dosimetry Around High Energy Accelerators, Proc. of the Workshop on Dosimetry for External Radiations, 19-20 January 1995, JAERI, Tokai, Japan, eds., Y. Yamaguchi and M. Yoshizawa, pp. 122-127, JAERI-Conf 95-007 (1995), *in Japanese*.

[2] S. Ban, H. Hirayama and S. Miura, *Health Phys*., 57 (1989), 407.

[3] S. Ban and H. Hirayama, KEK Preprint 94-22 (1994).

[4] ICRP Publication 60, Recommendations of the Internal Commission on Radiological Protection, adopted by the Commission in November 1990, Annals of the ICRP, 21 (1-3) (1991).

[5] G. Tromba and A. Rindi, *Nucl. Instr. Meth.*, A292 (1990), 700.

[6] A. Ferrari, M. Pelliccioni and P.R. Sala, *Nucl. Instr. Meth.* B83 (1993), 518.

[7] ICRP Publication 41, Nonstochastic Effects of Iionizing Radiation, Annals of the ICRP 14 (3) (1984).

[8] W.R. Nelson, H. Hirayama and D.W.O. Rogers, "The EGS4 Code System", Stanford Linear Accelerator Center Report SLAC-265 (Stanford, Calif.) (1985).

[9] S. Iwai, T. Uehara, O. Sata, N. Yoshizawa, S. Furihata, S. Takagi, S. Tanaka and Y. Sakamoto, "Evaluation Fluence to Dose Equivalent Conversion Coefficients for Energy Neutrons – Calculation of Effective Dose Equivalents and Effective Dose", in Proc. 2nd Specialists Meeting on Shielding Aspects of Accelerators, Targets and Irradiation Facilities (SATIF-2), CERN, Geneva, 12-13 October 1995.

Anthropomorphic Phantom

COMPARISON OF COMPUTER CODE CALCULATIONS FOR THE ICRU SLAB PHANTOM

Nobuaki Yoshizawa
MRI, Mitsubishi Research Institute, Japan
3-6, Otemachi 2-Chyome, Chiyoda-ku
Tokyo 100-8141, Japan
E-mail: yoshizaw@mri.jp

Noriaki Nakao
KEK, High Energy Accelerator Research Organisation
Tanashi Branch, Radiation Safety Control Office

Yukio Sakamoto
JAERI, Japan Atomic Research Institute
Accelerator Radiation Laboratory, Centre for Neutron Science

Satoshi Iwai*
MHI, Mitsubishi Heavy Industries, Japan
** Present address: Nuclear Development Corporation*
Omiya Research & Development Department Radiation Engineering

Abstract

For fluence to effective dose conversion coefficients on high-energy neutron, differences are described between computer codes. The maximum difference is factor 1.7 at 2 GeV neutron incidence for anterior-posterior (AP) irradiation. Absorbed dose and dose equivalent in ICRU four element 30 cm thick infinite slab phantom are also calculated for neutron in the energy range from 100 MeV to 10 GeV. HETC-3STEP and MARS13(98) are used in the calculations. Calculated results and other published data calculated by HADRON, LAHET, and FLUKA are compared. The maximum difference is about a factor of 1.5 for calculation of maximum absorbed dose in the slab.

Introduction

Several kinds of computer codes have been used for numerical dosimetry against high energy neutron irradiation. Alsmiller *et al.* [1] and Armstrong *et al.* [2] calculated absorbed dose and dose equivalent in a semi-infinite slab of tissue of 30 cm thickness for high energy neutrons and protons with HETC [3]. A different approach was taken by Belogorlov *et al.* [4]. Their results are presented in ICRP51 [5]. After the recommendation from ICRP Publication 60 [6], effective doses for high-energy neutrons were calculated by some authors [7-11] using several computer codes.

Neutron cross-section data is usually used for transport simulation below 20 MeV. The data library (ex. JENDL3.2 [12] is well verified, therefore computation results using it have high accuracy. Unfortunately, above 20 MeV there are not enough cross-section libraries because of a lack of experimental data. Consequently, computer codes, which do not need cross-section data, are used for effective dose calculation for high-energy neutron beams. In these computer codes, theoretical models or empirical formulae are used to calculate cross-sections.

Due to a lack of experimental data, accuracy of predictions by the computer codes for high-energy neutrons is less certain than that below 20 MeV. In this situation, comparison of calculated results by different codes is meaningful. Therefore, we calculated absorbed dose and dose equivalent in an infinite slab phantom with HETC-3STEP [13] and MARS13(98) [14] and compared calculated results and other published data.

Effective dose

Figure 1 shows fluence to effective dose conversion coefficients for AP, PA and ISO irradiation geometries. Nabelssi *et al.* [7] used LAHET [15] and HMCNP [15]. Ferrari *et al.* [9] and Yoshizawa *et al.* [11] used FLUKA [16] and HETC-3STEP [13] + MORSE-CG/KFA [17], respectively. Ratio of maximum to minimum value of effective dose is presented in Figure 2. The ratio is less than the factor of 1.2 up to 500 MeV. The maximum value of the ratio is 1.7 at 2 GeV for AP irradiation. One of the reasons for this discrepancy is attributed to differences in the anthropomorphic phantoms. The differences are described in Ref. [10]. Another reason is differences between the physical models in each computer code. To investigate the performance of computer codes for numerical high-energy neutron dosimetry, a simple problem is needed rather than complicated calculations utilising anthropomorphic phantoms.

ICRU slab phantom

To simplify code comparison, absorbed dose and dose equivalent in semi-infinite ICRU four element slab (H, 10.1% weight; C, 11.1%; N, 2.6%; O, 76.2%) were calculated. HETC-3STEP was used for calculations of absorbed dose and dose equivalent. For the calculations of dose equivalent, the Q-L relationship recommended in ICRP60 was used. MARS13(98) was also used only for calculations of absorbed dose. Published values of HADRON [18], FLUKA [19] and LAHET [20] were also used. For calculations with infinite slab phantom, pencil beam approximation was used.

Above incident neutron energy 100 MeV, contributions of low energy neutrons to absorbed dose and dose equivalent are less than about 10% [11]. The performance of computer programs for neutron transport below 20 MeV has been well investigated. In this study, therefore, code comparisons for incident neutron energy between 100 MeV to 10 GeV were performed.

Dose equivalent is one of the most significant quantities for radiation protection. To calculate it, the relationship between the quality factor and linear energy transfer of transported radiation in phantoms must be taken into account. Several kinds of treatments were introduced by some authors [10,11,18,19]. and differences of these treatments seem to produce discrepancy. Absorbed dose is a physical quantity, hence a clearer comparison is able to emerge than for dose equivalent. In this study, we mainly discuss absorbed dose and briefly describe dose equivalent.

Results of calculations

Figure 3 shows absorbed dose, calculated by HETC-3STEP and MARS13(98), as a function of depth in a 30-cm thick slab of ICRU tissue for normally incident neutron. For 100 MeV neutron incidence, results of MARS13(98) are lower than those of HETC-3STEP. However, the results of MARS13(98) are higher than those of HETC-3STEP in almost all depths for 1000 MeV and 10 GeV.

Absorbed dose at a depth of 1 cm is shown in Figure 4. An infinite slab phantom was used for calculation with HETC-3STEP, MARS13(98) and HADRON. Results of FLUKA were calculated with the ICRU sphere. Above 5 GeV, the results of FLUKA are lower than the others. One of the reasons for this discrepancy seems to be attributed to the difference between the slab and the sphere. The maximum absorbed dose is also plotted in Figure 5. The values of FLUKA are calculated with ambient dose equivalent and effective quality factors in Ref. [19].

In Figure 6, a ratio of maximum absorbed dose at 1 cm to minimum one and a ratio of maximum absorbed dose to minimum one are presented, respectively. Results by FLUKA were not included in these comparisons. The ratio for absorbed dose at 1 cm is decreasing from a factor of 1.4 to 1.1. For maximum dose, the ratio is lower than about a factor of 1.5 in the whole incident neutron energy range.

Figure 7 shows dose equivalent at 10 cm. The ICRU sphere was used in the calculations of Nabelssi *et al*. [20] and Ferrari *et al*. [19]. For calculations of HETC-3STEP and HADRON, infinite slab was used. The difference of calculated vale between HETC-3STEP and HADRON is about 20%. The lower value of FLUKA above 1 GeV seems to be attributed to the difference between slab and sphere.

Summary

Absorbed dose and dose equivalent in ICRU four element slab phantom were calculated by HETC-3STEP and MARS13(98). Calculated results and other published data calculated by HADRON, LAHET and FLUKA were compared. The maximum difference is about a factor of 1.5 for calculation of maximum absorbed dose in the slab.

To discover the reason for the discrepancies between the results of the various computer codes, some studies are needed, as follows:

1) comparison of calculated cross-section for H, C, N, O;

2) comparison of neutron, proton and other charged particle fluence in the phantom;

3) comparison of treatment for Q-L relationship;

4) experimental approach is also needed.

Acknowledgement

We wish to thank Dr. Nikolai Mokhov for his helpful suggestions and MARS13(98) calculations.

REFERENCES

[1] R.G. Alsmiller, Jr., T.W. Armstrong, W.A. Coleman, *Nucl. Sci. Eng.* 42, 367 (1970).

[2] T.W. Armstrong, K.C. Chandler, *Health Phys*. 24, 277 (1973).

[3] T.W. Armstrong, K.C. Chandler, ORNL-4869 (1973).

[4] E.A. Belogorlov *et al*., *Nucl. Instr. Meth*. 199, 563 (1982).

[5] International Commission on Radiological Protection, "Data for Use in Protection Against External Radiation", ICRP Publication 51, Pergamon Press, Oxford (1987).

[6] International Commission on Radiological Protection, "1990 Recommendations of the International Commission on Radiological Protection", ICRP Publication 60, Pergamon Press, Oxford (1991).

[7] B.K. Nabelssi, N.E. Hertel, *Radiat. Prot. Dosim*. 48[3], 227 (1993).

[8] V. Mares, G. Leuthold, H. Schraube, *Radiat. Prot. Dosim*. 70, 391 (1997).

[9] A. Ferrari *et al*., *Radiat. Prot. Dosim.* 71[3], 165 (1997).

[10] S. Iwai *et al*., Proc. of the Second Specialists Meeting on Shielding Aspects of Accelerators, Targets and Irradiation Facilities (SATIF-3), Tohoku Universitiy, Sendai, 1998, OECD Publ., 299 (1997).

[11] N. Yishizawa *et al*., *J. Nucl. Sci. Technol.*, to be published.
Appendix tables in: S. Iwai *et al*. "Overviews of Fluence to Dose Equivalent Conversion Coefficients for High Energy Radiations", Proc. of the 4th Specialists Meeting on Shielding Aspects of Accelerators, Targets and Irradiation Facilities (SATIF-4), Knoxville, 17-18 September 1998.

[12] T. Nakagawa *et al*., *J. Nucl. Sci. and Technol.* 32, 1259 (1995).

[13] N. Yoshizawa, K. Ishibashi, H. Takada, *J. Nucl. Sci. and Technol.* 32, 601 (1995).

[14] N.V. Mokhov, "The MARS Code System User's Guide", Fermilab-FN-628 (1995).
O.E. Krivosheev, N.V. Mokhov, "A New MARS and its Applications", Fermilab-Conf-98/43 (1998).
New version MARS13(98) of 26 August 1998 is now available replacing the previous version of 27 May 1998 (http://www-ap.fnal.gov/MARS/).

[15] R.E. Prael, H. Lichtenstein, LA-UR-89-3014 (1989).

[16] A. Fassò *et al*., Proc. of the 2nd Workshop on Simulating Accelerator Radiation Environments, Geneva, Switzerland, 1995, OECD Publ., 158 (1997).

[17] P. Cloth *et al*., KFA-IRE-EAN 12/88 (1988).

[18] A.V. Sannikov, E.N. Savitskaya, *Rad. Prot. Dosim*. 70[1-4], 383 (1997).

[19] A. Ferrari, M. Pelliccioni, *Rad. Prot. Dosim*. 76, 215 (1998).

[20] B.K. Nabelssi, N.E. Hertel, *Rad. Prot. Dosim.* 51[3], 169 (1994).

Figure 1. Comparison of effective dose for AP, PA and ISO irradiation neutron beams

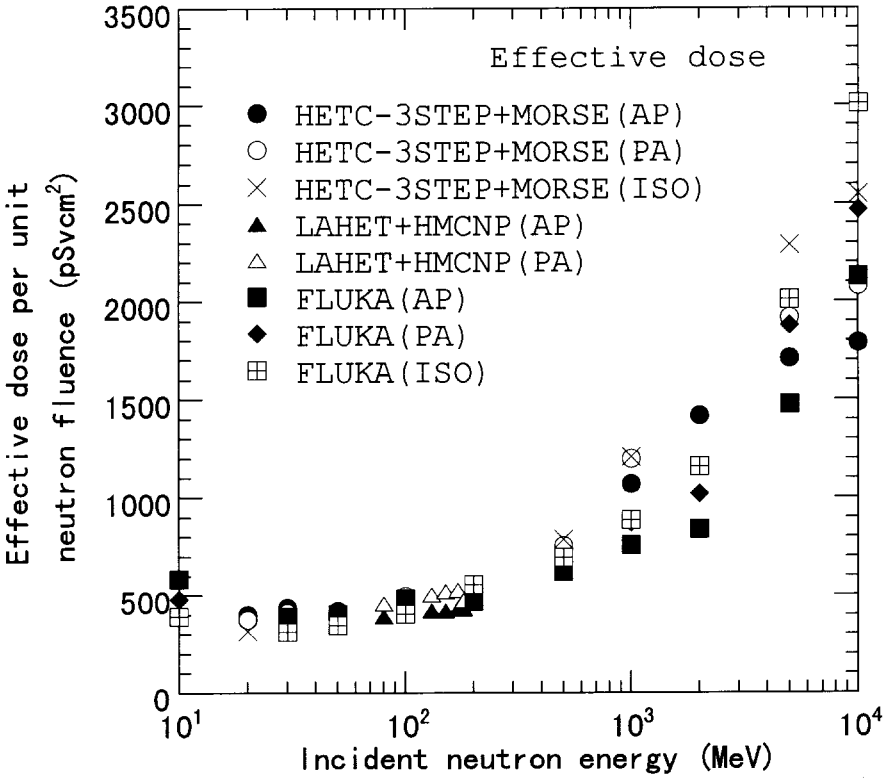

Figure 2. Ratio of max. to min. value of calculated effective dose as a function of incident neutron energy

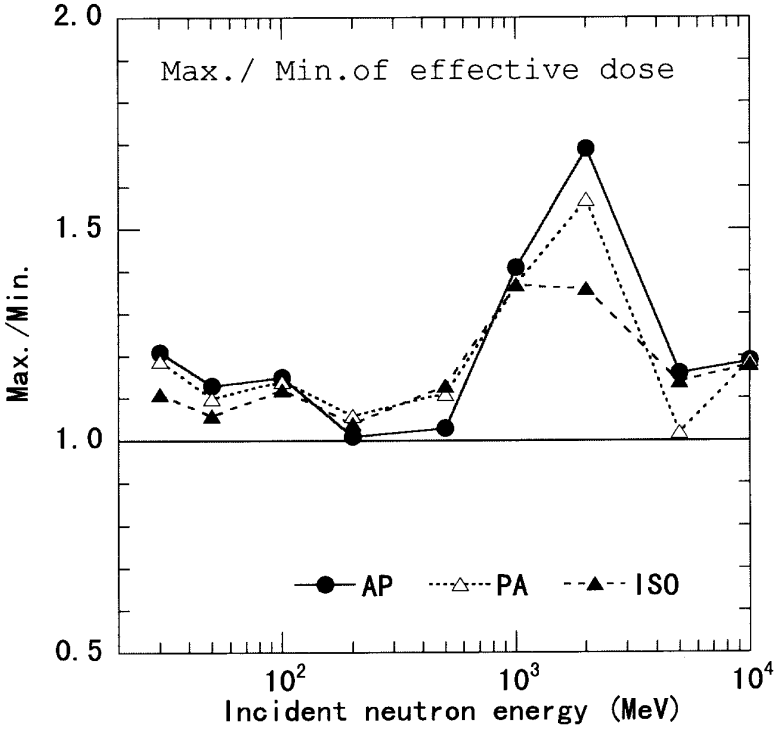

Figure 3. Absorbed dose vs. depth in a 30 cm thick slab of ICRU four element tissue for normally incident neutron

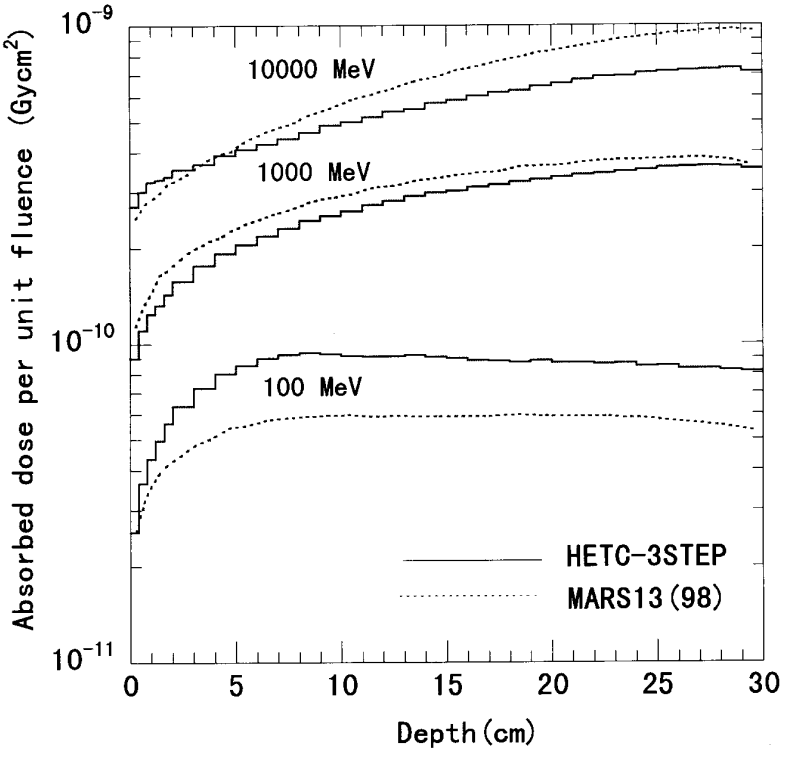

Figure 4. Absorbed dose at 1 cm in ICRU phantom as a function of incident neutron energy

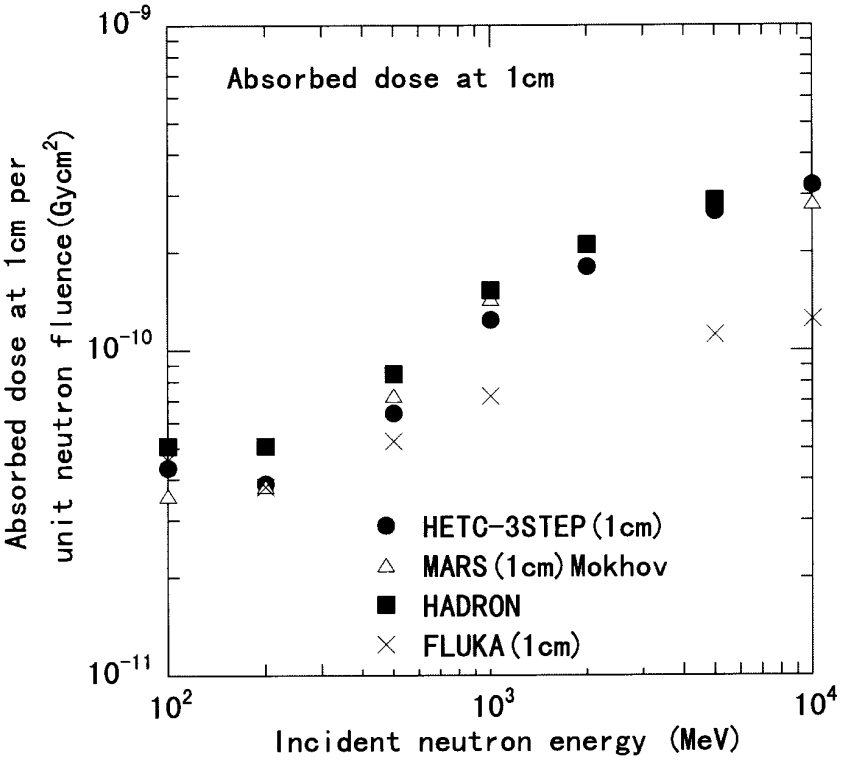

Figure 5. Maximum absorbed dose in ICRU phantom as a function of incident neutron energy

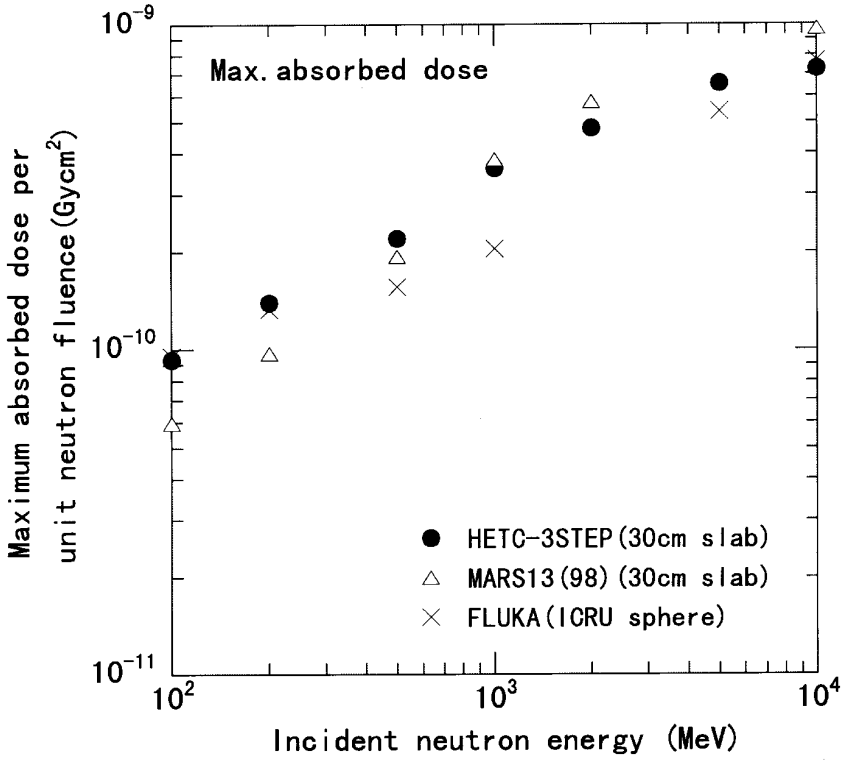

Figure 6. Ratio of max. and min. value of calculated absorbed dose in ICRU phantom as a function of incident neutron energy

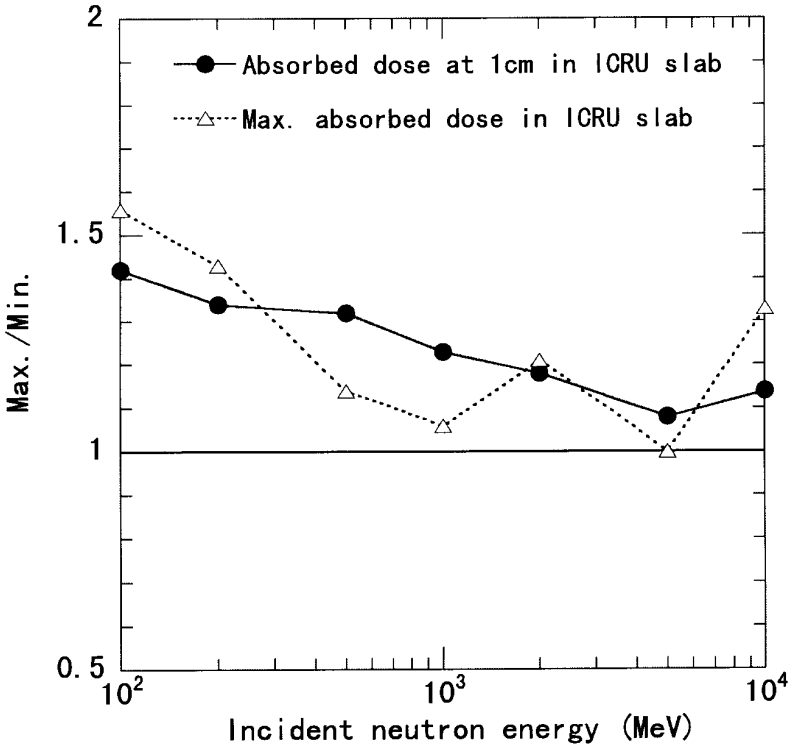

Figure 7. Dose equivalent at 1 cm in ICRU phantom as a function of incident neutron energy

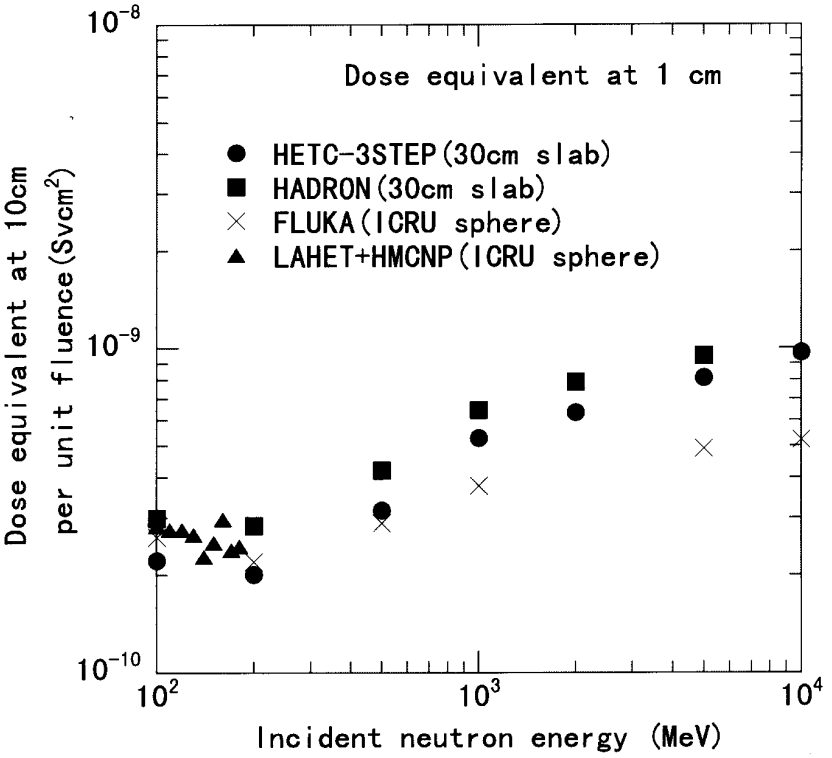

SESSION VI

Present Status of Computer Codes and Cross-Section and Shielding Data Libraries

Chairs: R. Roussin and M. Pelliccioni

PROGRESS REPORT ON THE COLLECTION OF COMPUTER CODES AND DATA SETS FOR ACCELERATOR SHIELDING ANALYSIS

Jennifer B. Manneschmidt, Hamilton T. Hunter and Bernadette L. Kirk
Radiation Safety Information Computational Centre (RSICC)
Oak Ridge National Laboratory
Oak Ridge, TN 37831-6362, USA

Enrico Sartori and Pedro Vaz
OECD/NEA Data Bank
12, Boulevard des Iles
92130 Issy-les-Moulineaux, France

Abstract

The three specialists meetings on Shielding Aspects of Accelerators, Targets and Irradiation Facilities (SATIF-1, SATIF-2, SATIF-3) held in Arlington, Texas (1994), Geneva, Switzerland (1996) and Sendai, Japan (1997) have produced an immense interest in the collection of computer software for accelerator shielding. The Nuclear Energy Agency Data Bank (NEA DB) and the Radiation Safety Information Computational Centre (RSICC) continue to pursue the task of collecting these codes for the interest of the community.

Progress since SATIF-3 (May 1997) – Highlights

Since the SATIF-3 meeting in Sendai, Japan in May 1997, the following codes have been made available from either RSICC or NEA DB. [Note: CCC (Computer Code Collection), PSR (Peripheral Shielding Routine) and DLC (Data Library Collection) are RSICC designations.]

- **ASOP (CCC-126)**
  Oak Ridge National Laboratory, Oak Ridge, Tennessee, contributed a new hardware version of ASOP to run on IBM RS/6000 workstations. ASOP is a shield optimisation calculational system based on the one-dimensional discrete ordinates transport code system ANISN (CCC-254).

- **ABAREX (PSR-248)**
  Argonne National Laboratory, Argonne, Illinois, contributed a newly frozen version of this optical-statistical model code system developed for the calculation of energy averaged neutron induced nuclear reaction cross-sections

- **ALICE-91 (PSR-146)**
  The International Atomic Energy Agency, Vienna, Austria, through the Nuclear Energy Agency Data Bank, Issy-les-Moulineaux, France, contributed a new hardware version of this statistical model code system with fission competition which originated at Lawrence Livermore National Laboratory.

- **BETA-S3.1 (CCC-657)**
  Atomic Energy of Canada Limited, Whiteshell Laboratories, contributed a code system to calculate multi-group beta-ray spectra. BETA-S calculates beta-decay source terms and energy spectra in multi-group format for time-dependent radionuclide inventories of actinides, fission products and activation products. BETA-S has been installed and verified on IBM RS/6000 and HP-750 workstations.

- **CALOR95 (CCC-610)**
  Oak Ridge National Laboratory contributed a replacement for the MORSE portion of this Monte Carlo code system for the design and analysis of calorimeter systems, Spallation Neutron Source (SNS) target systems, etc. CALOR95 was designed to assist experimentalists to evaluate and analyse different types of calorimeter systems used in many high-energy physics experiments to determine the energy and direction of incident hadrons, leptons and photons.

- **CCRMN (PSR-355 and IAEA1347)**
  The Nankai University, China and the China Institute of Atomic Energy, China, contributed this code system for calculating complex reactions of a medium-heavy nucleus with six light particles.

- **DOORS3.2 (CCC-650)**
  Oak Ridge National Laboratory, Oak Ridge, Tennessee, contributed corrections to this one-, two- and three-dimensional discrete ordinates neutron/photon transport code system. The changes incorporated when updating DOORS 3.1 to DOORS 3.2 include: the addition of an edit control variable to reduce the volume of print to standard output; the initialisation of the convergence map file, the elimination of the need to perform an extra iteration to save the directional fluxes when the user input time limit is reached and the update to circumvent

TORT's inability to obtain the correct system time charges from UNICOS during multitasking. Several other corrections and enhancements were made which improve portability among computing platforms.

- **ECIS (PSR-227 and NEA 0850)**
  The CEN Service de Physique Théorique, Saclay, France, through the OECD NEA Data Bank, Issy-les-Moulineaux, France, contributed a newly frozen version of this code system to solve the coupled differential equations arising in nuclear model calculations. ECIS-95 includes a few minor corrections and a revision of the statistical model which was used in ECIS-94.

- **EGS4 (CCC-331)**
  Radiation Physics Group, Stanford Linear Accelerator Centre, Stanford University, Stanford, California, and the National Research Council of Canada, Ottawa, contributed a newly frozen version of EGS4 for simulating almost any electron-photon transport problem conceivable.

- **ENDLIB-97 (DLC-179)**
  Lawrence Livermore National Laboratory, Livermore, California, contributed a newly frozen version of the evaluated photon interaction data library designated EPDL97. EPDL97 replaced EPDL89 in this package of atomic data, electron data, and photon data in Evaluated Nuclear Data Library (ENDL) type format.

- **FOTELP-EM (CCC-581)**
  The Institute of Nuclear Sciences "Vinca" Nuclear Engineering Laboratory "NET" Beograd, Yugoslavia, contributed a newly frozen version of this code system to compute photon/electron/positron radiation transport problems in three dimensions with or without the presence of macroscopic electric and magnetic fields for dosimetry, radiation damage, radiation therapy and other applications. FOTELP/EM runs on either IBM PC or VAX computers.

- **GMA (PSR-367)**
  Argonne National Laboratory-West, Idaho Falls, Idaho, contributed this computer code system for generalised least-squares evaluation of related cross-sections for ENDF/B based on Gauss, Markov, and Aitken. The simultaneous evaluation of the interrelated cross-section data of ^{6}Li(n,), ^{6}Li(n,n), ^{10}B(n,$_{0}$), ^{10}B(n,$_{1}$), ^{10}B(n,n), ^{197}Au(n,), ^{238}U(n,), ^{235}U(n,f), ^{239}Pu(n,f), ^{238}U(n,f) and the thermal constants was part of the evaluation of these data for ENDF/B-VI.

- **GNASH-FKK (PSR-125)**
  Los Alamos National Laboratory, Los Alamos, New Mexico, contributed a newly frozen version, designated Version gn9cp0, of this pre-equilibrium, statistical nuclear-model code system for calculation of cross-sections and emission spectra.

- **HERMES-KFA (NEA 1265)**
  HERMES-KFA consists of a set of Monte Carlo codes used to simulate particle radiation and interaction with matter. The main codes are HETC, MORSE, and EGS. This release (96b) is for multiple workstations running UNIX-like operating systems. Contributed by KFA Julich.

- **ICOM (CCC-651)**
  Chelyabinsk State University in Chelyabinsk, Russia, contributed this code system to calculate the transport characteristics of ion radiation for application to radiation protection, dosimetry and microdosimetry, and radiation physics of solids.

- **ITS3.0 (CCC-467)**
  An enhancement, known as BENGAL, was developed at the University of Tennessee Space Institute (UTSI) under contract for Arnold Engineering Development Center's (AEDC) DECADE project. BENGAL is a set of UPdate Directive (UPD) files for use with the Integrated TIGER Series (ITS) of Coupled Electron/Photon Monte Carlo Transport Codes System which enhances the ITS member codes by increasing their execution speed.

- **MARLOWE 14c (PSR-137)**
  Oak Ridge National Laboratory contributed a newly frozen version of this code system for simulating atomic collisions in crystalline targets using the binary collision approximation. The new release is designated Marlowe 14c and includes several corrections and enhancements.

- **MCNP4B2 (CCC-660)**
  Los Alamos National Laboratory, Los Alamos, New Mexico, contributed a correction for MCNP4B which supports Linux and Lahey Fortran 90 on PCs, includes a fix for PVM, and corrects a potentially significant problem which affects all repeated structures/lattice geometry problems with closely spaced surfaces.

- **MCNP-VISED25af (PSR-358)**
  Battelle Pacific Northwest National Laboratory, Richland, Washington, contributed this visual editor for creating MCNP4A input files. MCNP was developed at Los Alamos National Laboratory. MCNP-VISED25af enables a visual creation of an MCNP input file.

- **MIRDOSE 3.1 (CCC-528)**
  The Oak Ridge Institute for Science and Education (ORISE), Oak Ridge, Tennessee, contributed a newly frozen version of this code system to calculate internal dose estimates by the MIRD technique. MIRDOSE 3.1 allows the user to choose from 28 source organs and calculates the radiation-absorbed dose to 28 target organs, plus the effective dose and effective dose equivalent for ten phantoms representing adults, children and pregnant women. Several corrections and enhancements to MIRDOSE 3.0 were made in preparing version 3.1. In the following models, the noted bugs were fixed.

- **MRIPP (CCC-655)**
  Lawrence Livermore National Laboratory, Livermore, California, contributed the MRIPP (Magnetic Resonance Image Phantom Program) code system. MRIPP provides relative calibration factors for the *in vivo* measurement of internally deposited photon emitting radionuclides within the human body.

- **MSM-SOURCE (PSR-369 and IAEA1349)**
  The Department of Nuclear Reactions at Moscow State University, Russia, contributed this code system designed for quick and easy estimations of basic stopping characteristics of proton transmission for generation of the source definition (SDEF) portion of the input data for MCNP.

- **NJOY 97.0 (PSR-368)**
  Los Alamos National Laboratory, Los Alamos, New Mexico, contributed a new version of the NJOY Nuclear Data Processing System, a modular computer code for converting evaluated nuclear data in the ENDF format into libraries useful for application calculations.

- **PENELOPE (NEA 1525)**
  New version containing: i) the new package PENGEOM2 which allows to describe any material system as consisting of homogeneous bodies limited by quadric surfaces ii) the program GVIEW to display the geometry of the system on the computer screen.

- **POINT97 (DLC-192)**
  Lawrence Livermore National Laboratory, Livermore, California, contributed a new data library distributed as POINT97. The reference evaluated data includes cross-sections represented in the form of a combination of resonance parameters and/or tabulated energy dependent cross-sections, nominally at 0 Kelvin temperature.

- **PREPRO-96 (CCC-351)**
  Lawrence Livermore National Laboratory, Livermore, California, and the International Atomic Energy Agency, Vienna, Austria, contributed a newly frozen version of the pre-processing code system for data in ENDF/B format, designated PREPRO-96. The ENDF/B pre-processing codes are designed to be a modular set of computer codes, each of which reads evaluated nuclear data in the ENDF/B format, processes the data and writes it in the ENDF/B format.

- **RAF (IAEA1350)**
  Neutron and proton radiative capture differential and integrated cross-sections and angular distribution coefficients are determined as a function of the projectile energy in the region of the giant multipole resonances. Besides the isovector dipole resonance, isovector and isoscalar quadrupole resonances can be included in the calculation.

- **RESRAD 5.82 (CCC-552)**
  Argonne National Laboratory contributed a newly frozen version of this code system to calculate site-specific residual radioactive material guidelines and radiation dose and excess cancer risk to an on-site resident. The revised package includes RESRAD 5.82 and RESRAD-BUILD 2.36.

- **SINBAD97 (DLC-191 and NEA 1517)**
  Oak Ridge National Laboratory, Oak Ridge, Tennessee, and the OCDE/OECD NEA Data Bank, Paris, France, contributed a new data package called SINBAD version 97 (Shielding Integral Benchmark Archive and Database). Prompted by the closures of experimental facilities throughout the world, the effort to preserve benchmark information in formats acceptable to the international community began in 1992-93.

- **SKYIII-PC (CCC-0289)**
  This program is a PC version of SKYSHINE-III.

- **SKYSHINE-KSU (CCC-0646)**
  This program computes Gamma Skyshine Doses by different methods.

- **SOURCES3A (CCC-661)**
  Los Alamos National Laboratory, Los Alamos, New Mexico, contributed a new code system to determine alpha,n; spontaneous-fission; and beta-n delayed neutron sources and spectra due to the decay of radionuclides in homogeneous media.

- **SRIM-98.001 (NEA 0919)**
  SRIM is a group of programs which calculate the stopping and range (10 eV-2 GeV/amu) of ions in matter. Developed at the IBM Watson Centre and the Hahn-Meitner Institute in Berlin.

- **STAPRE-H95 (PSR-325 and IAEA0971)**
  The Institute for Physics and Nuclear Engineering, Bucharest-Magurele, Romania, through the NEA Data Bank, Issy-les-Moulineaux, France, contributed a newly frozen PC version of this code system designed to calculate energy-averaged cross-sections of particle induced nuclear reactions.

- **TART97 (CCC-638)**
  Lawrence Livermore National Laboratory, Livermore, California, contributed a newly frozen version of this coupled neutron-photon, three-dimensional, combinatorial geometry, Monte Carlo transport code system. TART97 can calculate 1) static reactivity problems, 2) dynamic reactivity problems, 3) source problems involving any combination of neutron and/or photon sources.

Please refer to Tables 1-4 for a more detailed description of the programs and data libraries available at present.

Progress report on SINBAD, the Shielding Benchmarks Database

The Shielding Integral Benchmark Archive and Database (SINBAD) is a PC-based electronic database (5,6) developed to store a variety of radiation shielding benchmark data in Hypertext Markup Language (HTML) format. A brief description of the selected benchmarks was first given in reference [4,5]. Since then, several actions have been undertaken in order to collect and add to the SINBAD database, relevant benchmark data (see Tables 14 and 15).

REFERENCES

[1] Proceedings of the Specialists Meeting on Shielding Aspects of Accelerators, Targets and Irradiation Facilities, held in Arlington, Texas (US) on 28-29 April 1994, published as an OECD document ISBN 92-64-14327-0.

[2] Proceedings of the Second Specialists Meeting on Shielding Aspects of Accelerators, Targets and Irradiation Facilities (SATIF-2), held at CERN, Geneva (Switzerland), on 12-13 Oct. 1995, published as an OECD document ISBN 92-64-15287-3.

[3] Proceedings of the Second Specialists Meeting on Shielding Aspects of Accelerators, Targets and Irradiation Facilities (SATIF-3), held at Tohoku University, Sendai, Japan, on 12-13 May 1997, published as an OECD document ISBN 92-64-16071-X.

[4] "SINBAD – A Shielding Integral Benchmark Archive and Database for PCs", by H.T. Hunter *et. al.*, in Proceedings of the 8th International Conference on Radiation Shielding, Arlington, Texas, 24-28 April 1994, p. 795, American Nuclear Society, La Grange Park, Illinois, 1994.

[5] "SINBAD – Shielding Integral Benchmark Archive and Database", by H.T. Hunter, D.T. Ingersoll, R.W. Roussin, C.O. Slater, I. Kodeli and E. Sartori, in Proceedings of the Second Specialists Meeting on Shielding Aspects of Accelerators, Targets and Irradiation Facilities, held at CERN, Geneva (Switzerland) on 12-13 October 1995, published as an OECD document ISBN92-64-15287-3.

Table 1. List of programs and data in alphabetical order

(*) *Programs available*
(**) *Programs known but not available*
(***) *Additions/updates since the SATIF-3 meeting*
CCC-,PSR-,DLC- *: original packaging by RSICC*
NESC *: original packaging by NESC (now ESTSC)*
USCD *: originated in US/Canada, packaged by NEA DB*
NEA, IAEA *: original packaging by NEA DB*
<blank> *: acquisition sought*
xsec *: cross-section*
lib. *: library*

Name	Identification	Function
ABAREX ***	PSR-248	optical statistical model to calculate energy averaged neutron induced reaction cross-sections
ACTIV-87	IAEA1275	library with fast neutron activation x-sections
AIRSCAT	CCC-0341	dose rate from gamma air scattering, single scat. approx.
ALBEDO	NEA 1353	gamma, neutron attenuation in air ducts
ALDOSE	CCC-0577	calculates absorbed dose and dose equivalent rates as function of depth in water irradiated by alpha source
ALICE91 ***	PSR-0146	precompound/compound nuclear decay model
ALPHN	CCC-0612	calculates the (alpha,n) production rate in a mixture receiving alpha particles from emitting actinides
AMALTHEE	NEA 0675	emission spectra for n, p, d, h3, he3, alpha reaction
ANISN	CCC-0650	1-D Sn, n, gamma transport in slab, cylinder, sphere
ASOP ***	CCC-0126	1-D Sn shield calculation (new version for AIX and Linux)
ASTAR	IAEA1282	calculates stopping power and range for alphas
ASTROS	CCC-0073	primary/secondary proton dose in sphere/slab tissue
AUJP	IAEA0906	optical potential parameters search by chi**2 method
BALTORO	NEA 0675	n, gamma transport perturbation from MORSE, ANISN calculation
BASACF	IAEA0953	integral neutron adjustment and dosimetry
BERMUDA	NEA 0949	1-D,2-D,3-D n. gamma transport for shielding
BETA-2B	CCC-0117	MC time-dependent bremsstrahlung, electron transport
BETA-S3.1 ***	CCC-657	calculates beta decay source terms and energy spectra
BREESE	PSR-0143	distribution function for MORSE from albedo data
BREMRAD	CCC-0031	external/internal bremsstrahlung
BRHGAM	CCC-0350	MC absorbed dose from x-rays in phantom
CADE	NEA 1020	multiple particle emission x-sections by Weisskopf-Ewing
CALOR95 ***	CCC-0610	MC system for design, analysis of calorimeter system
CAMERA	CCC-0240	radiation transport and computerised man model
CARP-82	PSR-0131	currents for BREESE from DOT flux
CASCADE	CCC-0176	high-energy electron-photon transport in matter
CASIM	NESC0742	MC high energy cascades in complex shields
CCRMN ***	PSR-355	computation of reactions of a medium-heavy nucleus with six light particles
CEM95	IAEA1247	MC calculation of nuclear reactions (Cascade Exciton Model)
CENDL	IAEA1256	Chinese Evaluated Nuclear Data Library (neutron, proton, deuteron, triton, He3 and He4)
CEPXS/ONELD	CCC-0544	1-D coupled electron photon multi-group transport
CFUP1	IAEA1266	n, charged-particle reaction of fissile nuclei E < 33 MeV
CHARGE-2/C	CCC-0070	electron, p, heavy particle flux/dose behind shield
CHUCK	USCD1021	n, charged particle x-sections, coupled channel model
CMUP2	IAEA1265	reaction x-sections for n ,p, d, t, he3, he4, E < 50 MeV
COLLI-PTB	NEA 1126	MC n fluence spectra for 3-D collimator system
COMNUC3B	PSR-0302	compound nucleus interaction in n reactions
COVFILES	DLC-0091	library of neutron x-sections covariance data, useful to estimate radiation damage or heating
DANTSYS	CCC-0547	1-D, 2-D, 3-D Sn neutron, photon transport
DASH	CCC-0366	void tracing Sn - MC coupling with fluxes from DOT
DCTDOS	CCC-0520	n,gamma penetration in composite duct system
DDCS	IAEA1290	calculation of neutron, proton, deuteron, triton, He3, and alpha induced reactions of medium heavy nuclei in the energy range up to 50 MeV
DISDOS	CCC-0170	dose from external photons in phantom
DOMINO	PSR-0064	coupling of Sn DOT with MC MORSE
DOORS3.2 ***	CCC-0650	Discrete ordinates system for deep penetration neutron and gamma transport
DORT	CCC-0543	1-D 2-D Sn n, photon transport with deep penetration
DOSDAT-2	DLC-0079	gamma, electron dose factors data lib. for body organs
DOSEDAT-DOE	DLC-0144	dose rate factors for external photon, electron exposure
DOT	CCC-0276	2-D Sn n, photon transport with deep penetration

Table 1. List of programs and data in alphabetical order (*continued*)

Name	Identification	Function
DROSG-87	IAEA1234	library of Legendre coefficients for neutron reactions
DUST	CCC-0453	albedo MC simulation of n streaming inducts
DWBA82	NEA 1209	Distorted Wave Born Approximation nuclear model
DWUCK-4	NESC9872	Distorted Wave Born Approximation nuclear model
E-DEP-1	CCC-0275	heavy ion energy deposition
EADL	DLC-0179	library of atomic subshell and relaxation data
ECIS-95 ***	NEA 0850	Schroedinger/Dirac nuclear model with experimental fit
ECPL-86	DLC-0106	evaluated charged particle cross-sections
EDMULT	NEA 0969	electron depth dose in multi-layer slab absorbers
EEDL	DLC-179	electron interaction x-section from 10 eV to 100 GeV
EGS4	CCC-0331	MC electron photon shower simulation
EGS4 ***	CCC-0331	version 3.0 of the UNIX distribution of EGS4
ELBA	CCC-0119	bremsstrahlung dose from electron flux on Al shield
ELPHIC-PC	IAEA1223	statistical model MC simulation of heavy ion reaction
ELPHO	CCC-0301	MC muon, electron, positron generation from pions
ELTRAN	CCC-0155	MC 1-D electron transport
EMPIRE-MSC	IAEA1169	multi-step compound nucleus/pre-equilibrium x-sections
ENLOSS	PSR-0047	energy loss of charged particles
ENDLIB-97 ***	DLC-0179	coupled electron & photon transport library (in LLL ENDL format)
EPDL-97	DLC-0179	photon interaction x-sections library (10 eV to 100 GeV)
EPICSHOW	IAEA1285	Interactive Viewing of the Electron-Photon Interaction (10 eV < E < 1 GeV)
EPICSHOW-96.1	CCC-638	Interactive Viewing of the Electron-Photon Interaction
ERINNI	NEA 0815	multiple cascades emission spectra by optical model
ESTAR	IAEA1282	calculates stopping power and range for electrons
ETRAN	CCC-0107	MC electron, gamma transport with secondary radiation
EVA		codes performing the nuclear evaporation processes (working on the output from ISABEL)
EVALPLOT	IAEA0852	plots x-sections in ENDF/B format, angular and energy distributions
EVAP_F **		modified version of the Dresner evaporation code
EXIFONGAMMA	IAEA1211	n, alpha, proton, gamma emission spectra model
FALSTF	CCC-0351	n, gamma flux detector response outside cylindrical shields
FEM-RZ	NEA 0566	2-D multi-group n transport in r-z geometry
FGR-DOSE	DLC-0167	library of dose coefficients for intake and exposure to radionuclides
FLEP	DLC-0022	neutron, proton non-elastic x-sections and spectra E < 400 MeV
FLUKA	CCC-0207	MC high energy extranuclear hadron cascades
FLUNEV-DESY		
FOTELP/EM ***	CCC-0581	MC photons, electrons and positron transport
FRITIOF (**)		hadronic cascades in high-energy heavy ion collisions
FSMN	IAEA1264	fission spectra by compound-nucleus optical model
FSXLIB-J3R2	NEA 1424	JENDL-3 Evaluated Nuclear Data File, fusion neutronics
G33-GP	CCC-0494	multi-group gamma scattering using gp build-up-factor
GAMMONE	NEA 0268	MC gamma penetration from various geometrical sources
GBANISN	CCC-0628	1-D neutron & gamma fluxes with group band fluxes
GEANT-CERN		
GGG-GP	CCC-0564	multi-group gamma-ray scattering - build-up factors
GMA ***	PSR-367	generalised least squares evaluation of related cross-sections
GNASH-FKK ***	PSR-0125	multi-step direct and compound and Hauser Feshbach models
GNASH-LANL	PSR-0125	pre-equilibrium/statistical x-sections, emission spectra
GRACE-1	NESC0045	multi-group gamma attenuation, dose in slab
GRAPE	NEA 1043	precompound/compound nuclear reaction models
GRPANL	PSR-0321	Germanium gamma and alpha detector spectra unfolding
HELLO	DLC-0058	47 n, 21 gamma group coupled x-sections from VITAMIN-C library
HERMES-KFA ***	NEA 1265	MC high-energy radiation transport
HERMES96b	NEA 1265	MC high-energy radiation transport
HETC NMTC	CCC-0178	MC high energy nucleon meson cascade transport
HETC-KFA	CCC-0496	MC high energy nucleon-meson cascades
HETC95 (**)		MC high energy nucleon-meson cascades and transport
HFMOD	IAEA1317	elastic and inelastic x-section calculation by Hauser-Feshbach and Moldauer
HFTT	IAEA0954	n x-sections by compound-nucleus evaporation model
HIC-1	CCC-0249	MC heavy ion reactions at E>50 MeV/nucleon
HIJET (**)		hadronic cascades in high-energy Heavy Ion Collisions
HILO86	DLC-0119	66 N, 22 gamma group x-section lib. for ANISN-ORNL, DORT, MORSE-CGA
HILO86R	DLC-0187	66 N, 22 gamma group x-section, up to 400 MeV (neutron) and 20 MeV (gamma)
HOMO	IAEA1253	program for mixing/converting libraries in ANISN format

Table 1. List of programs and data in alphabetical order (*continued*)

Name	Identification	Function
HUGO-VI	DLC-0146	photon interaction evaluated data library ENDF-6 format
ICOM	CCC-651	calculate transport characteristics of ion radiation
IDC	CCC-0384	ICRP dosimetric calculational system
IHEAS-BENCH	NEA 1468	high-energy accelerator shielding benchmarks
IMPACTS	ESTS0005	radiological assessment code
INFLTB	PSR-0313	dosimetric mass energy transfer and absorption coefficients
ISABEL	NEA 1413	intra-nuclear cascade model allowing hydrogen and helium ions and antiprotons as projectiles
ISAJET (**)		hadronic cascades in high-energy Heavy Ion Collisions
ISO-PC	CCC-0636	kernel integration code system for general purpose isotope shielding
ITS-3.0	CCC-0467	MC system of coupled electron photon transport, photon, neutron dose in electron accelerator
K009	CCC-0062	charged particle penetration – phantom quantum mechanical multi-step direct model
LA100	DLC-0168	evaluated data library for n, p up to 100 MeV, ENDF-6 format
LAHET **		MC nucleon, pion, muons, tritons, He-3, alpha transport
LAHIMAC	DLC-0128	neutron, gamma x-sections - response functions, E<800MeV
LEP	DLC-0001	results from intra-nuclear cascade and evaporation
LIMES	NEA 1337	intermediate mass fragments in heavy ion nuclear reactions
LPPC	CCC-0051	proton penetration, slab
LPSC	CCC-0064	p, n flux, spectra behind slab shield from p irradiation
LRSPC	CCC-0050	range and stopping power calculator for ions
MAGIK	CCC-0359	MC for computing induced residual activation dose rates
MAGNA	NEA 0163	dose rates from gamma source in slab or cylindrical shell shields
MARLOWE14c ***	PSR-0137	atomic displacement cascades in solids
MARMER	NEA 1307	point-kernel shielding, ORIGEN-S nuclide inventories
MATXS10	DLC-0176	library with 30n-12gamma energy groups for particle transport codes
MATXS11	DLC-0177	library with 80n-24gamma energy groups for particle transport codes
MCNP-4A	CCC-0200	MC 3-D time-dependent coupled n, photon, electron transport
MCNP-4B2 ***	CCC-0660	MC 3-D time-dependent coupled n, photon, electron transport
MCNPDAT	DLC-0105	x-section data library for the MCNP-4A transport code
MCNPDAT6	DLC-0181	x-section data library from ENDF/B-VI for MCNP-4A
MCNP-VISED ***	PSR-358	visual editor for MCNP input
MCNPXS	DLC-0189	x-section data for MCNP4B2
MECC-7	CCC-0156	medium energy intra-nuclear cascade model
MENSLIB	DLC-0084	neutron 60 group x-sections, E<60MeV
MERCURE-4	NEA 0351	MC 3-D gamma heating/gamma dose rate, fast flux
MEVDP	CCC-0157	radiation transport in computerised anatomical man
MICAP	PSR-0261	MC ionisation chamber responses
MIRDOSE3.1	CCC-0528	calculate internal dose estimates by the MIRD technique
MORSE-CGA	CCC-0474	MC n, gamma multi-group transport
MRIPP 1.0	CCC-0655	magnetic resonance image phantom for in vivo measurements
MSM-SOURCE ***	PSR-0369	estimate stopping characteristics of proton transmissions
MUONLM	NEA 1475	calorimeter Interaction of Muons
MUP-2	IAEA0907	fast n reaction x-sections of medium-heavy nuclei
MUTIL	NEA-1451	calculates the asymmetry factor of the Mott scattering of electrons and positrons by point nuclei
NDEM (**)		generates a gamma-ray source from the de-excitation of residual nuclei
NESKA	NEA 1422	electron, positron scattering from point nuclei
NFCLIST	ESTS0352	radionuclide decay data tabulations (240 radionuclides)
NJOY-94	PSR-0171	n, p, photon evaluated data processing system
NJOY-94.61		
NJOY97.0 ***	PSR-355	n, p, photon evaluated data processing system
NMTC/JAERI	NEA 0974	MC high-energy p, n, pion reactions
NMF-90	IAEA1279	database for neutron spectra unfolding
NUCDECAY	DLC-0172	nuclear decay data for radiation dosimetry calculations
NUCHART	IAEA1320	nuclear properties and decay data chart
NUCLEUS		nuclear spallation simulation and primary products
OPTMOD	IAEA1316	elastic & total x-section, polarisation calculations using the optical model
PACE2 (**)		codes performing the nuclear evaporation processes (working on the output from ISABEL)
PALLAS-2DY	NEA 0702	2-D n ,gamma transport for fixed source
PCROSS	IAEA1220	pre-equilibrium emission spectra in neutron reaction
PCNUDAT	USCD1205	nuclear properties database & retrieval system
PCNULIB	USCD1205	idem
PEGAS	IAEA1261	unified model of particle and gamma emission reactions
PELSHIE	IAEA0855	dose rates from gamma source, point-kernel method
PENELOPE ***	NEA 1525	Monte Carlo code for electron-photon transport

Table 1. List of programs and data in alphabetical order (*continued*)

Name	Identification	Function
PEQAG-2	IAEA1185	pre-equilibrium model nucleon, gamma spectra, x-sections
PEREGRINE (**)		used to model dose to humans from radiation therapy
PHOTX	DLC-0136	photon interaction x-section library for 100 elements
PICA	CCC-0160	MC calculation of nuclear cascade reactions caused by the collision of photons (30 < E < 400 MeV) with nuclei
PIPE	NEA 0416	1-D gamma transport for slab, spherical shields
PLACID	CCC-0381	MC gamma streaming in cylindrical duct shields
PNESD	IAEA1235	elastic x-sections of 3 MeV to 1000 MeV p on natural isotopes
POINT97 ***	DLC-0192	evaluated cross-sections in the form of a combination of resonance parameters and/or tabulated energy dependent cross-sections
POTAUS	IAEA1249	H through U ion ranges, stopping power for various materials
PREANG	NEA 0809	nuclear model particle spectra, angular distribution
PRECO-D2	PSR-0226	pre-equilibrium, direct reaction double differential x-sections
PREM	NEA 0888	nucleon emission pre-equilibrium energy spectra, x-sections
PREPRO-96 ***	CCC-351	pre-processing code system for data in ENDF/B format
PSTAR	IAEA1282	calculates stopping power and range for protons
PTRAN	CCC-0618	MC proton transport for 50 to 250 MeV
PUTZ	CCC-0595	point-kernel 3-D gamma shielding
QAD-CGGP-A	CCC-0645	fast neutron and gamma ray penetration in shields
QMD		intra-nuclear cascade and classical molecular dynamics
RADCOMPT	PSR-0348	sample analysis for alpha and beta dual channel detect
RADDECAY	DLC-0134	decay data library for radiological assessment
RADHEAT-V3	NEA 0467	transport, heat, radiation damage x-sections in reactor, shield
RAID	CCC-0083	gamma, n scattering into cylindrical or multi-bend duct
RAF ***	IAEA1350	neutron and proton radiative capture differential and integrated cross-section
REAC	CCC-0443	activation and transmutation
REAC-2	NESC9554	nuclide activation, transmutation
REAC*3	CCC-0443	isotope activation & transmutation in fusion reactors
REBEL-3	IAEA0846	MC radiation dose to human organs
RECOIL/B	DLC-0055	heavy charged particle recoil spectra lib. for radiation damage
REMIT	ESTS0579	Radiation Exposure Monitoring and Inf. Transmittal system
REPC	PSR-0195	dose from protons in tissue
RESRAD5.82 ***	CCC-0552	calculation of residual radioactive material guidelines, site specific radiation doses and risks
SAM-CE	CCC-0187	MC time-dependent 3-d n ,gamma transport in complex geometry
SAMSY	IAEA0837	n, gamma dose rates, heat source for multi-layer shields
SAND-II	PSR-0345	determines neutron energy spectra using multiple experimental activation detector data
SANDYL	CCC-0361	MC 3-d time-dependent gamma electron cascade transport
SCAP-82	CCC-0418	scattering, albedo, point-kernel anal. in complex geometry
SCINFUL	PSR-0267	MC to compute the response of scintillation neutron detector (incident neutron energies from 0.1 to 75 MeV)
SEECAL	CCC-0620	computes age-dependent effective energies for 54 and 32 target regions in the human body (825 radionuclides)
SFERXS	NEA 1239	photon absorption, coherent, incoherent x-sections for shielding
SHIELD (**)	IAEA1287	universal code for exclusive simulation of hadron cascades in complex macroscopic targets
SIGMA-A	DLC-0139	photon interaction and absorption data 1 KeV-100 MeV
SINBAD97 ***	DLC-191	Shielding INtegral Benchmark Archive DataBase
SITHA (**)	IAEA1179	SImulation Transport HAdron, calculates hadron transport
SKYIII-PC ***	CCC-0289	PC version of program SKYSHINE-III
SKYPORT	DLC-0093	importance of n, photon skyshine dose from accelerators
SKYSHINE-KSU ***	CCC-0646	computation of gamma skyshine doses by different methods
SNLRML	DLC-0178	dosimetry library compendium
SNL/SAND-II	PSR-0345	enhanced version of SAND-II
SOURCE (**)		description of the proton transmission and generation of n source
SOURCES3A ***	CCC-661	determines (α,n), spontaneous fission and (β,n) delayed neutron sources and spectra due to decay in homogeneous media
SPACETRAN	CCC-0120	radiation leakage from cylinder with ANISN flux
SPAR	CCC-0228	stopping power and ranges from muons, pions, protons ions
SPARES	CCC-0148	space radiation environment and shielding evaluation
SPEC	IAEA1332	computation of neutron and charged particle reactions using optical and evaporation models
SPCHAIN (**)		calculates accumulation and decay of nuclides
SPECTER-ANL	PSR-0263	n damage for material irradiation
SRIM-98.001 ***	NEA 0919	stopping power and ranges of ions (10 ev-2 GeV/amu)
STAC-8		transmitted, absorbed power/spectrum – synchrotron radiation

Table 1. List of programs and data in alphabetical order (*continued*)

Name	Identification	Function
STAPRE-H	IAEA0971	evaporation, pre-equilibrium model reaction x-sections
STAPRE-H95 ***	PSR-0325	evaporation, pre-equilibrium model reaction x-sections
STARCODES	PSR-0330	stopping power, ranges for electrons, protons, alpha
STOPOW	IAEA0970	stopping power of fast ions in matter
STR92	ESTS1041	energy deposition in accelerator ring components
STRAGL	CCC-0201	energy loss straggling of heavy charged particles
SWIMS	ESTS0682	calculates the angular dispersion of ion beams that undergo small-angle incoherent multiple scattering by gaseous or solid media
TART95		3D MC transport program for neutrons and photons
TART96		
TART97 ***	CCC-638	3D MC transport program for neutrons and photons
TEST	IAEA1252	program for sorting/listing/deleting ANISN libraries
TNG1	PSR-0298	N multi-step statistical model
TORT	CCC-0543	3-D Sn n, photon transport with deep penetration
TPASGAM	DLC-0088	library with gamma-ray decay data for 1438 radionuclides
TRANSX2.15	PSR-0317	code to produce neutron, photon transport tables for discrete ordinates and diffusion codes
TRAPP	CCC-0205	proton and alpha transport, reaction products neglected
TRIPOLI-2	NEA 0874	MC time-dependent 3-D N, gamma transport
TRIPOS	CCC-0537	MC ion transport
TWODANT-SYS	CCC-0547	1-D,2-D multi-group Sn n, photon transport
UNGER	DLC-0164	effective dose equivalent data for selected isotopes
UNIFY	IAEA1177	fast n x-sections, spectrum calculation for structural materials
UNSPEC	ESTS0827	X-ray spectrum unfolding using an iterative technique
VEGAS (**)		intra-nuclear cascade code (from which ISABEL is derived)
VIRGIN	IAEA0932	calculates uncollided neutron flux and neutron reactions due to transmission of a neutron beam through any thickness of material
VITAMIN-E	DLC-0113	x-section data library with 174n-38gamma energy groups
VITAMIN-B6	DLC-0184	x-section data library with 199n-42gamma energy groups from ENDF/B-VI Release 3
XCOM	DLC-0174	photon cross-sections from 1 KeV to 100 GeV

Table 2. Evaluated and processed data (cross-sections, dose conversion, ranges, stopping powers)

Name	Identification	Function
ACTIV-87	IAEA1275	library with fast neutron activation x-sections
CENDL	IAEA1256	Chinese Evaluated Nuclear Data Library (neutron, proton, deuteron, triton, He3 and He4)
COVFILES	DLC-0091	library of neutron x-sections covariance data, useful to estimate radiation damage or heating
DROSG-87	IAEA1234	library of Legendre coefficients for neutron reactions
DOSDAT-2	DLC-0079	gamma, electron dose factors data lib. for body organs
DOSEDAT-DOE	DLC-0144	dose rate factors for external photon, electron exposure
EADL	USCD1192	library of atomic subshell and relaxation data
ECPL-86	DLC-0106	evaluated charged particle cross-sections
EEDL	USCD1193	electron interaction x-section from 10 eV to 100 GeV
ENDLIB-94	DLC-0179	coupled electron & photon transport library (in LLL ENDL format)
ENDLIB-97 ***	DLC-0179	coupled electron & photon transport library (in LLL ENDL format)
EPDL-VI/MOD	USCD1187	photon interaction x-sections library (10 eV to 100 GeV)
FGR-DOSE	DLC-0167	library of dose coefficients for intake and exposure to radionuclides
FLEP	DLC-0022	neutron, proton non-elastic x-sections and spectra E < 400 MeV
FSXLIB-J3R2	NEA 1424	JENDL-3 Evaluated Nuclear Data File, fusion neutronics
HILO86	DLC-0119	66 N, 22 gamma group x-section lib. for ANISN-ORNL, DORT, MORSE-CGA
HILO86R	DLC-0187	66 N, 22 gamma group x-sections, up to 400 MeV (neutron) and 20 MeV (gamma)
HELLO	DLC-0058	47 n, 21 gamma group coupled x-section from VITAMIN-C library
HUGO-VI	DLC-0146	photon interaction evaluated data library ENDF-6 format
IDC	CCC-0384	ICRP dosimetric calculational system
IHEAS-BENCH	NEA 1468	high-energy accelerator shielding benchmarks
LA100	DLC-0168	evaluated data library for n, p up to 100 MeV, ENDF -6 format
LAHIMACK	DLC-0128	multi-group neutron and gamma x-sections up to 800 MeV
LEP	DLC-0001	results from intra-nuclear cascade and evaporation
LRSPC	CCC-0050	range and stopping power calculator
MATXS10	DLC-0176	library with 30n-12gamma energy groups for particle transport codes
MATXS11	DLC-0177	library with 30n-12gamma energy groups
MCNPDAT	DLC-0105	x-section data library for the MCNP-4A transport code
MCNPDAT6	DLC-0181	x-section data library from ENDF/B-VI for MCNP-4A
MENSLIB	DLC-0084	neutron 60 group x-sections, E<60MeV
NFCLIST	ESTS0352	radionuclide decay data tabulations (240 radionuclides)
NJOY97.0 ***	PSR-355	n, p, photon evaluated data processing system
NMF-90	IAEA1279	database for neutron spectra unfolding
NUCDECAY	DLC-0172	nuclear decay data for radiation dosimetry calculations
NUCHART	IAEA1320	nuclear properties and decay data chart
PCNUDAT	USCD1205	nuclear properties database & retrieval system
PCNULIB	USCD1205	nuclear properties database & retrieval system
PHOTX	DLC-0136	photon interaction x-section library for 100 elements
PNESD	IAEA1235	elastic x-sections of 3 MeV to 1000 MeV p on natural isotopes
POINT97 ***	DLC-0192	evaluated cross-sections in the form of a combination of resonance parameters and/or tabulated energy dependent cross-sections
RADDECAY	DLC-0134	decay data library for radiological assessment
RECOIL/B	DLC-0055	heavy charged particle recoil spectra lib. for radiation damage
SFERXS	NEA 1239	photon absorption, coherent, incoherent x-sections for shielding
SIGMA-A	DLC-0139	photon interaction and absorption data 1 KeV-100 MeV
SINBAD97***	DLC-191	Shielding INtegral Benchmark Archive DataBase
SKYIII-PC ***	CCC-0289	PC version of program SKYSHINE-III
SKYPORT	DLC-0093	importance of n, photon skyshine dose from accelerator
SKYSHINE-KSU ***	CCC-0646	computation of gamma skyshine doses by different methods
SNLRML	DLC-0178	dosimetry library compendium
SPAR	CCC-0228	stopping power and ranges from muons, pions, protons, ions
SRIM-98.001 ***	NEA 0919	stopping power and ranges of ions (10 eV-2 GeV/amu) in matter
STAC-8		transmitted, absorbed power/spectrum – synchrotron radiation
STARCODES	PSR-0330	stopping power, ranges for electrons, protons, alpha
STOPOW	IAEA0970	stopping power of fast ions in matter
TPASGAM	DLC-0088	library with gamma-ray decay data for 1438 radionuclides
UNGER	DLC-0164	effective dose equivalent data for selected isotopes
VITAMIN-E	DLC-0113	x-section data library with 174n-38gamma energy groups
VITAMIN-B6	DLC-0184	x-section data library with 199n-42gamma energy groups derived from ENDF/B-VI Release 3
XCOM	DLC-0174	photon cross-sections from 1 KeV to 100 GeV

Table 3. Cross-sections – Spectra from nuclear models (for E > 20 MeV)

Name	Identification	Function
ALICE91 ***	PSR-0146	precompound/compound nuclear decay model
AMALTHEE	NEA 0675	emission spectra for n, p, d, h3, he3, alpha reaction
ASOP	CCC-0126	1-D Sn shield calculation
AUJP	IAEA0906	optical potential parameters search by chi**2 method
CADE	NEA 1020	multiple particle emission x-sections by Weisskopf-Ewing
CCRMN ***	IAEA1347	computation of reactions of a medium-heavy nucleus with six light particles
CEM95	IAEA1247	MC calculation of nuclear reactions (Cascade Exciton Model)
CFUP1	IAEA1266	n, charged-particle reaction of fissile nuclei E < 33 MeV
CHUCK	USCD1021	n, charged particle x-sections, coupled channel model
CMUP2	IAEA1265	reaction x-sections for n ,p, d, t, he3, he4, E < 50 MeV
COMNUC3B	PSR-0302	compound nucleus interaction in n reactions
DWBA82	NEA 1209	Distorted Wave Born Approximation nuclear model
DWUCK-4	NESC9872	Distorted Wave Born Approximation nuclear model
ECIS-95 ***	NEA 0850	Schroedinger/Dirac nuclear model with experimental fit
ELPHIC-PC	IAEA1223	statistical model MC simulation of heavy ion reaction
EMPIRE-MSC	IAEA1169	multi-step compound nucleus/pre-equilibrium x-sections
ERINNI	NEA 0815	multiple cascades emission spectra by optical model
EVA		codes performing the nuclear evaporation processes
EVAP_F(**)		modified version of the Dresdner evaporation code
EXIFONGAMMA	IAEA1211	n, alpha, proton, gamma emission spectra model
FRITIOF (**)		MC high-energy heavy ion collisions
GNASH-FKK ***	PSR-0125	multi-step direct and compound and Hauser-Feshbach models
GNASH-LANL	PSR-0125	pre-equilibrium/statistical x-sections, emission spectra
GRAPE	NEA 1043	precompound/compound nuclear reaction models
HETC NMTC	CCC-0178	MC high energy nucleon meson cascade transport
HETC-KFA	CCC-0496	MC high energy nucleon-meson cascades
HETC95 (**)		MC high energy nucleon-meson cascades and transport
HFMOD	IAEA1317	elastic and inelastic x-section calculation by Hauser-Feshbach and Moldauer
HFTT	IAEA0954	n x-section by compound-nucleus evaporation model
HIJET (**)		MC high-energy heavy ion collisions
ISABEL	NEA 1413	intra-nuclear cascade model allowing hydrogen and helium ions and antiprotons as projectiles
ISAJET (**)		MC high-energy heavy ion collisions
KAPSIES		quantum mechanical multi-step direct model
LIMES	NEA 1337	intermediate mass fragments in heavy ion nuclear reactions
MARLOWE	PSR-0137	atomic displacement cascades in solids
MARLOWE14c ***	PSR-0137	atomic displacement cascades in solids
MECC-7	CCC-0156	medium energy intra-nuclear cascade model
MUP-2	IAEA0907	fast n reaction x-section of medium-heavy nuclei
MUTIL	NEA 1451	calculates the asymmetry factor of the Mott scattering of electrons and positrons by point nuclei
NDEM (**)		generates a gamma-ray source from the de-excitation of residual nuclei
NJOY-94	PSR-0171	n, p, photon evaluated data processing system
NJOY-94.61		idem
NJOY97.0 ***	PSR-355	n, p, photon evaluated data processing system
NMTC/JAERI	NEA 0974	MC high-energy p, n, pion reactions
NUCLEUS		nuclear spallation simulation and primary products
OPTMOD	IAEA1316	elastic & total x-section, polarisation calculations using the optical model
PACE2 (**)		codes performing the nuclear evaporation processes
PCROSS	IAEA1220	pre-equilibrium emission spectra in neutron reaction
PEGAS	IAEA1261	unified model of particle and gamma emission reactions
PELSHIE	IAEA0855	dose rates from gamma source, point-kernel method
PEQAG-2	IAEA1185	pre-equilibrium model nucleon, gamma spectra, x-section
PREANG	NEA 0809	nuclear model particle spectra, angular distribution
PRECO-D2	PSR-0226	pre-equilibrium, direct reaction double differential x-section
PREM	NEA 0888	nucleon emission pre-equilibrium energy spectra, x-section
QMD		intra-nuclear cascade and classical molecular dynamics
RAF (***)	IAEA1350	neutron and proton radiative capture differential and integrated cross-section
REAC	CCC-0443	activation and transmutation
REAC-2	NESC9554	nuclide activation, transmutation
REAC*3	CCC-0443	isotope activation & transmutation in fusion reactors
SOURCES3A ***	CCC-661	determine (,n), spontaneous fission and (,n) delayed
SPEC	IAEA1332	computation of neutron and charged particle reactions using optical and evaporation models
STAPRE-H	IAEA0971	evaporation, pre-equilibrium model reaction x-sections
STAPRE-H95 ***	PSR-0325	evaporation, pre-equilibrium model reaction x-sections
TNG1	PSR-0298	N multi-step statistical model
UNIFY	IAEA1177	fast n x-section, spectrum calculation for structural materials
VEGAS (**)		intra-nuclear cascade code (from which ISABEL is derived)

Table 4. Monte Carlo (MC) and deterministic radiation transport (neutron/photon)

Name	Identification	Function
ALBEDO	NEA 1353	gamma, neutron attenuation in air ducts
ANISN	CCC-0254	1-D Sn, n, gamma transport in slab, cylinder, sphere
ASOP ***	CCC-0126	1-D Sn shield calculation
BALTORO	NEA 0675	n, gamma transport perturbation from MORSE, ANISN calculation
BASACF	IAEA0953	integral neutron adjustment and dosimetry
BERMUDA	NEA 0949	1-D,2-D,3-D n gamma transport for shielding
BREESE	PSR-0143	distribution function for MORSE from albedo data
CARP-82	PSR-0131	docurrents for BREESE from DOT flux
COLLI-PTB	NEA 1126	MC n fluence spectra for 3-D collimator system
DANTSYS	CCC-0547	1-D, 2-D, 3-D Sn neutron, photon transport
DASH	CCC-0366	void tracing Sn - MC COUPLING with fluxes from DOT
DCTDOS	CCC-0520	n, gamma penetration in composite duct system
DOORS3.2 ***	CCC-0650	discrete ordinates system for deep penetration neutron and gamma transport
DORT	CCC-0543	1-D 2-D Sn n, photon transport with deep penetration
DOMINO	PSR-0064	coupling of Sn DOT with MC MORSE
DOT	CCC-0276	2-D Sn n, photon transport with deep penetration
DUST	CCC-0453	albedo MC simulation of n streaming inducts
FALSTF	CCC-0351	n, gamma flux detector response outside cylindrical shields
FEM-RZ	NEA 0566	FEM 2-D multi-group n transport in r-z geometry
GBANISN	CCC-0628	1-D neutron & gamma fluxes with group band fluxes
GEANT-CERN		MC hadron shower simulation
MAGIK	CCC-0359	MC induced residual activation dose rates
MCNP-4A	CCC-0200	MC 3-D time-dependent coupled n, photon, electron transport
MCNP-4B	CCC-0660	MC 3-D time-dependent coupled n, photon, electron transport
MCNP-4B2 ***	CCC-0660	MC 3-D time-dependent coupled n, photon, electron transport
MICAP	PSR-0261	MC to determine the response of gas filled cavity ionisation chamber, plastic scintillator or calorimeter in a mixed neutron and photon environment
MORSE-CGA	CCC-0474	MC n, gamma multi-group transport
PALLAS-2DY	NEA 0702	2-D n ,gamma transport for fixed source
RADHEAT-V3	NEA 0467	transport, heat, radiation damage x-sections in reactor, shield
QAD-CGGP-A	CCC-0645	fast neutron and gamma ray penetration in shields
RAID	CCC-0083	gamma, n scattering into cylindrical or multi-bend duct
SAMSY	IAEA0837	n, gamma dose rates, heat source for multi-layer shields
SAM-CE	CCC-0187	MC time-dependent 3-d n ,gamma transport in complex geometry
SAND-II	PSR-0345	determines neutron energy spectra using multiple experimental activation detector data
SCINFUL	PSR-0267	MC to compute the response of scintillation neutron detector (incident neutron energies from 0.1 to 75 MeV)
SCAP-82	CCC-0418	scattering, albedo, point-kernel anal. in complex geometry
SNL/SAND-II	PSR-0345	enhanced version of SAND-II
SPACETRAN	CCC-0120	radiation leakage from cylinder with ANISN flux
SPECTER-ANL	PSR-0263	n damage for material irradiation
TART95		3D MC transport program for neutrons and photons
TART96 (***)		
TART97 ***	CCC-638	3D MC transport program for neutrons and photons
TORT	CCC-0543	3-D Sn n, photon transport with deep penetration
TRANSX	PSR-0317	code to produce neutron, photon transport tables for discrete ordinates and diffusion codes
TRIPOLI-2	NEA 0874	MC time-dependent 3-D n, gamma transport
TWODANT-SYS	CCC-0547	1-D,2-D multi-group Sn n, photon transport
VIRGIN	IAEA0932	calculates uncollided neutron flux and neutron reactions due to transmission of a neutron beam through any thickness of material

Table 5. Monte Carlo (MC) and deterministic radiation transport (photon)

Name	Identification	Function
AIRSCAT	CCC-0341	dose rate from gamma air scattering, single scat. approx.
GAMMONE	NEA 0268	MC gamma penetration from various geometrical sources
MERCURE-4	NEA 0351	MC 3-D gamma heating/gamma dose rate, fast flux
PLACID	CCC-0381	MC gamma streaming in cylindrical duct shields
BRHGAM	CCC-0350	MC absorbed dose from x-rays in phantom
BREMRAD	CCC-0031	external/internal bremsstrahlung
GRPANL	PSR-0321	germanium gamma and alpha detector spectra unfolding
G33-GP	CCC-0494	multi-group gamma scattering using gp build-up-factor
ISO-PC	CCC-0636	kernel integration code system for general purpose isotope shielding
MAGNA	NEA 0163	dose rates from gamma source in slab or cylindrical shell shields
MARMER	NEA 1307	point-kernel shielding, ORIGEN-S nuclide inventories
PELSHIE	IAEA0855	dose rates from gamma source, point-kernel method
PIPE	NEA 0416	1-D gamma transport for slab, spherical shields
PUTZ	CCC-0595	point-kernel 3-d gamma shielding
STAC-8		transmitted, absorbed power/spectrum – synchrotron radiation
UNSPEC	ESTS0827	X-ray spectrum unfolding using an iterative technique

Table 6. Monte Carlo (MC) and deterministic radiation transport (electron/photon)

Name	Identification	Function
BETA-2B	CCC-0117	MC time-dependent bremsstrahlung, electron transport
BETA-S3.1 ***	CCC-0657	calculates beta decay source terms and energy spectra
CASCADE	CCC-0176	high energy electron-photon transport in matter
CEPXS ONELD	CCC-0544	1-D coupled electron photon multi-group transport
DOSDAT-2	DLC-0079	gamma, electron dose factors data lib. for body organs
EDMULT	NEA 0969	electron depth dose in multi-layer slab absorbers
EGS4	CCC-0331	MC electron photon shower simulation
EGS4 (***)	CCC-0331	version 3.0 of the UNIX distribution of EGS4
ELBA	CCC-0119	bremsstrahlung dose from electron flux on Al shield
EPICSHOW	IAEA1285	interactive viewing of the Electron-Photon Interaction Code (EPIC) system databases (10 eV < E < 1 GeV)
EPICSHOW-96.1		interactive viewing of the Electron-Photon Interaction Code (EPIC) system databases and neutron cross-section data
ESTAR	IAEA1282	calculates stopping power and range for electrons
ETRAN	CCC-0107	MC electron, gamma transport with secondary radiation
ELTRAN	CCC-0155	MC 1-D electron transport
FOTELP	CCC-0581	MC photons, electrons and positron transport
FOTELP/EM ***	CCC-0581	MC photons, electrons and positron transport
INFLTB	PSR-0313	dosimetric mass energy transfer and absorption coefficients
ITS-3.0	CCC-0467	MC tiger system of coupled electron photon transport
MCNP-4A	CCC-0200	MC 3-D time-dependent coupled n, photon, electron transport
MCNP-4B	CCC-0660	MC 3-D time-dependent coupled n, photon, electron transport
PENELOPE ***	NEA 1525	Monte Carlo for electron-photon transport
SANDYL	CCC-0361	MC 3-D time-dependent gamma electron cascade transport

Table 7. Monte Carlo (MC) and deterministic radiation transport (proton)

Name	Identification	Function
ASTROS	CCC-0073	primary/secondary proton dose in sphere/slab tissue
LPPC	CCC-0051	proton penetration, slab
PSTAR	IAEA1282	calculates stopping power and range for protons
PTRAN	CCC-0618	MC proton transport for 50 to 250 MeV
SOURCE (**)		description of the proton transmission and generation of n source
TRAPP	CCC-0205	proton and alpha transport, reaction products neglected

Table 8. Monte Carlo (MC) and deterministic radiation transport (alpha)

Name	Identification	Function
ALDOSE	CCC-0577	calculates of absorbed dose and dose equivalent rates as function of depth in water irradiated by alpha source
ALPHN	CCC-0612	calculates the (alpha,n) production rate in a mixture receiving alpha particles from emitting actinides
ASTAR	IAEA1282	calculates stopping power and range for alphas
GRPANL	PSR-0321	germanium gamma and alpha detector spectra unfolding
RADCOMPT	PSR-0348	sample analysis for alpha and beta dual channel detectors

Table 9. Monte Carlo (MC) and deterministic radiation transport (nucleons/hadrons/cascades)

Name	Identification	Function
CALOR89	CCC-0610	MC system for design, analysis of calorimeter system
CALOR93		idem
CALOR95 (***)		idem
CASIM	NESC0742	MC high energy cascades in complex shields
FLUKA	CCC-0207	MC high energy extranuclear hadron cascades
GEANT-CERN		MC hadron shower simulation
HERMES-KFA ***	NEA 1265	MC high-energy radiation transport
HERMES96b		idem
HETC NMTC	CCC-0178	MC high energy nucleon meson cascade transport
HETC-KFA	CCC-0496	MC high energy nucleon-meson cascade transport
LAHET		MC nucleon, pion, muons, tritons, He-3, alpha transport
LPSC	CCC-0064	p, n flux, spectra behind slab shield from p irradiation
NMTC/JAERI	NEA 0974	MC high-energy p, n, pion reactions
SITHA (**)	IAEA1179	SImulation Transport HAdron, used to calculate hadron transport
SHIELD (**)	IAEA1287	universal code for exclusive simulation of hadron cascades in complex macroscopic targets

Table 10. Monte Carlo (MC) and deterministic radiation transport (heavy ions)

Name	Identification	Function
E-DEP-1	CCC-0275	heavy ion energy deposition
ELPHIC-PC	IAEA1223	statistical model MC simulation of heavy ion reaction
HIC-1	CCC-0249	MC heavy ion reactions at E > 50 MeV/nucleon
STRAGL	CCC-0201	energy loss straggling of heavy charged particles
SWIMS	ESTS0682	calculates the angular dispersion of ion beams that undergo small-angle incoherent multiple scattering by gaseous or solid media
TRIPOS	CCC-0537	MC ion transport

Table 11. Monte Carlo (MC) and deterministic radiation transport (muons)

Name	Identification	Function
MUONLM	NEA 1475	calorimeter interaction of muons

Table 12. Monte Carlo (MC) and deterministic radiation transport (other cascades)

Name	Identification	Function
CHARGE-2/C	CCC-0070	electron, p, heavy particle flux/dose behind shield
DDCS	IAEA1290	calculation of neutron, proton, deuteron, triton, He3, and alpha induced reactions of medium heavy nuclei in the energy range up to 50 MeV
ELPHO	CCC-0301	MC muon, electron, positron generation from pions
IMPACTS-BRC	ESTS0005	radiological assessment code
JENKINS		photon, neutron dose in electron accelerator
PICA	CCC-0160	MC calculation of nuclear cascade reactions caused by the collision of photons (30 < E < 400 MeV) with nuclei
SPARES	CCC-0148	space radiation environment and shielding evaluation

Table 13. Monte Carlo (MC) and deterministic radiation transport (anthropomorphic phantom modelling)

Name	Identification	Function
BRHGAM	CCC-0350	MC absorbed dose from x-rays in phantom
CAMERA	CCC-0240	radiation transport and computerised man model
DISDOS	CCC-0170	dose from external photons in phantom
K009	CCC-0062	charged particle penetration – phantom
MEVDP	CCC-0157	radiation transport in computerised anatomical man
MIRDOSE3.1	CCC-0528	calculate internal dose estimates by the MIRD technique
MRIPP 1.0	CCC-0655	magnetic resonance image phantom for *in vivo* measurements
PEREGRINE (**)		used to model dose to humans from radiation therapy
REBEL-3	IAEA0846	MC radiation dose to human organs
REPC	PSR-0195	dose from protons in tissue
SEECAL	CCC-0620	computes age-dependent effective energies for 54 and 32 target regions in the human body (825 radionuclides)

Table 14. Benchmark data sets already added or in the process of being added in the SINBAD database at the NEA/DB

(*) Benchmarks available (**) Benchmarks available Sept. 1998

Name	Description
ASPIS-FE (*)	Winfrith Iron Benchmark Experiment (ASPIS)
ASPIS-FE88 (*)	Winfrith Iron 88 Benchmark Experiment (ASPIS)
ASPIS-GRAPHITE (*)	Winfrith Graphite Benchmark Experiment (ASPIS)
ASPIS-H2O (*)	Winfrith Water Benchmark Experiment (ASPIS)
ASPIS-H2O/Fe (*)	Winfrith Water/Iron Benchmark Experiment (ASPIS)
EURACOS-FE (*)	Ispra Iron Benchmark Experiment (EURACOS)
EURACOS-NA (*)	Ispra Sodium Benchmark Experiment (EURACOS)
HARMONIE-NA (*)	Cadarache Sodium Benchmark Experiment (HARMONIE)
JANUS-I (**)	Fast Reactor w/Mild Steel, SS, and Concrete -Phase I
JANUS-VIII (**)	Fast Reactor w/ Mild Steel, SS, Sodium, Polyeth, Lead
KFK-FE (*)	Karlsruhe Iron Sphere Benchmark Experiment
NESDIP-2 (*)	Winfrith NESDIP2 Radial Shield
NESDIP-3 (**)	Winfrith NESDIP3 Radial Shield w/Cavity
OKTAVIAN-FE (*)	Osaka Iron Benchmark Experiment (OKTAVIAN)
PCA-REPLICA (*)	Winfrith Water/Iron Benchmark Experiment (PCA-Replica)
PROTEUS-FE (*)	Wuerenlingen Iron Benchmark Experiment (PROTEUS)
TUD Iron Slab (**)	Dresden Iron Slab (TUD)

Table 15. Benchmark data sets added to the SINBAD database, at ORNL/RSICC

Name	Description
STD1 (**)	Iron Broomstick Benchmark Experiment (TSF-ORNL)
STD2 (**)	Oxygen Broomstick Benchmark Experiment (TSF-ORNL)
STD3 (**)	Nitrogen Broomstick Benchmark Experiment (TSF-ORNL)
STD4 (**)	Sodium Broomstick Benchmark Experiment (TSF-ORNL)
STD5 (**)	Stainless Steel Broomstick Benchmark Experiment (TSF-ORNL)
SB5 (**)	Fusion Reactor Shielding Experiment (ORNL)
ENEA Bulk SS (**)	FNG SS Bulk Shield Benchmark Experiment (Frascati)
ENEA Blanket (**)	FNG ITER Blanket (Frascati)
Illinois Iron Sphere (**)	Univ. of Illinois Iron Sphere
LL Pulsed Spheres (**)	LLNL Pulsed Spheres
PCA-PV(**)	Pool Critical Assembly - Pressure Vessel Experiment (PCA)
SB2 (**)	Gamma Production Cross-Sections from Thermal Neutrons
SB3 (**)	Gamma Production Cross-Sections from Fast Neutron
SDT 11 (**)	ORNL Neutron Transport in Iron and SS
SDT 12 (**)	ORNL Neutron Transport in Thick Sodium
YAYOI Iron (**)	Univ. of Tokyo's Iron Benchmark Experiment
Accelerators:	
U. of Tokyo INS (**)	Penetration of Secondary Neutrons and Photons through Concrete, Fe, Water, C
Osake U. AVF (**)	Penetration of Secondary Neutrons and Photons through Concrete, Fe, Pb, and C

PENELOPE: TAKING ADVANTAGE OF CLASS II SIMULATION

F. Salvat, J.M. Fernández-Varea, N. Leinfellner
Facultat de Física (ECM), Universitat de Barcelona
Diagonal 647, 08028 Barcelona, Spain

J. Sempau
Institut de Tècniques Energètiques
Universitat Politècnica de Catalunya
Diagonal 647, 08028 Barcelona, Spain

A. Sánchez-Reyes
Servicio de Oncología Radioterápica
Hospital Clínic Universitari de Barcelona
Villarroel 170, 08036 Barcelona, Spain

Abstract

PENELOPE is a general-purpose Monte Carlo code for the simulation of electron-photon showers in arbitrary materials. It covers the energy range from ~1 keV up to ~1 GeV. The simulation of electron and positron transport is based on a mixed (Class II) simulation scheme. The cut-off angular deflection, which separates soft and hard (catastrophic) elastic collisions, is allowed to vary with the energy of the particle in such a way that the multiple soft interactions which occur between two consecutive hard events produce only gentle deflections of the track. Space displacements are generated by a simple and accurate algorithm that works even in the vicinity of interfaces. In this communication we briefly describe the physics of PENELOPE, the simulation algorithm for charged particle transport and the structure and operation of the code system. The distribution package also includes subroutines for simulation in quadric geometries (i.e. material systems consisting of homogeneous bodies limited by quadric surfaces) and a simple geometry viewer.

Introduction

A general-purpose Monte Carlo code system for the simulation of coupled electron-photon transport in arbitrary materials has been developed at the University of Barcelona over the last ten years [1]. The code was named PENELOPE (an acronym for PENetration and Energy LOss of Positrons and Electrons). Its most characteristic feature is the systematic use of mixed simulation (Class II schemes in the terminology of Berger [2]) for electrons and positrons. This not only improves the accuracy of the simulation but also simplifies the structure and operation of the code.

The core of the code system is a FORTRAN subroutine package that generates electron-photon showers in material systems consisting of a number of homogeneous regions of given composition (bodies). These subroutines are invoked from a main steering program, to be provided by the user, which controls the evolution of the tracks and keeps score of the relevant quantities. The code system also includes a simple subroutine package for simulation within quadric geometries (i.e. systems consisting of bodies limited by quadric surfaces) and a geometry viewer and debugger. The distribution package (FORTRAN source files, database and geometry viewer) is available from the NEA Data Bank.

The reliability of PENELOPE was initially tested by a variety of experimental benchmarks and comparisons with results from high-energy codes [1,3]. We have also shown that it provides electron backscattering coefficients that agree well with available experimental data for energies between ~2.5 keV and ~100 keV [4]. Currently, the code is being applied to a variety of problems ranging from quantitative electron probe microanalysis (energies of the order of 10 keV, planar geometries) to the simulation of medical electron accelerators (energies up to 50 MeV, complex geometries).

Interaction cross-sections

To facilitate the formulation of mixed simulation algorithms and to minimise interpolation errors in random sampling, the differential cross-sections (DCS) of the various interaction mechanisms are approximated by analytical expressions derived from simple, but physically sound approximations. The reliability of the simulation is ensured by fitting the DCS model parameters to reproduce the most accurate available values of relevant transport integrals (see below). With the use of analytical DCS, only those transport integrals need to be stored in the numerical database and, furthermore, the user may alter the physical model by simply changing the values of the transport integrals (e.g. to analyse their influence on the simulation results).

In this section we assume that particles[1] of energy E move within a single-element material of atomic number Z. In the case of compounds, the molecular DCS is set equal to the sum of the atomic cross-sections of all the atoms in the molecule (additivity rule). Each scattering event is described in terms of the energy transfer (if any) and the polar and azimuthal scattering (or emission) angles, for which we shall use the notation indicated in Figures 1 and 2. With the adopted DCS, random values of these variables are generated by using exact analytical sampling formulas.

Photon interactions

Photon simulation is performed by using the conventional detailed simulation scheme, i.e. all interactions in a photon history are sampled in chronological succession. When a photon crosses an

[1] For the sake of brevity, we use the term "particle" to refer to either electrons, positrons or photons.

interface (i.e. a surface that separates two bodies of different compositions) the geometry subroutines "stop" the photon just after the interface and restart its simulation in the new medium (which means calculating the macroscopic cross-sections and sampling the value of the free path length to the next interaction). This "interface crossing" method is legitimate due to the Markovian character (lack of memory) of the interaction process. Although photon simulation in complex geometries could be done by means of simpler methods that do not require control of interface crossings [5], it is preferable to use the one described here since it is also applicable to charged particles.

Coherent (Rayleigh) scattering

The atomic DCS per unit solid angle for coherent scattering, obtained from the Born approximation, is given by:

$$\frac{\mathrm{d}\sigma_{\mathrm{co}}}{\mathrm{d}\Omega} = r_{\mathrm{e}}^2 \frac{1+\cos^2\theta}{2}\left[F(q,Z)\right]^2 \tag{1}$$

where $\Omega = (\theta,\phi)$ denotes the angular deflection, r_e is the classical electron radius and q is the magnitude of the momentum transfer given by:

$$q = 2(E/c)\sin(\theta/2) = (E/c)\left[2(1-\cos\theta)\right]^{-1/2} \tag{2}$$

The atomic form factor $F(q,Z)$ is approximated by an analytical expression, which reproduces the values tabulated by [6] to within 0.5%.

Incoherent (Compton) scattering

The DCS for Compton scattering is obtained from the relativistic impulse approximation [7], which accounts for electron binding effects and Doppler broadening. Contributions from different atomic electron shells are considered separately. After a Compton interaction with the i-th shell, the target electron is ejected to a free state with kinetic energy $E_e = E$ - E'-U_i, where U_i is the ionisation energy of the considered shell.

The Compton atomic DCS is expressed as (Eq. (21) in [8]):

$$\frac{\mathrm{d}^2\sigma_{\mathrm{in}}}{\mathrm{d}E'\mathrm{d}\Omega} = \frac{r_{\mathrm{e}}^2}{2}\left(\frac{E_C}{E}\right)^2\left(\frac{E_C}{E}+\frac{E}{E_C}-\sin^2\theta\right)\times G(p_z)\left(\sum_i Z_i J_i(p_z)\Theta(E-E'-U_i)\right) \tag{3}$$

where:

$$E_C = \frac{E}{1+\left(E/mc^2\right)(1-\cos\theta)} \tag{4}$$

is the energy of the Compton line, $G(p_z)$ is a kinematical factor, Z_i is the number of electrons in the i-th shell and $J_i(p_z)$ is the Compton profile of this shell. $\Theta(x)$ (= 1 if $x > 0$, = 0 otherwise) is the Heaviside step function, which accounts for the effect of binding. mc^2 is the electron rest energy (= 511 keV).

Photoelectric effect

Photoelectric cross-sections are obtained by interpolation in a table that was generated by using the XCOM program of Berger and Hubbell [9]. In order to minimise the simulation time and computer memory, for compound materials (and also for mixtures) PENELOPE interpolates the inverse attenuation coefficient (i.e. the molecular cross-section) instead of the atomic cross-sections of the constituent elements. Knowledge of the atomic cross-sections is needed – only when a photoabsorption event has effectively occurred – to determine the element that has been ionised. Atomic cross-sections are calculated from an approximate analytical expression.

After photoabsorption in the *i*-th shell, a photoelectron with kinetic energy $E_e = E - U_i$ is emitted. The direction of emission is sampled from Sauter's hydrogenic angular distribution [10].

Electron-positron pair production

Pair production is simulated by means of the modified Bethe-Heitler DCS described in Ref. [11], which assumes an exponentially screened field and includes Coulomb and low-energy corrections. The DCS for a photon of energy E to create an electron-positron pair, in which the electron has a kinetic energy $E_- = \varepsilon E - mc^2$, is expressed as:

$$\frac{\mathrm{d}\sigma_{\mathrm{pp}}}{\mathrm{d}\varepsilon} = \alpha r_{\mathrm{e}}^2 C_{\mathrm{r}} Z[Z+\eta]\frac{2}{3}\left[2\left(\frac{1}{2}-\varepsilon\right)^2 \phi_1(\varepsilon)+\phi_2(\varepsilon)\right] \tag{5}$$

where α is the fine-structure constant, $\phi_1(\varepsilon)$ and $\phi_2(\varepsilon)$ are screening functions and $C_r = 1.0093$ is the high-energy limit of Mork and Olsen's radiative correction [12]. The quantity η accounts for triplet production, i.e. pair production in the field of the atomic electrons [12].

To avoid systematic errors, the mean free paths for pair production used in PENELOPE are obtained by interpolation in a table generated with the XCOM program [9]. The Bethe-Heitler DCS is only used to sample the kinetic energies of the produced pair. Although the Bethe-Heitler DCS accounts for pair and triplet production, all the events are simulated as if they were pairs.

Electron and positron interactions

Elastic scattering

Accurate elastic DCSs, $\mathrm{d}\sigma_{\mathrm{el}}/\mathrm{d}\Omega$, for all the elements and energies in the range from 0.1 keV to 1 GeV were evaluated using partial wave analysis for electrons and positrons with kinetic energy $E \le 100$ keV [13] and a screened Mott formula for higher energies [14]. A database was produced that contains the total (integrated) elastic cross-section (Eq. 6) and the first and second transport cross-sections (Eq. 7):

$$\sigma_{\mathrm{el}} = 2\pi\int_0^{\pi}\frac{\mathrm{d}\sigma_{\mathrm{el}}}{\mathrm{d}\Omega}\sin\theta\,\mathrm{d}\theta \tag{6}$$

$$\sigma_1 \equiv \sigma_{\mathrm{el}}\,2\langle\mu\rangle, \qquad \sigma_2 \equiv \sigma_{\mathrm{el}}\,6\left(\langle\mu\rangle-\langle\mu^2\rangle\right) \tag{7}$$

where $\mu = (1 - \cos\theta)/2$ and $\langle\ldots\rangle$ denotes the average value in a single collision.

The mean free path between elastic collisions is given by:

$$\lambda_{el} = 1/\mathcal{N}\sigma_{el} \tag{8}$$

where $\mathcal{N}$ is the number of scattering centres per unit volume in the medium. Other parameters of primary interest are the first and second transport mean free paths, λ_1 and λ_2, which are defined by:

$$\lambda_1^{-1} = \mathcal{N}\sigma_1 = \frac{\langle\mu\rangle}{\lambda_{el}} \tag{9}$$

and

$$\lambda_2^{-1} = \mathcal{N}\sigma_2 = \frac{6\left(\langle\mu\rangle - \langle\mu^2\rangle\right)}{\lambda_{el}} \tag{10}$$

Notice that the inverse of the first transport mean free path gives the average angular deflection per unit path length. By analogy with the scattering power, which is defined as the mean energy loss per unit path length (see below), λ_1^{-1} is also known as the "scattering power".

Elastic collisions are simulated by means of the following DCS (W2D model):

$$\frac{d\sigma_{el}^{(W_2D)}}{d\Omega} = \sigma_{el}\left[(1-B)\frac{A(1+A)}{(\mu+A)^2} + B\delta(\mu-\mu_0)\right] \tag{11}$$

The quantity in square brackets is the statistical admixture of a screened Rutherford distribution (which describes the scattering by an exponentially screened Coulomb field within the Born approximation) and a δ-distribution (a fixed-scattering-angle process). The parameters A, B and μ_0 are determined in such a way that the values of the characteristic functions λ_{el}, λ_1 and λ_2 (as obtained from the database) are exactly reproduced [11].

Of course, the analytical DCS is only approximate, but it leads to multiple scattering angular distributions that agree closely with the ones that are obtained from the more accurate partial wave DCS. The slight loss of accuracy is largely compensated by the fact that the random sampling of μ can be performed analytically and mixed simulation algorithms are trivially formulated [15].

Inelastic collisions

Individual inelastic interactions are specified by the scattering angle θ and the energy loss W of the projectile. Instead of the scattering angle, it is convenient to use the recoil energy Q defined by [16]:

$$Q\left(Q + 2mc^2\right) = (cq)^2 \tag{12}$$

where q is the magnitude of the momentum transfer. Notice that, in the particular case of collisions with a free electron at rest, Q coincides with the recoil energy of the target electron after the collision, i.e. $Q = W$.

The non-relativistic Born inelastic DCS can be expressed as:

$$\frac{\mathrm{d}^2\sigma_{\mathrm{col}}}{\mathrm{d}Q\mathrm{d}W} = \frac{\pi e^4}{E}\frac{1}{WQ}\frac{\mathrm{d}f(Q,W)}{\mathrm{d}W} \tag{13}$$

where the quantity $\mathrm{d}f(Q,W)/\mathrm{d}W$ is the generalised oscillator strength (GOS), which completely characterises the response of the target. We use a simple GOS model [17] in which the excitations of the i-th atomic electron shell are represented by an "oscillator" with the following excitation spectrum:

$$F(W_i;Q,W) = \delta(W-W_i)\Theta(W_i-Q) + \delta(W-Q)\Theta(Q-W_i) \tag{14}$$

where $\delta(\mathrm{x})$ is the Dirac delta function and $\Theta(\mathrm{x})$ is the unit step function. Following Sternheimer [18], the oscillator strength is set equal to Z_i, the number of electrons in the shell, and the resonance energy W_i is set equal to aU_i where a is an adjustable parameter. Our GOS reads:

$$\frac{\mathrm{d}f(Q,W)}{\mathrm{d}W} \equiv \sum_i Z_i F(W_i;Q,W) \tag{15}$$

After introducing relativistic, exchange and density corrections, the inelastic DCSs for electrons and positrons can be expressed in a closed analytical form [19]. The parameter a is determined from the equation:

$$\sum f_i \ln(aU_i) = Z\ln I \tag{16}$$

where I is the mean excitation energy of the material. This implies that for high-energy projectiles the calculated stopping power reproduces the values obtained from the Bethe formula (see Ref. [20]).

The energy-loss DCS is obtained by integrating the double-differential DCS over the kinematically allowed recoil energies:

$$\frac{\mathrm{d}\sigma_{\mathrm{col}}}{\mathrm{d}W} \equiv \int_{Q_-}^{Q_+}\frac{\mathrm{d}^2\sigma_{\mathrm{col}}}{\mathrm{d}Q\mathrm{d}W}\mathrm{d}Q \tag{17}$$

The inelastic mean free path λ_{col} between inelastic collisions is given by:

$$\lambda_{\mathrm{col}} = \mathcal{N}\int_0^E \frac{\mathrm{d}\sigma_{\mathrm{col}}}{\mathrm{d}W}\mathrm{d}W \tag{18}$$

Other quantities of practical interest are the collision stopping power S_{col}, which is defined as the average energy loss per unit path length:

$$S_{\mathrm{col}} = \mathcal{N}\int_0^E W\frac{\mathrm{d}\sigma_{\mathrm{col}}}{\mathrm{d}W}\mathrm{d}W = \frac{\langle W\rangle}{\lambda_{\mathrm{col}}} \tag{19}$$

and the energy straggling parameter:

$$\Omega^2_{\mathrm{col}} = \mathcal{N}\int_0^E W^2\frac{\mathrm{d}\sigma_{\mathrm{col}}}{\mathrm{d}W}\mathrm{d}W = \frac{\langle W^2\rangle}{\lambda_{\mathrm{col}}} \tag{20}$$

which gives the "variance increase" of the energy distribution per unit path length of the transported particles [3]. With our analytical DCS these integrals can be evaluated analytically. The resulting stopping power agrees very closely with the tabulations of Berger and Seltzer [20], when the default *I*-values are used.

Bremsstrahlung emission

Bremsstrahlung emission is described by using a modified Bethe-Heitler DCS that assumes exponential screening and includes Coulomb and low-energy corrections. The DCS for emission of a photon of energy W by an electron with kinetic energy E is given by:

$$\frac{\mathrm{d}\sigma_{\mathrm{rad}}^{(-)}}{\mathrm{d}W} = r_{\mathrm{e}}^2 \alpha Z[Z+\eta]\left(\varphi_1(W)W + \varphi_2(W)\frac{1}{W}\right) \tag{21}$$

where $\varphi_1(W)$ and $\varphi_2(W)$ are analytical screening functions analogous to those in Eq. (5). The DCS for positrons includes an additional factor that was calculated by Kim *et al.* [21]. The direction of the emitted photon is sampled from the dipole distribution in the rest frame of the projectile [1].

The total cross-section for bremsstrahlung emission is infinite due to the divergence of the DCS (21) for small reduced photon energies. Nevertheless, the cross-section for emission of photons with energy larger than a given cut-off value W_{cr} is finite. The corresponding mean free path is:

$$\lambda_{\mathrm{rad}}^{-1}\left(E; W_{\mathrm{cr}}\right) \equiv \mathcal{N}\int_{W_{\mathrm{cr}}}^{E} \frac{\mathrm{d}\sigma_{\mathrm{rad}}}{\mathrm{d}W}\mathrm{d}W \tag{22}$$

The radiative stopping power and the radiative energy straggling parameter:

$$S_{\mathrm{rad}}(E) \equiv \mathcal{N}\int_{0}^{E} W\frac{\mathrm{d}\sigma_{\mathrm{rad}}}{\mathrm{d}W}\mathrm{d}W \tag{23}$$

$$\Omega_{\mathrm{rad}}^2(E) \equiv \mathcal{N}\int_{0}^{E} W^2\frac{\mathrm{d}\sigma_{\mathrm{rad}}}{\mathrm{d}W}\mathrm{d}W \tag{24}$$

are both finite.

Our stopping powers are in good agreement with the Berger and Seltzer [20] values for energies above 1 MeV. The relative differences are less than 5% for energies of the order of 1 MeV and decrease with energy, becoming smaller than 1% at ~100 MeV. To improve the accuracy of the model, PENELOPE renormalises the DCS so as to exactly reproduce Berger and Seltzer's radiative stopping powers for electrons.

Positron annihilation

The simulation of positron annihilation is similar to the one adopted in the EGS4 code [22]. Positrons can annihilate in flight, or when they are brought to rest, with emission of two photons.

Atomic relaxation

PENELOPE simulates the emission of characteristic X-rays and Auger electrons that result from vacancies produced in a K-shell by photon interactions. Radiation resulting from the filling of vacancies in outer shells is not followed; in these cases, the excitation energy is taken out by the emitted Compton electron or photoelectron. This limits the validity of the simulation to photons with energies larger than the L-shell ionisation energy of the heaviest element in the medium. The probability of inner-shell ionisation by electron impact is very small; when it occurs, it is assumed that the excitation energy of the residual ion is locally deposited.

Mixed simulation algorithm

Detailed simulation of high-energy electrons and positrons is impracticable because of the large number of interactions necessary to bring the particles to rest. To reduce computing effort, Monte Carlo codes often use condensed (Class I) schemes. The particle track is divided into a large number of segments (steps) of preselected lengths such that many interactions occur along each step (i.e. the steps must be long enough). The energy loss and the global angular deflection of the particle due to the interactions in each step are sampled from suitable multiple-scattering theories. The procedure is not completely satisfactory due to the fact that the distribution of space displacements is partially unknown. Moreover, when particles approach an interface, the length of the steps must be progressively reduced to ensure that the complete segment is contained within the initial medium, which conflicts with the use of preselected step lengths.

PENELOPE uses a mixed (Class II) simulation scheme in which hard (catastrophic) events are simulated in a detailed way, whereas the effect of the soft interactions between each pair of hard events is described by means of simple approximations [15]. Let us introduce cut-off values μ_c, W_{cc} and W_{cr}. Elastic collisions with angular deflection $\mu > \mu_c$, inelastic collisions with energy loss $W > W_{cc}$ and emission of bremsstrahlung photons with energy $W > W_{cr}$ are considered as hard interactions. The mean free paths for these interactions are given by:

$$\left[\lambda_{\rm el}^{(\rm h)}\right]^{-1} = \mathcal{N}\int_{\mu_c}^{1}\frac{{\rm d}\sigma_{\rm el}}{{\rm d}\mu}{\rm d}\mu \tag{25}$$

$$\left[\lambda_{\rm col}^{(\rm h)}\right]^{-1} = \mathcal{N}\int_{W_{cc}}^{W_{\max}}\frac{{\rm d}\sigma_{\rm col}}{{\rm d}W}{\rm d}W \tag{26}$$

and:

$$\left[\lambda_{\rm rad}^{(\rm h)}\right]^{-1} = \mathcal{N}\int_{W_{cr}}^{E}\frac{{\rm d}\sigma_{\rm rad}}{{\rm d}W}{\rm d}W \tag{27}$$

In practice, it is useful to consider the cut-off deflection μ_c as an energy-dependent parameter and to determine it from Eq. (25) by setting:

$$\lambda_{\rm el}^{(\rm h)}(E) = \max\left\{\lambda_{\rm el}(E), \min\left[C_1\lambda_1(E), C_2\frac{E}{S_{\rm col}(E)+S_{\rm rad}(E)}\right]\right\} \tag{28}$$

where C_1 and C_2 are preselected small constants (less than ~0.05). When μ_c is determined in this way, the average angular deflection $\langle\mu\rangle = (1 - \langle\cos\theta\rangle/2$ and the average energy loss ΔE in a path segment of $\lambda_{el}^{(h)}$ are less than C_1 and C_2, respectively.

Consider that the particle travels a distance t between a pair of consecutive hard interactions, interacting only through soft processes which produce an energy loss ΔE_s and an angular deflection μ_s. As the energy of the particle remains essentially unaltered along the step (whenever C_2 is small), these variables are not correlated and their *exact* average values and variances can be obtained from simple arguments [3,14]. We have:

$$\langle\mu_s\rangle = \frac{1}{2}\left[1-\exp\left(-t/\lambda_1^{(s)}\right)\right], \quad \langle\mu_s^2\rangle = \langle\mu_s\rangle - \frac{1}{6}\left[1-\exp\left(-t/\lambda_2^{(s)}\right)\right] \tag{29}$$

where $\lambda_1^{(s)}$ and $\lambda_2^{(s)}$ stand for the first and second transport mean free paths for soft collisions (including contributions from soft inelastic collisions). On the other hand:

$$\langle\Delta E_s\rangle = S_s t, \quad \mathrm{var}\langle\Delta E_s\rangle = \Omega_s^2 t \tag{30}$$

where:

$$S_s(E) = \mathcal{N}\int_0^{W_{cc}} W\frac{\mathrm{d}\sigma_{col}}{\mathrm{d}W}\mathrm{d}W + \mathcal{N}\int_0^{W_{cr}} W\frac{\mathrm{d}\sigma_{rad}}{\mathrm{d}W}\mathrm{d}W \tag{31}$$

and:

$$\Omega_s^2(E) = \mathcal{N}\int_0^{W_{cc}} W^2\frac{\mathrm{d}\sigma_{col}}{\mathrm{d}W}\mathrm{d}W + \mathcal{N}\int_0^{W_{cr}} W^2\frac{\mathrm{d}\sigma_{rad}}{\mathrm{d}W}\mathrm{d}W \tag{32}$$

are the stopping power and the energy straggling parameter associated with soft interactions.

Random values of μ_s and ΔE_s are sampled from certain "artificial" distributions, which have their first and second moments equal to the values given by the expressions above, but are otherwise arbitrary [3,14]. Notice that the segment length between hard interactions, which follows an exponential distribution, may be exceedingly small (the most probable value of t is zero!). This prevents the use of elaborate multiple scattering theories such as that of Goudsmit and Saunderson [23]. In practice, the details of the artificial distributions are washed out after multiple scattering and the only requirement to get realistic results with our procedure is that each particle must suffer (on average) a "statistically sufficient" number of hard interactions, say of the order of twenty or larger. To satisfy this condition, we define $\lambda_{el}^{(h)}(E)$ by means of the expression (cf. Eq. (28)):

$$\lambda_{el}^{(h)}(E) = \max\left\{\lambda_{el}(E), \min\left[C_1\lambda_1(E), C_2\frac{E}{S_{col}(E)+S_{rad}(E)}, \lambda_{el,max}^{(h)}\right]\right\} \tag{33}$$

where $\lambda_{el,max}^{(h)}$ is an energy-independent value selected by the user. If the body where the particles propagate has a characteristic thickness T, we can then make sure that each particle experiences

(on average) ~20 hard elastic collisions, irrespective of the values of C_1 and C_2, by simply taking $\lambda_{el,max}^{(h)} \sim T/20$. Notice that the prescription (33) yields a cut-off deflection μ_c that varies with the energy E of the particle. It can be easily seen that hard elastic interactions occur more frequently when elastic scattering is more intense and that, for low-energy projectiles, $\lambda_{el}^{(h)}(E)$ reduces to $\lambda_{el}(E)$ and the simulation becomes purely detailed.

The space displacement at the end of a step is determined by using the following simple algorithm (see Figure 3). The particle is allowed to advance a random distance τ in the forward direction, which is sampled uniformly in the interval $(0,t)$. After travelling this distance, an artificial soft event is simulated in which the particle is deflected and its energy is reduced. The applied deflection μ_s and energy loss ΔE_s are sampled from the corresponding "artificial" distributions for the complete step length t. Finally, the particle is allowed to move the remaining distance $t - \tau$ in the new direction, to reach the point where the next hard collision occurs. The average longitudinal displacement obtained in this way has a relative error of the order of $\left(t/\lambda_1^{(s)}\right)^2$, which is small due to the fact that $\lambda_1^{(s)} >> \lambda_1$. As shown in Fernández-Varea *et al.* [14], the displacement algorithm also works well in the vicinity of interfaces; special action has to be taken only when the particle has crossed an interface. This allows a large simplification of the simulation code.

Structure and operation of the code

PENELOPE has been structured in such a way that a particle track is generated as a sequence of free flights or "jumps"; at the end of each jump, the particle suffers an interaction with the medium (a "knock") where it loses energy, changes its direction of flight and, in certain cases, produces secondary particles. For electrons and positrons, the alternating sequence of hard and artificial soft events is handled internally by the simulation routines.

The connection between PENELOPE and the MAIN program is done via the named common block:

→ COMMON/TRACK/E,X,Y,Z,U,V,W,WGHT,DS,DE,KPAR,IBODY,MAT,ICOL

containing the following quantities:

- **Particle state variables:**
  - KPAR … Kind of particle (1, electron; 2, photon; 3, positron).
  - E … Current particle energy (eV) (kinetic energy for electrons and positrons).
  - X, Y, Z … Position co-ordinates (cm).
  - U, V, W … Direction cosines of the direction of movement.
  - WGHT … In analogue simulations, this is a dummy variable. When using variance reduction methods, the particle weight can be stored here.
  - IBODY … This flag serves to identify different bodies in complex material structures.
  - MAT … Material in which the particle moves (the one in the body labelled IBODY).
- **Changes in state variables** performed by the simulation routines (see below):

DS … Length (cm) of the following step (output from JUMP).

DE … Energy (eV) deposited in the material in the last event (output from KNOCK).

ICOL … Gives the kind of the last event (output from KNOCK).

Electrons and positrons:

ICOL=1 artificial soft event

ICOL=2 hard elastic collision

ICOL=3 hard inelastic collision

ICOL=4 hard bremsstrahlung emission

ICOL=5 positron annihilation

Photons:

ICOL=1 coherent scattering

ICOL=2 incoherent scattering

ICOL=3 photoelectric absorption

ICOL=4 electron-positron pair production

The position co-ordinates $\mathbf{r}$ = (X,Y,Z) and the direction cosines $\hat{\mathbf{d}}$ = (U,V,W) of the direction of movement are referred to a fixed rectangular co-ordinate system, the "laboratory" system, which can be arbitrarily defined. During the simulation, all energies and lengths are expressed in eV and cm, respectively.

Electron-photon showers are simulated by successively calling the following subroutines:

- SUBROUTINE CLEANS
  Initialises the secondary stack.

- SUBROUTINE START
  Forces the following event to be a soft artificial one. This subroutine must be called before starting a new *primary or secondary* track and also when a track crosses an interface. Invoking START is strictly necessary only for electrons and positrons; for photons this subroutine has no physical effect. However, it is advisable to call START for any kind of particle since it checks whether the energy is within the expected range, and can thus help to detect bugs in the MAIN program.

- SUBROUTINE JUMP
  Determines the length DS of the step to the following event.

- SUBROUTINE KNOCK
  Simulates the following event, computes new energy and direction of movement, and stores the initial states of the generated secondary particles, if any.

- SUBROUTINE SECPAR(LEFT)
  Sets the initial state of a secondary particle and removes it from the secondary stack. The output value of LEFT is the number of secondary particles that remained in the stack at the calling time.

- SUBROUTINE STORES(E,U,V,W,WGHT,KPAR)
  Stores a particle in the secondary stack. Arguments have the same meaning as in COMMON/TRACK/, but refer to the particle that is being stored. Calling STORES from the MAIN program is required to store particles produced by splitting, a variance reduction method. It may also be useful for the simulation of multiple radiations emitted in a nuclear de-excitation cascade.

Subroutines JUMP and KNOCK keep the position co-ordinates unaltered; the positions of successive events have to be followed by the MAIN program (by performing a displacement of length DS along the direction of movement after each call to JUMP. The energy of the particle is automatically reduced by subroutine KNOCK, after generating the energy loss from the relevant probability distribution. KNOCK also modifies the direction of movement according to the scattering angles of the simulated event.

Figure 4 displays the flow diagram of the MAIN program. Notice that the sequence of calls to generate a random track is independent of the kind of particle that is being simulated. In order to avoid problems related with possible overflows of the secondary stack, when a secondary particle is produced its energy is temporarily assumed as locally deposited (the deposited energy in each event is given by the variable DE in common block TRACK). Hence, the energy E of a secondary must be subtracted from the corresponding dose counter when the secondary track is started. Occasional overflows of the secondary stack are remedied by eliminating the less energetic secondary electron or photon in the stack[2]; positrons are not eliminated since they will eventually produce quite energetic annihilation radiation. As the main effect of secondary particles is to spread out the energy deposited by the primary, the elimination of the less energetic secondary electrons and photons does not invalidate local dose calculations.

General variance reduction methods [24] are not contemplated in the simulation routines. Splitting and Russian roulette do not require changes in PENELOPE; the necessary manipulations on the numbers and weights WGHT of particles can be done in the MAIN program. Particles resulting from splitting can be stored in the secondary stack by invoking subroutine STORES. Interaction forcing implies changing the inverse mean free paths of the forced interactions and, at the same time, redefining the weights of the generated secondary particles. These manipulations are performed automatically by calling the auxiliary subroutines JUMPF and KNOCKF, instead of JUMP and KNOCK.

The subroutine package PENGEOM2 [25] allows the simulation of radiation transport in material systems defined by quadric surfaces. It differs from the simpler package PENGEOM (also included in the code system) in the fact that bodies can be grouped into modules that, in turn, can form part of larger modules. This hierarchic modular structure simplifies the operation and optimises the speed of the geometry routines. The code system includes the program GVIEW (operable on IBM-compatible personal computers under MS-DOS) that displays 2-D images of the geometry on the computer screen and is useful for debugging the geometry definition file. The displayed pictures are generated by using the PENGEOM2 subroutines and, therefore, errors and inconsistencies in the geometry definition file that would affect the results of actual simulations are readily identified.

[2] The control, and required modifications, of the secondary stack are performed by PENELOPE.

It is a fortunate coincidence that the logic of our geometry definition is very similar to the "Constructive Quadric Geometry" used by the POV-Ray[3] ray-tracing program. Recently, a FORTRAN "translator" of the PENGEOM2 definition files to POV-Ray format has been developed to generate true 3-D pictures of the geometry on a variety of platforms. It will be made available in the near future.

REFERENCES

[1] J. Sempau, E. Acosta, J. Baró, J.M. Fernández-Varea and F. Salvat (1997), *Nucl. Instr. Meth.* B132, 377.

[2] M.J. Berger (1963), *Methods in Computational Physics*, Vol. 1, eds. B. Alder, S. Fernbach and M. Rotenberg (Academic Press, New York) p. 135.

[3] J. Baró, J. Sempau, J.M. Fernández-Varea and F. Salvat (1995), *Nucl. Instr. Meth*. B100, 31.

[4] E. Acosta, E. Coleoni, G. Castellano, J.A. Riveros, J.M. Fernández-Varea and F. Salvat (1996), *Scanning Microsc*. 10, 625.

[5] V.S. Snyder, M.R. Ford, G.G. Warner and H.L. Fisher (1969), MIRD Pamphlet No. 5, *J. Nucl. Med*. 10, suppl. No. 3.

[6] J.H. Hubbell, Wm.J. Veigele, E.A. Briggs, R.T. Brown, D.T. Cromer and R.J. Howerton (1975), *J. Phys. Chem. Ref. Data* 4, 471. Erratum: ibid. 6 (1977) 615.

[7] R. Ribberfors (1983), *Phys. Rev*. A27, 3061.

[8] D. Brusa, G. Stutz, J.A. Riveros, J.M. Fernández -Varea and F. Salvat (1996), *Nucl. Instr. Meth*. A79,167.

[9] M.J. Berger and J.H. Hubbell (1987), National Bureau of Standards, *Report NBSIR 87-3797* (Washington).

[10] F. Sauter (1931), *Ann. Phys*. 11, 454.

[11] J. Baró, M. Roteta, J.M. Fernández-Varea and F. Salvat (1994a), *Radiat. Phys. Chem*. 44, 531.

[12] J.H. Hubbell, H.A. Gimm and I. Øverbø (1980), *J. Phys. Chem. Ref. Data* 9, 1023.

[13] F. Salvat and R. Mayol (1993), *Comput. Phys. Commun.* 74, 358.

[3] Persistence of Vision™ Ray Tracer (POV-Ray™ version 3.02 (1997).

[14] J.M. Fernández-Varea, R. Mayol, J. Baró and F. Salvat (1993a), *Nucl. Instr. Meth*. B73, 447. J.M. Fernández-Varea, R. Mayol and F. Salvat (1993b), *Nucl. Instr. Meth*. B82, 39.

[15] J. Baró, J. Sempau, J.M. Fernández-Varea and F. Salvat (1994b), *Nucl. Instr. Meth*. B84, 465.

[16] U. Fano (1963), *Ann. Rev. Nucl. Sci*. 13, 1.

[17] D. Liljequist (1978), *J. Phys. D: Appl. Phys*. 11, 839.

[18] R.M. Sternheimer (1952), *Phys. Rev*. 88, 851.

[19] F. Salvat and J.M. Fernández-Varea (1992), *Nucl. Instr. and Meth*. B63, 255.

[20] M.J. Berger and S.M. Seltzer (1982), National Bureau of Standards, *Report NBSIR 82-2550* (Washington). Also available as ICRU Report 37 (1984).

[21] L. Kim, R.H. Pratt, S.M. Seltzer and M.J. Berger (1986), *Phys. Rev*. A33, 3002.

[22] W.R. Nelson, H. Hirayama and D.W.O. Rogers (1985), Stanford Linear Accelerator Center Report SLAC-265 (Stanford).

[23] S. Goudsmit and J.L. Saunderson (1940), *Phys. Rev*. 57, 24 and 58, 36.

[24] A.F. Bielajew and D.W.O. Rogers (1988) in *Monte Carlo Transport of Electrons and Photons*. Ed by T.M. Jenkins, W.R. Nelson and A. Rindi (Plenum, New York) 407.

[25] F. Salvat (1998). Internal report, University of Barcelona.

[26] S.M. Seltzer and M.J. Berger (1985), *Nucl. Instr. and Meth*. B12, 95.

Figure 1. Photon interactions and notation

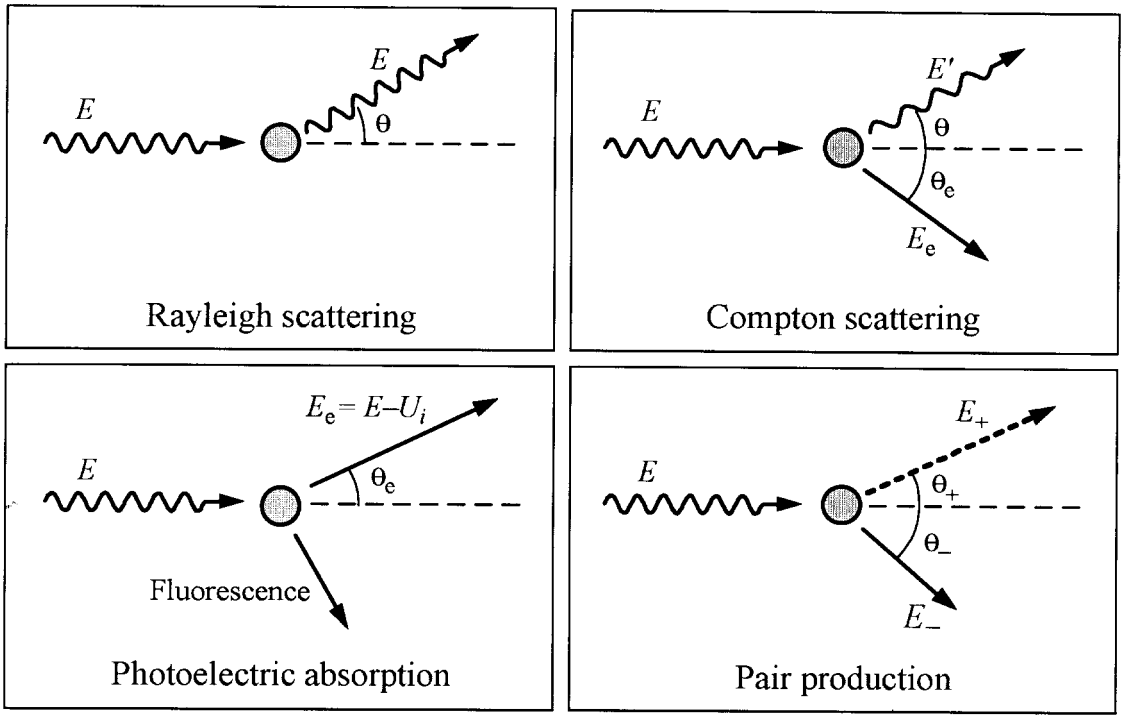

Figure 2. Electron and positron interactions and notation

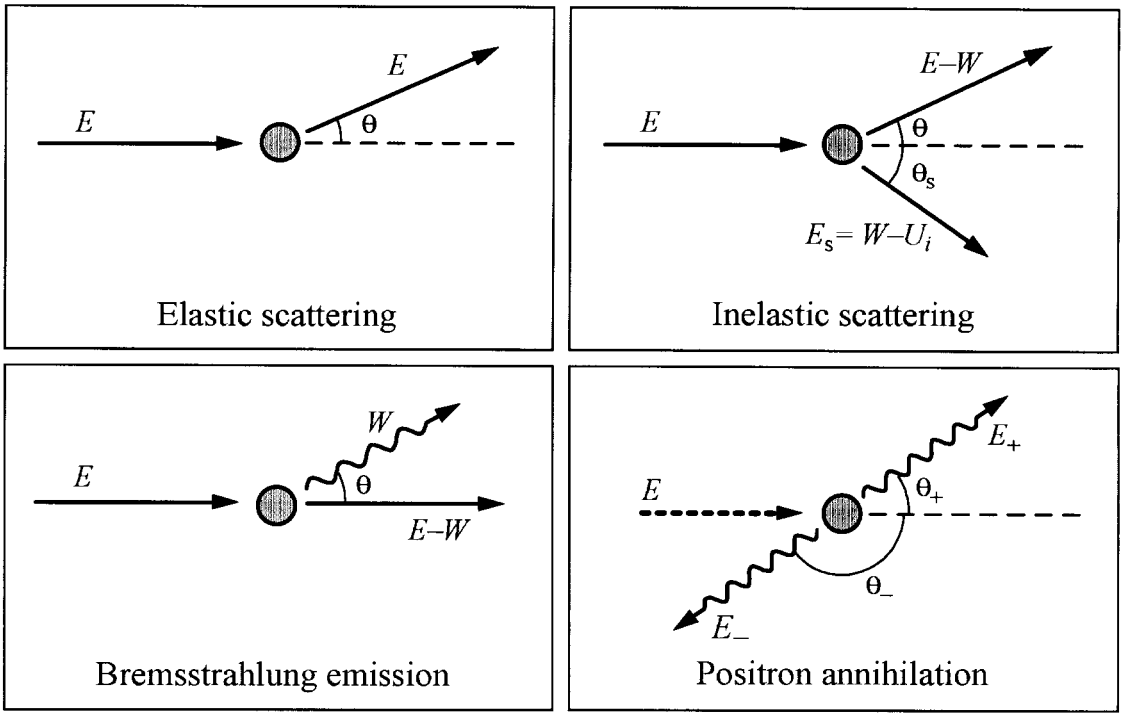

Figure 3. Space displacement algorithm

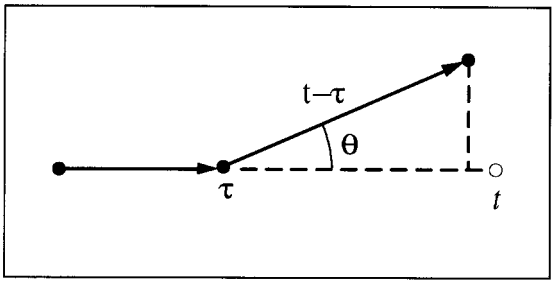

Figure 4. Flow diagram of the MAIN program

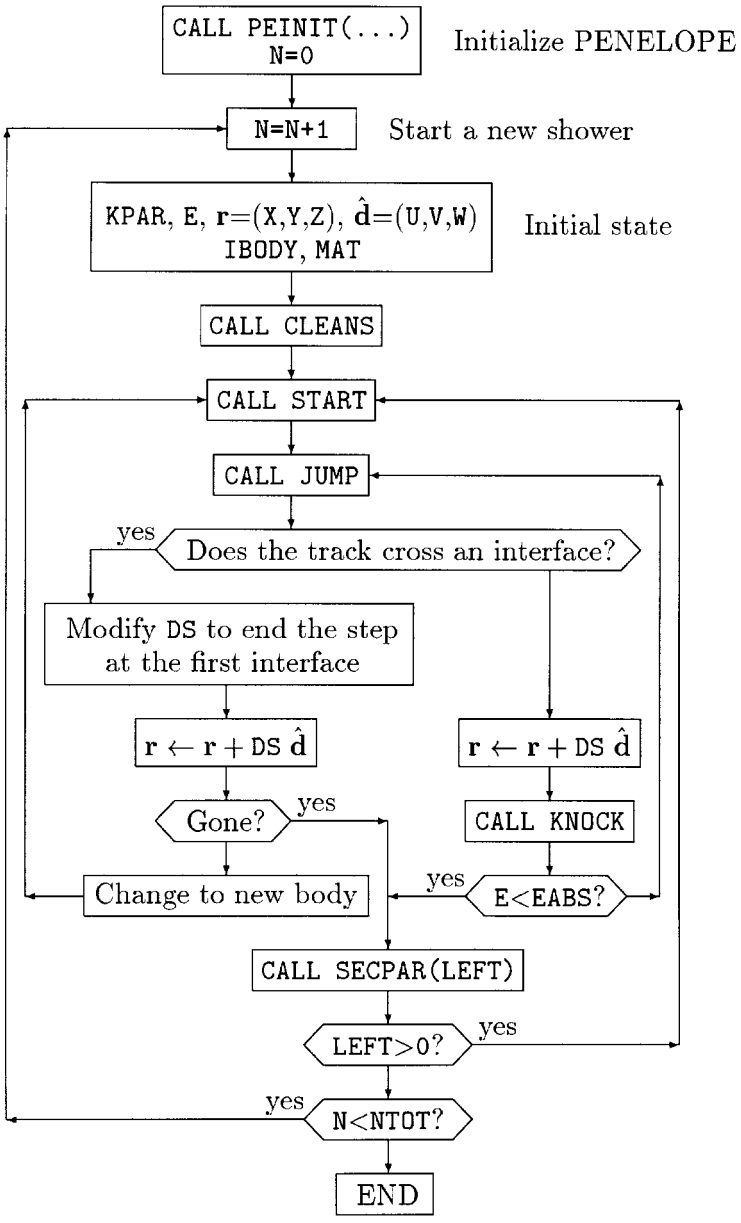

RECENT DEVELOPMENTS, BENCHMARKING AND STATUS OF THE MARS CODE SYSTEM

N.V. Mokhov
Fermi National Accelerator Laboratory
P.O. Box 500, Batavia, Illinois 60510

Abstract

This paper describes the MARS code developments and benchmarking since the previous SATIF meeting in 1997. This time the main efforts have been on the physics model improvements and extensions both in the electromagnetic and strong interaction sectors. The code capabilities to simulate cascades and generate a variety of results in complex media have also been enhanced. Examples of recent applications and MARS benchmarking are presented. The code status is described.

Introduction

The MARS Monte Carlo code system, developed over 24 years, allows fast reliable inclusive simulation of three-dimensional hadronic and electromagnetic cascades in shielding, accelerator and detector components in the energy range from a fraction of an electronvolt up to about 100 TeV [1]. It has been demonstrated at the previous SATIF-3 meeting how nicely the MARS13 code [2,3] reproduces the data for all the considered benchmark problems [4,5,6]. Recent challenging applications at Fermilab induced further significant developments of the code physics model and result scoring capabilities. The main improvements in the current version – MARS13(98) [1] – are described in [7] and highlighted in this paper. Also presented are results of recent benchmarking and several typical examples of recent applications. The code web site, tutorials and future plans are briefly described.

Recent developments

This time the main efforts have been on the physics model improvements and extensions both in the electromagnetic and strong interaction sectors [7]. The code capabilities to simulate cascades and generate a variety of results in complex media have been also enhanced. The main changes compared to the previous release are listed briefly below.

Precise treatment of mixtures and compounds

Precise treatment of individual elements in mixtures and compounds defined through the weight or atomic fractions is done for all the electromagnetic and nuclear elastic and inelastic processes. Homogenisation (averaging) is obsolete now (not recommended). Atomic masses for 100 elements of the periodic table [8] and ionisation and Sternheimer parameters [9,10] are used by the code. All the needed nuclear and electromagnetic cross-sections and other parameters are calculated at the initialisation stage for the chemical elements of the given run with a sample printout. Corresponding array sizes are adjusted according to the energy. A number of composite materials in a given run is up to 50.

Automatic MARS-MCNP interface

The code now includes an automatic interface of MARS materials to the MCNP code [11] for transport of low-energy neutrons and photons.

Hadron-nucleon cross-sections

New compilations and parameterisations of elastic and inelastic σ_{hN} are implemented covering a hadron kinetic energy range 1 MeV <E < 100 TeV.

Photon and hadron-nucleus cross-sections

New compilations, parameterisations and integration algorithms for total, inelastic, production and elastic σ_{hA} and total $\sigma_{\gamma A}$ are implemented at 1 MeV< E <100 TeV (see e.g. [7,8,12]). Examples are shown in Figure 1.

Figure 1. MARS nuclear cross-sections in comparison with experimental data versus projectile momentum: (a) proton-nucleus inelastic and production; (b) photon-nucleus total

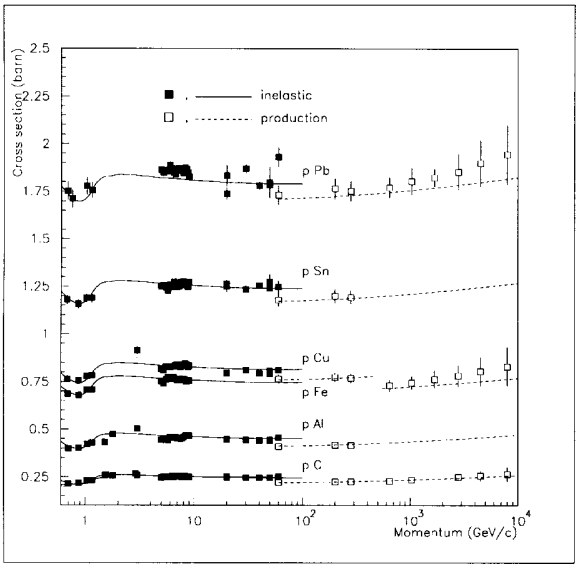

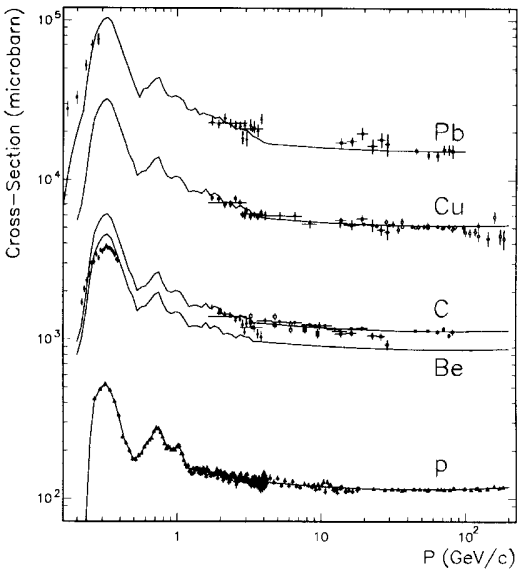

Cascade-exciton model CEM95 and radionuclide production

The Cascade-Exciton Model (CEM95) of nuclear reactions [13] is now implemented as default at 1-10 MeV < E< 3-5 GeV. The 1994 *International Code Comparison for Intermediate Energy Nuclear Data* has shown that CEM95 adequately describes nuclear reactions at intermediate energies and has one of the best predictive powers for double differential cross-sections of secondary particles as compared to other available models. Besides that, it adds to MARS reliable π^--capture description (with a few modifications, e.g. radiative capture $\pi^- p \rightarrow n\gamma$), better description of photon induced reactions in the intermediate energy range and radionuclide production. To be used in MARS, the CEM95 code has been converted into double precision and noticeably modified.

New model for π-production at 5 Ge -100 TeV

A new phenomenological model has been developed and embedded into the MARS code as a default to describe pion production in high-energy proton-nucleus interactions [14]. Special attention is paid to low-momentum pions ($0.1 < p < 2$ GeV/c) for intermediate proton momenta ($5 < p_0 < 30$ GeV/c). Rather sophisticated algorithms have been developed to treat pion production on nuclei in the forward ($x_F > 0$) and backward ($x_F < 0$) hemispheres separately. It is shown that the model predictions are in a good agreement with data in the entire kinematic region (see e.g. Figure 2).

Implementation of DPMJET for primary interactions

The DPMJET-2.3/2.4 code [15] has been implemented into MARS to sample the very first *hN*, *hA*, *AA* and ν*A* interaction at 5 GeV <E < 100 TeV. The coupling – adding the new features to the code – is very time-consuming and is used optionally only.

Figure 2. (a) $pCu \to \pi^- X$ momentum spectra at 5 angles at p_0 = 24 GeV/c; (b) $pCu \to \pi^+ X$ energy spectra at $\theta \approx 0$ for proton momenta of 6 to 13 GeV/c; two curves presented on one plot correspond to higher (top) and lower (bottom) p_0 shown

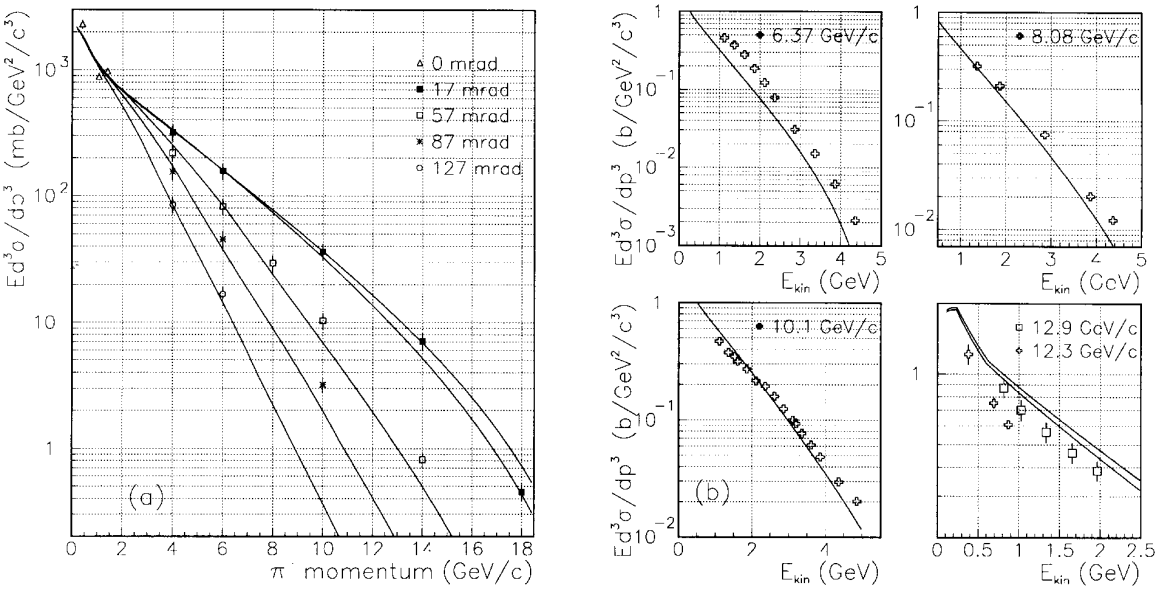

Other developments and enhancements

These include:

- improved description of hadron-nucleus elastic scattering;
- improved description of deuteron-nucleus and neutrino-nucleus interactions;
- detailed description of μ^-, π^- and $\bar{p}$ absorption;
- careful treatment of processes near and below Coulomb barrier in hadron transport (ionisation absorption vs. nuclear interaction vs. decay);
- unified treatment of multiple Coulomb scattering and δ-ray and e^+e^- production for hadrons and muons;
- muon bremsstrahlung update;
- further developments of the Object-Oriented geometry module and visualisation tools;
- improved algorithms for splitting and Russian roulette at *hA* verticies and in particle transport;
- improved algorithms for a particle "deep penetration" problem;
- extended histograming.

Recent benchmarking

The new modules described in the previous section have been thoroughly verified and tested against available data (see e.g. [7,14] and Figures 1 and 2 above). Detailed analysis of the improved electromagnetic algorithms assures that straggling, multiple Coulomb scattering and radiative processes for muons and charged hadrons are described in MARS with a precision of a few per cent. The completed KEK benchmarking on ^{22}Na production at 12 GeV [6], numerous MARS verifications at Fermilab Booster, in fixed target experiments, CDF and DØ collider experiments, results presented by several authors at the recent SARE and SATIF meetings have shown high level of reliability of MARS predictions. A few examples of benchmarking on a macroscopic level are presented below.

Figure 3(a) shows a total yield of neutrons (E < 10.5 MeV) from a 60-cm long lead absorber (R = 10 cm) irradiated with protons of 100 MeV to 100 GeV kinetic energy. MARS13(98) predictions agree very well with those by the SHIELD code [16] and data taken by several groups (see [16] for the references). Dose rates at the outer surface (R = 5.3 m) of the soil shielding of the Fermilab Booster tunnel are shown in Figure 3(b) for a 7.1 GeV proton beam loss in the lattice. Again, MARS results are close to the ionisation chamber data even for such a thick shielding. Calculations with the MARS13(98) code of the pion double differential spectra after a thick copper target for 6 GeV/c protons agree nicely with data (see [14] for the references) in the low momentum region so crucial for $\mu^+\mu^-$ collider applications (see Figure 4(a)).

Figure 4(b) shows attenuation of dose equivalent (E > 20 MeV neutrons only) in a thick iron absorber for parallel almost monoenergetic neutron beams [17]. Results calculated with HETC, ANISN, NMTC, MARS and MCNP codes agree over eight decades (with the exception of HETC) for 400 MeV incident neutrons. For the lower energy beam, agreement is not as good (it seems that statistics in the MARS run was not enough here). Results presented in [17] for a 5-m thick concrete slab agree very well for all 50, 100, 200 and 400 MeV quasi-monoenergetic neutron beams.

Figure 3. (a) Neutron yield (E < 10.5 MeV) out of a cylindrical lead target (L = 60 cm, R = 10 cm) vs. incident proton energy as calculated with the MARS and SHIELD Monte Carlo codes and measured by several groups (see [16]); (b) dose equivalent outside a soil shielding (R = 5.3 m) per a 7.1 GeV proton lost in the Fermilab Booster as calculated with MARS and measured with an ionisation chamber.

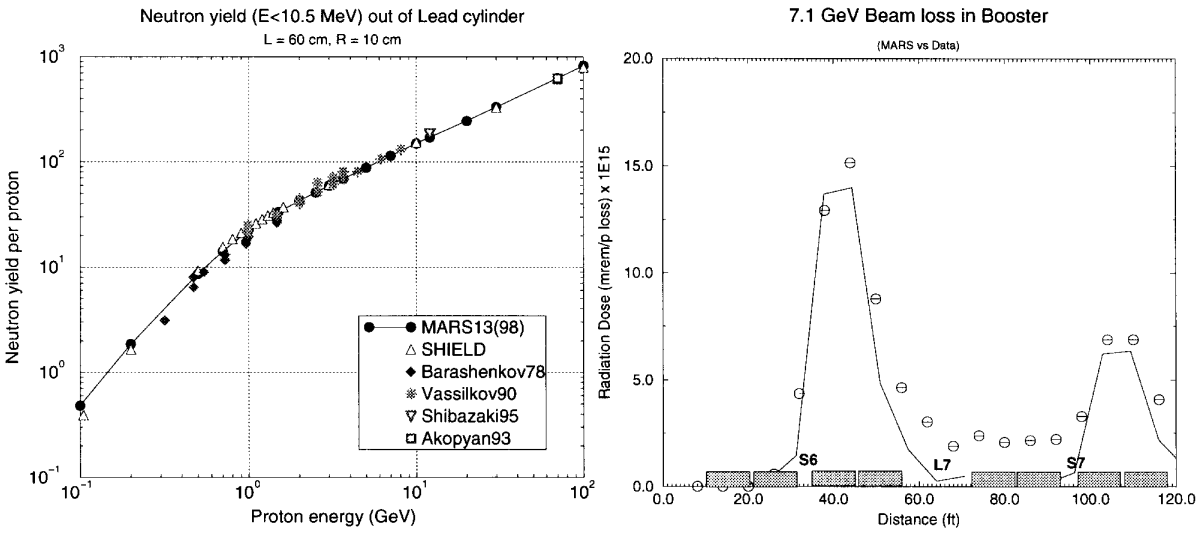

Figure 4. (a) Double differential π^- spectra from a 6-inch thick copper target at p_0 = 6 GeV/c as calculated with GEANT-FLUKA and MARS13(98) and measured (see [14]); (b) dose equivalent due to neutrons (E > 20 MeV) in a thick iron absorber irradiated with 100 and 400 MeV neutron beams as calculated with HETC, ANISN, NMTC, MARS and MCNP codes.

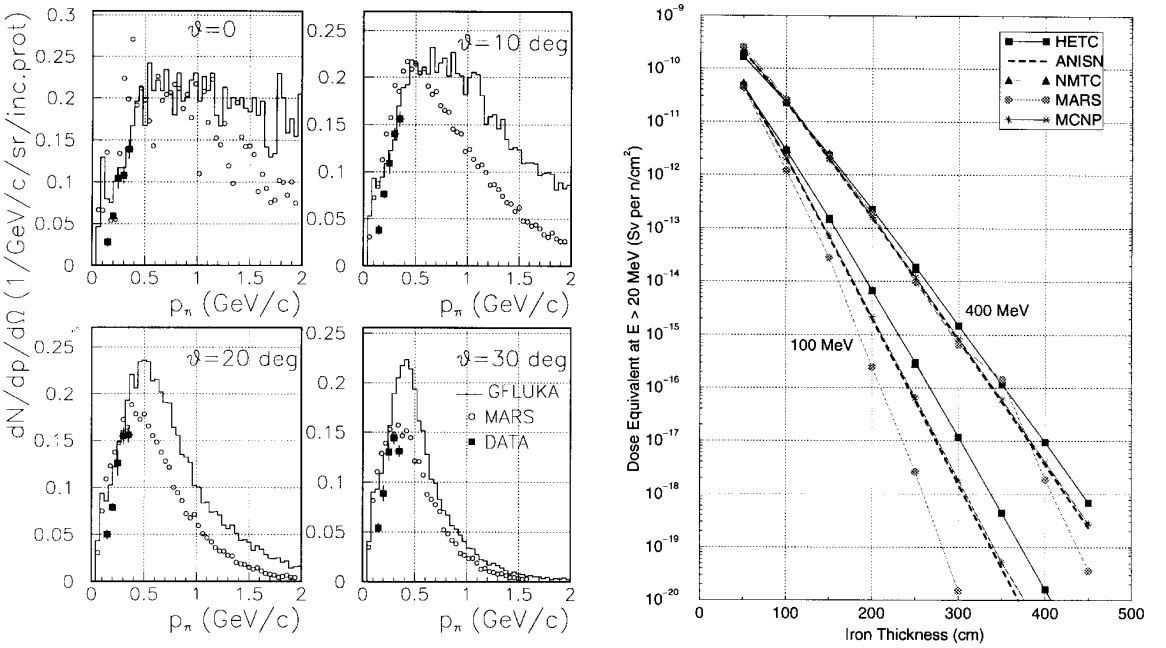

Another benchmarking has been presented at this meeting for a 30-cm thick tissue-equivalent phantom irradiated with a parallel monoenergetic neutron beam of 0.1 to 10 GeV energy [18]. In most cases MARS results are rather close to those by HETC-3STEP (see e.g. Figure 5).

Figure 5. MARS code calculated absorbed dose per unit neutron fluence in a slab tissue-equivalent phantom: (a) maximum dose versus neutron energy in comparison with the HETC-3STEP and FLUKA code predictions; (b) longitudinal dose distributions for several neutron energies.

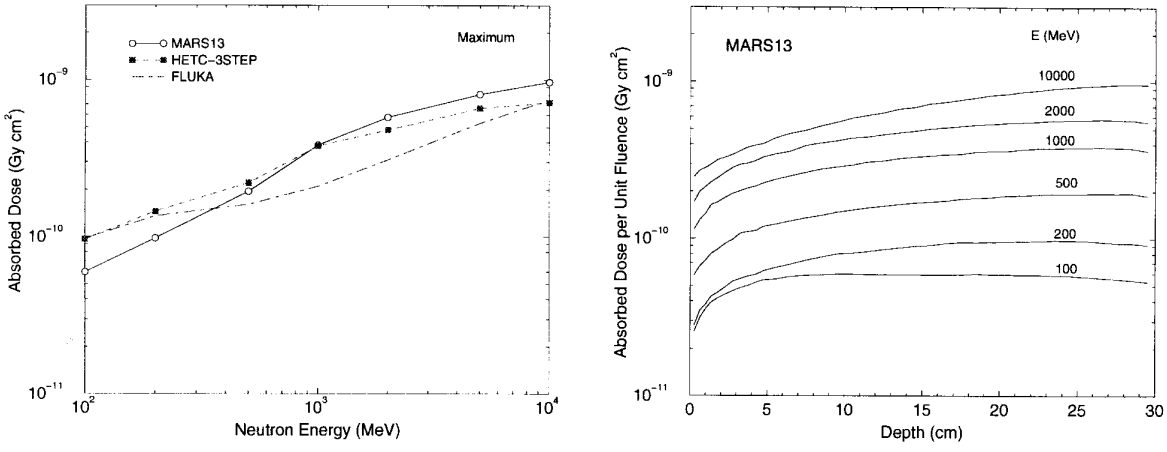

Recent applications

A list of the recent MARS13(98) applications is rather extensive.

Fermilab

- Extensive shielding calculations for the Neutrinos at the Main Injector (NuMI) project to study targetry issues, external shielding, residual activation of components, soil activation and its effects on ground water. All these – for the target station, beam line, tunnel, shielding and beam dump components in the 800 m decay region.
- Beam loss, background and shielding studies for the Forward Proton Detector of the DØ collider experiment.
- Source term, ground water and shielding studies at the 8-GeV Booster.
- Full-scale beam loss, equipment activation and ground water activation studies in the Main Injector 120-GeV beam extraction system.
- Optimisation of a new Tevatron beam collimation system.
- Neutron Therapy Facility collimator optimisation.
- Study of p, n, π^+, π^-, μ^+, μ^-, $\bar{p}$ beams stopped in tissue-equivalent phantoms.

Other projects

- Further optimisation of the LHC low-β interaction regions.
- Machine and collider detector protection at beam accidents at LHC.
- Engineering design of the LHC inner triplet collimators and neutral beam absorbers.
- Beam loss and radiation studies for the Japan Hadron Facility.
- Design of protective measures at beam loss in the 500 × 500 GeV e^+e^- linear collider (TESLA).
- Miscellaneous: target and beam line designs in several fixed target experiments, cosmic rays in ice (AMANDA detector), muons in Gran Sasso experiment, etc.

Code status

The official MARS site on the World Wide Web is *http://www-ap.fnal.gov/MARS/*. There is information about the code, its users and its uses (see Figure 6). One can also register as a user and download the code for various platforms. There are about sixty registered MARS users. A two-day tutorial *The MARS Code System* was conducted at Fermilab in February 1998 for 45 participants.

Figure 6. MARS code web page

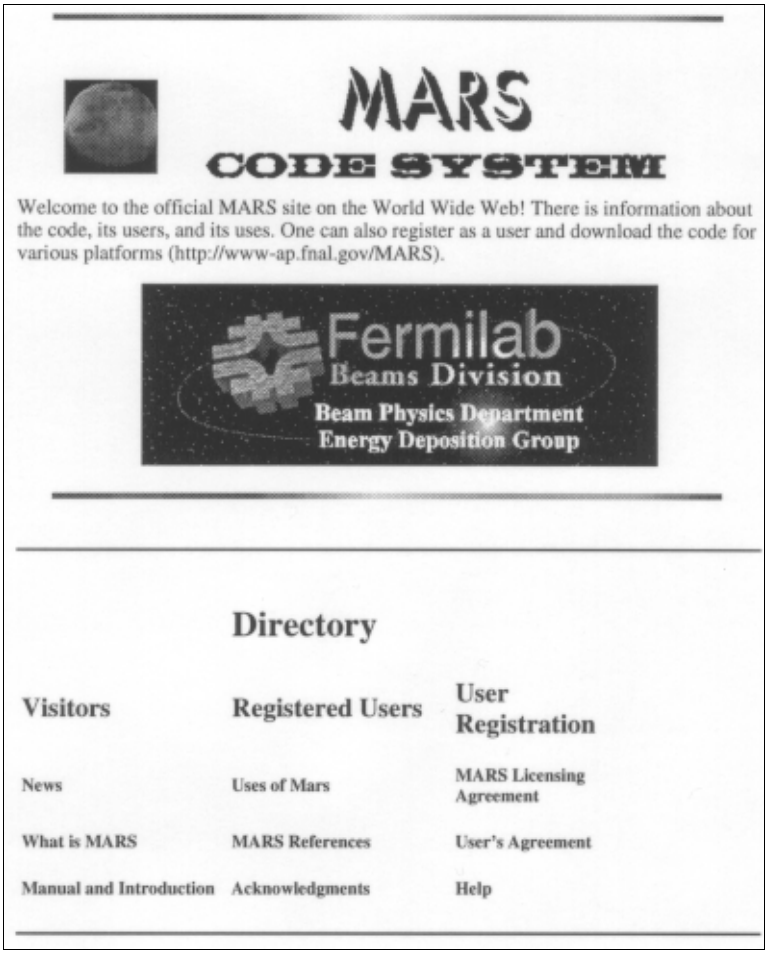

Conclusions

The MARS code possibilities have been substantially extended since the previous SATIF meeting. The code's reliability is confirmed by benchmarking described in this paper and at the recent SATIF/SARE meetings as well as in several recent applications, where MARS predictions have been in excellent agreement with data. The MARS code reliability and unique features allow its successful use in many projects world-wide. The near-term plans include a completion of the manual for the current version, release of a user interface to the Object-Oriented geometry module and visualisation package, improved description of electrons and photons in the 1 keV to 1 MeV energy region and another tutorial in 1999.

REFERENCES

[1] *http://www-ap.fnal.gov/MARS/*

[2] N.V. Mokhov, "The MARS Code System Users Guide, Version 13(95)", Fermilab–FN–628, 1995.

[3] O.E. Krivosheev and N.V. Mokhov, "New MARS and its Applications", Proc. of the Third Workshop on Simulating Accelerator Radiation Environments (SARE3), KEK Proceedings 97-5, June 1997, pp. 12-20; Fermilab–Conf–98/043, 1998.

[4] Y. Nakane *et al*., "Intercomparison of Neutron Transmission Benchmark Analyses for Iron and Concrete Shields in Low, Intermediate and High Energy Proton Accelerator Facilities", OECD Proc. of the Third Specialists Meeting on Shielding Aspects of Accelerators, Targets and Irradiation Facilities (SATIF-3), Tohoku University, Sendai, Japan, May 1997, pp. 151-182.

[5] H. Hirayama, "Intercomparison of the Medium-Energy Neutron Attenuation in Iron and Concrete", see [4], pp. 185-195.

[6] T. Suzuki *et al*., "Comparison Between Soil Benchmark Experiment and MARS Calculation", see [3], pp. 277-283; KEK pre-print 97-15, May 1997.

[7] N.V. Mokhov, S.I. Striganov, A. Van Ginneken, S.G. Mashnik, A.J. Sierk and J. Ranft, "MARS Code Developments", Proc. of the Fourth Workshop on Simulating Accelerator Radiation Environments (SARE4), Knoxville, TN, 14-16 September 1998.

[8] "Review of Particle Physics", *Eur. Phys. J.* C3, 1998.

[9] "Stopping Powers for Electrons and Positrons", ICRU Report No. 37, 1984.

[10] R.M. Sternheimer *et al*., "The Density Effect for the Ionization Loss of Charged Particles in Various Substances", Atomic Data and Nucl. Data Tables, 30, p. 261, 1984.

[11] J.F. Briesmeister, ed., "MCNP – A General Monte Carlo N-Particle Transport Code", Version 4A. Pub. LA–12625–M, LANL, 1993.

[12] V.S. Barashenkov and A. Polanski, "CROSEC", Comm. JINR E2-94-417, Dubna, 1994.

[13] S.G. Mashnik, "User Manual for the Code CEM95", Dubna, 1995, RSIC-PSR-357, Oak Ridge, 1995; S.G. Mashnik and A.J. Sierk, "Improved Cascade-Exciton Model of Nuclear Reactions", Proc. of the Fourth Workshop on Simulating Accelerator Radiation Environments (SARE4), Knoxville, TN, 14-16 September 1998.

[14] N.V. Mokhov and S.I. Striganov, “Model for Pion Production in Proton-Nucleus Interactions”, Proc. of the Workshop on Physics at the First Muon Collider, Fermilab, November 1997, AIP Conf. Proc. No. 435, pp. 453-459; Fermilab–Conf–98/053, 1998.

[15] J. Ranft, *Phys. Rev*., D51, 64, 1995; Gran Sasso report INFN/AE-97/45, 1997.

[16] A.V. Dementyev and N.M. Sobolevsky, “SHIELD – Universal Monte Carlo Hadron Transport Code: Scope and Applications”, Proc. of the Third Workshop on Simulating Accelerator Radiation Environments (SARE3), KEK Proceedings 97-5, June 1997, pp. 21-31.

[17] H. Hirayama, “Intercomparison of the Medium-Energy Neutron Attenuation in Iron and Concrete”, this SATIF-4 meeting.

[18] N. Yoshizawa, “Comparison of Computer Code Calculations for the ICRU Slab Phantom”, this SATIF-4 meeting.

ATLAS OF APPROXIMATIONS OF EXCITATION FUNCTIONS OF PROTON-NUCLEUS REACTIONS

V.G. Semenov
Research Centre of Spacecraft Radiation Safety
of the Heals Ministry of Russia, 123182 Moscow, Russia

N.M. Sobolevsky
Institute for Nuclear Research RAS, 117312 Moscow, Russia

Abstract

The atlas of excitation functions of about 300 proton-nucleus reactions is based on the compilation of radionuclide production cross-sections at intermediate energies (Vol. I/13 of Landolt Boernstein series issued by Springer). The presentation covers only those excitation functions that are measured in detail and includes the expert estimation of data. All functions are fitted with either smoothing spline or Pade-approximant. The proton energy ranges from reaction threshold to 10 GeV. Each page of the atlas concerns a specific excitation function and includes a figure depicting experimental points and the fitting curve as well as a table representation of the fitting curve on a detailed energy grid.

The intent of this work is to present the data on radionuclide production cross-sections in proton-induced nuclear reactions in the form of an atlas of approximations of excitation functions (by definition, an excitation function gives the dependence of the cross-section for the formation of a reaction product on projectile energy).

The atlas includes a representative set of nuclei-targets from Li to U while the incident proton energy varies from a reaction threshold up to 10 GeV. Each excitation function has been presented both in graphical and tabular form for the sake of convenience.

The advantages of this atlas are the experimentally justified description of the threshold behaviour of excitation functions and a wide range of the projectile energy. The main criterion for inclusion of an excitation function into the atlas is its good experimental justification.

The atlas includes a total of about 300 excitation functions for near 50 nuclei-targets.

The initial data set for the approximations is based on the experimental data on radionuclide production cross-sections in proton-nucleus reactions collected in compilation [1], which is presently the most complete collection of such type data in the literature. For fitting and subsequent incorporation into the atlas we have chosen those excitation functions from [1] which include a representative amount of experimental points, cover a wide range of proton energy and describe properly the threshold behaviour. For each excitation function that was accepted for approximation the corresponding experimental values were subjected to an expert estimation based on a number of subjective criteria such as newness, measurement technique, authority of an experimental group, etc.

In some cases the experimental data were supplemented with values calculated on the basis of the known semi-empirical formulas of Silberberg and Tsao [2]. The calculations were performed with the modern version of a computer code, which was kindly put at the disposal of one of the authors (N.S.) by Prof. C.H. Tsao; we are profoundly thankful to Prof. C.H. Tsao for this very useful code. Let us note that the Silberberg-Tsao formulas do not claim to describe the threshold behaviour of an excitation function and are applicable at proton energies above 50-100 MeV. Therefore the calculated values were used at proton energies above 100-200 MeV when they agreed with experimental data tendency with 30-50%.

The excitation functions were fitted either by a smoothing cubic spline or by a Pade-approximant. The type of the fitting function as well as the smoothing parameter for the spline or the rank of the Pade-approximant were chosen with regards to the shape of the excitation function and the number of points used in the fitting procedure.

Each excitation function occupies one page of the atlas and is presented with both plot and table (see Figures 1-4). Every plot depicts experimental points (open rectangles), fitting curve and Silberberg-Tsao points (solid triangles) if they were used in the fitting procedure.

The table of an excitation function contains a set of values of the fitting function on a fixed energy grid. This grid is dense enough to depict all details of the function behaviour (20 steps per logarithmic decade). It seems that such representation is more convenient for the user than tabulation of the matrix of spline coefficients or of the Pade coefficients. The accuracy of the tabulated values corresponds to the accuracy of the experimental data used for the approximation.

Acknowledgements

This work is supported by the International Science and Technology Centre, Project No. 187.

REFERENCES

[1] Production of Radionuclides at Intermediate Energies, ed., H. Schopper. Landolt-Boernstein, Springer Verlag, Berlin-Heidelberg-New York-London-Paris-Tokyo, Subvolumes I/13a (1991), I/13b (1992), I/13c (1993), I/13d (1994), I/13i (1998).

[2] R. Silberberg, C.H. Tsao, *Astrophys. J.*, Suppl. Ser. 25 (1972) 315; *Phys. Rep*. 191 (1990) 351.

Figure 1. Reaction $_{7}N \rightarrow {}^{11}_{6}C$

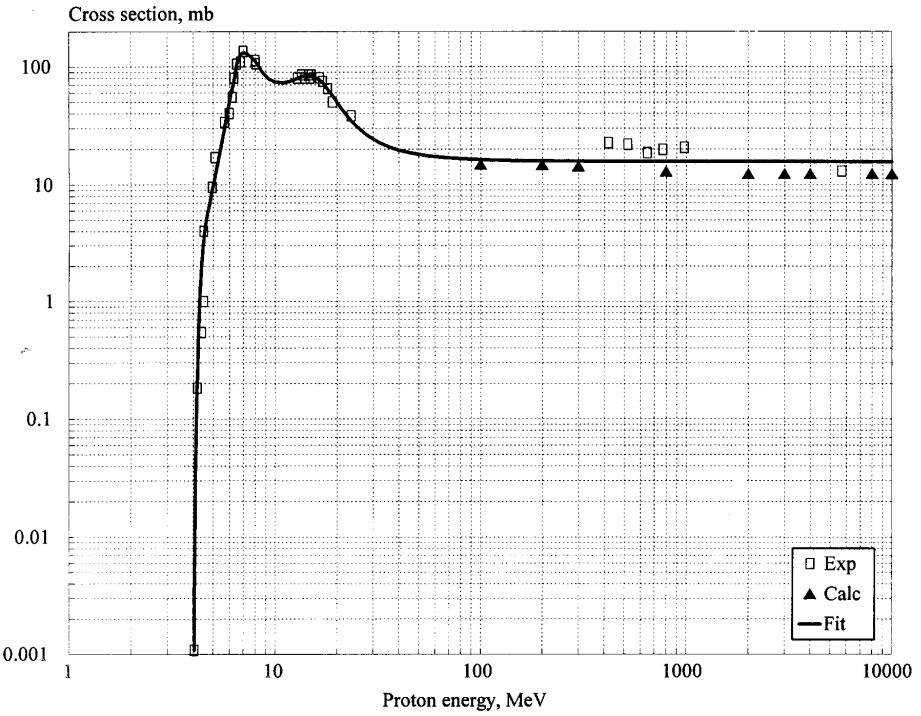

N_0	E_p, MeV	σ, mb	N_0	E_p, MeV	σ, mb	N_0	E_p, MeV	σ, mb
1	4.1	0.001	24	56.0	17.549	47	790	15.695
2	4.5	3.448	25	63.0	17.162	48	890	15.688
3	5.0	9.715	26	70.0	16.896	49	1000	15.683
4	5.6	25.974	27	79.0	16.659	50	1100	15.679
5	6.3	73.621	28	89.0	16.476	51	1250	15.674
6	7.0	131.250	29	100	16.336	52	1400	15.670
7	7.9	114.414	30	110	16.241	53	1600	15.667
8	8.9	85.529	31	125	16.138	54	1800	15.664
9	10.0	74.139	32	140	16.064	55	2000	15.661
10	11.0	72.916	33	160	15.993	56	2250	15.659
11	12.5	78.080	34	180	15.942	57	2500	15.657
12	14.0	83.743	35	200	15.903	58	2800	15.655
13	16.0	79.713	36	225	15.867	59	3200	15.654
14	18.0	64.443	37	250	15.893	60	3600	15.652
15	20.0	49.858	38	280	15.814	61	4000	15.651
16	22.5	37.900	39	320	15.788	62	4500	15.650
17	25.0	30.984	40	360	15.769	63	5000	15.649
18	28.0	26.221	41	400	15.755	64	5600	15.648
19	32.0	22.747	42	450	15.740	65	6300	15.647
20	36.0	20.807	43	500	15.729	66	7000	15.647
21	40.0	19.612	44	560	15.719	67	7900	15.646
22	45.0	18.662	45	630	15.709	68	8900	15.646
23	50.0	18.045	46	700	15.702	69	10000	15.645

Figure 2. Reaction $_{13}Al \rightarrow {}^{7}_{4}Be$

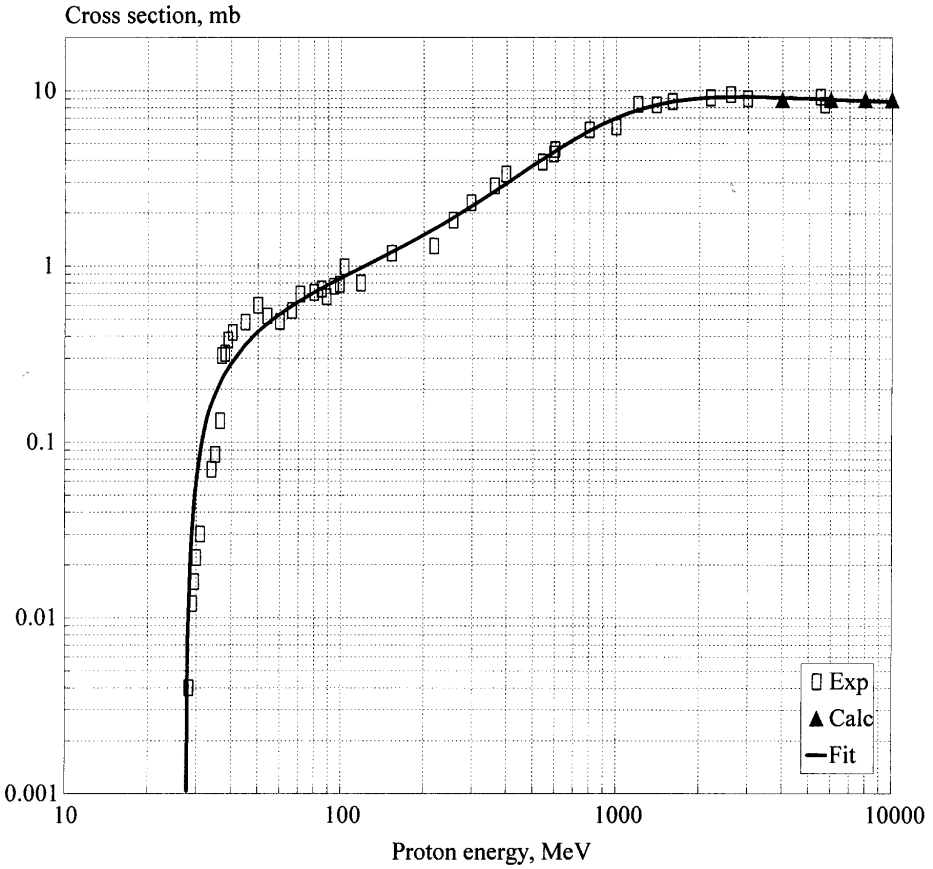

N_0	E_p, MeV	σ, mb	N_0	E_p, MeV	σ, mb	N_0	E_p, MeV	σ, mb
1	27.8	0.001	19	200	1.502	37	1600	8.630
2	28.0	0.008	20	225	1.670	38	1800	8.862
3	32.0	0.118	21	250	1.843	39	2000	9.011
4	36.0	0.206	22	280	2.057	40	2250	9.118
5	40.0	0.280	23	320	2.351	41	2500	9.171
6	45.0	0.358	24	360	2.654	42	2800	9.192
7	50.0	0.425	25	400	2.964	43	3200	9.179
8	56.0	0.494	26	450	3.357	44	3600	9.143
9	63.0	0.565	27	500	3.750	45	4000	9.099
10	70.0	0.628	28	560	4.217	46	4500	9.040
11	37.0	0.701	29	630	4.744	47	5000	8.983
12	89.0	0.776	30	700	5.245	48	5600	8.919
13	100	0.853	31	790	5.838	49	6300	8.853
14	110	0.920	32	890	6.422	50	700	8.795
15	125	1.018	33	1000	6.973	51	7900	8.731
16	140	1.114	34	1100	7.393	52	8900	8.672
17	160	1.242	35	1250	7.898	53	10000	8.618
18	180	1.371	36	1400	8.276			

Figure 3. Reaction $_{26}Fe \rightarrow {}^{51}_{24}Cr$

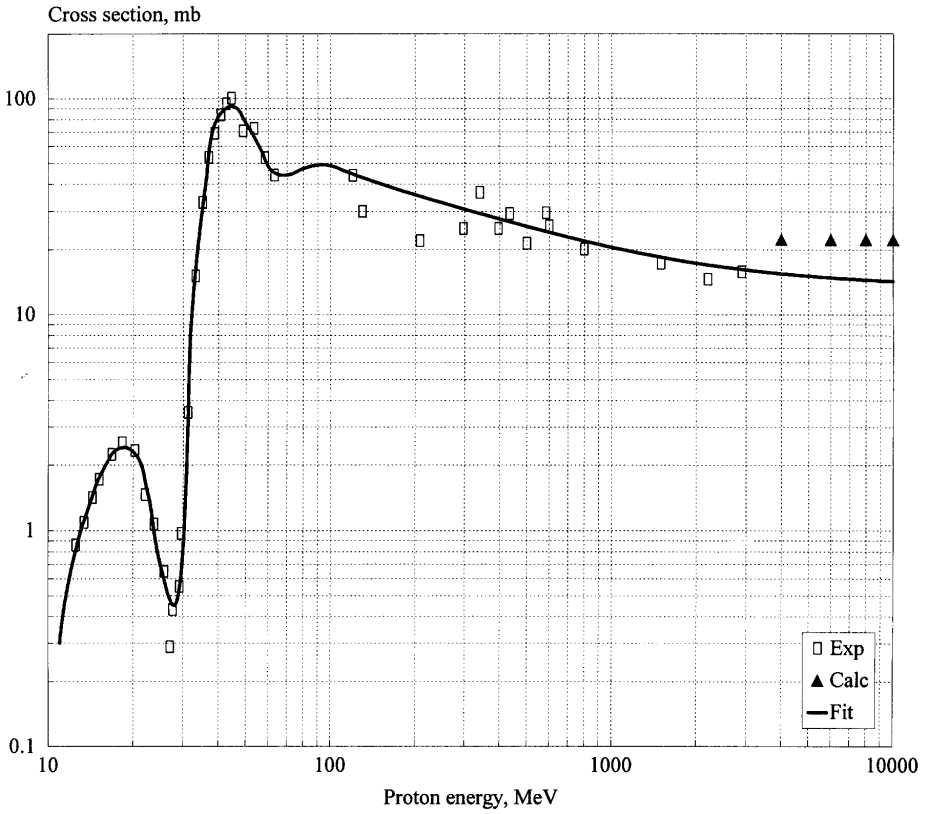

N_0	E_p, MeV	σ, mb	N_0	E_p, MeV	σ, mb	N_0	E_p, MeV	σ, mb
1	11.0	0.301	21	110	46.543	41	1100	19.967
2	12.5	0.805	22	125	43.738	42	1250	19.295
3	14.0	1.298	23	140	41.518	43	1400	18.749
4	16.0	2.002	24	160	39.185	44	1600	18.162
5	18.0	2.399	25	180	37.328	45	1800	17.691
6	20.0	2.303	26	200	35.796	46	2000	17.306
7	22.5	1.495	27	225	34.199	47	2250	16.913
8	25.0	0.704	28	250	32.858	48	2500	16.592
9	28.0	0.449	29	280	31.495	49	2800	16.278
10	32.0	8.837	30	320	29.984	50	3200	15.944
11	36.0	39.733	31	360	28.728	51	3600	15.680
12	40.0	82.290	32	400	27.663	52	4000	15.467
13	45.0	92.062	33	450	26.534	53	4500	15.251
14	50.0	76.998	34	500	25.579	54	5000	15.076
15	56.0	59.403	35	560	24.607	55	5600	14.906
16	63.0	45.248	36	630	23.658	56	6300	14.747
17	70.0	44.138	37	700	22.861	57	7000	14.619
18	79.0	47.007	38	790	22.004	58	7900	14.487
19	89.0	48.994	39	890	21.220	59	8900	14.371
20	100	48.791	40	1000	20.509	60	10000	14.269

Figure 4. Reaction $_{92}U \rightarrow {}^{86}_{37}Rb$

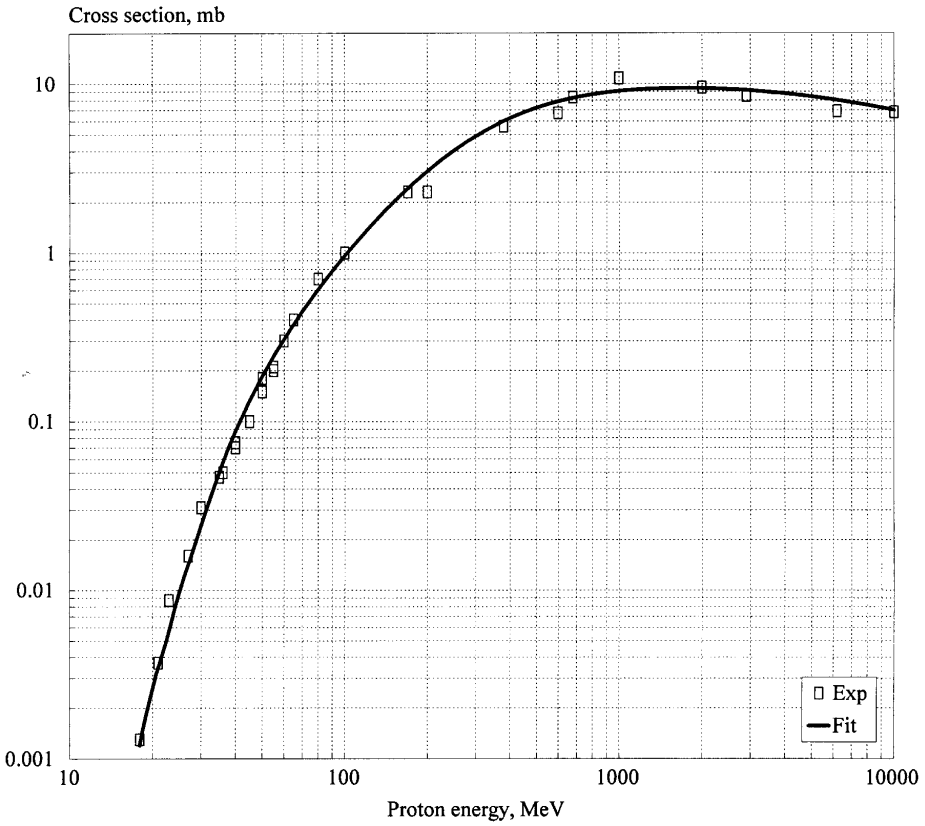

N_0	E_p, MeV	σ, mb	N_0	E_p, MeV	σ, mb	N_0	E_p, MeV	σ, mb
1	18.0	0.001	20	160	2.204	39	1400	9.372
2	20.0	0.003	21	180	2.631	40	1600	9.417
3	22.5	0.005	22	200	3.049	41	1800	9.422
4	25.0	0.010	23	225	3.553	42	2000	9.399
5	28.0	0.017	24	250	4.030	43	2250	9.348
6	32.0	0.033	25	280	4.562	44	2500	9.279
7	36.0	0.057	26	320	5.198	45	2800	9.183
8	40.0	0.088	27	360	5.754	46	3200	9.042
9	45.0	0.133	28	400	6.237	47	3600	8.895
10	50.0	0.185	29	450	6.750	48	4000	8.746
11	56.0	0.256	30	500	7.177	49	4500	8.563
12	63.0	0.348	31	560	7.599	50	5000	8.385
13	70.0	0.449	32	630	7.990	51	5600	8.181
14	79.0	0.592	33	700	8.297	52	6300	7.955
15	89.0	0.763	34	790	8.600	53	7000	7.744
16	100	0.966	35	890	8.848	54	7900	7.493
17	110	1.159	36	1000	9.043	55	8900	7.238
18	125	1.463	37	1100	9.171	56	10000	6.984
19	140	1.778	38	1250	9.298			

LIST OF PARTICIPANTS

FRANCE

M. Francois CLAPIER
Ingenieur de Radioprotection
CNRS-IN2P3
Institut Physique Nucleaire
SPR
91406 ORSAY

Tel: +33 (1) 6915 7170
Fax: +33 (1) 6915 6470
E-mail: clapier@ipncls.in2p3.fr

GERMANY

Dr. Detlef FILGES
Institut fuer Kernphysik
Forschungszentrum Juelich GmbH
D-52425 JUELICH

Tel: +49 (2461) 61 5232
Fax: +49 (2461) 61 3930
E-mail: d.filges@fz-juelich.de

* Mr. Vladimir MARES
Universitaet Muenchen
Strahlenbiologisches Institut
Schillerstrasse 42g
D-80336 MUENCHEN

Tel: +49 (89) 5996 838 or 3187 2652
Fax: +49 (89) 5996 840 or 3187 3323
E-mail: mares@gsf.de

Mr. Brunhilde A. RACKY
DESY
Notkestrasse 85
D-22607 HAMBURG

Tel: +49 (49) 89 98 36 90
Fax: +49 (40) 89 98 32 82
E-mail: brunhilde.racky@desy.de

Mr. Hartwig SCHAAL
KFA-Juelich, IKP
Forschungszentrum Juelich GmbH
Institut fuer Kernphysik
D-52425 JUELICH

Tel: +49 (2461) 61 4004
Fax: +49 (2461) 61 3930
E-mail: h.schaal@fz-juelich.de

Mr Guenter STERZENBACH
Institut fuer Kernphysik
Forschungszentrum Juelich GmbH
D-52425 JUELICH

Tel: +49 2461 / 61 - 5232
Fax: +49 2461 / 61 - 3930
E-mail: G.Sterzenbach@fz-juelich.de

ITALY

Dr. Kenneth W. BURN
ENEA
Via Martiri di Monte Sole 4
I-40129 BOLOGNA

Tel: +39 (51) 6098 486
Fax: +39 (51) 6098 629
E-mail: kburn@bologna.enea.it

Dr. Enzo MENAPACE
ENEA, Applied Physics Division
Via Don G. Fiammelli 2
I-40128 BOLOGNA
Tel: +39 (51) 60 98 239
Fax: +39 (51) 60 98 359
E-mail: menapace@bologna.enea.it

Dr. Carla ONGARO
Dip. Fisica Sperimentale
Università di Torino
Via Pietro Giuria 1
I-10125 TORINO
Tel: +39 (11) 670 7314
Fax: +39 (11) 669 1104
E-mail: ongaro@to.infn.it

Prof. Maurizio PELLICCIONI
INFN
Laboratori Nazionali di Frascati
Casella Postale 56
I-00044 FRASCATI
Tel: +39 (6) 940 32246
Fax: +39 (6) 940 32364
E-mail: maurizio.pelliccioni@lnf.infn.it

JAPAN

Mr. Michihiro FURUSAKA
KENS, KEK
101 Oho
TSUKUBA 305-0801
Tel: +81 292 64 5618
Fax: +81 298 64 3202
E-mail: michihiro.furusaka@kek.jp

* Dr. Katsumi HAYASHI
Hitachi Engineering Company
3-2-1 Saiwai-cho
Hitachi-shi
IBARAKI-KEN 317-0073
Tel: +81 (294) 21 7330
Fax: +81 (294) 23 6700
E-mail: k_hayashi@psg.hitachi-hec.co.jp

Prof. Hideo HIRAYAMA
KEK, High Energy Accelerator
Research Organisation
1-1 Oho
Tsukuba-shi
IBARAKI-KEN 305-0801
Tel: +81 (298) 64 5489
Fax: +81 (298) 64 1993
E-mail: hideo.hirayama@kek.jp

Dr. Satoshi IWAI
Nuclear Development Corp.
1-297 Kitabukuro-cho
Omiya-shi
SAITAMA-KEN 330-0835
Tel: +81 (48) 642 4404
Fax: +81 (48) 645 0189
E-mail: iwais@atom.hq.mhi.co.jp

Dr. Masayoshi KAWAI
High Energy Accelerator Research Org.
1-1 Oho
Tsukuba-shi
IBARAKI-KEN 305-0801
Tel: +81(0)298 64 5637
Fax: +81(0)298 64 3202
E-mail: masayoshi.kawai@kek.jp

Prof. Takashi NAKAMURA
Cyclotron and Radioisotope Centre
Tohoku University
Aramaki, Aoba, Aoba-ku
SENDAI 980-8578
Tel: +81 (22) 217 7805
Fax: +81 (22) 217 7809
E-mail: nakamura@cyric.tohoku.ac.jp

Dr. Hiroshi NAKASHIMA
Applied Radiation Laboratory
JAERI
Tokai Research Establishment
Tokai-Mura
IBARAKI-KEN 319-1195
Tel: +81 29 282 6144
Fax: +81 29 282 5996
E-mail: nakasima@shield4.tokai.jaeri.go.jp

Dr. Yukio SAKAMOTO
Accelerator Radiation Lab.
Center for Neutron Science
JAERI
Tokai-mura, Naka-gun
IBARAKI-KEN 319-1195
Tel: +81 (29) 282 5355
Fax: +81 (29) 282 5663
E-mail: sakamoto@shield4.tokai.jaeri.go.jp

* Prof. Kazuo SHIN
Dept. of Nuclear Engineering
Kyoto University
Yoshida
Sakyo-ku
KYOTO 606-8501
Tel: +81 (75) 753 5825
Fax: +81 (75) 753 5845
E-mail: shin@east.nucleng.kyoto-u.ac.jp

Dr. Yoshitomo UWAMINO
Safety Center
RIKEN
2-1, Hirosawa
Wako, SAITAMA 351-0198
Tel: +81 (48) 467 9292
Fax: +81 (48) 462 4616
E-mail: uwamino@postman.riken.go.jp

Dr. Nobuaki YOSHIZAWA
Mitsubishi Research Institute
3-6, Otenachi 2-Chome
Chiyoda-ku
TOKYO, 100-8141
Tel: +81 (3) 3277 0772
Fax: +81 (3) 3277 3480
E-mail: yoshizaw@mri.co.jp

P.R. OF CHINA

Mr. Huazhi ZHENG
Institute of Modern Physics
Chinese Academy of Sciences
363 Nanchang Road
LANZHOU 730000
Tel: ++86 (931) 885 4949
Fax: ++86 (931) 888 1100
E-mail: zhz@ns.lzb.ac.cn

RUSSIAN FEDERATION

Mr. Lokhovitskii ARKADY
Institute for High Energy Physics
Protvino, Pobeda Str. 1
142284 Moscow Region
Tel: +7 (0967) 713 248
Fax: +7 (0967) 744 907
E-mail: lokhovitskii@mx.ihep.su

Dr. Igor DEGTYAREV
Institute for High Energy Physics
Protvino, Pobeda Str. 1
142284 Moscow Region
Tel: +7 (0967) 713 248
Fax: +7 (0967) 744 907
E-mail: degtyarev@mx.ihep.su

* Elena GELFAND
Moscow Radiotechnical Inst.
Russian Academy of Sciences
Varshavskoe shosse, 132
MOSCOW 113519
Tel: +7 (095) 315 3122
Fax: +7 (095) 314 1053
E-mail: gelfand@mankobv.msk.ru

Dr. Nikolay M. SOBOLEVSKY
Instit. for Nuclear Research
of Russian Academy of Science
60-th October Anniversary
Prospect, 7a
MOSCOW 117312
Tel: +7 (095) 242 5366
Fax: +7 (095) 135 2268
E-mail: sobolevsky@al20.inr.troitsk.ru

Boris SYCHEV
Moscow Radiotechnical Inst.
Russian Academy of Sciences
Varshavskoe shosse, 132
MOSCOW, 113519
Tel: +7 (095) 315 3122
Fax: +7 (095) 314 1053
E-mail: sychev@mankobv.msk.ru

SPAIN

Prof. Francesc SALVAT
Facultat de Fisica (ECM)
Universitat de Barcelona
Diagonal 647
08028 BARCELONA
Tel: +34 93 402 11 86
Fax: +34 93 402 11 74
E-mail: cesc@ecm.ub.es

UNITED STATES OF AMERICA

Dr. R.G. ALSMILLER
Oak Ridge National Laboratory
P.O. Box 2008
Oak Ridge TN 37831-6418
Tel: +1 423 574 6081
Fax: +1 423 574 9619
E-mail: tut@ornl.gov

Mr. H.I. AMOLS
Department of Medical Physics
Memorial Sloan-Kettering Cancer Center
1275 York St.
NEW YORK, NY 10021
Tel: +1 (212) 639 6807
Fax: +1 (212) 717 3010
E-mail: amolsh@mskcc.org

Mr. Alex F. BIELAJEW
Dept. of Nuclear Eng. & Radiological Science
The University of Michigan
Cooley Bldg. (North Campus),Room 2927
2355 Bonisteel Boulevard
ANN ARBOR, MI 48109-2104
Tel: +1 734 764 6364
Fax: +1 734 763 4540
E-mail: alex@aeh.engin.umich.edu

Dr. Jeffrey BULL
Los Alamos National Laboratory
P.O. Box 1663
LOS ALAMOS, NM 87545
Tel: +1 (505) 667 8313
Fax: +1 (505) 664 4049
E-mail: jsbull@lanl.gov

Dr. Marcia M. CAMPOS TORRES
Argonne National Laboratory
Env. Safety and Health Div.
4700 South Cass Avenue
ARGONNE, IL 60439
Tel: +1 (630) 252 9257
Fax: +1 (630) 252 5778
E-mail: mtorres@fnalc.fnal.gov

Lowell A. CHARLTON
ORNL
P.O. Box 2008
MS 6363
OAK RIDGE, TN 37831-6363
Tel: +1 (423) 574 0628
Fax: +1 (423) 574 9619
E-mail: lac@ornl.gov

Mr. Dermott E. CULLEN
Lawrence Livermore National Laboratory
L-59
P.O. Box 808
LIVERMORE, CA 94550
Tel: +1 (925) 423 7359
Fax: +1 (925) 422 9560
E-mail: cullen1@llnl.gov

* Dr. Pavel DEGTIARENKO
Radiation Control Group
Jefferson Laboratory MS89
12000 Jefferson Avenue
NEWPORT NEWS, VA 23606
Tel: +1 (757) 269-6274
Fax: +1 (757) 269-7352
E-mail: pavel@jlab.org

Dr. Alberto FASSÒ
SLAC
Radiation Physics Dept.
MS-48
P.O. BOX 4349
STANFORD, CA 94309
Tel: +1 (650) 926 4062
Fax: +1 (650) 926 3569
E-mail: fasso@slac.stanford.edu

Dr. Tony A. GABRIEL
Oak Ridge National Laboratory
P.O. Box 2008
OAK RIDGE, TN 37831-6364
Tel: +1 (615) 574 6082
Fax: +1 (615) 574 9619
E-mail: tag@ornl.gov

Mr. Melvyn L. HALBERT
Oak Ridge National Laboratory
Building 6000
MS 6368
OAK RIDGE, TN 37831-6368
Tel: +1 (423) 574 4723
Fax: +1 (423) 574 1268
E-mail: halbert@mail.phy.ornl.gov

Dr. Nolan E. HERTEL
George Woodroof School of
Mechanical Engineering
Georgia Institute of Technology
ATLANTA, GA 30332-0405
Tel: +1 (404) 894 3717
Fax: +1 (404) 894 3733
E-mail: nolan.hertel@me.gatech.edu

Mr. Grady HUGHES
Los Alamos National Laboratory
MS B226
LOS ALAMOS, NM 87547-1663
Tel: +1 (505) 667 5957
Fax: +1 (505) 665 5538
E-mail: hgh@lanl.gov

Dr. Nisy E. IPE
SLAC
Radiation Physics Dept. MS-48
P.O. Box 4349
STANFORD, CA 94309
Tel: +1 (650) 926 4324
Fax: +1 (650) 926 3569
E-mail: ipe@slac.stanford.edu

Dr. Pankakkal JOB
Advanced Photon Source
Argonne National Laboratory
9700 South Cass Avenue
ARGONNE, IL 60439-4803
Tel: +1 (630) 252 6573
Fax: +1 (630) 252 3222
E-mail: pkj@aps.anl.gov

Ms. Bernadette L. KIRK
Radiation Safety Information
Computational Center
Oak Ridge National Laboratory
P.O. Box 2008
OAK RIDGE, TN 37831-6362
Tel: +1 (423) 574 6176
Fax: +1 (423) 574 6182
E-mail: blk@ornl.gov

* Mr. H.B. KNOWLES
Physics Consulting
4030 Hillcrest Road
EL SOBRANTE, CA 94803
Tel: +1 (510) 758 4630
Fax: +1 (510) 758 5449
E-mail: hbknowls@ix.netcom.com

Dr. Robert C. LITTLE
Los Alamos National Laboratory
Radiation Transport Group
Group X-CI, MS F633
P.O. Box 1663
LOS ALAMOS, NM 87545
Tel: +1 505 665-3487
Fax: +1 505 665-5538
E-mail: rcl@lanl.gov

Mrs. Jennie MANNESCHMIDT
Radiation Shielding Information Center
Oak Ridge National Laboratory
P.O. Box 2008
OAK RIDGE, TN 37830-6362
Tel: +1 (423) 574 6176
Fax: +1 (423) 574 6182
E-mail: jib@ornl.gov

Dr. Nikolai MOKHOV
FERMILAB
MS 220
P.O. Box 500
BATAVIA, IL 60510-500
Tel: +1 (630) 840 4409
Fax: +1 (630) 840 6039
E-mail: mokhov@fnal.gov

Dr. Eric PITCHER
LANL-LANSCE
MS H816
Los Alamos National Laboratory
LOS ALAMOS, NM 87545
Tel: +1 (505) 665 0651
Fax: +1 (505) 667 7443
E-mail: pitcher@lanl.gov

Dr. Sayed H. ROKNI
Radiation Physics Department
SLAC
P.O. Box 4349
STANFORD, CA 94309
Tel: +1 (650) 926 3544
Fax: +1 (650) 926 3569
E-mail: rokni@slac.stanford.edu

Dr. Robert W. ROUSSIN
Director of Radiation
Information Analysis
Oak Ridge National Laboratory
P.O. Box 2008
OAK RIDGE, TN 37831-6362
Tel: +1 (423) 574 6176
Fax: +1 (423) 574 6182
E-mail: rwr@ornl.gov

Mr. Edward C. SNOW
Bechtel Nevada/Lockheed Martin Technology
182 Eastgate Drive
P.O. Box 809
LOS ALAMOS, NM 87544
Tel: +1 505 667 0227
Fax: +1 505 667 2672
E-mail: snowec@nv.doe.gov

Mr. Michele R. SUTTON
Georgia Institute of Technology
900 Atlantic Drive
ATLANTA, GA 30332
Tel: +1 404 894 9954
Fax: +1 404 894 9325
E-mail: sutton@nukeisit.gatech.edu

Mr. Jeremy E. SWEEZY
Georgia Institute of Technology
Neely Nuclear Research Center
909 Atlantic Drive
ATLANTA, GA 30332-0425
Tel: +1 404 894 3600
Fax: +1 404 894 9325
E-mail: sweezy@nukeisit.gatech.edu

Mr. Ken. A. VAN RIPER
White Rock Science
P.O. Box 4729
LOS ALAMOS, NM 87544
Tel: +1 505 672 1105
Fax:
E-mail: kvr@rt66.com

Dr. K. VAZIRI
MS 119
Fermi National Accelerator Laboratory
(FNAL)
P.O. Box 500
BATAVIA IL 60510
Tel: +1 (630) 840 3457
Fax: +1 (630) 840 3390
E-mail: vaziri@fnal.gov

Dr. Laurie S. WATERS
MS H816
Los Alamos National Laboratory
LOS ALAMOS, NM 87544
Tel: +1 (505) 665 4127
Fax: +1 (505) 667 7443
E-mail: lsw@lanl.gov

Dr. Morgan C. WHITE
Los Alamos National Laboratory
Group X-CI, MS F663
LOS ALAMOS, NM 87545
Tel: +1 (505) 665 3684
Fax: +1 (505) 665 5553
E-mail: morgan@lanl.gov

Ms. Suzanne WILLIS
Physics Department
Northern Illinois University
DEKALB, IL 60115
Tel: +1 (815) 753 0667
Fax: +1 (815) 753 8565
E-mail: swillis@niu.edu

INTERNATIONAL ORGANISATIONS

* Dr. Enrico SARTORI
OECD/NEA Data Bank
Le Seine-Saint Germain
12, Boulevard des Iles
F-92130 ISSY-LES-MOULINEAUX
Tel: +33 (0)1 45 24 10 72
Fax: +33 (0)1 45 24 11 10
E-mail: sartori@nea.fr

Dr. Pedro VAZ (Secretary)
OECD/NEA Data Bank
Le Seine-Saint Germain
12, Boulevard des Iles
F-92130 ISSY-LES-MOULINEAUX
Tel: +33 (0)1 45 24 10 74
Fax: +33 (0)1 45 24 11 10
E-mail: vaz@nea.fr

Stefan ROESLER
CERN/EST-Div.
CH-1211 GENEVA 23
Tel: +41 (22) 767 8864
Fax: +41 (22) 767 9089
E-mail: Stefan.Roesler@cern.ch

Dr. Marco SILARI
CERN
TIS-RP
CH-1211 GENEVA 23
Tel: +41 (22) 767 3937
Fax: +41 (22) 767 5700
E-mail: marco.silari@cern.ch

Dr. Graham Roger STEVENSON
CERN
CH-1211 GENEVA 23
Tel: +41 (22) 767 4623
Fax: +41 (22) 767 9800
E-mail: Graham.Stevenson@cern.ch

** Regrets not being able to attend.*

FINAL AGENDA OF SATIF-4

Thursday, 17 September 1998

Registration

Welcome – *R.W. Roussin*

Opening remarks – *T. Gabriel*

Session I: Source Term and Related Data – Electron Accelerator
Chairs: H. Hirayama and A. Bielajew

Dose Measurements of Bremsstrahlung Produced Neutrons from Thick Targets at the Advanced Photon Source (25′)	(P.K. Job)
Further Measurements of Gas Bremsstrahlung from the Insertion Device Beamlines of the Advanced Photon Source (25′)	(P.K. Job)

Session II: Source Term and Related Data – Proton and Ion Accelerator
Chairs: D. Filges and G. Stevenson

A Systematic Experimental Study of Thick-Target Neutron Yield for High-Energy Heavy Ions (25′)	(T. Nakamura)
Thin and Thick Target Spallation Target Benchmark Investigations of Neutron Multiplicities to Validate Spallation Physics Models (25′)	(D. Filges)
Radiation Shielding at the Heavy Ion Research Facility in Lanzhou (HIRFL) (25′)	(H. Zheng)

Session III: Shielding Design Problem on High Intensity Medium Energy Accelerators and Target Facilities
Chairs: T. Nakamura and T. Gabriel

Methods to Calculate Spallation Source Shields and Comparison with Experiment (25′)	(H. Schaal)
Shielding Design of the SNS (25′)	(J. Johnson)
Shielding Design of the ESS (25′)	(D. Filges)
Design of the Spallation Neutron Source in Japan (25′)	(M. Kawai)

Shielding Design of RIKEN RI Beam Factor (25′) (Y. Uwamino)

Summary and Discussion (25′) (T. Nakamura)

Session IV: Shielding Benchmark Calculations and Results
Chairs: A. Fassò and L. Waters

Proposal for an International Benchmark Exercise on e-/e+ Photon Physics (25′) (A. Bielajew)

Intercomparison of the Medium-Energy Neutron Attenuation in Iron and Concrete (25′) (H. Hirayama)

Intercomparison of Neutron Transmission Benchmark Analysis for Iron and Concrete Shields in TIARA (25′) (Y. Sakamoto)

Friday, 18 September 1998

Session V: Miscellaneous Topics
Chairs: B. Kirk and M. Silari

Radioactive Ion Beam Facilities

Radioactive Beam Facilities: New Thick Targets, Highlights and Challenges (25′) (F. Clapier)

Dose Conversion Coefficient

Conversion Coefficients, Fluence-to-Effective Dose for Charged Pions and Radiation Weighting Factors for High-Energy Radiation (25′) (M. Pelliccioni)

Overview of Dose-Conversion Coefficient (25′) (S. Iwai)

The Concept of Dose Equivalent for Beam Exposure (25′) (S. Iwai)

Anthropomorphic Phantom

Comparison of Computer Code Calculations for the ICRU Slab Phantom (25′) (N. Yoshizawa)

Session VI: Present Status of Computer Codes and Cross-Section and Shielding Data Libraries
Chairs: R. Roussin and M. Pelliccioni

Report on the Collection of Computer Codes and Data Sets for Accelerator Shielding Modelling (25′) (B. Kirk)

PENELOPE: Taking Advantage of Class II Simulation (25′) (F. Salvat)

Recent Developments, Benchmarking and Official Status of the MARS Code System (25′)	(N. Mokhov)
Atlas of Approximations of Excitation Functions of Proton Induced Reactions (25′)	(N. Sobolevski)

Session VII: Discussion and Future Actions
Chair: N. Ipe

Monitoring the Actions Undertaken Since SATIF-3; Scrutinising Priority Areas and Future Actions	(A. Fassò, M. Silari)
General Discussion	

Closing remarks	(R.W. Roussin, P. Vaz)

OECD PUBLICATIONS, 2, rue André-Pascal, 75775 PARIS CEDEX 16
PRINTED IN FRANCE
(66 1999 06 1 P) ISBN 92-64-17044-8 – No. 50669 1999